

**Analysis of wedge-shaped waveguides and
desing of multipactor-resistant microwave
bandpass filters**

JAIME HUESO GONZÁLEZ

EDITORIAL
UNIVERSITAT POLITÈCNICA DE VALÈNCIA



UNIVERSIDAD
POLITECNICA
DE VALENCIA

UNIVERSIDAD POLITÉCNICA DE VALENCIA

Departamento de Comunicaciones

**ANALYSIS OF WEDGE-SHAPED WAVEGUIDES
AND DESIGN OF MULTIFACTOR-RESISTANT
MICROWAVE BANDPASS FILTERS**

Jaime Hueso González

Directores:

Dr. Vicente E. Boria Esbert (Universidad Politécnica de Valencia)

Dr. Benito Gimeno Martínez (Universitat de València Estudi General)

**Tesis Doctoral presentada en la Universidad Politécnica de
Valencia para la obtención del título de Doctor Ingeniero
de Telecomunicación**

Valencia, Octubre 2013

Collection Doctoral Theses

© Jaime Hueso González

First Edition, 2013

© of the present edition:

Editorial Universitat Politècnica de València
www.lalibreria.upv.es

ISBN: 978-84-9048-066-3 (printed version)

Any unauthorized copying, distribution, marketing, editing, and in general any other exploitation, for whatever reason, of this piece of work or any part thereof, is strictly prohibited without the authors' expressed and written permission.

*A mi mujer Cécile,
a mi madre María Ángela y a mi padre José Luis,
y a mis abuelos Emilia, Abilio, Begoña y Jaime.*

Agradecimientos

Echando la vista atrás, parece que fue ayer cuando presenté mi proyecto fin de carrera, allá por finales de 2002. Pero ha pasado mucho tiempo, y puedo decir que han sido los años más apasionantes de mi vida. Los lugares que he recorrido, las personas que he encontrado en el camino, las alegrías y las penas, lo que ha cambiado y lo que sigue igual, todo viene a la mente al escribir estas líneas, como si mi tesis doctoral hubiera sido una fiel acompañante, un testigo mudo de lo sucedido en este periodo. Y ahora que este proyecto se acerca a su culminación, es de justicia acordarse de todos los que han compartido una parte o todo el camino, y que en cierta medida han hecho posible el resultado final.

En primer lugar quisiera agradecer a mis directores de tesis, Vicente y Benito. Me han apoyado con paciencia desde el principio, a pesar de estar a distancia la mayor parte del tiempo, ayudándome a superar los momentos más difíciles, que siempre aparecen en los proyectos importantes. También me gustaría nombrar a mis compañeros de las universidades de Valencia, que han aportado mucho al trabajo: Carlos, Antonio María, Mariam, Stephan, Jordi, Sergio. Desde Holanda, mis supervisores en la Agencia Espacial Europea, David y Dietmar, me abrieron los ojos y me impulsaron hacia delante. Mis jefes del Centro Aeroespacial Alemán en Munich, Manfred y Marco, apostaron por mí y me permitieron participar en las misiones radar en satélite más punteras, TerraSAR-X, TanDEM-X y Sentinel-1. Del mismo modo, no dudaron en darme facilidades para continuar en paralelo mis investigaciones para la tesis.

Todos los doctorandos sabemos que escribir una tesis te deja un poco “tocado del ala”. En mi caso, mi mujer Cécile, con su amor y comprensión, ha sido mi referencia y mi ilusión en estos años de electrones rebeldes. Mis padres, José Luis y Marián, y mis hermanos, Andrés y Fernando, han estado siempre ahí cuando les he necesitado, lo cual a veces damos equivocadamente por sentado. No hay palabras que puedan expresar el agradecimiento que os debo a todos. Por último, me gustaría dedicar también esta tesis a mis abuelos, Emilia, Abilio, Begoña y Jaime, porque sé que la culminación de este reto les hace igual o más felices que a mí.

Jaime Hueso González

Resumen

El efecto multipactor de ruptura en RF ha sido objeto de numerosos estudios desde hace más de 80 años, a partir del desarrollo de los primeros aceleradores de partículas en la primera mitad del siglo XX. A mediados de ese siglo, con el desarrollo de fuentes de alta potencia para aplicaciones radar y la llegada de los satélites artificiales, la investigación del multipactor cobró una considerable relevancia, al convertirse este fenómeno en un riesgo determinante para costosos proyectos comerciales. Las guías de onda con secciones rectas canónicas, como las rectangulares o las coaxiales, han sido tradicionalmente las más utilizadas en dispositivos de microondas. Sus principales ventajas son que sus campos electromagnéticos pueden resolverse analíticamente, lo que permite su aplicación directa en diseños complejos, y la simplicidad de su fabricación. Pero las capacidades de computación y las prestaciones de los algoritmos se han multiplicado con los años, lo que ha permitido ampliar el espectro de posibles topologías a geometrías casi arbitrarias, ofreciendo al diseñador una mayor libertad creativa. En todo caso, gran parte de los dispositivos de microondas actuales siguen confiando en la madurez y fiabilidad de las tecnologías de guía de onda tradicionales, que no requieren una inversión adicional en equipos de fabricación. La supresión del efecto multipactor es la motivación para arriesgarse a probar topologías de guía de onda innovadoras, como la guía en forma de cuña.

Es en este contexto donde este trabajo de doctorado pretende ofrecer una contribución. En primer lugar, se ha desarrollado un modelo numérico para predecir el efecto multipactor de ruptura en guías de onda huecas en forma de cuña. Esta herramienta ha permitido la identificación de criterios óptimos de diseño. Así mismo, se ha adaptado un método de síntesis de filtros paso-banda en guía rectangular para poder realizar un diseño similar pero basado en la nueva topología. Como culminación, las estructuras diseñadas se han fabricado y medido, con el fin de comprobar sus prestaciones electromagnéticas y su sensibilidad al efecto multipactor. Se ha registrado además una patente para proteger estos nuevos filtros. En resumen, el trabajo ha abarcado el ciclo de actividades relacionadas con el desarrollo industrial completo de un dispositivo pasivo de microondas: investigación básica, análisis, diseño, fabricación y calificación con medidas en el laboratorio.

Estas medidas han comprobado la mejora prevista en los umbrales de multipactor de los filtros de microondas con topología en forma de cuña, y han confirmado que pueden ofrecer respuestas en frecuencia similares a aquéllas de filtros basados en una guía de onda rectangular equivalente. Las implicaciones de los resultados han sido evaluadas a fondo y resumidas

en este documento. Como observación final, se ha intentado redactar esta investigación de manera que refleje el proceso natural de aprendizaje, mostrando los aciertos y errores experimentados en el camino, todos los cuales han conducido al resultado final. Este reto no hubiera sido posible sin el apoyo y compromiso de varios profesionales de diferentes centros de investigación e industrias europeas (Universidad Politécnica de Valencia, Universidad de Valencia, Agencia Espacial Europea, Thales Alenia Espacio España, Technische Universität Darmstadt, École Polytechnique Fédérale de Lausanne, Tesat, Aurora Software and Testing y Val Space Consortium), a los cuales estoy agradecido.

Resum

L'efecte multipactor de ruptura en RF ha estat objecte de nombrosos estudis des de fa més de 80 anys, a partir del desenvolupament dels primers acceleradors de partícules a la primera meitat del segle XX. A mitjans d'aquest segle, amb el desenvolupament de les fonts d'alta potència per a aplicacions radar i amb l'arribada dels satèl·lits artificials, la recerca del multipactor va cobrar una rellevància considerable, ja que aquest fenomen es va convertir en un risc determinant per costosos projectes comercials. Les guies d'ona amb seccions rectes canòniques, com les rectangulars o les coaxials, s'han utilitzat tradicionalment en la majoria de dispositius de microones. Els seus principals avantatges són que els seus camps electromagnètics es poden resoldre analíticament, la qual cosa permet la seva aplicació directa en dissenys complexos, i la seva simplicitat de fabricació. D'altra banda, les capacitats de computació i les prestacions dels algorismes s'han multiplicat amb els anys, el que ha permès ampliar l'espectre de topologies possibles a geometries gairebé arbitràries, oferint al dissenyador una major llibertat creativa. No obstant això, gran part dels dispositius de microones actuals segueixen confiant en la maduresa i fiabilitat de les tecnologies de guia d'ona tradicionals, que no requereixen una inversió addicional en equips de fabricació. La supressió de l'efecte multipactor és la motivació per arriscar-se a provar topologies de guia d'ona innovadores, com la guia en forma de falca.

És en aquest context on aquest treball de doctorat pretén oferir una contribució. En primer lloc, s'ha desenvolupat un model numèric per predir l'efecte multipactor de ruptura en guies d'ona buides en forma de falca. Aquesta eina ha permès l'identificació de criteris òptims de disseny. Així mateix, s'ha adaptat un mètode de síntesis de filtres passa-banda en guia rectangular per poder realitzar un disseny similar però basat en la nova topologia. Com culminació, les estructures dissenyades s'han fabricat i mesurat, per tal de comprovar les seves prestacions electromagnètiques i la seva sensibilitat a l'efecte multipactor. S'ha registrat a més una patent per protegir aquests nous filtres. En resum, el treball ha comprès el cicle d'activitats relacionades amb el desenvolupament industrial complet d'un dispositiu passiu de microones: recerca bàsica, l'anàlisi, disseny, fabricació i qualificació amb mesures en el laboratori.

Aquestes mesures han comprovat la millora prevista en els límits de multipactor dels filtres de microones amb topologia en forma de falca, i han confirmat que poden oferir respostes en freqüència similars a aquelles de filtres basats en una guia d'ona rectangular equivalent. Les implicacions dels resultats han estat avaluades a fons i resumides en aquest

document. Com a observació final, s'ha intentat redactar aquesta investigació de manera que reflecteixi el procés natural d'aprenentatge, mostrant els encerts i errors experimentats en el camí, tots els quals han conduït al resultat final. Aquest repte no hagués estat possible sense el suport i compromís de diversos professionals de diferents centres de recerca i indústries europees (Universitat Politècnica de València, Universitat de València, Agència Espacial Europea, Thales Alenia Espacio Espanya, Technische Universität Darmstadt, École Polytechnique Fédérale de Lausanne, Tesat, Aurora Software and Testing i Val Space Consortium), als quals estic agraït.

Abstract

The multipactor RF breakdown effect has been object of numerous studies for over 80 years, since the development of the first particle accelerators in the beginning of the 20th century. Around the middle of that century, with the development of high power sources for radar applications and with the emergence of the artificial satellites, a new impulse was given to the multipactor research, since it became a risk for expensive commercial projects. Traditionally, waveguides with canonical cross sections, like rectangular or coaxial ones, have been the building blocks of most microwave devices. Their main advantages are that their electromagnetic fields can be solved analytically, enabling their direct application in complex designs, as well as their manufacturing simplicity. But over the years the computation capabilities and algorithms have continuously evolved, which has broadened the spectrum of possible topologies to almost arbitrary geometries, offering the designer more room for creativity. However, most of the current microwave devices still trust on the mature canonical waveguide technologies, which do not require an additional investment in manufacturing equipment. The suppression of the multipactor effect is the motivation for considering an innovative waveguide topology, like the wedge-shaped waveguide.

It is within this context where this PhD work aims to offer a contribution. On the one hand, a numerical model for predicting the multipactor breakdown effect in wedge-shaped hollow waveguides has been developed. This tool has aided in the derivation of optimised design criteria. On the other hand, a bandpass filter synthesis method for rectangular waveguide has been adapted in order to calculate a similar design based on the new topology. As a culmination, the designed structures have been manufactured and tested, in order to verify their electromagnetic performance and their multipactor sensibility. A patent was also filed to protect these new filters. In short, this work has comprised the cycle of activities related to the whole industrial development of a passive microwave device: basic research, analysis, design, manufacturing and qualification through testing.

These measurements have verified the predicted improvement in the multipactor thresholds of microwave filters with wedge-shaped topology, and have confirmed that they can offer similar frequency responses to the equivalent rectangular waveguide ones. The implications of the results have been thoroughly evaluated and summarised in this document. As a final remark, this research document has been drafted to reflect the natural learning process, and to show the rights and wrongs experienced in the way, which all have led to the final result. Such an endeavour would not have been possible without the support and commitment

of several professionals from different European research centres and industries (Universidad Politécnica de Valencia, Universidad de Valencia, European Space Agency, Thales Alenia Espacio Spain, Technische Universität Darmstadt, École Polytechnique Fédérale de Lausanne, Tesat, Aurora Software and Testing and Val Space Consortium), for which I am grateful.

Index

1	Introduction	1
1.1	Background and Motivation	1
1.2	Objectives and Challenges	11
1.3	Thesis Structure	14
2	Electromagnetic Analysis of Wedge-shaped Waveguides	17
2.1	Computation of the Modal Solution	17
2.1.1	Wedge-shaped Waveguide and Rectangular Reference Box	17
2.1.2	Normalised Arbitrary TE Modes	19
2.1.3	Normalised Arbitrary TM Modes	20
2.1.4	Unnormalised Arbitrary TE Modes	20
2.1.5	Unnormalised Arbitrary TM Modes	21
2.1.6	Grid Interpolation	21
2.2	Simulation of the EM Behaviour	23
2.2.1	Comparison Wedge-Rectangular Field Patterns	23
2.2.2	Inclination Angle Limits	27
2.2.3	Modes and Cutoff Frequencies	28
2.3	Discontinuities and S-Parameters of Stepped Waveguide Devices	31
2.3.1	Discontinuities with Wedge-shaped Waveguides	31
2.3.2	Analysis of Stepped Waveguide Structures	34
3	Multipactor Effect Analysis of Wedge-shaped Waveguides	37
3.1	Electron Emission in Metals	37
3.1.1	Models for the Secondary Emission Yield	37
3.1.2	Rebound Energy Models	40
3.1.3	Multipactor Susceptibility Regions	43
3.2	Multipactor Prediction Tool	44
3.2.1	Overview	44
3.2.2	Electron Dynamics	47
3.2.3	Algorithm for the Prediction of the Multipactor Discharge	50
3.2.4	Trapped Trajectories and Launch Position Prediction	52
3.3	Validation of the Formulation	57
3.3.1	Example of Chojnacki	57

3.3.2	Example of Semenov	59
3.4	Study of the Optimal Inclination Angle	62
3.4.1	Introduction to the Angle Sweep Analysis	62
3.4.2	Results and Interpretation	62
3.5	Susceptibility Maps	66
3.5.1	Definition	66
3.6	Summary	68
4	Design of a Wedge-shaped Bandpass Filter	69
4.1	From Waveguide to Filter	69
4.1.1	Searching an Implementation	69
4.1.2	Filter Requirements	70
4.1.3	Filter Topology and Cross Section	72
4.1.4	Design Procedure	74
4.1.5	Simulation Results	79
4.2	Hardware and S-parameters Measurement	79
4.2.1	Preparation of the Manufacturing Models	79
4.2.2	Manufactured Bandpass Filters	84
4.2.3	Contact Problems and Workaround	85
4.2.4	Comparison Between Measured and Simulated Filter Responses	88
4.2.5	Out-of-band Frequency Response	91
4.3	Multipactor Prediction	93
4.3.1	Extension of Multipactor Prediction Tool	93
4.3.2	Traditional Multipactor Prediction Tools	94
4.4	Measured Multipactor Thresholds	96
4.4.1	Multipactor Test Report	96
4.4.2	Comparison Between Measurements and Predictions	97
4.5	Summary	98
4.5.1	Demonstration of Multipactor Resistance	98
4.5.2	Potential Design Improvements	98
5	Optimum Design of Wedge-shaped Bandpass Filters for Improved Multipactor Resistance	101
5.1	Optimisation Studies	101
5.1.1	New Design Target	101
5.1.2	Inclination Angle	102
5.1.3	Out-of-band Frequency Response	103
5.1.4	Manufacturing Enhancements	106
5.2	Second Wedge-shaped Bandpass Design	108
5.2.1	Structure Characteristics and Requirements	108
5.2.2	Simulation Results	114
5.2.3	Manufactured Hardware	114
5.3	Electrical Performance	116

5.3.1	Narrow-band Comparison	116
5.3.2	Wide-band Comparison	116
5.4	Multipactor Performance	118
5.4.1	Multipactor Predictions	118
5.4.2	Multipactor Test Campaign Results	120
5.4.3	Evaluation of Results	120
5.5	Guidelines for Optimal Design	122
6	Conclusiones y Perspectivas	125
A	Formulation of the Electromagnetic Fields of Rectangular Waveguides	131
A.1	Fields and Power	131
A.2	Normalised Electromagnetic Fields	133
A.2.1	Transverse Electric Case	133
A.2.2	Transverse Magnetic Case	134
A.3	Retrieval Electromagnetic Fields	135
A.3.1	Transverse Electric Case	135
A.3.2	Transverse Magnetic Case	136
B	Losses in Waveguides due to the Finite Conductivity of the Metallic Walls	139
B.1	Losses in the Frontal Walls	139
B.1.1	Implication of Considering Losses in Wedge-shaped Waveguides	139
B.1.2	Coupling Integrals in the Frontal Walls	140
B.2	Losses in Propagation	143
B.2.1	Derivation of the Attenuation Constant	143
B.2.2	Resolution for the Wedge-shaped Waveguide Case	145
C	Multipactor Detection Test	151
C.1	Test Setup and Procedure	151
C.2	Detection Methods	157
D	Curriculum Vitae	163
D.1	Education	163
D.2	Professional Experience	163
D.3	Fields of Expertise	164
D.4	Informatics Skills	165
D.5	Languages	165
E	Publications	167
E.1	Papers in International Scientific Journals	167
E.2	Patent	167
E.3	Papers in International Congresses	168
E.4	Research Reports	168

List of Acronyms**169****List of Symbols****173****Bibliography****177**

Figure Index

1.1	Paschen curves indicating the breakdown voltage over the pressure-gap distance product for different gases. Source: Liebermann and Lichtenberg, “Principles of Plasma Discharges”, Wiley 2005.	2
1.2	Scheme showing the electron density growth that leads to a multipactor avalanche phenomenon. The sequence shows a multipactor resonance of order one, since the time between consecutive wall collisions is equal to a half RF cycle.	3
1.3	Electron density over altitude. Source: www.radartutorial.eu	4
1.4	Electronic microscope photo of the damage caused by a multipactor discharge in a black anodised filter. Source: ESA.	5
1.5	TWT of the X-SAR synthetic aperture radar instrument flown aboard the Shuttle during the MRSE mission in 1983 (left). Detail of the burn-out caused by the corona discharge (right). Source: German Aerospace Center (DLR).	6
1.6	Simplified block diagram of a satellite transponder with input/output multiplexers (IMUX/OMUX). These 1:2 multiplexers can be implemented with waveguide diplexers like the one shown in the photo on the right. Source photo: ESA.	7
1.7	Photo of the destructive effect of an RF breakdown on a lowpass filter. Source: Thales Alenia Space France.	7
1.8	Evolution of the output power requirements of satellite microwave instruments over time for the different frequency bands. Source: ESA.	8
1.9	Susceptibility maps for the parallel-plate case. Multipactor discharges might occur within the susceptibility regions. The slope constants indicate the MP behaviour for the different materials. Source: M. Yu, “Power Handling Capability for RF Filters”, IEEE Microwave Magazine, 2007.	9
1.10	Cross sections of a wedge-shaped waveguide and of its equivalent rectangular one. Both waveguides have the same width a and average height $b = (h_1 + h_2)/2$, resulting in equal cross-section areas. Inside the wedge-shaped cross section, the colours indicate the distribution of the transverse electric field of the fundamental mode, similar to the TE_{10} fundamental mode of a rectangular waveguide. Grey arrows show the electric field vectors along an arc between top and bottom plates.	11

1.11	Satellite assembly undergoing qualification tests. Multipactor tests are usually conducted for individual payload devices. They are a small, but critical fraction of all required system and subsystem tests. Source: ESA.	13
2.1	Cross section of a discontinuity between a rectangular and a wedge-shaped waveguide. The rectangular waveguide can be used as a reference box for deriving the modes of the wedge-shaped one.	18
2.2	Grid of a wedge-shaped waveguide for EM field interpolation.	22
2.3	Modal chart of rectangular waveguides. The cutoff frequencies of the different modes, normalised to the one of the fundamental mode TE_{10} , are represented for the different values of the ratio between the height b and the width a of the rectangular waveguide.	24
2.4	Electric field pattern (absolute value and vector grid) of the fundamental mode in the cross section of a wedge-shaped waveguide with the following dimensions: $a_{\text{Wedge}} = 19.05$ mm, $h_1 = 8.641$ mm, $h_2 = 15.359$ mm, $\alpha = 20^\circ$	25
2.5	Schematic representation of a multi-modal impedance matrix that characterises a discontinuity between waveguides.	32
2.6	Example of a discontinuity between a rectangular ($WG 1$) and a wedge-shaped waveguide ($WG 2$). The dash-dotted green rectangle represents one of the possible reference boxes for calculating the modal chart of $WG 2$	33
2.7	Different cases in which a special reference box, different from $WG 1$, has to be used.	34
2.8	Circuitual model of a series of waveguide elements, a rectangular, a wedge-shaped, and another rectangular, and their corresponding discontinuities.	35
3.1	Typical SEY curve measurement for a certain material and for a fix impact angle.	38
3.2	SEY curve model that takes into account the impact angle of the electrons, and with a corrected low-energy model. Proposed by Vaughan.	39
3.3	SEY curve model that takes into account the impact angle and the elastic rebounds for low energy. Proposed by Vicente.	41
3.4	2-D projection of an electron rebound under elastic conditions.	41
3.5	2-D projection of an electron impact (in blue) causing the emission of secondary electrons (in red) at random angles.	42
3.6	Definition of the spherical coordinates around a collision for the determination of the outbound direction.	42
3.7	Example of the multipactor susceptibility regions.	43
3.8	Block diagram of the multipactor prediction tool. Different modules are inside blue dashed boxes, in order of execution. Elements marked in orange are input data for the tool, whereas the ones marked in green are outputs.	45
3.9	Two examples of simulated electron trajectories in a wedge-shaped waveguide and its collisions against the walls. XY -plane is perpendicular to the propagation direction.	51

3.10	Magnetic field of the fundamental mode (TE_{10}) in a rectangular waveguide. XY -plane shows the rectangular cross section. Vectors in the horizontal plane (XZ) represent the absolute value of the magnetic field. The z -component of the real part of the magnetic field is colour-coded in the YZ - and XY -cuts.	53
3.11	Magnetic field of the fundamental mode in a wedge-shaped waveguide. XY -plane shows the wedge-shaped cross section. Vectors in the horizontal plane (XZ) represent the absolute value of the magnetic field. The z -component of the real part of the magnetic field is colour-coded in the YZ - and XY -cuts.	53
3.12	Definition of the dimensions of an annular section waveguide and its corresponding wedge-shaped waveguide (convention). R_1 and R_2 are the internal and external radii of the annular section, and R_{crit} is a critical radius with a trapped electron trajectory.	54
3.13	Launch radii with trapped electron trajectories of the annular section waveguide with dimensions $R_1 = 216$ mm, $R_2 = 648$ mm and $\alpha = 0.23$ rad, depending on the initial launch phase of the electron within the RF signal cycle. The initial velocity of the electron is assumed to be zero.	55
3.14	Cross section of the wedge-shaped waveguide including the region with trapped electron radii and the equivalent voltage amplitude distribution. Qualitative (unitless) distribution of the equivalent voltage for the whole radii range. Radius with maximum equivalent voltage $R_{\text{maxV}} = 454.4$ mm ($x_{\text{maxV}} = 22.4$ mm at $y = 0$).	57
3.15	Comparison of our simulation results (blue- and red-dotted lines) with the results of Chojnacki (black-solid lines). Top: rectangular waveguide with dimensions $a = 432$ mm, $b = 102$ mm and the launch position of the initial electron at $x = 0$. Bottom: wedge-shaped waveguide with dimensions $a_{\text{Wedge}} = 432$ mm, $h_1 = 49.9841$ mm, $h_2 = 149.952$ mm, $\alpha = 13.2^\circ$ and the launch radius at $R = 290$ mm.	58
3.16	Comparison of our simulation results (blue- and red-dotted lines) with the results of Semenov (black-solid lines). Top: rectangular waveguide with dimensions $a = 414.9$ mm, $b = 103.6$ mm and the launch position of the initial electron at $x = 0$. Bottom: wedge-shaped waveguide with dimensions $a_{\text{Wedge}} = 432$ mm, $h_1 = 49.9$ mm, $h_2 = 149.7$ mm, $\alpha = 0.23$ rad and the launch radius at $R = 390.1$ mm.	60
3.17	Schematic overview of the cross sections of the waveguides applied in this analysis. The cutoff frequency f_C is constant.	64
3.18	Multipactor thresholds and voltage values at the multipactor critical locations for multiple inclination angles.	65
3.19	Susceptibility map for different inclination angles. (Left) voltage threshold and (right) relative voltage thresholds with respect to the rectangular case. Thresholds after 20 collisions.	67
4.1	Sketch and dimensions of a conventional inductive bandpass filter with its hollow resonators and irises.	70

4.2	Typical bandpass filter frequency response. Main requirement parameters are defined here.	71
4.3	3-D plot of the electric field magnitude distribution perpendicular to the metallic surfaces of a rectangular waveguide (left) and a wedge-shaped waveguide (right) bandpass filter, calculated with FEST ^{3D} . Colour table ranges from dark blue (minimum) to dark red (maximum).	72
4.4	3-D view of the wedge-shaped waveguide central resonator stages (left) and the input waveguide and the first resonator (right) of the wedge-shaped waveguide filter.	73
4.5	Overlapped cross-sectional schematic view of the wedge-shaped waveguide (black-solid lines) and rectangular waveguide (red-dashed lines) filters. Vertical black lines correspond to the irises walls, as seen from the front of the filter. Input waveguides (green-dotted rectangle) are standard WR90 for both filters. The inclination angle is $\alpha = 19^\circ$	73
4.6	Circuit models used for the design procedure of a microwave waveguide filter.	74
4.7	Attenuation function of a Chebyshev normalised lowpass filter. It can be then transformed to a bandpass filter by means of proper frequency variable substitutions.	75
4.8	Reflection coefficients of the input and output irises of a resonator.	77
4.9	3-D view of a standard inductive filter (left), and a filter with the novel topology based on wedge-shaped waveguides (right).	78
4.10	Simulated S-parameters of the rectangular (top) and the wedge-shaped (bottom) filter. Each plot includes the results obtained with HFSS and FEST ^{3D} for comparison.	80
4.11	Examples of waveguide filter manufacturing processes. Milling (left), plunge EDM (centre) and wire EDM (right).	81
4.12	Autocad model of the rectangular bandpass filter dimensions.	82
4.13	Autocad model of the wedge-shaped bandpass filter dimensions.	83
4.14	Standard rectangular waveguide flange for the input and output interfaces.	84
4.15	Photo of the rectangular waveguide bandpass filter. Front view (left) and overall view (right). Manufactured by Tesat-Spacecom, Germany.	86
4.16	Photo of the wedge-shaped waveguide bandpass filter. Front view (left) and inner view of cavities and irises (right). Manufactured by Alcatel Espacio (now Thales Alenia Espacio), Spain.	86
4.17	Photo of the inner part of the manufactured wedge-shaped filter. Lid has been removed to better visualise the structure.	87
4.18	Photo of the inner part of the manufactured wedge-shaped filter. Lid has been removed to better visualise the structure.	87
4.19	Photo with a close zoom on the wedge-shaped cavities of the manufactured filter.	88
4.20	Comparison between the measured S-parameters of the wedge-shaped filter with electrical contact problems, and the expected simulated results.	89

4.21	Roll of indium foil (left) and indium strips placed on the contact surface between the top filter lid and the filter iris walls (right).	89
4.22	Check of the correct placement of the indium foil contact patches to improve the filter conductivity in the junction plane of the tow filter parts. Pictures were taken with an optical-fibre camera, introduced inside the device through the holes of the waveguide filter.	90
4.23	Comparison between the S-parameters of the wedge-shaped filter with and without contact problems. Once solved the connection problem, the S-parameters before and after the thermal cycling process can be compared.	90
4.24	Measured S-parameters of the rectangular (top) and the wedge-shaped (bottom) waveguide filter. Each plot includes the simulated results of FEST ^{3D} for comparison. In the bottom plot, the simulated response with (simplified approximation) and without (original) contact foils is presented.	92
4.25	Broadband comparison of the S-parameters for the two considered filter structures. The effect of the higher-order modes of the resonator results in filter repetitions at different frequencies placed above the pass-band.	93
4.26	Magnitude of the electric field and field vectors on the horizontal plane for the rectangular (top) and the wedge-shaped waveguide bandpass filter (bottom). The maximum values of the fields concentrate in the second and third resonators.	94
4.27	Magnitude of the electric field and voltage along the cross section (XY -plane) in the centre plane of the second cavity of the rectangular (left) and of the wedge-shaped (right) filter. The RF input power is 1 W.	96
5.1	Cross-section view of a wedge-shaped (black-solid line) and a rectangular (red-dashed line) waveguide with the same area. The region shaded in green within the wedge-shaped geometry contains the multipactor-critical trapped electron trajectories.	102
5.2	Schematic overview of the cross sections of different waveguides covering a sweep of different inclination angles. The width $a_{\text{Wedge}} = a$ is kept constant.	103
5.3	Voltage (for 1 W RF input power) in the critical multipactor radius for all the wedge-shaped waveguides considered in the inclination angle sweep: constant width $a_{\text{Wedge}} = a$ and, whenever possible, constant cross-section area. A reference rectangular waveguide with dimensions $a = 19.05$ mm and $b = 6.26$ mm has been selected. Operating frequency 12 GHz. Green curves are assigned to the right axis and represent the location of the trapped trajectories region.	104
5.4	Cutoff frequencies of the first two propagating modes of a wedge-shaped waveguide versus the inclination angle: constant width $a_{\text{Wedge}} = a$ and, whenever possible, constant cross-section area. Values are compared to the ones of the reference rectangular waveguide with dimensions $a = 19.05$ mm and $b = 6.26$ mm (b remains constant up to $\approx 50^\circ$).	105

5.5	Cutoff frequencies of the first two propagating modes of a wedge-shaped waveguide inclination angle sweep: constant cutoff frequency $f_C = 7.869$ GHz and, whenever possible, constant average height. Values are compared to the ones of the reference rectangular waveguide with dimensions $a = 19.05$ mm and $b = 6.26$ mm. Blue-solid curve represents the values of a_{Wedge}	106
5.6	Voltage (for 1 W RF input power) in the critical multipactor radius for all the wedge-shaped waveguides considered in the inclination angle sweep: constant f_C and, whenever possible, constant average height. A reference rectangular waveguide with dimensions $a = 19.05$ mm and $b = 6.26$ mm has been selected. Operating frequency 12 GHz. Green curves are assigned to the right axis and represent the location of the trapped trajectories region.	107
5.7	Wedge-shaped filter halves during the manufacturing process.	108
5.8	3-D views of the quasi-inductive rectangular (left) and the wedge-shaped filters (right).	109
5.9	3-D plot of the electric field distribution along the rectangular (left) and the non-parallel plate filters (right).	110
5.10	Comparison of the group delays of both designs ($\sigma = 6.1 \cdot 10^7$ S/m). Simulation with FEST ^{3D}	110
5.11	Comparative detail of the cross sections of the two considered filter designs. The mean wedge height is slightly different from the rectangular filter height b_{rect} in order to match the Q factors.	111
5.12	Autocad model of the rectangular bandpass filter dimensions.	112
5.13	Autocad model of the wedge-shaped bandpass filter dimensions. The dimensions marked in red correspond to the re-adjusted dimensions due to the ball-end mill with a high radius of curvature.	113
5.14	Comparison between the simulated S-parameters of both filters (perfect conductor). Simulations have been performed with FEST ^{3D}	114
5.15	Milling process of the two halves of the gold-plated rectangular waveguide filter. Milling tool (0.5 mm radius of curvature) is also shown in this photo.	115
5.16	Milling process of the two halves of the aluminium wedge-shaped waveguide filter. Inner cavities have been carved with a milling tool with 1.5 mm radius of curvature.	116
5.17	Photo of the two manufactured gold-plated filters: wedge-shaped filter (left) and quasi-inductive rectangular filter (right), both with a zoom of the front view.	117
5.18	Comparison between the simulated and measured S-parameters of the gold-plated rectangular filter.	117
5.19	Comparison between the simulated and measured S-parameters of the gold-plated wedge-shaped filter.	118
5.20	Measured out-of-band frequency responses of the gold-plated quasi-inductive and the wedge-shaped filters.	119
5.21	Screenshot of the network analyser of the nulling detection chain when indicating a multipactor discharge in the rectangular waveguide filter.	121

5.22	Screenshot of the network analyser of the harmonics detection chain when indicating a multipactor discharge in the wedge-shaped waveguide filter. . .	121
6.1	Clasificación de niveles de madurez tecnológica - Technology Readiness Level (TRL). Aplicado por NASA y ESA a todo tipo de tecnologías espaciales. Source: https://telecom.esa.int/telecom/media/document/TRL_Handbook.pdf	129
A.1	Cross section of a rectangular waveguide with width a , height b and infinite in the z (propagation) direction. The origin of the Cartesian coordinate system has been placed at the geometric centre of the cross-section surface.	132
B.1	Contours of a wedge-shaped WG cross section and perpendicular unitary vector.	144
C.1	Vacuum chamber. It reaches a pressure below 10^{-7} mbar.	152
C.2	Metallic plate for the temperature control of the microwave elements inside the vacuum chamber.	152
C.3	Thermal cycling chamber. Device under test is placed in a hermetic bag. . .	153
C.4	Scheme of the multipactor test-bed. Source: ESA-Val Space Consortium High Power Laboratory.	154
C.5	Device under test, radioactive source, and multipactor detection sensors inside the vacuum chamber.	156
C.6	Design of venting holes for hollow waveguide device multipactor testing. . .	156
C.7	Photo of the multipactor detection setup.	158
C.8	Reading of the electron probe sensor with the peaks in the graph indicating a multipactor discharge.	160
C.9	Screenshot of the spectrum analyser of the third-harmonic detection chain showing a multipactor discharge, indicated by the gap between the maximum curve and the lower actual spectrum measurement. The “Max hold” display mode has been activated.	160
C.10	Screenshot of the spectrum analyser of the nulling detection chain showing a multipactor discharge, indicated by the gap between the maximum curve (blue line) and the lower actual spectrum measurement (yellow line). Note that the attenuators and phase shifters need to be re-adjusted again to null the actual spectrum. The “Max hold” display mode has been activated.	161
C.11	Recorded photoemission generated by a corona discharge in a microstrip device. Source: ESA.	161

Table Index

2.1	EM field patterns (absolute value) of the first four modes in order of increasing cutoff frequencies for a rectangular and an equivalent wedge-shaped waveguide. The colours are coded like in the previous figure. Dimensions of the rectangular waveguide: $a = 19.05$ mm, $b = 12$ mm. Wedge-shaped waveguide is identical to the one of the previous figure.	26
2.2	Dimensions of the wedge-shaped waveguides included in the sweep. For all examples: $a_{\text{Wedge}} = 19.05$ mm. Minimum value for $h_{1,\text{min}} = 1$ mm.	27
2.3	EM field patterns (absolute value) of the fundamental mode of wedge-shaped waveguides with different inclination angles (rectangular for $\alpha = 0^\circ$). The colours are coded like in the previous images.	29
2.4	Cutoff frequencies of the first two propagating modes of different wedge-shaped waveguides in terms of the inclination angles. Each column/graph uses a different rectangular waveguide as a reference, each with a different b but all with a constant $a = 19.05$ mm. The minimum height of the wedge side-walls is $h_{1,\text{min}} = 1$ mm. b remains constant for each column, except when $h_1 = h_{1,\text{min}}$	30
3.1	Inclination angle sweep - Multipactor (MP) prediction.	63
4.1	Bandpass filter requirements.	71
4.2	Dimensions of the wedge-shaped bandpass filter.	78
4.3	Dimensions of the rectangular bandpass filter.	78
4.4	Dimensions of a WR90 standard flange.	84
4.5	Input parameters and outputs of the venting analysis of the bandpass filters.	85
4.6	Values of the characteristic SEY parameters for silver.	95
4.7	Multipactor threshold predictions and measurements.	97
5.1	Requirements of the bandpass filters.	109
5.2	Dimensions of the rectangular waveguide bandpass filter.	111
5.3	Dimensions of the wedge-shaped waveguide bandpass filter.	112
5.4	Values of the characteristic SEY parameters for gold and aluminium.	119
5.5	Multipactor (MP) threshold predictions and measurements at 12 GHz (measurement limit 6.5 kW).	121

C.1 Typical parameters and requirements of a multipactor test. 155
C.2 Power steps schedule. Predicted threshold is 500 W. 157

Chapter 1

Introduction

1.1 Background and Motivation

A lightning is a natural phenomenon originated in the atmosphere, as electric charges build up and concentrate in different cloud locations, or between the clouds and the Earth surface. When the electric potential rises over the resistance of the air, the electricity flows between the opposite charges, resulting in an electrostatic discharge. The ionisation of the surrounding air causes a flash of visible light, and the blasting sound is due to air shock-waves. This particular case of gas discharge has always fascinated mankind, but it was not until the eighteenth century when Benjamin Franklin and other scientists conducted some serious experiments, proving the link between lightnings and electrical discharges. In the following centuries, low frequency gas discharges were better understood: an electron density avalanche turned an isolating gas into conducting plasma. Paschen's law [1] described in 1889 the breakdown voltage of a gas between parallel plate electrodes as a function of the pressure and the gap distance (see Fig. 1.1). This helped in the development of related commercial objects, like neon tubes. In the beginning of the twentieth century, the working frequencies of electromagnetic applications shifted to the radio-frequency (RF) and microwave band. This motivated the discovery of microwave gas discharges, which allowed advances in the field of ionised plasmas. Analogously, optical breakdowns can also occur at optical frequencies.

Multipactor (or "multipaction") [2] is essentially an RF or microwave breakdown effect at very low pressures. The word comes from the combination of "multiple" and "impactor" or "impaction". Distinctly to gas discharges, the multipactor effect occurs at vacuum conditions, where the free electrons have a longer mean free path and do neither collide against neutral atoms nor get absorbed by them. It is known that electrons are accelerated under the influence of an electromagnetic field. During a particular fraction of a signal period, the free electrons present in the structure are shifted towards a direction that is linked to the vector orientation of the fields. Assuming a time-harmonic excitation, as it happens in almost all practical applications, the accelerations induced in the free electrons would follow a periodic pattern. In high power applications, the field strength might reach the point where the free electrons would be pushed as far as to collide against the conductor metallic walls.

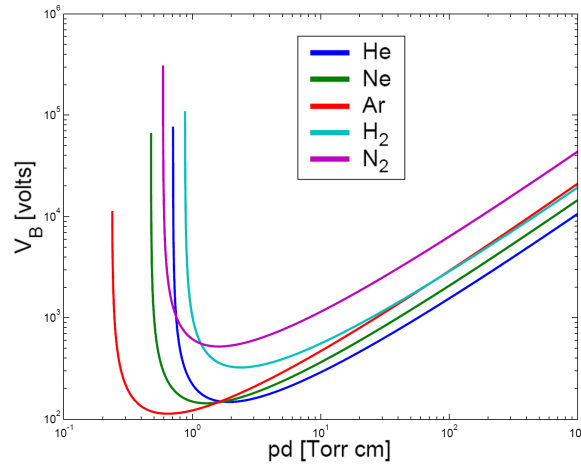


Figure 1.1: Paschen curves indicating the breakdown voltage over the pressure-gap distance product for different gases. Source: Liebermann and Lichtenberg, “Principles of Plasma Discharges”, Wiley 2005.

These collisions would trigger different reactions, depending on the impact energy and angle as well as on the material properties: the free electrons might be absorbed, might be reflected elastically, or more free electrons might be generated due to secondary emission of the metallic surface. For certain RF signal frequency and power values, the electrons would synchronise their collisions against the walls with the RF period, eventually leading to a resonant regime. If the number of secondary electrons generated is higher than the electrons lost due to diffusion or absorption in the walls, the electron density grows exponentially, creating an avalanche process and an electrostatic discharge (see symbolic description in Fig. 1.2). Hence, the main factors that govern the multipactor discharge mechanism are: the material of the electrodes or conducting walls (unlike gas discharges), the distance between them and the frequency of the present electromagnetic fields. Formally, there are four conditions that determine a multipactor discharge, as it is defined by the European Space Agency (ESA) in its harmonisation documents [3]:

1. Presence of free electrons

In a test environment, this can be provided by the high energy particles of a radioactive source.

2. Long mean free path for the electrons

This happens under vacuum conditions ($< 10^{-5}$ mbar), in the absence of dielectric.

3. Resonance

The interval between wall collisions has to be an odd integer factor of half of the RF cycle duration. In this way, a resonance can appear. This factor is also known as the multipactor order, being 1 the most simple case, like in Fig. 1.2.

4. Exponential electron growth

Electron population has to grow exponentially until causing an avalanche effect.

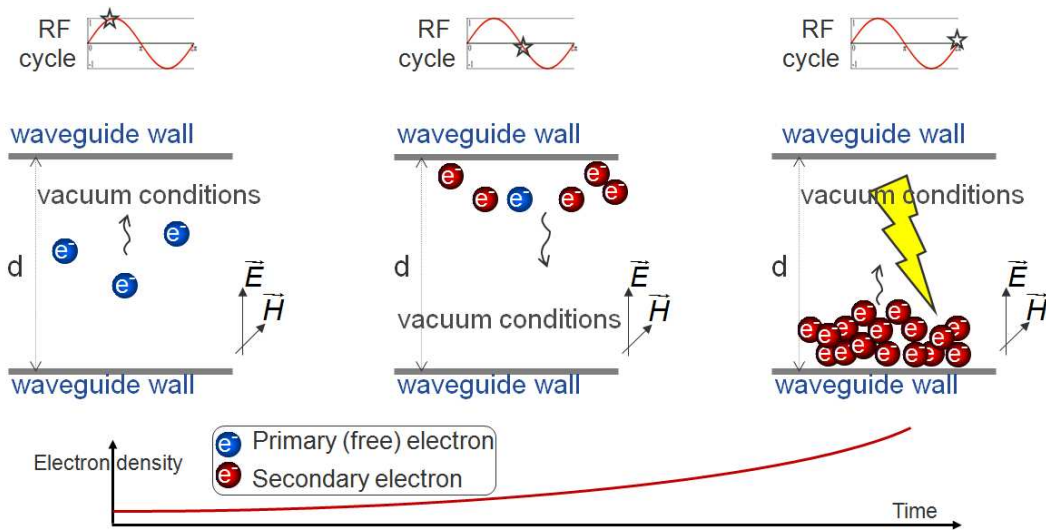


Figure 1.2: Scheme showing the electron density growth that leads to a multipactor avalanche phenomenon. The sequence shows a multipactor resonance of order one, since the time between consecutive wall collisions is equal to a half RF cycle.

Additionally, [3] states that these conditions have to be kept during a period of 20 electron crossings between the resonant walls (20-gap-crossing rule), in order to be considered a multipactor discharge. Although the “20-gap-crossing rule” has been accepted as a standard definition by the space industry community, scientific studies on the subject usually analyse the electron density at several stages (not only after 20 collisions). This can give additional information on the nature and sustainability of the multipactor discharge.

Multipactor discharges were first observed in vacuum electron tubes [4] at the beginning of the 20th century. Apart from its damaging potential, [5] saw this phenomenon as an amplification method, and implemented the so-called “Multipactors”, which were electron tubes for the early television receivers. It promptly became a matter of investigation for the particle accelerators community, since it also affected cyclotrons [6]. Microwave high-power applications were flourishing at that time, namely with the development of the radar on the brink of World War II. Starting in 1957, with the launch of Sputnik 1, the first artificial satellite, a new momentum was given to the multipactor research. Satellites orbit outside of the atmosphere under very low pressure or even vacuum conditions. Depending on their orbit altitude, they are subject to different radiation sources: the ionosphere, the Van Allen belts, solar wind and cosmic radiation. For instance, Earth observation satellites typically orbit fully within the ionosphere, with a high free electron density (cf. Fig. 1.3), which creates the ideal conditions that enable multipactor discharges. Ageing of the microwave hardware is also a determinant factor that increases the risk of multipactor: oxidation and contamination of metallic surfaces can trigger metallic field emissions under the influence of even moderate electric fields, which would increase the density of free electrons in the device. Examples of typical satellite microwave devices are diplexers and multiplexers, coupled cavity filters, power dividers, antenna feed networks and amplifiers like travelling-wave tubes (TWT) or

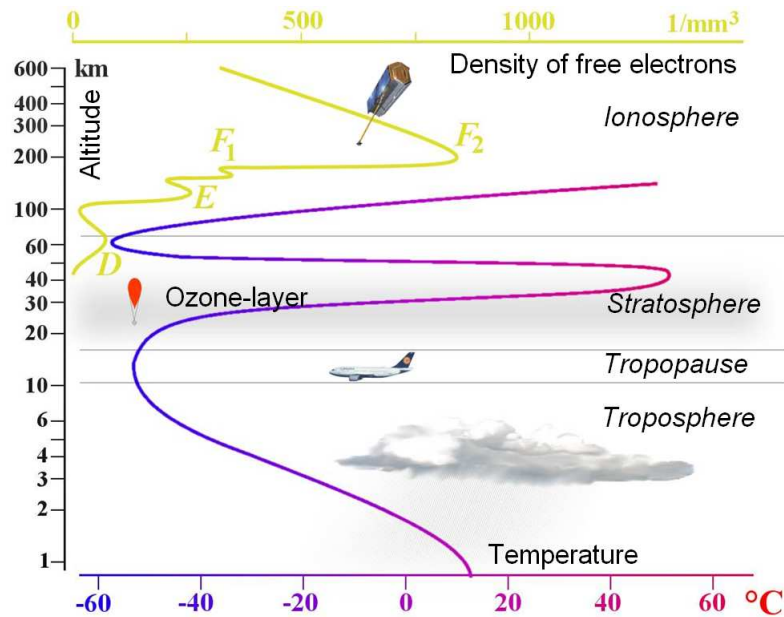


Figure 1.3: Electron density over altitude. Source: www.radartutorial.eu .

Klystrons [7].

Multipactor discharges cause a non-linear interaction with the nominal electromagnetic fields, which can considerably modify the electrical behaviour of the device that suffers it. Here is a list of the different effects resulting from this phenomenon:

- Increase of signal-to-noise ratio and phase noise.
- Increase of return losses.
- Spread of the power over the spectrum (harmonics).
- Increase of temperature due to power dissipation in the wall collisions.

An example of the damage caused by this phenomenon on a waveguide filter can be seen in Fig. 1.4. As it happens in this case, most multipactor discharges cause surface erosion effects that are barely visible to the naked eye, but that still compromise the electrical signal transmission. Additionally to the direct effects listed above, sustained multipactor discharges cause out-gassing of the metallic walls due to the temperature increase, which can derive into even more serious problems.

In fact, out-gassing increases the pressure in an originally vacuum environment, which might induce a particular type of gas discharge known as corona [8,9]. A corona discharge turns gas molecules into ionised plasma (like lightnings) and is more dangerous than a simple multipactor discharge, since it can physically damage the structure, even rendering it useless by melting metal pieces. The corona effect appears typically at pressures below ambient, varying from 10^{-2} mbar to 10 mbar depending on the gas. They are more likely to happen

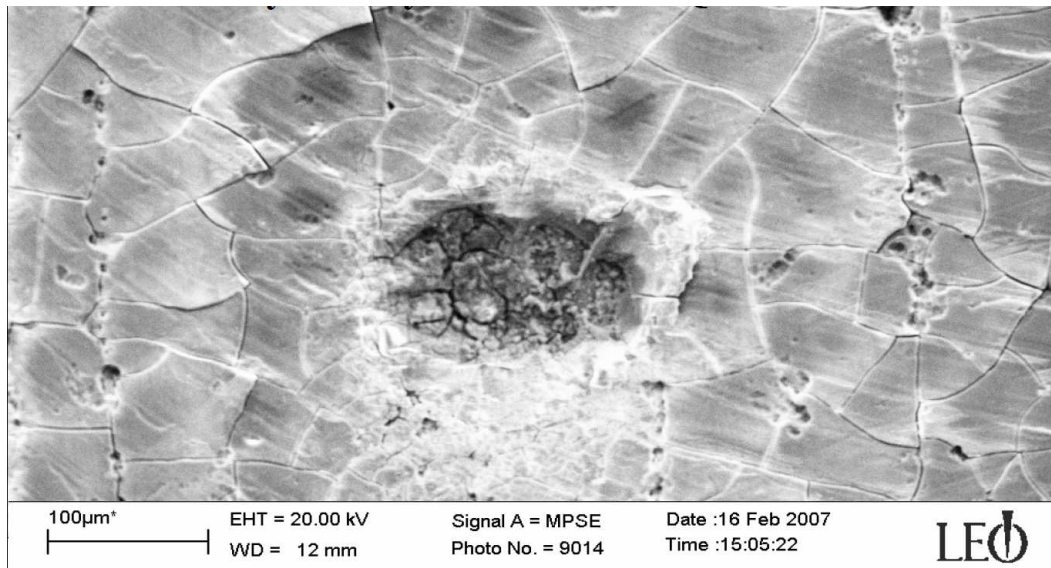


Figure 1.4: Electronic microscope photo of the damage caused by a multipactor discharge in a black anodised filter. Source: ESA.

close to the characteristic critical pressure of the gas molecules present in the space between the electrodes. The critical pressure is the one at which the breakdown voltage curve of a gas reaches a minimum, as it can be seen in Fig. 1.1. There are mainly two mechanisms that create this minimum value. At higher pressures, the gas molecules absorb most of the free electrons, inhibiting the generation of plasma. At pressures below the critical value, the collisions with gas molecules are less likely and the electrons need more energy in average to develop to plasma in a sufficient amount. If the breakdown voltage is not reached, the free electron density decays due to diffusion and recombination. In the transition band between corona and multipactor, approximately from 10^{-4} mbar to 10^{-2} mbar, some authors define an effect called multipactor plasma, but the classification here is merely a matter of interpretation. Basically, a contribution to the increase in electron density is caused by wall collisions, and the rest by ionisation of the neutral gas molecules. In this work, we will however focus on pure multipactor. Beyond the definition of the different discharge types, the fundamental idea is that microwave space applications, which fly during the launch phase through the whole range of pressures from ambient to vacuum, should be protected against multipactor, corona, and their combined effects.

An example of a corona-related failure in an operational space mission happened in the TWT of the X-SAR synthetic aperture radar (SAR) instrument [10] in 1983 (see photo in Fig. 1.5). The instrument was embarked in the Space Shuttle at an altitude of 225 km during the Spacelab Microwave Remote Sensing Experiment (MRSE). Although passing the on-ground radiation tests at 0.1 mbar, corona discharges at pressure levels between 1 mbar and 10 mbar in the high tension input coaxial cable (nominal voltage up to 12 kV) of the TWT spoiled the instrument operation. It caused a malfunction of the amplifier, which did not provide enough power to the system to send radar pulses, and no data could be acquired

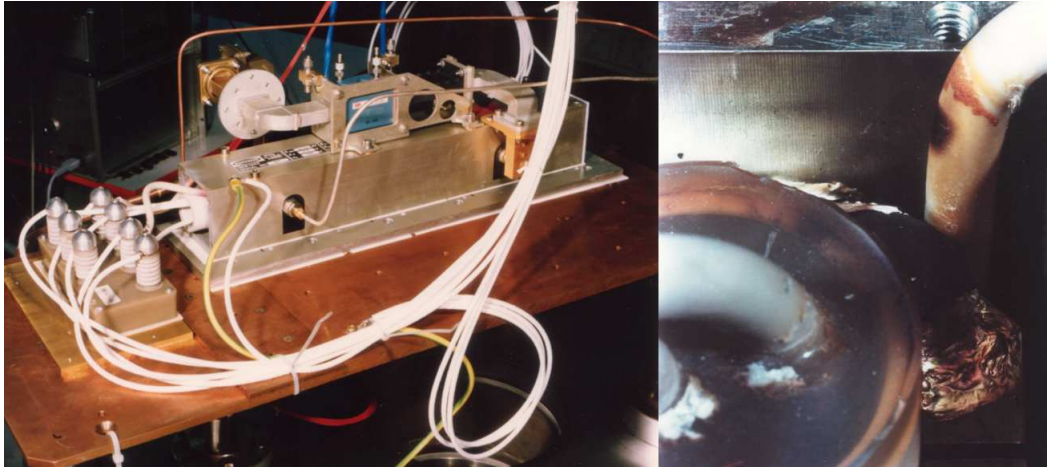


Figure 1.5: TWT of the X-SAR synthetic aperture radar instrument flown aboard the Shuttle during the MRSE mission in 1983 (left). Detail of the burn-out caused by the corona discharge (right). Source: German Aerospace Center (DLR).

during the whole experiment. The most probable reason for the generation of the discharge was the ageing and partial erosion of the coating at the input coaxial location. Since the Shuttle returned back to Earth, the coating could be replaced and the X-SAR instrument could successfully operate during next acquisition campaigns.

Unlike the Shuttle, common satellites cannot be repaired after being launched, which entails that such failures would jeopardise the whole mission. Even smaller performance perturbations are to be avoided, since an essential aspect is the long-term stability of the electrical performance of the satellite during its operational life. Not only satellites with radar instruments are affected, but also any of them carrying payload subsystems with high-power requirements in the RF and microwave bands. Examples of these subsystems are transponders in communication satellites (see block diagram in Fig. 1.6). The input and output multiplexers (diplexers in the simplified case depicted there) in such transponders might be composed of passive rectangular waveguide filters, that can be damaged by multipactor and corona discharges, like in the case of the lowpass filter shown in Fig. 1.7. Other sensitive subsystems are the RF chains used for data downlink, typically in the X- and Ku-bands, or for telemetry, tracking and telecommand (TT&C), typically operating at S-band.

From the mission requirements point of view, there has been a sustained increase in the output power of the microwave transmission channels over the last years in all frequency bands, as highlighted in Fig. 1.8. The multipactor problematic entails a limitation on the power the payload can handle [11, 12], which justifies the concern of the space industry. Usually a very conservative approach is taken in the designs to avoid the discharge, and considerable resources are invested into the multipactor testing process for flight qualification.

Nevertheless, the support of Universities and leading technology centres has been often requested for investigating solutions to suppress the multipactor discharges, or to shift them towards higher power levels, while keeping the electrical and mechanical properties of the

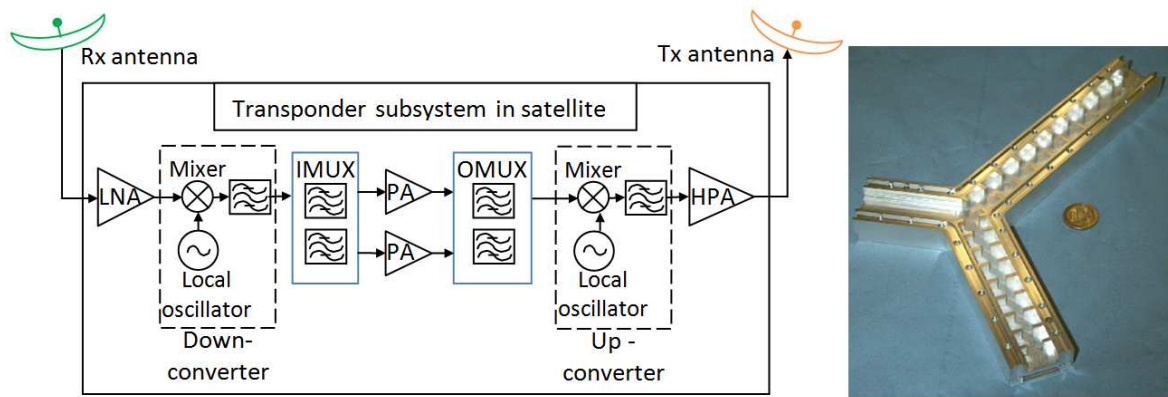


Figure 1.6: Simplified block diagram of a satellite transponder with input/output multiplexers (IMUX/OMUX). These 1:2 multiplexers can be implemented with waveguide diplexers like the one shown in the photo on the right. Source photo: ESA.

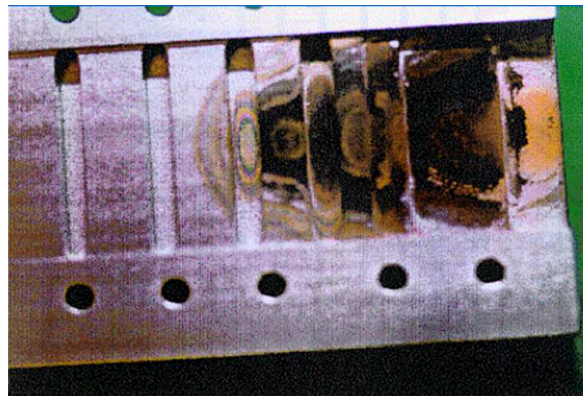


Figure 1.7: Photo of the destructive effect of an RF breakdown on a lowpass filter. Source: Thales Alenia Space France.

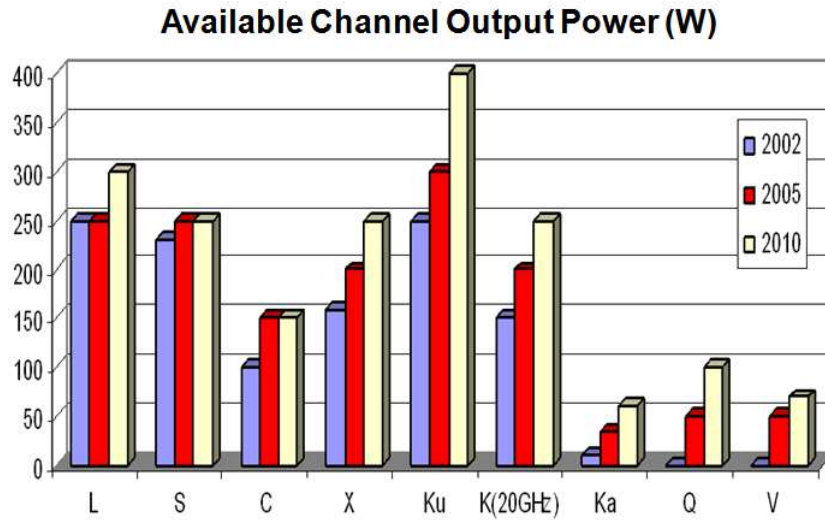


Figure 1.8: Evolution of the output power requirements of satellite microwave instruments over time for the different frequency bands. Source: ESA.

devices. Over the last decades, ESA has tried to coordinate these efforts, and to set some standards for normalising the multipactor analysis and the related testing procedures [3]. Any new design rule/idea to achieve multipactor-free devices would contribute to reduce the associated testing costs, and it would be of great interest for the microwave space community.

Multipactor analysis theory has also evolved during the last century. The first efforts considered simplified scenarios, such as assuming single-carrier signals in an infinite parallel-plate topology, a one-dimensional electron motion and a deterministic emission energy of secondary electrons [2, 13–15]. A basic parallel-plate topology has the advantage of having an homogeneous electrostatic field that can be computed analytically. ESA developed a series of parallel-plate susceptibility charts [11], which are still widely used to determine a conservative power handling boundary for rectangular waveguide filters. These charts are based on empirical measurements considering different gap sizes, frequencies and materials, and are easy to use due to the linear dependence of the threshold over the frequency times gap-distance product ($f \times d$), as can be seen in Fig. 1.9.

More recent studies have abandoned the simple assumptions of classical theory and are capable of considering, e.g., secondary electron emission velocities not directly linked to the impact energy [16], or three-dimensional trajectories of the electrons in waveguide devices with finite dimensions. Some studies still focus on rectangular waveguides [17] and irises [18], but also on coaxial structures [19–21]. Apart from the described top-bottom wall resonance, single-surface multipactor also exists [22], and even in waveguides partly covered with dielectrics [23]. The existence of hybrid two-sided multipactor modes have also been documented [24], where the bottom-to-top travel time of the electrons is different from the top-to-bottom one. Modern satellite applications often deal with multi-carrier signals, i.e. for navigation and digital broadcasting satellite services. More advanced multi-carrier mul-

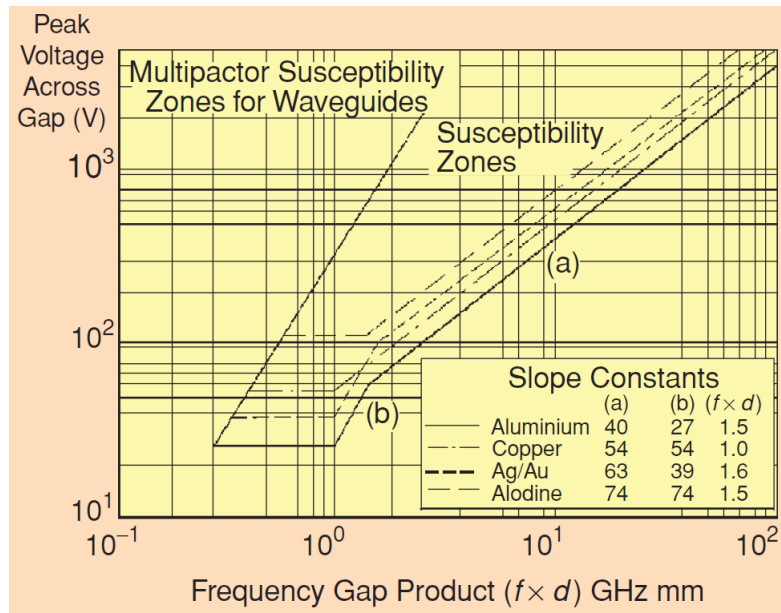


Figure 1.9: Susceptibility maps for the parallel-plate case. Multipactor discharges might occur within the susceptibility regions. The slope constants indicate the MP behaviour for the different materials. Source: M. Yu, “Power Handling Capability for RF Filters”, IEEE Microwave Magazine, 2007.

tipactor analysis theories, based on the non-stationary single-carrier method [25, 26], were developed to cope with these cases. Other advanced algorithms consider the contribution of the space charge fields [27] in the multipactor prediction. These fields are generated by the electron resonant cloud, and are also responsible for the electromagnetic effects of a multipactor discharge. In certain cases they are so strong that they should not be neglected in the prediction calculations.

The state-of-the-art techniques to minimise the multipactor problem in microwave devices try to avoid the electrons entering in a resonant state. The typical approach is to modify one of the conditions that are expected to lead to the discharge, e.g. frequency, pressure, geometry, electromagnetic fields, wall materials, etc. Here are some of the known strategies collected from the literature, where their advantages and drawbacks are also indicated.

- Pressurisation

By introducing gas molecules in a hollow waveguide structure under low-pressure conditions, the mean free path of the electrons is reduced [28]. Then, free electrons have a higher probability of being absorbed by the molecules and less chances to hit the waveguide metallic walls. Pressurisation may reduce multipactor risks, but there is still a risk of corona breakdown due to the presence of gas inside the device. It can also increase the payload weight and create a source of potential intermodulation products (PIM).

- **Dielectric filling**
Foam or solid dielectrics reduce the mean free path of the electrons [23,29], but cause an increase of the dissipation losses.
- **Direct Current (DC) biasing**
The superposition of DC fields over the RF fields disturbs the resonant electron trajectories [30,31]. A potential implementation consists of an electric spiral coil around the multipactor-critical regions of the device. The axial magnetic field generated within the coil might deviate potential electrons from their resonant path (Hall effect [32]). Extra equipment is needed, with the consequent increase in power consumption and weight.
- **Slot on broad walls**
Opening narrow slots in the structure lets electrons drift out, altering the resonance condition [33,34]. One of the problems of this option is a severe risk of RF leakages. Furthermore, the corners generated when creating the slots might have a negative impact on the multipactor suppression. The slot itself might even contain new parallel-plate geometries with very narrow gaps.
- **Change of the surface properties**
Special coatings and chemical treatments can reduce the Secondary Electron Emission Coefficient (SEEC) of the surfaces, like the commonly used Alodine, or Titanium [35]. Different tests conducted at ESA-European Research and Technology Centre (ESTEC) [36] have identified TiN, CrN and CN coatings as the best solutions against multipactor. A recent patent [37] also presents a porous material with good discharge suppression. However, a common drawback of these techniques is that they may introduce higher losses.
- **Change of the gap size**
A component can be especially designed to avoid narrow gaps, so that a higher power level would be needed to induce a discharge than in a conventional structure. Unfortunately, this may modify the electrical response and seriously affect an RF design. In particle accelerator applications, the reduction of the gap size below the multipacting cutoff also proved useful [38].

Generally, methods that involve an increase in the weight, volume or power consumption of the devices, or even the introduction of additional equipment, are not suited for space applications. Modifications of the electrical response imply also a drawback, since a re-design of the structure might not be feasible in a limited time frame. Moreover, most of the research on multipactor suppression methods concentrates on the physics and the modelling of the discharge mechanism, and usually lack on practical implementations or experimental verifications. Very few novel designs have been presented, which involve geometry changes in the device [34,39,40].

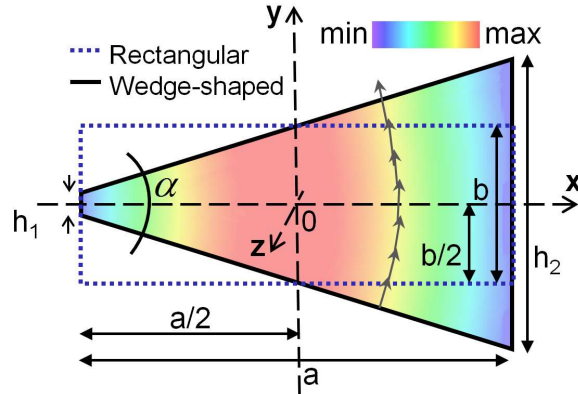


Figure 1.10: Cross sections of a wedge-shaped waveguide and of its equivalent rectangular one. Both waveguides have the same width a and average height $b = (h_1 + h_2)/2$, resulting in equal cross-section areas. Inside the wedge-shaped cross section, the colours indicate the distribution of the transverse electric field of the fundamental mode, similar to the TE_{10} fundamental mode of a rectangular waveguide. Grey arrows show the electric field vectors along an arc between top and bottom plates.

1.2 Objectives and Challenges

The original motivation behind this work is to identify a novel hollow waveguide geometry that offers a better multipactor behaviour than conventional rectangular waveguides for space applications, while keeping similar dimensions, weight, electromagnetic properties, bandwidth and intermodulation noise. This structure should be versatile enough to allow its usage within a wide range of microwave devices. The complexity of the geometry should be limited, since eventually new electromagnetic computation algorithms have to be implemented for analysing it, and existing design procedures adapted. Additionally, it should be manufactured at a reasonable cost and tested in the laboratories with standard testing interfaces.

The selected approach was to use a geometry with a wedge-shaped cross section. This topology is determined by symmetrically inclined top and bottom walls and straight vertical side-walls (cf. Fig. 1.10). Hence, the height of the cross section changes linearly from the narrow side-wall to the broad side-wall [41]. Each of the different possible inclination angles α might offer a particular electric and multipactor behaviour. We define a wedge-shaped waveguide as a microwave transmission line with such a constant cross section in the propagation direction. The first time that a similar structure was mentioned in the literature was for particle accelerator systems [42,43]. Triggered by the first publications about wedge-shaped waveguides [41, 44], a series of theoretical studies of their multipactor discharge behaviour followed [17, 45–47].

The study and implementation of this novel structure for usage in microwave devices, as well as the verification of its resistance to multipactor discharges, entail a series of challenges, which have been established as the objectives of this PhD thesis. Firstly, the electromag-

netic analysis has to be adapted to wedge-shaped geometries, whose electromagnetic fields cannot be solved analytically. Existing commercial analysis tools can compute such fields, like High Frequency Structure Simulator (HFSS) [48] and Computer Simulation Technology (CST) [49]. These general purpose software packages are capable of analysing almost any arbitrary geometry, but with the drawback of a high computational cost. This is not suitable for our purposes, since CPU efforts related to the electromagnetic field computation is one of the determining contributions to the whole simulation long times. Therefore, a tool shall be developed that focuses on the analysis of wedge-shaped waveguides. This allows implementing time-efficient and precise algorithms, not as flexible as the mentioned commercial tools in terms of input geometries, but still accepting different wedge-shaped configurations.

A similar strategy is followed by another commercial tool, Full-wave Electromagnetic Simulation Tool (FEST^{3D}) [50]. With a modular architecture, FEST^{3D} integrates several modules with very efficient algorithms for specific geometries in a common environment. The combination of all modules covers most of the microwave structures of interest for the space industry. Through a cooperation with Aurora Software and Testing (the company that presently takes care of this software, on behalf of ESA-ESTEC), a goal of this work is to develop a module that could be included within FEST^{3D} as a package feature or add-on.

Once the electromagnetic fields of wedge-shaped waveguides are available, their real advantage from a multipactor point of view has to be quantified. Traditional tools based on the parallel-plate model [3, 11, 14], e.g. the European Cooperation for Space Standardisation (ECSS) Multipactor Tool [51], rely on empirical results. Furthermore, they are only configured for dealing with standard waveguide technologies like rectangular waveguides, whose modal behaviour is well-known, contrarily to wedge-shaped ones. Another existing tool is the Multipactor Electron Simulation Tool (MEST) [52], more precise and complex than the ECSS Multipactor Tool, but still unable to handle arbitrarily-shaped geometries. Therefore, a multipactor prediction tool needs to be developed, which can provide reliable results within an acceptable time frame. Most of the multipactor prediction algorithms available in the literature [17, 42] study waveguide models invariants in the propagation direction. Hence, a two-dimensional (2-D) model is used to study the electron behaviour. Since it is intended to apply the wedge-shaped waveguide to more complex structures, like bandpass filters and transformers, where there are waveguide discontinuities and non-homogeneous fields, the potential three-dimensional (3-D) trajectory of the electrons has to be considered, with the corresponding increase in terms of complexity.

Suitable results from the prediction tool would be multipactor susceptibility curves (like the ones existing for rectangular and parallel plate geometries [14]), as well as predicted voltage and input power thresholds. With the help of these predictions, knowledge about different wedge-shaped configurations can be systematically obtained and design rules might be derived. This would be a preliminary requirement for trying to apply the wedge-shaped topology to more complex devices. A potential implementation of the multipactor prediction functionalities within FEST^{3D} shall be considered.

The final objective of this work is to design, manufacture and test more complex microwave devices, of interest for the space industry, containing at least a wedge-shaped geometry



Figure 1.11: Satellite assembly undergoing qualification tests. Multipactor tests are usually conducted for individual payload devices. They are a small, but critical fraction of all required system and subsystem tests. Source: ESA.

in any of its stages (e.g. filters), and to experimentally prove the validity of the theory. In order to design such devices, like bandpass filters, existing design synthesis methods [53,54] have to be adapted and extended to allow arbitrary wedge-shaped geometries. Manufacturing aspects must also be taken into account, since an increase in the geometry complexity infers an increase in the costs and eventually the need of new milling equipment. Manufacturing tolerances are therefore a critical requirement that has to be considered in the design process of these new structures.

One of the fundamental problems in multipactor research is the expensive testing procedures for verifying the simulation results. It depends on multiple issues, and the results are not always repeatable. Electron seeding, materials and coatings, pressure and temperature conditions, detection methods and criteria, all have an influence in the practical/experimental results. Well established test procedures exist [3], but their proper execution in a clean environment are always a challenge, however essential to obtain reliable and comparable test results. Safer microwave design could contribute in reducing the multipactor testing costs of satellite payload hardware.

By joining the simulation and the measurement experiences, it is intended to identify optimal design rules for the application of wedge-shaped topologies on operational space hardware, as well as to assess its impact and practical applicability.

1.3 Thesis Structure

This PhD Thesis consists of six chapters that are devoted to the main research path of this work, the development of new multipactor-resistant waveguides, plus five appendices with the derivation of useful formulas, describing the multipactor test setup and with additional information about the author's professional and scientific background. The current chapter is the introduction, where the motivations, objectives and the state-of-the-art have been presented. An exhaustive reference list is given here, which can assist the reader in getting in touch with the multipactor physics and applications and with the most current developments in the field. It focuses on the relevance of this project from the point of view of the space industry.

In Chapter 2, the fundamentals of the derivation of the electromagnetic fields in wedge-shaped waveguides are presented. This algorithm is an essential feature of the simulation tools developed in this work, since both the multipactor prediction tools and the filter design algorithm rely on the derived field values. This dependency also reflects on the total simulation duration, which will directly benefit from the numerical efficiency in the calculation of the electromagnetic fields.

Chapter 3 is a detailed description of the multipactor prediction tool that has been developed for wedge-shaped waveguides. It is based on an effective electron model, where a high energy particle is tracked with a numerical electron dynamics model throughout an excited waveguide. Its results are validated against existing results from the literature. Moreover, several parametric simulation studies provide the first insights on the future wedge-shaped waveguide design guidelines, including the generation of multipactor susceptibility maps.

Chapter 4 explains how wedge-shaped geometries can be used as waveguide bandpass filter building blocks. A wedge-shaped filter has been designed and manufactured in order to demonstrate its advantages with respect to a conventional rectangular waveguide filter from a multipactor discharge threshold point of view. It is also the first time that this new topology has been used to design a complex microwave device, and that it has been successfully manufactured and tested. Another similar rectangular waveguide bandpass filter serves as reference for allowing a rigorous comparison.

The measurement of this first wedge-shaped bandpass filter showed very promising results, but also identified issues with a clear improvement potential. This motivated the design of a "second generation" wedge-shaped bandpass filter, as described in Chapter 5. On the one hand, the chosen inclination angle between top and bottom plates is the theoretically optimal one from a multipactor threshold point of view. On the other hand, a preliminary analysis of the modal behaviour of the wedge-shaped geometry of the filter resonator cavities has provided the necessary information to synthesise a higher-order mode filter response (repetition frequency) and a Q factor comparable with the rectangular ones. Nevertheless, mechanical aspects have also been improved to ensure a satisfactory manufacturing process. The measured electrical and multipactor performances of this device are included in this chapter, together with a summary of the optimal design rules for designing bandpass filters

with wedge-shaped waveguides.

Finally, Chapter 6 summarises the main contributions of this work towards the design of wedge-shaped bandpass filters, and it discusses the potentials of this waveguide geometry and the practical implications of the resulting power range extension. Some guidelines for future research activities in the field are proposed as a consequence of the work performed in this PhD Thesis.

Appendix A defines the expression of the normalised electromagnetic modes of rectangular waveguides. This is required for an efficient analysis of wedge-shaped waveguides and the related discontinuities based on an integral equation method.

Appendix B comprises the study of ohmic losses in the metallic walls of hollow waveguide devices. These losses are not only considered in the walls parallel to the propagation direction or the RF signal, but also in walls perpendicular to it, like the ones corresponding to irises in transformers, low- and bandpass filters. The mathematical formulation for computing the ohmic losses in arbitrary waveguides like wedge-shaped waveguides is given here. This allows determining the S-parameters of stepped waveguide devices including the conductivity of the metallic material of the waveguide walls as a configurable input parameter.

More information about the multipactor test bed and an overview on the applied detection methods are included in Appendix C.

Appendix D lists the author's technical and professional formation, as well as his most relevant research highlights.

A compilation of the author's scientific publications is included in Appendix E.

Chapter 2

Electromagnetic Analysis of Wedge-shaped Waveguides

2.1 Computation of the Modal Solution

2.1.1 Wedge-shaped Waveguide and Rectangular Reference Box

Several electromagnetic analysis and simulation tools have been developed or extended in the frame of this work. The first one, which will be described in this chapter, is an analysis tool for stepped waveguide structures, like filters and transformers, accepting both rectangular and wedge-shaped waveguide building blocks. The second one is a tool for the synthesis of wedge-shaped waveguide bandpass filters based on typical design requirements. The specific details of this design method are part of Chapter 4. The third one is a multipactor prediction tool for all these devices, and it is the subject of Chapters 3 and 4.

All these tools require the computation of the electromagnetic fields, or of some parameters related to the modal solutions of the corresponding waveguides. Therefore, an efficient computation of the electromagnetic fields is a key factor to the overall performance, establishing a potential advantage with respect to other commercially available tools. The modal charts of hollow waveguides with almost arbitrary cross sections (basically shapes that can consist of series of straight lines, circular and elliptical arcs) can be efficiently computed with the Boundary Integral - Resonant Mode Expansion (BI-RME) method (see [55] and [56]).

In our case, the target waveguides have a wedge-shaped cross section with symmetrically inclined top and bottom walls and straight vertical walls, as it is shown in Fig. 2.1. The horizontal length of the wedge-shaped waveguide is called a_{Wedge} and the lengths of the narrow and broad side-walls are h_1 and h_2 , respectively. As a basis for the computation of the electromagnetic fields in wedge-shaped waveguides, the BI-RME method proposes to use the normalised modal expressions of a reference canonical waveguide (whose modes can be calculated analytically), also called reference box. It shall contain the whole arbitrary waveguide within its rectangular cross section. Here, this can be done with a rectangular waveguide with width a and height b , also placed centred in the origin of the coordinate sys-

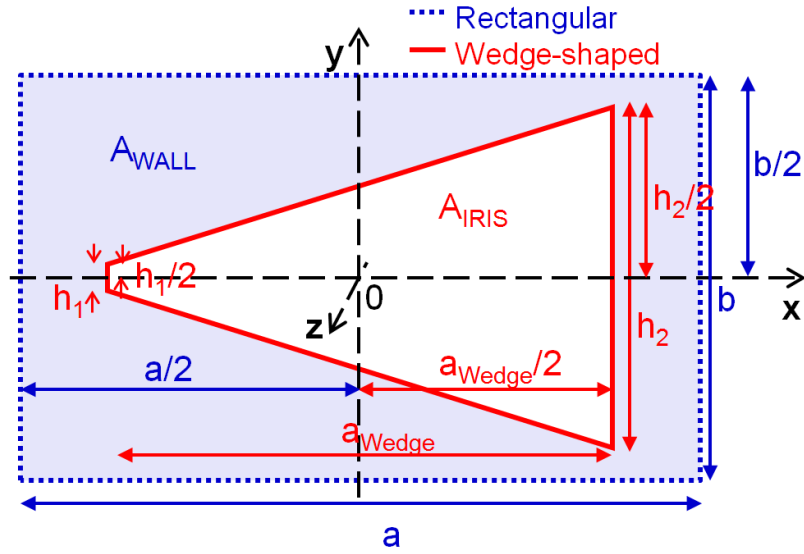


Figure 2.1: Cross section of a discontinuity between a rectangular and a wedge-shaped waveguide. The rectangular waveguide can be used as a reference box for deriving the modes of the wedge-shaped one.

tem, like the one shown in Fig. 2.1. This figure shows the junction plane of both waveguides, perpendicular to the propagation direction. The cross-section area of the iris created by the wedge-shaped waveguide A_{IRIS} can be computed as follows:

$$A_{\text{IRIS}} = a_{\text{Wedge}} \frac{h_1 + h_2}{2} \quad (2.1)$$

Accordingly, the area of the transversal wall around the iris in the discontinuity plane A_{WALL} (blue-shaded region in Fig. 2.1) can be obtained as:

$$A_{\text{WALL}} = a \cdot b - A_{\text{IRIS}} \quad (2.2)$$

Please note that the x -axis of the coordinate system is located in the horizontal symmetry plane of both rectangular and wedge-shaped cross sections, and the y -axis is in the vertical symmetry plane of the rectangular one (and it is placed at a distance of $a_{\text{Wedge}}/2$ from both wedge-shaped vertical side-walls). The names assigned to the different dimensions in this picture will be used throughout the whole work.

The BI-RME technique efficiently computes both the modal cutoff frequencies (eigenvalues), and the electric and magnetic field patterns (eigenvectors) of the wedge-shaped waveguide, as a solution of two generalised eigenvalue problems related with the TE and TM modes of the reference rectangular waveguide. The normalised modal expressions of a rectangular waveguide is included in Appendix A. Propagation in z -direction is assumed in this chapter as well.

2.1.2 Normalised Arbitrary TE Modes

The normalised rectangular modes (with “□” as superscript) of a reference box like the blue-dotted one in Fig. 2.1 (usually with $a = a_{\text{Wedge}}$) serve as basis functions for the derivation of the wedge-shaped waveguide modes (with “arb” as superscript). The basis functions are weighted by certain coefficients in a series summation to deliver the arbitrary waveguide modes. The arbitrary modes can be classified as well into transverse electric (TE) and transverse magnetic (TM) modes. In (2.3), the expression of the electric field for the TE case is shown:

$$\vec{e}_{T,m}^{\text{arb(TE)}} = \sum_{\substack{\text{(TE)} \\ i=1}}^{\infty} \left[\left\langle \vec{e}_{T,m}^{\text{arb(TE)}}; \vec{e}_i^{\square(\text{TE})} \right\rangle \cdot \vec{e}_i^{\square(\text{TE})} \right] + \sum_{\substack{\text{(TM)} \\ i'=1}}^{\infty} \left[\left\langle \vec{e}_{T,m}^{\text{arb(TE)}}; \vec{e}_{i'}^{\square(\text{TM})} \right\rangle \cdot \vec{e}_{i'}^{\square(\text{TM})} \right] \quad (2.3)$$

being m the index of the arbitrary waveguide mode, and the subscript T the transversal vector components, i.e. x, y under the current assumptions. The z -component is equal to 0, as corresponds to TE modes. The arbitrary waveguide fundamental mode is the one for $m = 1$ (it has a lower cutoff frequency than the corresponding TM mode, like in a rectangular waveguide). The theoretically infinite summations are in practice interrupted after including a sufficiently high number of elements, established empirically based on convergence tests. The coefficients of the basis functions in the summations are the terms within angle brackets $\langle \cdot; \cdot \rangle$, and are the coupling integrals between the arbitrary waveguide normalised modes and the rectangular ones. A coupling integral between any two waveguide modes is defined in (2.4):

$$\langle \vec{e}_m; \vec{e}_i \rangle = \int_S \vec{e}_m \cdot \vec{e}_i dS = \int_S \vec{h}_m \cdot \vec{h}_i dS \quad (2.4)$$

being S the transversal cross-section area of the smallest waveguide, in this case the arbitrary one. Since the modes are normalised according to Appendix A, both the electric or the magnetic fields can be used for the calculation. The coupling integrals between arbitrary and rectangular waveguide modes can be directly derived from the BI-RME method [56].

The expressions of the normalised magnetic field components of the arbitrary waveguide modes for the TE case are the following ones:

$$\vec{h}_{T,m}^{\text{arb(TE)}} = \sum_{\substack{\text{(TE)} \\ i=1}}^{\infty} \left[\left\langle \vec{e}_{T,m}^{\text{arb(TE)}}; \vec{e}_i^{\square(\text{TE})} \right\rangle \cdot \vec{h}_{T,i}^{\square(\text{TE})} \right] + \sum_{\substack{\text{(TM)} \\ i'=1}}^{\infty} \left[\left\langle \vec{e}_{T,m}^{\text{arb(TE)}}; \vec{e}_{i'}^{\square(\text{TM})} \right\rangle \cdot \vec{h}_{i'}^{\square(\text{TM})} \right] \quad (2.5)$$

$$h_{z,m}^{\text{arb(TE)}} = \sum_{\substack{\text{(TE)} \\ i=1}}^{\infty} \left[\left\langle \vec{e}_{T,m}^{\text{arb(TE)}}; \vec{e}_i^{\square(\text{TE})} \right\rangle \cdot h_{z,i}^{\square(\text{TE})} \right] \quad (2.6)$$

There is an alternative way to compute (2.5):

$$\vec{h}_{T,m}^{\text{arb(TE)}} = \hat{z} \times \vec{e}_{T,m}^{\text{arb(TE)}} \quad (2.7)$$

This saves computation time if (2.3) has been previously calculated, since the magnetic field can be derived avoiding the costly summation loop in (2.5).

2.1.3 Normalised Arbitrary TM Modes

The corresponding electric field for the TM case is shown here:

$$\vec{e}_{T,m}^{\text{arb(TM)}} = \sum_{\substack{\text{(TM)} \\ i'=1}}^{\infty} \left[\left\langle \vec{e}_{T,m}^{\text{arb(TM)}}; \vec{e}_{i'}^{\square(\text{TM})} \right\rangle \cdot \vec{e}_{T,i'}^{\square(\text{TM})} \right] \quad (2.8)$$

$$e_{z,m}^{\text{arb(TM)}} = \sum_{\substack{\text{(TM)} \\ i'=1}}^{\infty} \left[\left\langle \vec{e}_{T,m}^{\text{arb(TM)}}; \vec{e}_{i'}^{\square(\text{TM})} \right\rangle \cdot e_{z,i'}^{\square(\text{TM})} \right] \quad (2.9)$$

The expression of the normalised arbitrary magnetic modes in the TM case are the following:

$$\vec{h}_{T,m}^{\text{arb(TM)}} = \sum_{\substack{\text{(TM)} \\ i'=1}}^{\infty} \left[\left\langle \vec{e}_{T,m}^{\text{arb(TM)}}; \vec{e}_{i'}^{\square(\text{TM})} \right\rangle \cdot \vec{h}_{i'}^{\square(\text{TM})} \right] \quad (2.10)$$

Here as well, (2.10) can be alternatively computed as:

$$\vec{h}_{T,m}^{\text{arb(TM)}} = \hat{z} \times \vec{e}_{T,m}^{\text{arb(TM)}} \quad (2.11)$$

which saves computation time.

2.1.4 Unnormalised Arbitrary TE Modes

For obtaining the actual field values for the electromagnetic fields in the arbitrary waveguide, a similar unnormalisation procedure as the one described in Appendix A.3 has to be applied.

Arbitrary E-fields

$$\vec{E}_T^{\text{arb(TE)}} = K^{\text{arb(TE)}} \vec{e}_T^{\text{arb(TE)}} \quad (2.12)$$

where

$$K^{\text{arb(TE)}} = \sqrt{2P_{\text{Transm}} Z^{\text{arb(TE)}}} \quad (2.13)$$

and

$$Z^{\text{arb(TE)}} = \frac{\omega\mu}{\beta^{\text{arb(TE)}}} \quad (2.14)$$

The value of $\beta^{\text{arb(TE)}}$ is given by BI-RME for all possible modes. The instantaneous electric field can then be retrieved by multiplying by the complex propagation exponential

($e^{-j\beta^{\text{arb}}(\text{TE})z}$) and then applying (A.2). Note that the characteristic impedance of an arbitrary waveguide Z_C^{arb} is, like for the rectangular case (compare with Appendix A.3), the one of the fundamental mode (2.15):

$$Z_C^{\text{arb}} = \frac{\omega\mu}{\beta_1^{\text{arb}}} \quad (2.15)$$

Arbitrary H-fields

$$H_z^{\text{arb}}(\text{TE}) = K^{\text{arb}}(\text{TE}) h_z^{\text{arb}}(\text{TE}) \quad (2.16)$$

$$\vec{H}_T^{\text{arb}}(\text{TE}) = \frac{K^{\text{arb}}(\text{TE})}{Z^{\text{arb}}(\text{TE})} \vec{h}_T^{\text{arb}}(\text{TE}) \quad (2.17)$$

The instantaneous magnetic field can then be retrieved by multiplying by the complex propagation exponential ($e^{-j\beta^{\text{arb}}(\text{TE})z}$) and then applying (A.7).

2.1.5 Unnormalised Arbitrary TM Modes

Arbitrary H-fields

$$\vec{H}_T^{\text{arb}}(\text{TM}) = K^{\text{arb}}(\text{TM}) \vec{h}_T^{\text{arb}}(\text{TM}) \quad (2.18)$$

where

$$K^{\text{arb}}(\text{TM}) = \sqrt{\frac{2P_{\text{Transm}}}{Z^{\text{arb}}(\text{TM})}} \quad (2.19)$$

and

$$Z^{\text{arb}}(\text{TM}) = \frac{\beta^{\text{arb}}(\text{TM})}{\omega\epsilon} \quad (2.20)$$

The value of $\beta^{\text{arb}}(\text{TM})$ is given by BI-RME for all possible modes. The instantaneous magnetic field can then be retrieved by multiplying by the complex propagation exponential ($e^{-j\beta^{\text{arb}}(\text{TE})z}$) and then applying (A.7).

Arbitrary E-fields

$$E_z^{\text{arb}}(\text{TM}) = K^{\text{arb}}(\text{TM}) e_z^{\text{arb}}(\text{TM}) \quad (2.21)$$

$$\vec{E}_T^{\text{arb}}(\text{TM}) = K^{\text{arb}}(\text{TM}) Z^{\text{arb}}(\text{TM}) \vec{e}_T^{\text{arb}}(\text{TM}) \quad (2.22)$$

The instantaneous electric field can then be retrieved by multiplying by the complex propagation exponential ($e^{-j\beta^{\text{arb}}(\text{TE})z}$) and then applying (A.2).

2.1.6 Grid Interpolation

In the application of multipactor prediction algorithms with loops that require to evaluate the electromagnetic fields in different positions of the waveguide cross section, a direct computation of the series in Chapter 2.1.2 or 2.1.3 with a sufficient accuracy would involve an extreme computational cost. The solution proposed here is the pre-computation of the normalised EM fields in a grid covering the whole cross section, as shown in Fig. 2.2. The grid

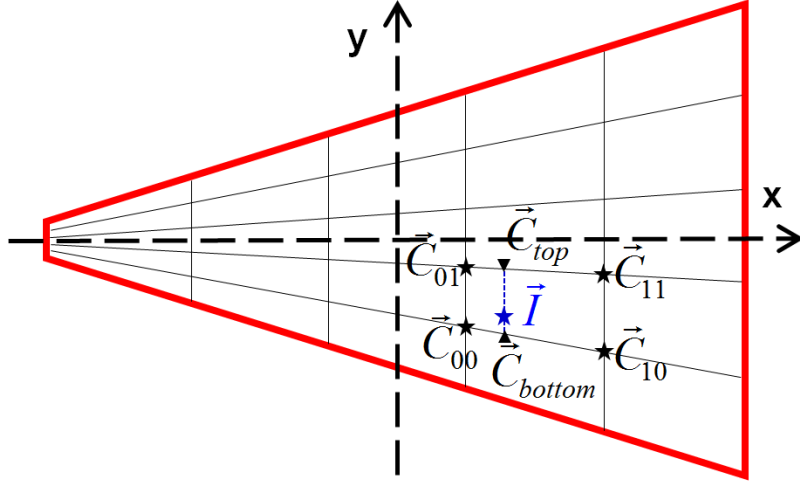


Figure 2.2: Grid of a wedge-shaped waveguide for EM field interpolation.

is not regular, but follows instead the shape of the wedge-shaped waveguide. The vertical grid lines are parallel to each other and equi-distant. The left and right side-walls contain the starting and end points, respectively, of the almost-horizontal grid lines. The starting points are placed equidistantly to each other, and the ending points as well. This gives an uneven distribution of grid nodes, which have a denser sampling towards the narrow side-wall of the waveguide. By defining the grid in this way, any point inside the arbitrary cross section has four corners around it with known EM field values. This simplifies the interpolation algorithm procedure.

The field values in the target point \vec{I} are then retrieved by a simple bilinear interpolation of the values in the four grid nodes \vec{C}_{00} , \vec{C}_{10} , \vec{C}_{01} and \vec{C}_{11} (see Fig. 2.2). First, the interpolated electric field (the same applies for the magnetic field) is calculated at \vec{C}_{bottom} and \vec{C}_{top} , which are the points defined by the intersections between a vertical line through \vec{I} and the polygon formed by the four corner points. This is expressed mathematically in (2.23) and (2.24):

$$\vec{e}_{C_{bottom}}^{interp} = \vec{e}_{C_{00}} + (\vec{e}_{C_{10}} - \vec{e}_{C_{00}}) \frac{I_x - C_{00,x}}{C_{10,x} - C_{00,x}} \quad (2.23)$$

$$\vec{e}_{C_{top}}^{interp} = \vec{e}_{C_{01}} + (\vec{e}_{C_{11}} - \vec{e}_{C_{01}}) \frac{I_x - C_{01,x}}{C_{11,x} - C_{01,x}} \quad (2.24)$$

where I_x is the x -coordinate of \vec{I} . Then, the field in \vec{I} can be obtained with (2.25):

$$\vec{e}_I^{interp} = \vec{e}_{C_{bottom}}^{interp} + (\vec{e}_{C_{top}}^{interp} - \vec{e}_{C_{bottom}}^{interp}) \frac{I_y - C_{bottom,y}}{C_{top,y} - C_{bottom,y}} \quad (2.25)$$

Substituting (2.23) and (2.24) into (2.25):

$$\begin{aligned}
\vec{e}_I^{\text{interp}} &= \vec{e}_{C_{00}} + (\vec{e}_{C_{10}} - \vec{e}_{C_{00}}) \frac{I_x - C_{00,x}}{C_{10,x} - C_{00,x}} + \\
&+ \left(\vec{e}_{C_{01}} - \vec{e}_{C_{00}} + (\vec{e}_{C_{11}} - \vec{e}_{C_{01}} - \vec{e}_{C_{10}} + \vec{e}_{C_{00}}) \frac{I_x - C_{00,x}}{C_{10,x} - C_{00,x}} \right) \cdot \\
&\cdot \frac{I_y - C_{\text{bottom},y}}{C_{\text{top},y} - C_{\text{bottom},y}} \quad = \\
&= \vec{e}_{C_{00}} + (\vec{e}_{C_{10}} - \vec{e}_{C_{00}}) \frac{I_x - C_{00,x}}{C_{10,x} - C_{00,x}} + (\vec{e}_{C_{01}} - \vec{e}_{C_{00}}) \frac{I_y - C_{\text{bottom},y}}{C_{\text{top},y} - C_{\text{bottom},y}} + \\
&+ (\vec{e}_{C_{11}} - \vec{e}_{C_{01}} - \vec{e}_{C_{10}} + \vec{e}_{C_{00}}) \frac{(I_x - C_{00,x})(I_y - C_{\text{bottom},y})}{(C_{10,x} - C_{00,x})(C_{\text{top},y} - C_{\text{bottom},y})} \quad (2.26)
\end{aligned}$$

The y -components of \vec{C}_{top} and \vec{C}_{bottom} can be expressed as:

$$C_{\text{top},y} = C_{01,y} + \frac{C_{11,y} - C_{01,y}}{C_{10,x} - C_{00,x}} (I_x - C_{00,x}) \quad (2.27)$$

$$C_{\text{bottom},y} = C_{00,y} + \frac{C_{10,y} - C_{00,y}}{C_{10,x} - C_{00,x}} (I_x - C_{00,x}) \quad (2.28)$$

This procedure can also save some time in the rectangular waveguide problems. In that case, and assuming a regular grid, the expression of the bilinear interpolation is slightly simpler:

$$\begin{aligned}
\vec{e}_I^{\text{interp}} &= \vec{e}_{C_{00}} + (\vec{e}_{C_{10}} - \vec{e}_{C_{00}}) \frac{I_x - C_{00,x}}{C_{10,x} - C_{00,x}} + (\vec{e}_{C_{01}} - \vec{e}_{C_{00}}) \frac{I_y - C_{00,y}}{C_{01,y} - C_{00,y}} + \\
&+ (\vec{e}_{C_{11}} - \vec{e}_{C_{01}} - \vec{e}_{C_{10}} + \vec{e}_{C_{00}}) \frac{(I_x - C_{00,x})(I_y - C_{00,y})}{(C_{10,x} - C_{00,x})(C_{01,y} - C_{00,y})} \quad (2.29)
\end{aligned}$$

2.2 Simulation of the EM Behaviour

2.2.1 Comparison Wedge-Rectangular Field Patterns

The field patterns can give us a first indication of the properties of wedge-shaped waveguides. Since we want to offer an alternative topology to rectangular waveguides, their fields and modal solutions will serve as reference for a comparison. Here, it is useful to remember the modal chart of rectangular waveguides, shown in Fig. 2.3 (cf. also Appendix A). The mode with the lowest cutoff frequency (i.e. the fundamental mode) is the TE_{10} , and this is the one to consider for multipactor prediction simulations.

In order to allow a proper one-to-one comparison, our basic approach consists of having a wedge-rectangular pair with the same width and cross-section area, as it is also the case in

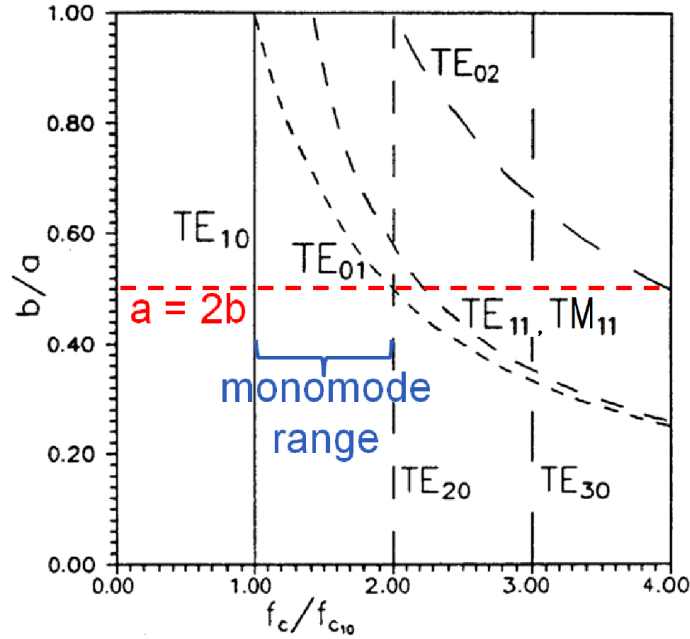


Figure 2.3: Modal chart of rectangular waveguides. The cutoff frequencies of the different modes, normalised to the one of the fundamental mode TE_{10} , are represented for the different values of the ratio between the height b and the width a of the rectangular waveguide.

Fig. 1.10. As explained in Chapters 1.2 and 2.1.1, equal cross-section areas can be achieved if the average height of the wedge-shaped waveguide is equal to the b dimension of the rectangular one. The following dimensions have been chosen here: $a = a_{\text{Wedge}} = 19.05$ mm, $b = 12$ mm, and $\alpha = 20^\circ$. The rest of the dimensions can be directly derived from the considered equivalence criteria: $h_1 = 8.641$ mm and $h_2 = 15.359$ mm.

From this point and on, all simulations have been performed with the developed tool for the calculation of the EM fields (including the interpolation procedure just described before), and the plots were generated with the aid of FEST^{3D} v.6.6 [50]. The first step was the calculation of the electric field of the fundamental mode of the wedge-shaped waveguide, as shown in Fig. 2.4. The resemblance with the rectangular TE_{10} mode is clear. However, unlike the pure vertical electric fields of the rectangular case, there is a bending of the field vectors. These deviations seem to follow concentric circle arcs, which would have as a centre the imaginary intersection of the top and bottom wedge wall planes. This brings up an analogy with coaxial waveguides. The wedge-shaped waveguide is indeed very similar to a coaxial waveguide section. The curvature of the field vectors compared to the rectangular case is supposed to be the main contribution to the improvement of the multipactor behaviour of these structures, which will be described with more detail in Chapter 3.

A visual comparison between the field patterns of the selected waveguide examples is presented in Table 2.1. It is an overview of the first four modes sorted in terms of increasing cutoff-frequency values (note that the computed rectangular modes agree with the ones in-

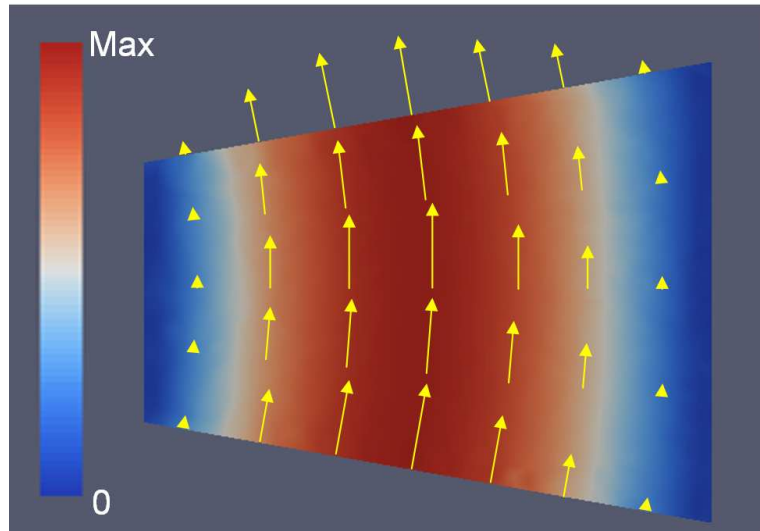


Figure 2.4: Electric field pattern (absolute value and vector grid) of the fundamental mode in the cross section of a wedge-shaped waveguide with the following dimensions: $a_{\text{Wedge}} = 19.05$ mm, $h_1 = 8.641$ mm, $h_2 = 15.359$ mm, $\alpha = 20^\circ$.

indicated in the chart of Fig. 2.3 for a value $b/a = 0.63$). When comparing the electric field patterns, the distributions of the first and the third modes are almost identical for the rectangular and wedge-shaped cases. Similarities can also be found for the second mode, but there is a stronger distortion in the wedge-shaped case. The fourth mode is completely different, which indicates that there is no connection between them. In fact, the fourth wedge-shaped waveguide mode looks very similar to the fifth rectangular mode, the TE_{20} according to Fig. 2.3. This means that the cutoff frequencies do not follow exactly the same order in both waveguides. Furthermore, the wedge cutoff frequencies are different from the rectangular ones, even for the modes that are almost identical (compare the first two columns of Table 2.1). This phenomenon will be analysed in more detail in Chapter 2.2.3 and later on in this document. Note also that the wedge-shaped modes can also be classified in TE and TM modes, as defined in Chapter 2.1. However, the numbering cannot be interpreted in the same way as for the rectangular case, where it directly symbolises the number of periodic variations of the field in the horizontal and vertical directions. Apart from the electric fields, additional columns have been included in Table 2.1 for the magnetic field patterns, which are also interesting from a multipactor behaviour perspective. The similarities and differences observed for the electric fields are also confirmed with the magnetic fields.

Table 2.1: EM field patterns (absolute value) of the first four modes in order of increasing cutoff frequencies for a rectangular and an equivalent wedge-shaped waveguide. The colours are coded like in the previous figure. Dimensions of the rectangular waveguide: $a = 19.05$ mm, $b = 12$ mm. Wedge-shaped waveguide is identical to the one of the previous figure.

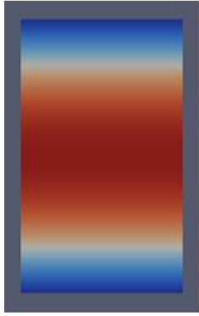
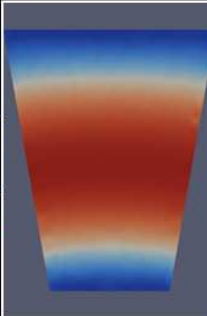

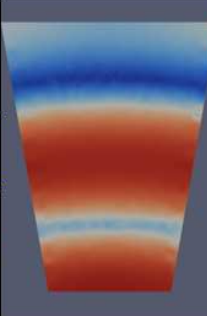
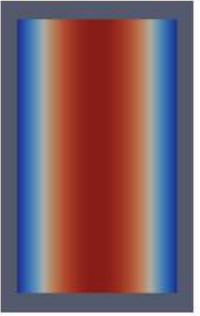
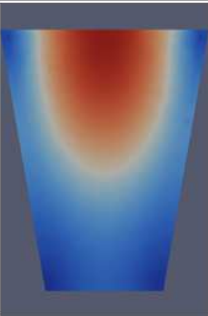

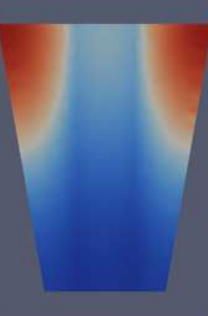
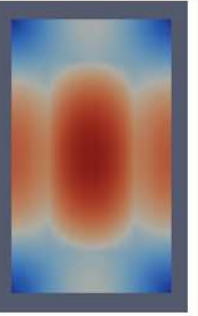
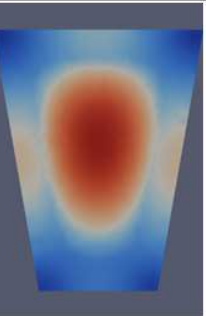
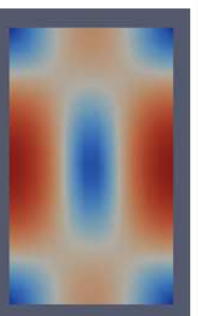
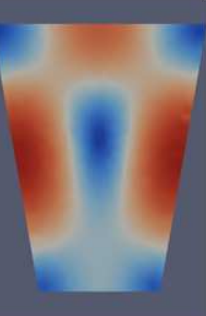
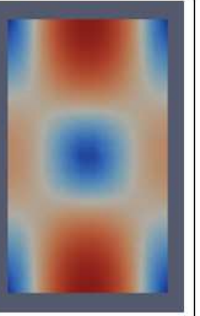
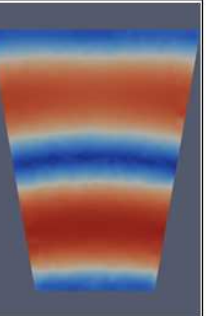
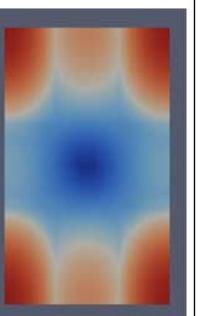
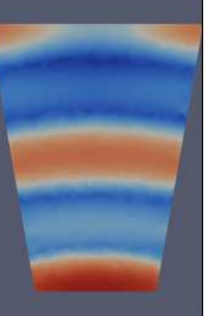
Mode		Electric field (absolute value)		Magnetic field (absolute value)	
Rectangular	Wedge-shaped	Rectangular	Wedge-shaped	Rectangular	Wedge-shaped
TE ₁₀ $f_c =$ 7,869 GHz	TE ₁₀ $f_c =$ 7,922 GHz				
TE ₀₁ $f_c =$ 12,491 GHz	TE ₂₁ $f_c =$ 11,441 GHz				
TM ₁₁ $f_c =$ 14,763 GHz	TM ₁₂ $f_c =$ 14,812 GHz				
TE ₁₁ $f_c =$ 14,763 GHz	TE ₃₃ $f_c =$ 15,691 GHz				

Table 2.2: Dimensions of the wedge-shaped waveguides included in the sweep. For all examples: $a_{\text{Wedge}} = 19.05$ mm. Minimum value for $h_{1,\text{min}} = 1$ mm.

α [deg]	h_1 [mm]	h_2 [mm]	h_{mean} [mm]
5	11.168	12.832	12
20	8.641	15.359	12
40	5.066	18.934	12
60	1.001	22.999	12
70	1	27.678	14.339

2.2.2 Inclination Angle Limits

Focusing on the fundamental mode of wedge-shaped waveguides, Chapter 2.2.1 has confirmed that, for a moderate inclination angle of 20° , it has a TE_{10} -like electric field pattern and a similar (but not identical) cutoff frequency to the one of the equivalent rectangular waveguide. It is expected that, for lower inclination angles (note that a wedge becomes a rectangle for $\alpha \rightarrow 0$), the similarity is even stronger. However, the behaviour and design limits of structures with $\alpha > 20^\circ$ must still be studied. From a multipactor resistance point of view, it could be assumed that, the bigger the inclination, the more distortion would be introduced in the field patterns, and the less likely the formation of a resonance path would be. However, if the distortion exceeds certain limits, the use of the wedge-shaped waveguide as a substitute for rectangular ones would not be feasible any more (i.e. preserving good properties for filtering applications).

Therefore, a sweep over α has been done here taking as a reference the same rectangular waveguide used in Table 2.1, and the field patterns have been calculated for the different resulting structures (see dimensions in Table 2.2). Note that, if the cross-section area has to be kept constant for equivalence reasons, there is a limit on the inclination angle applicable to the wedge. In this case, for a constant $a = a_{\text{Wedge}} = 19.05$ mm, this happens for an angle slightly over 60° , when h_1 reaches the value 0 mm. Since we are interested in even higher inclinations, our approach in this and for next inclination sweeps is to assign a minimum value to h_1 , here $h_{1,\text{min}} = 1$ mm, due to manufacturing limitations. For inclination angles over 60° , $h_1 = h_{1,\text{min}}$, and we deliberately allow h_{mean} to grow bigger than b . This choice does not fulfil the “equal cross-section area” criterion, but it still helps to the understanding of the wedge-shaped waveguide nature.

Table 2.3 includes the electric and magnetic field patterns simulated for the selected structures considered in this sweep. The field patterns show a good agreement (for the fundamental mode) with the rectangular case up to 40° . At 60° and above, the distribution of the field pattern becomes very different to the rectangular one, as can be seen in the last rows of Table 2.3. The transition where the fundamental mode stops being a TE_{10} -like mode happens close to 60° . This is caused by the fact that, at this angle, the wedge-shaped waveguide becomes an equilateral triangular waveguide [57], with considerable different properties from the rectangular case. Consequently, this result sets a limitation on the range of α values to consider for multipactor applications. It is also interesting to point out that the cutoff fre-

quency constantly increases with α up to $\alpha = 60^\circ$. Then, it decreases again, even below the value of the rectangular waveguide, at $\alpha = 70^\circ$. These transition phenomena around $\alpha = 60^\circ$ will be discussed in more detail in the following subchapter.

2.2.3 Modes and Cutoff Frequencies

In most microwave waveguide applications it is wished that only one mode is propagating in the frequency range (monomode regime). Thus, the operating frequency f is chosen slightly above the cutoff of the fundamental mode $f_C(1)$, and below the one of the second mode $f_C(2)$. The distance between the operating frequency and the cutoff of the second mode determines the monomode bandwidth, which is a key aspect to take into account when evaluating the design capabilities of wedge-shaped waveguides.

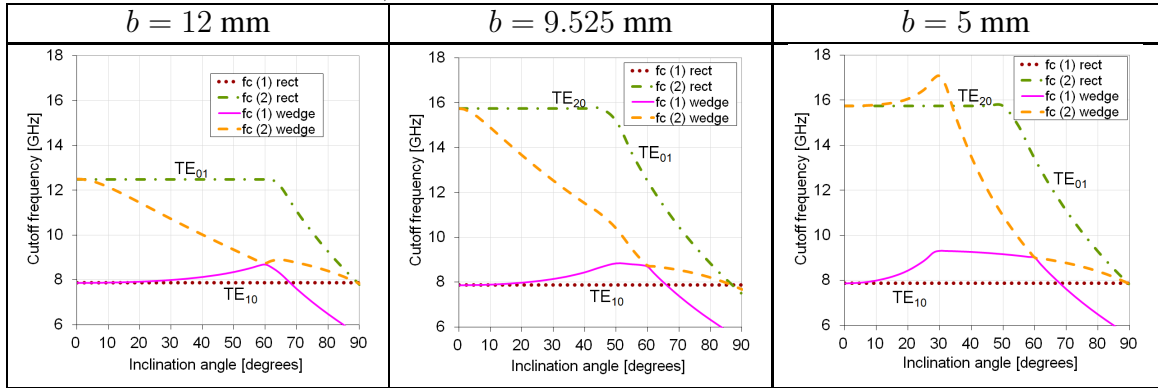
In rectangular waveguides, for a given f , the monomode bandwidth depends on the b/a ratio, as can be seen in Fig.2.3. Assuming that $a > b$, the cutoff frequencies of TE_{10} (fundamental mode) and TE_{20} (second mode for $b/a < 0.5$) are independent from b . However, for $b/a > 0.5$, TE_{01} becomes the second mode, and its cutoff frequency comes constantly closer to the one of TE_{10} for an increasing b/a -ratio, which considerably reduces the monomode bandwidth. Therefore, it is more convenient to keep TE_{20} as the second-order mode. The typical ratio selected for rectangular waveguides is 1:2 (marked with a red-dashed line in Fig.2.3), which is a trade-off between monomode frequency range and propagation losses, since losses are minimal when the ratio goes to 1 (rectangle becomes a square). As already observed in the previous chapter, the cutoff frequencies of the wedge-shaped waveguides are different from the rectangular ones, hence it is worth to study them and identify the corresponding implications on the design. In particular, it has to be determined which range of average heights and α -values offer an acceptable monomode bandwidth. Other considerations related to multipactor behaviour criteria will be handled in the following chapters.

With this goal in mind, three rectangular waveguides with width $a = 19.05$ mm have been considered. Their height values b are: 12 mm (like the example of Chapters 2.2.1 and 2.2.2), 9.525 mm (standard WR75 waveguide) and $b = 5$ mm. For each of these references, a set of equivalent wedge-shaped waveguides with inclination angles ranging from 0° to 90° , and with the same width $a = a_{\text{Wedge}}$ has been obtained. For each structure in these sweeps, the cutoff frequencies of the first couple of propagating modes have been calculated and the results are included in Table 2.4 (magenta-solid and orange-dashed curves in each of the plots). The cutoff frequencies of the reference rectangular waveguides have been also depicted to facilitate the comparison (brown-dotted and green-dashed-dotted curves in each of the plots). Note that the indices “1” and “2” are dynamically assigned to the first two propagating modes, ordered according to the ascending cutoff-frequency value. Moreover, a minimum value for the narrow side of the wedges of $h_{1,\text{min}} = 1$ mm has been chosen. Once this minimum value is reached, the mean height of the wedge-shaped waveguides has to exceed the b of the original reference rectangular waveguides. In such cases, the height of the reference rectangular waveguide will be adjusted to said mean height value in order to facilitate the interpretation of the plots.

Table 2.3: EM field patterns (absolute value) of the fundamental mode of wedge-shaped waveguides with different inclination angles (rectangular for $\alpha = 0^\circ$). The colours are coded like in the previous images.

Inclination angle	Fundamental mode	Electric field (absolute value)	Magnetic field (absolute value)
0° (rectangular)	TE ₁₀ f _c = 7,869 GHz		
5°	TE ₁₀ f _c = 7,871 GHz		
20°	TE ₁₀ f _c = 7,922 GHz		
40°	TE ₁₀ f _c = 8,133 GHz		
60°	TE ₁₀ f _c = 8,691 GHz		
70°	TE ₁₀ f _c = 7,381 GHz		

Table 2.4: Cutoff frequencies of the first two propagating modes of different wedge-shaped waveguides in terms of the inclination angles. Each column/graph uses a different rectangular waveguide as a reference, each with a different b but all with a constant $a = 19.05$ mm. The minimum height of the wedge side-walls is $h_{1,\min} = 1$ mm. b remains constant for each column, except when $h_1 = h_{1,\min}$.



In the first column of Table 2.4 ($b = 12$ mm), the behaviour of the cutoff frequency of the fundamental mode of the wedge-shaped waveguide $f_{C,\text{wedge}}(1)$ already observed in the previous subchapter is confirmed: its value increases with the inclination angle until 60° , where it starts decreasing again. For $\alpha > 68^\circ$, it descends below the cutoff of the fundamental mode of the rectangular case $f_{C,\text{rect}}(1)$. Due to the fact that the reference rectangular waveguide has a ratio $b/a > 0.5$, TE_{01} is here the second-order mode, with a cutoff frequency $f_{C,\text{rect}}(2)$. A consequence of this: there is a relatively small rectangular monomode bandwidth. An even lower monomode bandwidth is available for the different equivalent wedge-shaped waveguides, since the $f_{C,\text{wedge}}(2)$ -curve keeps always below $f_{C,\text{rect}}(2)$. When observing the evolution of the $f_{C,\text{wedge}}(1)$ and $f_{C,\text{wedge}}(2)$ curves, it can be detected that they are equal at $\alpha \approx 60^\circ$. This can be understood as a mode swap, which explains the sudden discontinuity in the slope of both curves. Once the $h_{1,\min}$ value has been reached, at $\alpha \approx 62^\circ$, it has to be noted that the value $f_{C,\text{rect}}(2)$ is not calculated any more for b , but for the corresponding (higher) h_{mean} -value, since this suits better for comparison with the wedge-shaped cases. Hence, at the mentioned inclination $\alpha \approx 62^\circ$, the $f_{C,\text{rect}}(2)$ curve experiences a bend resulting from the direct dependency of $f_{C,\text{rect}}(2)$ on the height value.

The second rectangular waveguide example (second column of Table 2.4, $b = 9.525$ mm) is a standard WR75 waveguide, with the most common ratio $b/a = 0.5$. Indeed, the cutoff frequency of the second mode $f_{C,\text{rect}}(2)$ is much higher than in the case of the first column. Except for this detail, the graph is similar to the previous one. Here as well, the $f_{C,\text{wedge}}(2)$ curve has smaller values than $f_{C,\text{rect}}(2)$ for all wedge-shaped waveguide cases. This indicates that, for this particular case, we have to count on a non-negligible reduction in the monomode bandwidth with respect to the one of the equivalent rectangular waveguide. For moderate angles, the second-order mode is the TE_{20} , which has a cutoff value independent from the b/a ratio. $h_{1,\min}$ is reached at $\alpha \approx 50^\circ$. From this α -value on, h_{mean} starts growing over

b , which increases the h_{mean}/a ratio, immediately exceeding 0.5. Hence, the swap in the second-order mode of the rectangular waveguide between TE_{20} and TE_{01} takes place at this precise inclination $\alpha \approx 50^\circ$.

A rather interesting interpretation can be extracted from the third case, shown in the last column of Table 2.4 ($b = 5$ mm). Here, the ratio $b/a \approx 0.25$. Unlike the other examples, the wedge-shaped monomode bandwidth remains almost identical to the rectangular one for inclination angles up to 40° . Above this value, the usual drop in $f_{\text{C,wedge}}(2)$ and the slope jump between the $f_{\text{C,wedge}}(1)$ and $f_{\text{C,wedge}}(2)$ curves occur. In this last example, $h_{1,\text{min}}$ is reached at $\alpha \approx 30^\circ$, and h_{mean}/a becomes > 0.5 at $\alpha \approx 50^\circ$, like in the case of the second column.

After this preliminary analysis, several conclusions become clear:

- The maximum α value applicable to a wedge is limited by the b/a ratio of the equivalent rectangular waveguide, assuming it is wished to keep the criterion $h_{\text{mean}} = b$.
- Wedge-shaped waveguides with $\alpha < 60^\circ$ have a fundamental mode very similar to the rectangular waveguide case.
- The cutoff frequency of the fundamental mode of wedge-shaped waveguides within this range of α -values is always higher than the one of a rectangular waveguide with the same width.
- The monomode bandwidth is generally lower than for the rectangular waveguide case (reduction is significant for values of $h_{\text{mean}}/a > 0.5$), decreasing with α .
- In the case $h_{\text{mean}}/a < 0.5$ a monomode bandwidth comparable to the rectangular one can be achieved for all feasible α -values (that fulfil $h_{\text{mean}} = b$). This will be the scenario where appropriate applications for a multipactor-resistant wedge-shaped waveguide must be found.

2.3 Discontinuities and S-Parameters of Stepped Waveguide Devices

2.3.1 Discontinuities with Wedge-shaped Waveguides

For the efficient analysis of passive waveguide devices, such as filters or transformers, the proposed method for calculating the modal solution of infinite waveguides (Chapter 2.1) has to be extended to solve also discontinuities and consider standing waves. An integral equation formulation [58] has been applied here. It consists of characterising planar discontinuities (perpendicular to propagation direction) between waveguides through multi-modal impedance or admittance matrices. Each waveguide element is necessarily uniform (constant cross section), but can have a different shape and dimensions from the other ones, which creates a planar discontinuity in the junction plane like the one shown in Fig. 2.1.

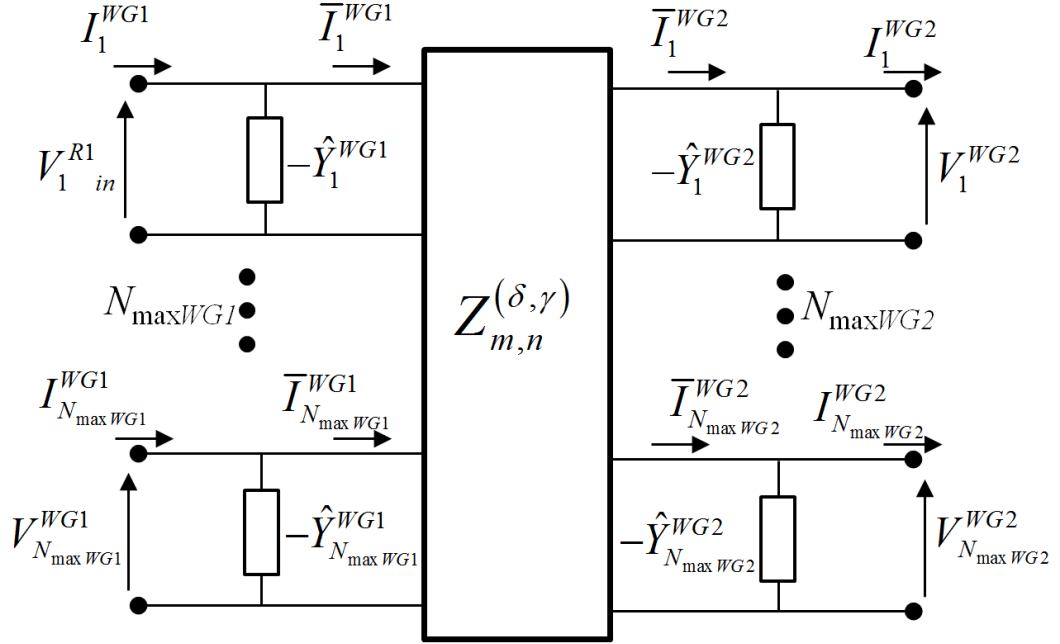


Figure 2.5: Schematic representation of a multi-modal impedance matrix that characterises a discontinuity between waveguides.

An example of a multimodal impedance matrix representation is given in Fig. 2.5 [59,60]. Each plane (input and output) of the matrix involves a modal solution of the input (left) or output (right) waveguide. The asymptotic admittance matrices are defined, according to the corresponding modal solutions derived in Chapter 2.1, as follows:

$$\hat{Y}_n \approx \begin{cases} -j \frac{k_{C,n}}{\omega \mu} & \text{TE mode} \\ j \frac{\omega \epsilon}{k_{C,n}} & \text{TM mode} \end{cases} \quad (2.30)$$

where $k_{C,n}$ is the cutoff wavenumber of the corresponding n -th mode.

Discontinuity matrices can be combined together with the ones of transmission lines to provide the scattering parameters (S-parameters) of the whole structure. Here, the formulation for the resolution of the discontinuity is extended to cover interfaces between rectangular and wedge-shaped waveguides, and between two wedge-shaped waveguides. The main update is the computation of the coupling integrals between the modes of both waveguides at the discontinuity (2.31):

$$\langle \vec{e}_m^{WG1}, \vec{e}_i^{WG2} \rangle = \int_{A_{IRIS}} \vec{e}_m^{WG1} \cdot \vec{e}_i^{WG2} dS \quad (2.31)$$

where $WG1$ is the blue-dotted rectangular waveguide shown in Fig. 2.6, and $WG2$ is the red-solid wedge-shaped one. By convention, $WG1$ will be the waveguide with the larger

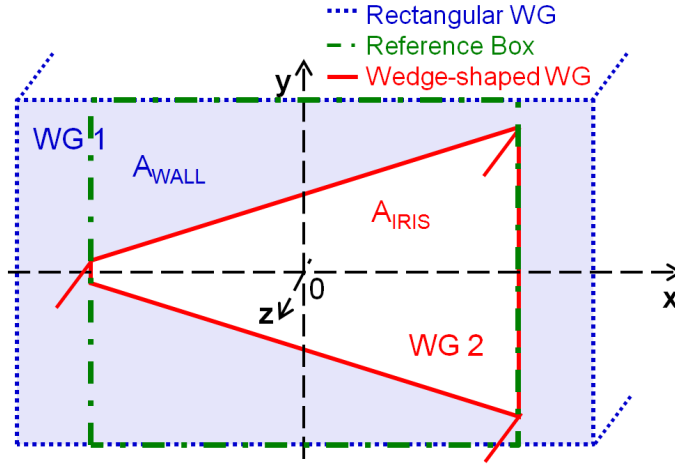


Figure 2.6: Example of a discontinuity between a rectangular ($WG 1$) and a wedge-shaped waveguide ($WG 2$). The dash-dotted green rectangle represents one of the possible reference boxes for calculating the modal chart of $WG 2$.

cross-section area. The solutions of these coupling integrals are given by the BI-RME method.

As a general rule, reference boxes that are tightly adjusted to its corresponding arbitrary waveguide converge faster to the desired solution. Hence, in most discontinuities between rectangular and wedge-shaped waveguides, instead of using as a reference box the waveguide present at the discontinuity, it is more efficient to use a different one (refbox), like the green dot-dashed rectangle in Fig.2.6. Here, the way to calculate the coupling integrals is slightly different from (2.31):

$$\langle \vec{e}_m^{WG1}, \vec{e}_i^{WG2} \rangle = \sum_{r(\text{refbox modes})} \langle \vec{e}_m^{WG1}, \vec{e}_r^{\text{refbox}} \rangle \langle \vec{e}_r^{\text{refbox}}, \vec{e}_i^{WG2} \rangle \quad (2.32)$$

In (2.32), the first coupling integral in the summation product is between the modes of two rectangular waveguides (see analytical solution in [60]), whereas the second one is the one that BI-RME would deliver for this particular reference box. Apart from increasing the efficiency, there are other reasons for using tailored reference boxes in the rectangular to arbitrary discontinuities (examples can be found in Table 2.7). If the ratio between the areas A_{IRIS} and A_{WALL} is an integer number (first row, first column of Figure 2.7), there might be instabilities in the resolution of the BI-RME problem. Therefore, it is advisable to use a reference box with a smaller surface. If $WG 1$ is already the smallest possible rectangular geometry that contains $WG 2$ (first row, second column of Table 2.7), it is also possible to use a reference box larger than $WG 1$. Larger reference boxes also apply when $WG 1$ does not fully contain $WG 2$. Finally, reference boxes have to be also selected if we deal with a discontinuity between two wedge-shaped waveguides (second row, second column of Table 2.7). In this case, using the same reference box for both waveguides saves some computation time. On the other hand, the modes of $WG 2$ might converge slower than with

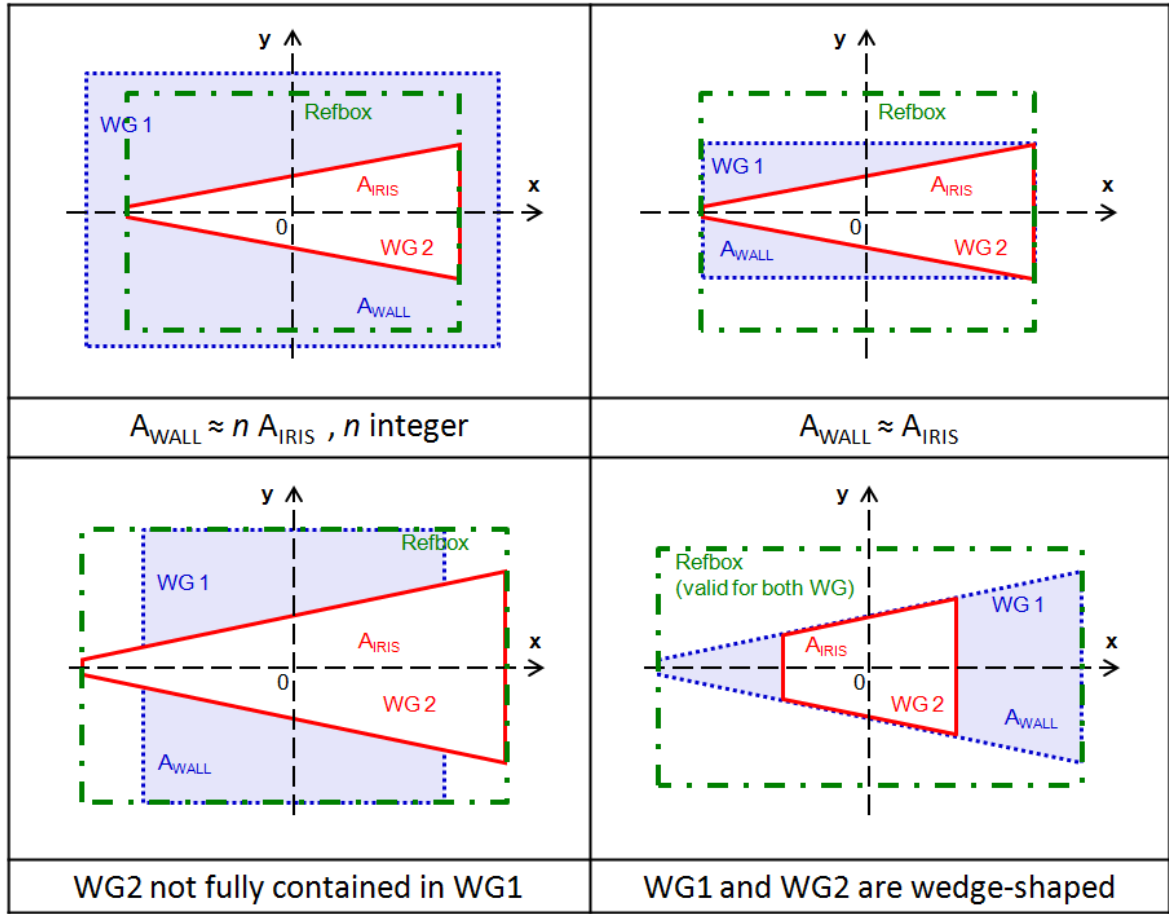


Figure 2.7: Different cases in which a special reference box, different from $WG 1$, has to be used.

a specifically tailored reference box. An algorithm has been implemented that calculates the ratio A_{IRIS}/A_{WALL} when analysing a discontinuity and that uses the suitable reference box in each case.

2.3.2 Analysis of Stepped Waveguide Structures

Combining several impedance matrices, a structure composed of a series of waveguide sections connected in cascade can be analysed. The circuitual model for an example of a cascaded structure can be seen in Fig. 2.8. The modal voltages V and currents I are the unknowns, and the admittances \hat{Y} , the transmission line lengths l and the propagation constants β are given.

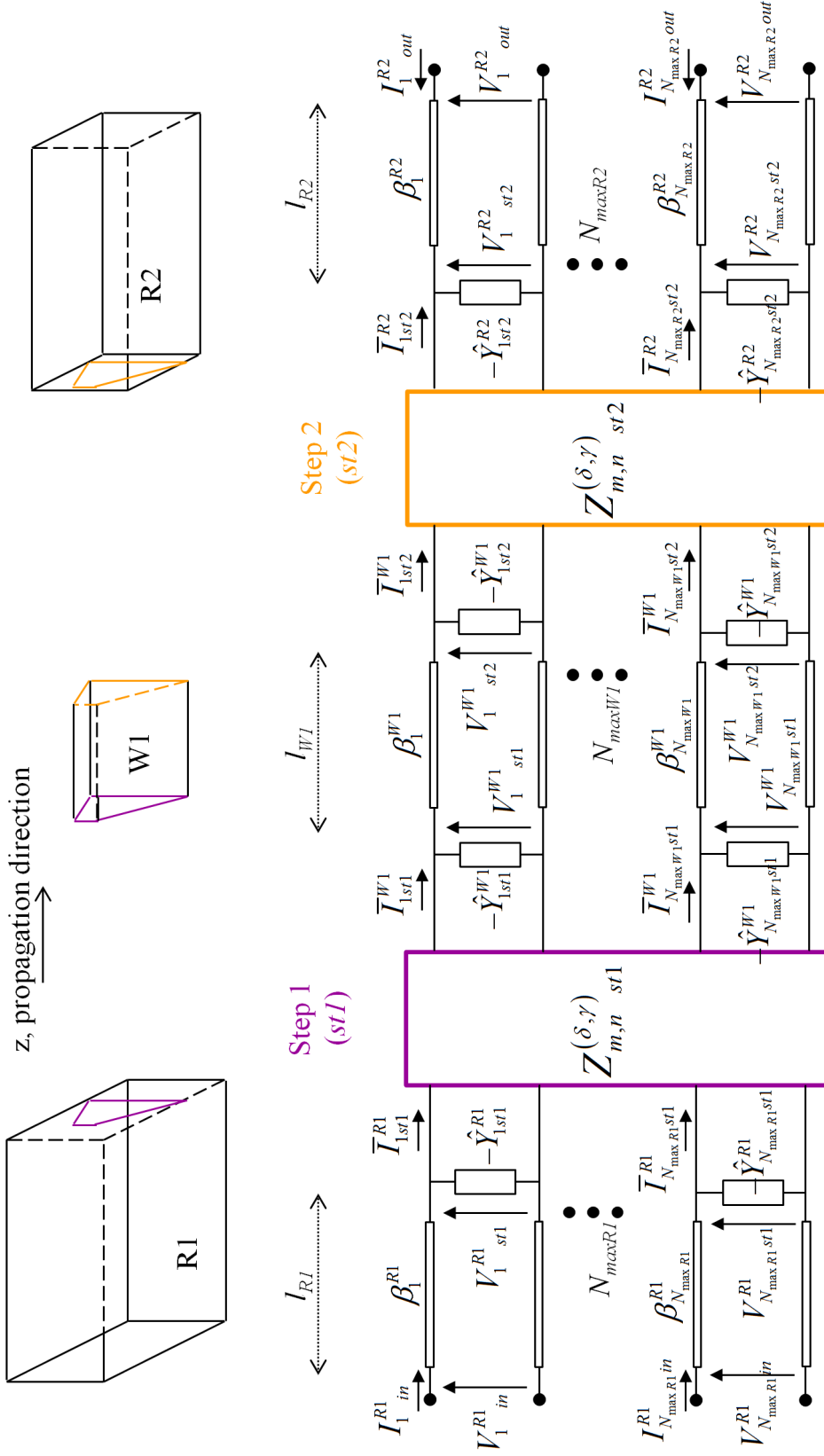


Figure 2.8: Circuitual model of a series of waveguide elements, a rectangular, a wedge-shaped, and another rectangular, and their corresponding discontinuities.

The transmission lines are modelled by means of a π -equivalent admittance circuit. A detailed description of the derivation of the S-parameters of the whole structure (charge of the matrices) is given in [59, 60].

Chapter 3

Multipactor Effect Analysis of Wedge-shaped Waveguides

3.1 Electron Emission in Metals

3.1.1 Models for the Secondary Emission Yield

The multipactor discharge mechanism relies on the electron emissivity of the metallic walls to build up a sufficient electron density, as depicted in Fig.1.2 of Chapter 1.1. When an electron impacts a metallic wall, it can trigger different physical mechanisms, which depend on parameters like the kinetic impact energy, the impact angle and the properties of the material. Basically, the incident electron can be absorbed, elastically rebounded, or additional electrons (secondary electrons) can be generated and released into the waveguide hollow region. The Secondary Emission Yield (SEY) curve describes the average number of emitted electrons from a metallic wall per incident electron impact, in terms of the cited parameters. Each metal has a different characteristic SEY curve. Since the shapes of the curves are similar to each other, all can be fitted by the same kind of mathematical functions, having each metal a set of characteristic coefficients. A couple of the most common models will be described here, each with a different level of complexity. The first models were relatively simple, but they had to be extended or their fitting functions optimised following the need to better emulate the physical secondary emission phenomenon. Please note that the term SEY is often named Secondary Electron Emission Coefficient (SEEC), or simply δ .

The first SEY curves were directly derived from measurements of the different materials [61] and looked like the one in Fig. 3.1. The SEY values were determined in terms of the kinetic impact energy $W[eV]$ for a fix incidence angle, normal to the impact surface. The measured curves typically show an optimum energy W_{\max} where the electron emission probability δ_{\max} is the highest. The curve constantly decays for lower and higher impact energies. As long as the SEY value is above 1, it is assumed that secondary electrons are likely to be generated. The points where the curve crosses the value 1 are known as the first and second crossover points (W_1 and W_2 , below and above W_{\max} , respectively). These points mark the thresholds of the absorption regions, where the electron density would start

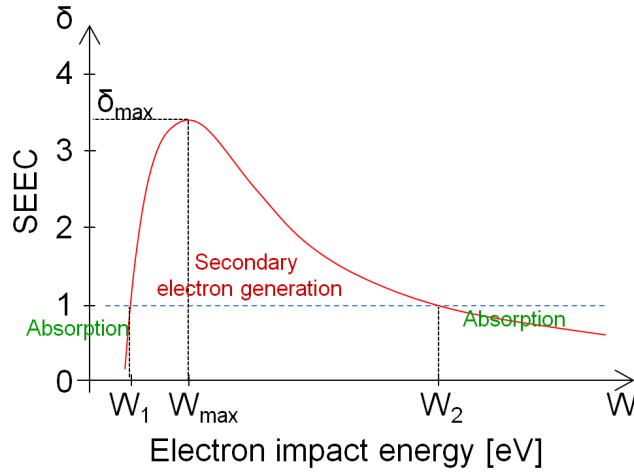


Figure 3.1: Typical SEY curve measurement for a certain material and for a fix impact angle.

decaying. The measurements can then be fitted by appropriate mathematical functions based on these parameters. A first option to describe δ over W is presented here (3.1):

$$\delta(W) = \delta_{\max} \frac{1 - e^{-A\left(\frac{W}{W_{\max}}\right)^B}}{C\left(\frac{W}{W_{\max}}\right)^D} \quad (3.1)$$

where A, B, C, D are constant coefficients that result from fitting the curve to the crossover and W_{\max} points. Hence, this function can be applied to any material once the characteristic values W_1, W_2, W_{\max} and δ_{\max} are known.

In [62], Vaughan extended the model to cope with different impact incidence angles θ , and to improve the accuracy at low energies. This angle is defined with respect to the vector normal to the impact surface. Hence, $\theta = 0^\circ$ for a normal impact, and will tend to a maximum value of 90° for an almost parallel impact. The formulation is given in (3.2):

$$\delta(W, \theta) = \begin{cases} \delta_{\max}(\theta) \cdot (\gamma e^{1-\gamma})^{\kappa(\gamma)} & \gamma \leq 3.6 \\ \delta_{\max}(\theta) \frac{\gamma}{\gamma^s} & \gamma > 3.6 \end{cases} \quad (3.2)$$

where

$$\gamma = \frac{W - W_0}{W_{\max}(\theta) - W_0} \quad (3.3)$$

$$\kappa(\gamma) = \frac{\kappa_1 + \kappa_2}{2} - \frac{\kappa_1 - \kappa_2}{\pi} \arctan(\pi \ln \gamma) \approx \begin{cases} \kappa_1 = 0.56 & \gamma < 1 \\ \kappa_2 = 0.25 & \gamma > 1 \end{cases} \quad (3.4)$$

$$\delta_{\max}(\theta) = \delta_{\max}(0) \cdot \left(1 + k_\delta \frac{\theta^2}{2\pi}\right) \quad (3.5)$$

$$W_{\max}(\theta) = W_{\max}(0) \cdot \left(1 + k_W \frac{\theta^2}{2\pi}\right) \quad (3.6)$$

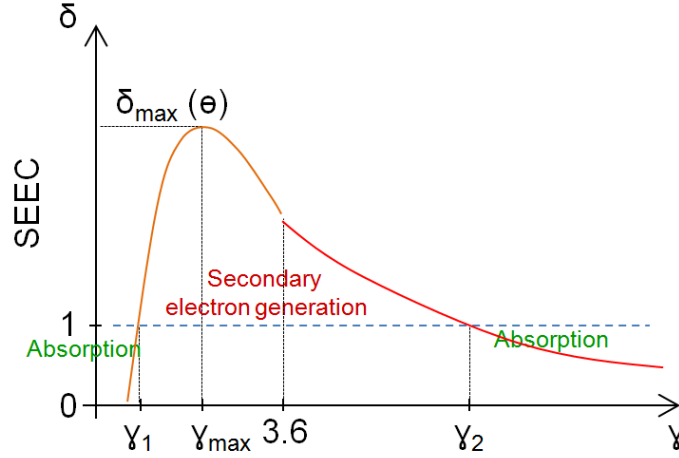


Figure 3.2: SEY curve model that takes into account the impact angle of the electrons, and with a corrected low-energy model. Proposed by Vaughan.

The following parameters are empirically assigned: $W_0 = 12.5$ eV, $r = 1.125$, $s = 0.35$, and k_W and k_δ are constants that depend on the roughness of the material, and get assigned by default the value 1 [63].

Note that (3.2) is not conceived for negative γ values:

$$(\gamma e^{1-\gamma})^\kappa = (-|C|)^\kappa \notin \mathbb{R} \quad \gamma < 0, \quad \kappa \in \mathbb{R} \quad (3.7)$$

This means that (3.2) is not defined for $W < W_0$. A plot of the function is included in Fig. 3.2. It looks similar to Fig. 3.1, but over the variable γ , which also depends on the impact incidence angle.

A further modification is proposed by Vicente [64] in order to overcome the drawbacks of the formulation in (3.2). On the one hand, W_1 is not properly fitted by (3.2), since W_0 has been chosen rather arbitrarily. The solution is to adjust this W_0 -value taking the W_1 -crossover into account. On the other hand, (3.2) is not defined for impact energies below W_0 . In such cases, the electron would experiment an elastic rebound, without generating secondary electrons. This can be described by a constant δ -value ($\delta_{\text{start}} = 1$). The new formulation is the following:

$$\delta(W, \theta) = \begin{cases} \delta_{\text{start}} = 1 & \gamma < 0 \\ \delta_{\text{max}}(\theta) \cdot (\gamma e^{1-\gamma})^{\kappa(\gamma)} & 0 \leq \gamma \leq 3.6 \\ \delta_{\text{max}}(\theta) \frac{r}{\gamma^s} & \gamma > 3.6 \end{cases} \quad (3.8)$$

Apart from the extension of the definition of δ to the range of negative γ -values, W_0 is not arbitrarily set any more, but is chosen so that $\delta(W_1, 0) = 1$. This is done by evaluating (3.8) at $W = W_1$ and $\theta = 0$. The value of $\gamma(W_1, 0)$ can then be obtained by solving the following transcendental equation:

$$1 = \delta_{\text{max}}(W_1, 0) \cdot (\gamma(W_1, 0) e^{1-\gamma(W_1, 0)})^{\kappa(W_1, 0)} \quad (3.9)$$

Substituting $\gamma(W_1, 0)$ in (3.3) at $W = W_1$ gives us directly W_0 .

However, this correction might shift the rest of the model, generating a discontinuity at $\gamma = 3.6$ and shifting the crossover point from W_1 . A solution to this problem is to redefine the values of the constants r and s proposed in the model of (3.2), so that the δ -function becomes continuous. Considering this, (3.10) shows how to derive $W(\gamma = 3.6)$ from (3.3):

$$W(\gamma = 3.6) = 3.6 (W_{\max}(0) - W_0) + W_0 \quad (3.10)$$

This allows obtaining, after substituting in (3.8), a first relationship between s and r (3.11):

$$\begin{aligned} \delta_{\max}(0) \cdot (3.6e^{-2.6})^{\kappa(3.6)} &= \delta_{\max}(0) \frac{r}{3.6^s} \\ \Leftrightarrow & \\ r &= k_v 3.6^s \end{aligned} \quad (3.11)$$

where $k_v \simeq 0.69665$. A second equation to solve the system can be obtained by forcing γ to be equal 1 at W_2 (3.12):

$$1 = \delta_{\max}(0) \frac{r}{\gamma_2^s} \quad (3.12)$$

where

$$\gamma_2 = \frac{W_2 - W_0}{W_{\max}(0) - W_0} \quad (3.13)$$

Combining (3.11) and (3.12), we can solve for s (3.15):

$$k_v \delta_{\max}(0) = \left(\frac{\gamma_2}{3.6} \right)^s \quad (3.14)$$

\Leftrightarrow

$$s = \frac{\ln(k_v \delta_{\max}(0))}{\ln\left(\frac{\gamma_2}{3.6}\right)} \quad (3.15)$$

The value of r is deduced by substitution of (3.15) in (3.11), which completes the model. A graphical realisation of it can be found in Fig. 3.3. Note that we might assign a different value to δ_{start} in our multipactor prediction software based on empirical results.

All these models have been implemented in our software and can be selected for the simulations via input parameter. Nevertheless, the model proposed in [64] and (3.8) has been the one chosen for the multipactor prediction of the manufactured hardware devices that will be presented in Chapters 4 and 5.

3.1.2 Rebound Energy Models

The incidence collision angle θ_C of an electron on a waveguide metallic wall influences the secondary emission mechanism, as suggested by several models in Chapter 3.1.1. Assuming a local Cartesian coordinate system, the incidence angle can be calculated as follows (3.16):

$$\theta_C = \arccos\left(\frac{-\vec{v}_C \cdot \hat{n}_{\text{Wall}}}{\|\vec{v}_C\|}\right) = \arccos\left(\frac{-v_{C,x} \cdot n_{\text{Wall},x} - v_{C,y} \cdot n_{\text{Wall},y} - v_{C,z} \cdot n_{\text{Wall},z}}{\sqrt{v_{C,x}^2 + v_{C,y}^2 + v_{C,z}^2}}\right) \quad (3.16)$$

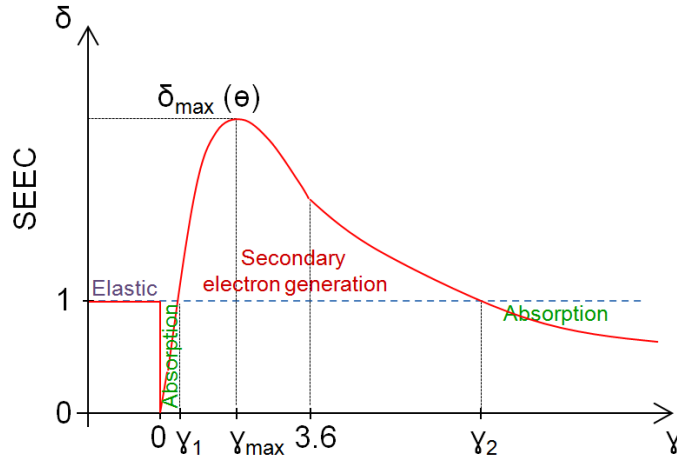


Figure 3.3: SEY curve model that takes into account the impact angle and the elastic rebounds for low energy. Proposed by Vicente.

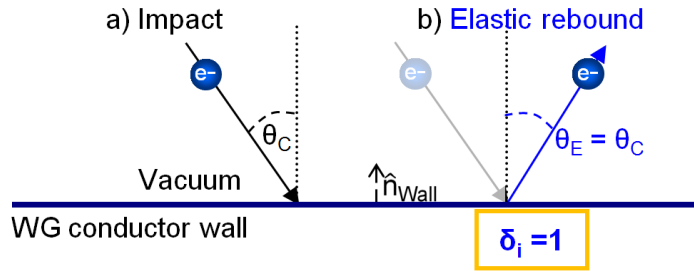


Figure 3.4: 2-D projection of an electron rebound under elastic conditions.

being \vec{v}_C the velocity vector of the electron in the impact instant, and \hat{n}_{Wall} any of the contour vectors $\hat{n}_{C1,4}$ defined in Appendix B.2 for rectangular and wedge-shaped cross sections.

The different potential interactions between the incoming electron and the waveguide wall are: elastic rebound, absorption or generation of secondary electrons. For very low impact energies ($\gamma < 0$), the electron hitting the wall experiments a specular rebound (elastic), like the one schematically shown in Fig. 3.4. The outbound angle θ_E is equal to the collision incidence angle θ_C . Such events do not modify the electron density in the environment.

If the SEEC value is < 1 , it is likely that the electron gets absorbed, which infers a reduction of the free electron density. Otherwise, SEEC values over unity symbolise the generation of secondary electrons, like in Fig. 3.5, where two electrons have been emitted after the collision. Here, the emission angles satisfy $\theta_{E1,2} \neq \theta_C$, but are randomly distributed over the hemispheric space around the collision location, assuming a 3-D formulation. A model proposed by [52], the cosine law, has been adopted here to describe the statistical distribution of the emitted electron spherical angles θ and ϕ (see definition in Fig. 3.6):

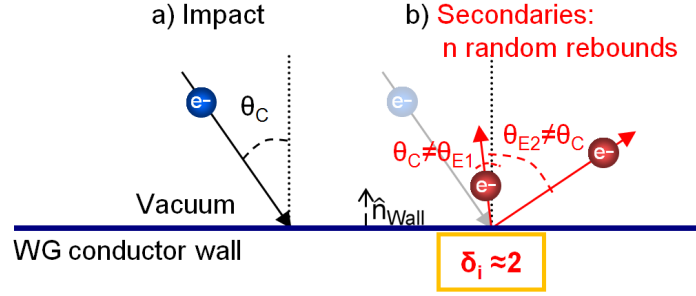


Figure 3.5: 2-D projection of an electron impact (in blue) causing the emission of secondary electrons (in red) at random angles.

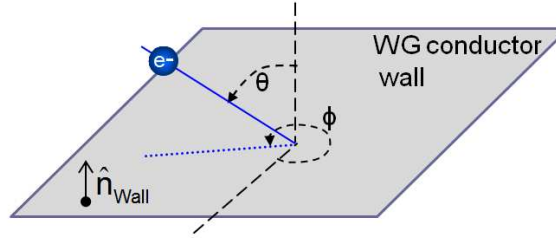


Figure 3.6: Definition of the spherical coordinates around a collision for the determination of the outbound direction.

$$\theta = \arcsin \left(\sqrt{m^2 + n^2} \right) \quad ; \quad m, n \in [-1, +1] \quad \Rightarrow \quad \theta \in [0, \pi/2[\quad (3.17)$$

$$\phi = \arctan \left(\frac{m}{n} \right) \quad ; \quad m, n \in [-1, +1] \quad \Rightarrow \quad \phi \in [0, 2\pi[\quad (3.18)$$

Note that, although the 2-D projection of Fig. 3.5 seems to suggest that all outbound velocity vectors lie on the same collision plane, which is the one defined by \hat{n}_{Wall} and the velocity vector \vec{v}_C , (3.18) outlines the normal distribution of the ϕ -coordinate between 0 and 2π .

The magnitude of the outbound velocities of the secondary electrons is also a random variable, which has to be appropriately modelled to retrieve reliable simulation results. However, some authors assign it a constant value for all secondary electrons, independent from the incoming speed. We usually apply a Maxwell-Boltzmann energy distribution function $f(x)$ to determine the outbound energy (3.19):

$$f(x) = e^{-\frac{(x-W_C)^2}{2W_G^2}} \quad (3.19)$$

where W_C is the mean energy, and W_G the standard deviation, both characteristic of the material of the wall. An additional constraint establishes that the emission energy cannot be higher than the impact energy. Hence, outbound energies are clipped to the impact energy in such events.

The electron energy values can be converted into speeds $v[m/s]$ with the following for-

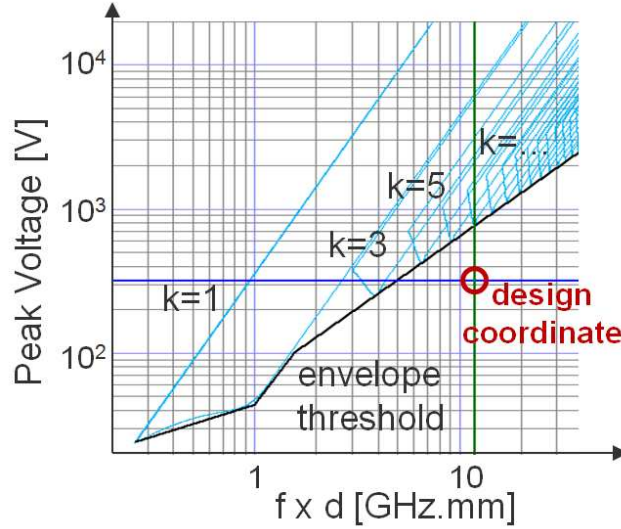


Figure 3.7: Example of the multipactor susceptibility regions.

mula:

$$v[m/s] = \sqrt{2W[eV] \frac{e}{m_0}} \quad (3.20)$$

with constants $e \simeq 1.60218 \cdot 10^{-19}$ C and $m_0 \simeq 9.10938 \cdot 10^{-31}$ kg, which are the absolute value of the charge and the mass at rest of the electron, respectively.

3.1.3 Multipactor Susceptibility Regions

The SEY models described in Chapter 3.1.1 establish an impact energy region (between W_1, γ_1 and W_2, γ_2) where secondary electrons can be generated and, therefore, the multipactor effect can occur. This means that, under impact energies below or above this region, the free electron density in the structure will naturally decrease. This concept helps in the understanding of the multipactor susceptibility curves (see example for silver in Fig. 3.7). Such a chart warns about the risk of multipactor discharge in terms of the input power/voltage and the frequency-gap-product between parallel-plates cathodes. The blue polygons mark the boundaries of the multipactor susceptible regions. There is one blue curve for each value of k , also known as multipactor order, which is an odd integer constant indicating the number of half RF signal cycles between consecutive collisions of the electrons against the top and bottom walls, as already mentioned in the list of conditions for a multipactor discharge in Chapter 1.1.

For a fix $f \times d$ product, and considering only the blue polygon corresponding to $k = 1$, we start-off from 0 and travel towards positive peak voltages between the parallel-plates. Once the first blue line is crossed, a voltage value has been reached capable of inducing a multipactor discharge. Further increasing the voltage will cause, at a certain point, a second crossing with the blue polygon, which indicates the exit from the multipactor-sensitive re-

gion. The same principle applies for the rest of multipactor-order polygons, although high orders are more unstable due to the longer travel time of the electron between impacts. Nevertheless, a common practice is to set an envelope threshold (black line in Fig. 3.7) below the lower boundaries of all the multipactor order regions, which establishes a conservative maximum threshold for design purposes. Moreover, [3] suggests a 8 dB margin below this envelope to ensure the flight qualification of space hardware. For margins between 8 dB and 3 dB, testing is required. Powers that have less than 3 dB margin are not allowed. Taking as an example the green line in Fig. 3.7, a parallel plate structure with $f \times d = 12$ GHz.mm has been considered. This structure would have a multipactor voltage threshold of around 730 V. The design coordinate marked with a dark-red circle in Fig. 3.7, at around 310 V, would indicate the need of testing, since there would be an input power margin with respect to the multipactor threshold of less than 8 dB.

3.2 Multipactor Prediction Tool

3.2.1 Overview

In order to study the multipactor phenomena in hollow waveguides, an efficient multipactor prediction tool has been implemented. It simulates the electron behaviour within the structure under the influence of EM fields, and predicts the multipactor power threshold by statistically analysing the electron density after a certain time. A functional block diagram of the tool can be found in Fig. 3.8. The blue-dashed rectangles show the main four modules of the tool, numbered in order of execution. The inputs needed by the different elements are highlighted in orange, whereas the generated outputs are marked in green.

The basic version of the tool accepts as input structure any rectangular or wedge-shaped infinite waveguide, as defined in Chapter 1.2, with metallic walls of a specific material. The materials are assumed lossless, but the tool could be extended to lossy conductors by applying the formulation presented in Appendix B. With the structure dimensions and the working frequency information, the first two modules can be executed. The first one is the “Launch Position Prediction Module”, which suggests an initial position from which the simulation electrons should be launched. This will be explained in more detail in Chapter 3.2.4. The EM fields are calculated in the module 2, as described in Chapter 2.1 and Appendix A. The normalisation and interpolation procedure described there allows performing the calculations outside of the main program loops, which considerably saves computation time.

Once the first two modules have been executed, the module 3 “Electron Tracking Module” is executed multiple times within three embedded loops. The objective of this module is to track the trajectory over time of an effective electron located within the waveguide under the influence of the harmonic EM fields, by means of a Finite-Difference Time-Domain (FDTD) method that will be presented in Chapter 3.2.2. The tracking of the electron has been implemented in 3-D, in order to enable the extension of the tool to stepped waveguides with standing waves, in contrast with most of the contributions of the literature. Potential collisions against the walls are recorded, and the corresponding SEY curves are calculated using

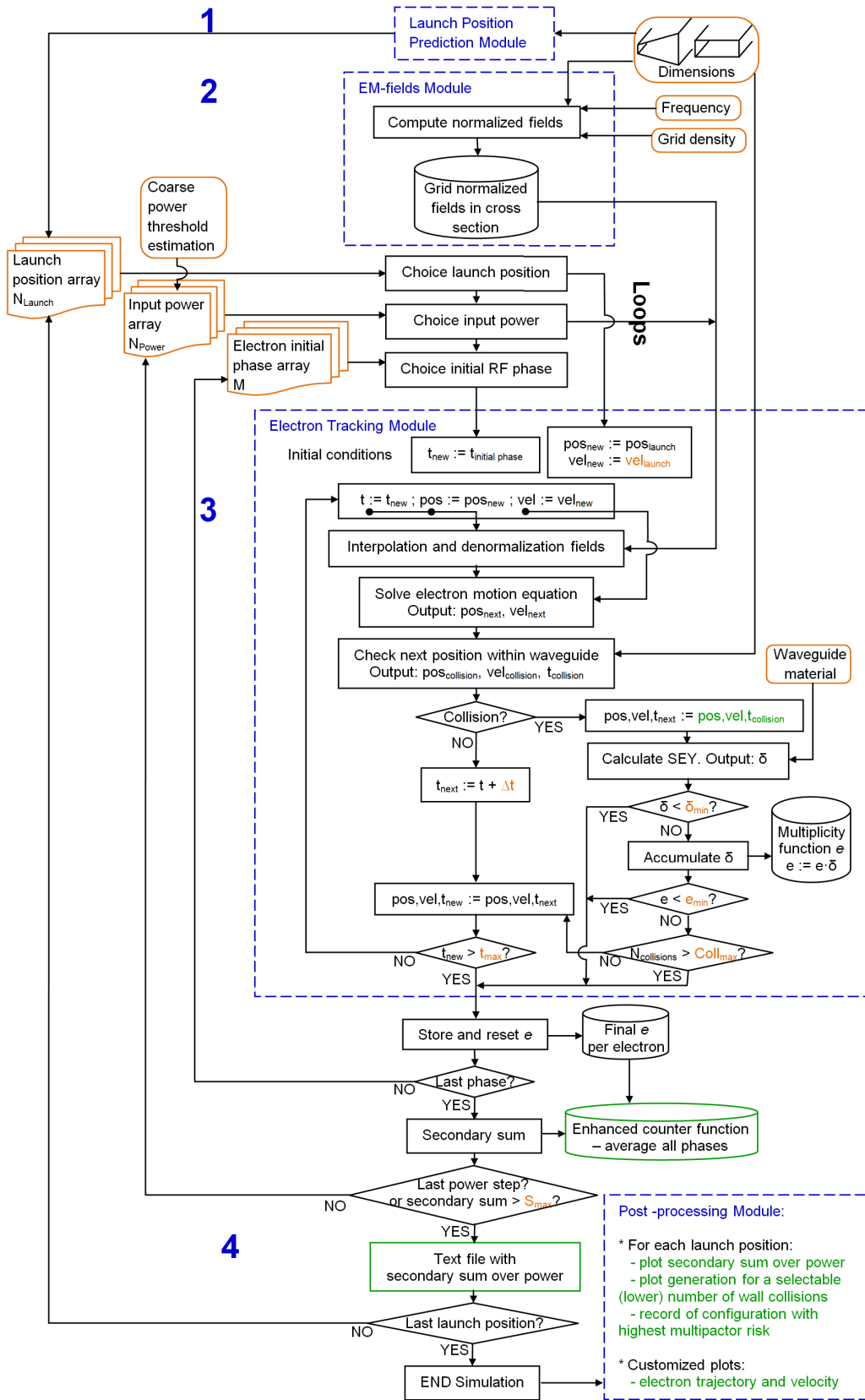


Figure 3.8: Block diagram of the multipactor prediction tool. Different modules are inside blue dashed boxes, in order of execution. Elements marked in orange are input data for the tool, whereas the ones marked in green are outputs.

the models of Chapter 3.1. After a certain number of collisions, the accumulated SEEC values (called multiplicity function e in Fig. 3.8) give a statistical indication of the electron density in the device.

These variables storing statistical electron density information are precisely defined in Chapter 3.2.3, and will serve as multipactor risk indicators. The tracking of each effective electron concludes when one of the following criteria is fulfilled: maximum electron life time reached (t_{\max} , usually chosen in the order of thousands of RF cycles), maximum number of collisions reached ($Coll_{\max}$, usually 20, 30, or even 50), SEEC of a collision below the minimum (δ_{\min} , usually in the order of 10^{-3}) or accumulated multiplicity function below the minimum (e_{\min} , usually in the order of 10^{-3}). The first loop that iteratively calls module 3 ensures that a considerable number of phases within an RF cycle are covered by the simulation. M effective electrons are launched instead of 1, each one starting to interact with the EM fields at a different instant. Usually, the M launch instants/phases are equally distributed over a complete RF cycle. The consequent risk of multipactor discharge at the selected frequency and input power results from a summation of the multiplicity functions of these M electrons (enhanced counter function or secondary sum in Fig. 3.8). The second loop repeats the analysis for N_{Power} different input power steps, in increasing order, but not necessarily uniformly distributed. A coarse estimation of the expected threshold is useful for properly defining the input power array and reducing the number of iterations. An additional criterion for ending the simulation can be defined here, in case we would only be interested in the lower multipactor boundary of a device. In this case, a maximum secondary sum parameter (S_{\max}) can be defined, which would interrupt the input power loop if a sufficiently high secondary sum value is reached. Finally, a third loop considers N_{Launch} different launch positions for the initial electron. This is especially required by wedge-shaped waveguides, for which there is no unique optimal launching position, due to the instability of the trapped trajectories in this kind of topology (cf. Chapter 3.2.4). Module 1 offers a good approximation to this value, but it is still necessary to execute the simulation from a range of starting electron positions around the suggested value.

Once the embedded loops have finished, the useful output information is stored in text files. Interesting reports and graphic representations can then be generated with the “Post-processing Module”. The overall simulation time of the tool is mainly determined by the duration of one run of module 3, multiplied by $M \cdot N_{\text{Power}} \cdot N_{\text{Launch}}$. The simulation duration of the rest of the modules can be neglected in comparison. There is almost no difference in the simulation duration of module 3 between the rectangular and the wedge-shaped waveguide case, thanks to the pre-calculation of the EM fields in module 2. However, since N_{Launch} is usually equal 1 for the rectangular case (optimal electron launch position is known, namely the centre of the waveguide), the overall simulation duration is $N_{\text{Launch}}^{(\text{Wedge})}$ times shorter for the rectangular case.

An important difference with respect to existing prediction tools is the specific adaptation to wedge-shaped waveguides. The functionalities of this tool have been implemented in FEST^{3D}, including its extension to deal with more complex stepped waveguide structures, as will be explained in Chapter 4. The following sub-chapters give more details on the electron

dynamics and on the algorithm for the detection of the multipactor threshold, including the determination of the ideal launch position for the simulated electrons for the wedge-shaped waveguide.

3.2.2 Electron Dynamics

The key for understanding the mechanism of the multipactor discharge is to study the behaviour of the electrons within a harmonically excited waveguide. A significant growth in the electron density in the device can only happen if the electrons hit the top and bottom walls with the appropriate energy and at periodically suitable instants. Furthermore, stable trajectories of the electrons have to be found in order to confirm the potential existence of resonance paths. These would prevent the electrons from drifting away towards regions of the cross section with lower fields, and would enable sustainable increases of electron density. The collisions against the walls can be predicted if the electrons are properly tracked within the EM field.

The electron dynamics are governed by the equation of motion (Lorentz force equation, at the left-hand side of (3.21)). This force has to fulfil the Theory of Special Relativity [65] (right-hand side of (3.21)), resulting in the following equation:

$$\vec{F}_L = q(\vec{E} + \vec{v} \times \vec{B}) = \frac{d\vec{p}}{dt} \quad (3.21)$$

where $q = -e$ is the electron charge, \vec{E} and \vec{B} are, respectively, the instantaneous electric and magnetic field vectors interacting with the electron (as defined in Appendix A.1), and \vec{v} is the velocity vector of the electron. The relativistic linear momentum is defined as:

$$\vec{p} = m_0 \gamma \vec{v} \quad (3.22)$$

where m_0 is the electron mass at rest, $\gamma = 1/\sqrt{1 - (v/c)^2}$ is the relativistic factor, v being the magnitude of the velocity vector, $c = 1/\sqrt{\mu_0 \varepsilon_0}$ is the free-space light velocity (where μ_0 is the free-space magnetic permeability and ε_0 is the free-space electric permittivity) and t is the time.

The proposed algorithm launches an electron at $t = t_{\text{initial phase}}$ from the bottom waveguide plate with a configurable initial velocity v_0 perpendicular to the wall. For determining the position of the electron at the instant $t + \Delta t$, (3.21) can be solved numerically by means of the Velocity-Verlet algorithm (see [66] and [67]). Usually (when $v \ll c$), the relativistic term is discarded ($\gamma \rightarrow 1$). Expanding then (3.21), (3.23) is obtained:

$$-\vec{E} - \vec{v} \times \vec{B} = A\gamma \vec{a} + \frac{A}{c^2} \gamma^3 (\vec{v} \cdot \vec{a}) \vec{v} \approx A \vec{a} \quad (3.23)$$

where \vec{a} is the acceleration vector and $A = m_0/e$. The acceleration vector is the derivative over time of the velocity vector \vec{v} , which in turn is the derivative over time of the position

vector \vec{r} : $\vec{a} = \dot{\vec{v}} = \ddot{\vec{r}}$, where the dot represents the time derivative. The differential equation system to solve becomes then (3.24):

$$\begin{cases} \ddot{r}_x = (\dot{r}_z \mathbf{B}_y - \dot{r}_y \mathbf{B}_z - \mathbf{E}_x) / A \\ \ddot{r}_y = (\dot{r}_x \mathbf{B}_z - \dot{r}_z \mathbf{B}_x - \mathbf{E}_y) / A \\ \ddot{r}_z = (\dot{r}_y \mathbf{B}_x - \dot{r}_x \mathbf{B}_y - \mathbf{E}_z) / A \end{cases} \quad (3.24)$$

with the initial position \vec{r}_0 and speed \vec{v}_0 of the electron as initial conditions.

Although the relativistic component of this equation can be discarded for the typical power ranges of most space waveguide devices, it should be considered in cases when extreme speeds are reached ($v/c \gtrsim 0.1$), like for plasma physics applications or high-power multipactor testing simulations. The differential problem to be solved in this case would be (3.25):

$$\begin{cases} \ddot{r}_x = \left(\dot{r}_z \mathbf{B}_y - \dot{r}_y \mathbf{B}_z - \mathbf{E}_x + \dot{r}_x \cdot \dot{\vec{r}} \cdot \vec{\mathbf{E}} / c^2 \right) / (A\gamma) \\ \ddot{r}_y = \left(\dot{r}_x \mathbf{B}_z - \dot{r}_z \mathbf{B}_x - \mathbf{E}_y + \dot{r}_y \cdot \dot{\vec{r}} \cdot \vec{\mathbf{E}} / c^2 \right) / (A\gamma) \\ \ddot{r}_z = \left(\dot{r}_y \mathbf{B}_x - \dot{r}_x \mathbf{B}_y - \mathbf{E}_z + \dot{r}_z \cdot \dot{\vec{r}} \cdot \vec{\mathbf{E}} / c^2 \right) / (A\gamma) \end{cases} \quad (3.25)$$

The Velocity-Verlet resolution of (3.25) will be proposed here, since the relativistic problem is the more general case. The algorithm is a FDTD method: at the time instant $t + \Delta t$ (iteration step i), the position and velocities can be derived from the ones at the previous time step t (iteration $i - 1$). These are the approximations applied for their computation:

$$\begin{cases} a) \quad \vec{r}(t + \Delta t) = \vec{r}(t) + \Delta t \cdot \vec{v}(t) + \frac{\Delta t^2}{2} \vec{a}(t) \\ b) \quad \vec{v}(t + \Delta t) = \vec{v}(t) + \frac{\Delta t}{2} (\vec{a}(t) + \vec{a}(t + \Delta t)) \end{cases} \quad (3.26)$$

The update procedure of the position and velocity values during the i -th iteration is shown here:

1. Equation a) of (3.26) is applied to obtain the new position of the electron $\vec{r}(t + \Delta t) \equiv \vec{r}_i$, based on the previous position and velocity.
2. The EM fields are calculated at this new position and at the current time step $\vec{\mathbf{B}}(\vec{r}(t + \Delta t))$, $\vec{\mathbf{E}}(\vec{r}(t + \Delta t)) \equiv \vec{\mathbf{B}}_i$, $\vec{\mathbf{E}}_i$.
3. The current acceleration $\vec{a}(t + \Delta t) \equiv \vec{a}_i$ is calculated according to (3.25) by substituting the new values of $\vec{\mathbf{B}}_i$, $\vec{\mathbf{E}}_i$. The result will depend on the unknown $\vec{v}(t + \Delta t) \equiv \vec{v}_i$.
4. The past speed (\vec{v}) and the past (\vec{a}) and current (\vec{a}_i) acceleration are substituted in Equation b) of (3.26). The final result is an equation where the only unknown is \vec{v}_i .

An expanded formulation of this last step is included here (3.27), where $\vec{r}' \cdot \vec{E}/c^2$ has been substituted by the constant C_{rel} :

$$\begin{cases} v_{x,i} = v_x + \frac{\Delta t}{2A\gamma} (v_z \mathbf{B}_y - v_y \mathbf{B}_z - \mathbf{E}_x + v_x C_{\text{rel}} + v_{z,i} \mathbf{B}_{y,i} - v_{y,i} \mathbf{B}_{z,i} - \mathbf{E}_{x,i} + v_{x,i} C_{\text{rel}}) \\ v_{y,i} = v_y + \frac{\Delta t}{2A\gamma} (v_x \mathbf{B}_z - v_z \mathbf{B}_x - \mathbf{E}_y + v_y C_{\text{rel}} + v_{x,i} \mathbf{B}_{z,i} - v_{z,i} \mathbf{B}_{x,i} - \mathbf{E}_{y,i} + v_{y,i} C_{\text{rel}}) \\ v_{z,i} = v_z + \frac{\Delta t}{2A\gamma} (v_y \mathbf{B}_x - v_x \mathbf{B}_y - \mathbf{E}_z + v_z C_{\text{rel}} + v_{y,i} \mathbf{B}_{x,i} - v_{x,i} \mathbf{B}_{y,i} - \mathbf{E}_{z,i} + v_{z,i} C_{\text{rel}}) \end{cases} \quad (3.27)$$

Note that $C_{\text{rel},i}$ has been approximated as C_{rel} . The error is negligible, since c^2 is still much higher than $\vec{r}' \cdot \vec{E}$ or $\vec{r}'_i \cdot \vec{E}_i$. The system to be solved is (3.28):

$$\begin{pmatrix} v_x + \frac{\Delta t}{2A\gamma} (v_x C_{\text{rel}} + v_z \mathbf{B}_y - v_y \mathbf{B}_z - \mathbf{E}_x - \mathbf{E}_{x,i}) \\ v_y + \frac{\Delta t}{2A\gamma} (v_x \mathbf{B}_z + v_y C_{\text{rel}} - v_z \mathbf{B}_x - \mathbf{E}_y - \mathbf{E}_{y,i}) \\ v_z + \frac{\Delta t}{2A\gamma} (v_y \mathbf{B}_x - v_x \mathbf{B}_y + v_z C_{\text{rel}} - \mathbf{E}_z - \mathbf{E}_{z,i}) \end{pmatrix} = \begin{pmatrix} 1 - \frac{\Delta t}{2A\gamma} C_{\text{rel}} & \frac{\Delta t}{2A\gamma} \mathbf{B}_{z,i} & -\frac{\Delta t}{2A\gamma} \mathbf{B}_{y,i} \\ -\frac{\Delta t}{2A\gamma} \mathbf{B}_{z,i} & 1 - \frac{\Delta t}{2A\gamma} C_{\text{rel}} & \frac{\Delta t}{2A\gamma} \mathbf{B}_{x,i} \\ \frac{\Delta t}{2A\gamma} \mathbf{B}_{y,i} & -\frac{\Delta t}{2A\gamma} \mathbf{B}_{x,i} & 1 - \frac{\Delta t}{2A\gamma} C_{\text{rel}} \end{pmatrix} \cdot \begin{pmatrix} v_{x,i} \\ v_{y,i} \\ v_{z,i} \end{pmatrix} \quad (3.28)$$

The analytical expression of the future velocities is:

$$\vec{v}_i = \frac{\overrightarrow{au\hat{x}}}{(2A\gamma - C_{\text{rel}}\Delta t) ((2A\gamma)^2 - 4A\gamma C_{\text{rel}}\Delta t + \Delta t^2(\mathbf{B}_{x,i}^2 + \mathbf{B}_{y,i}^2 + \mathbf{B}_{z,i}^2 + C_{\text{rel}}^2))} \quad (3.29)$$

where $\overrightarrow{au\hat{x}}$ is:

$$\begin{aligned} aux_x = (2A\gamma)^3 v_x + \\ + 2A\gamma\Delta t \left[\begin{aligned} & 2A\gamma (v_z(\mathbf{B}_y + \mathbf{B}_{y,i}) - v_y(\mathbf{B}_z + \mathbf{B}_{z,i}) - \mathbf{E}_x - \mathbf{E}_{x,i} - C_{\text{rel}}v_x) + \\ & + \Delta t \mathbf{B}_{y,i} (v_y(\mathbf{B}_x + \mathbf{B}_{x,i}) - v_x \mathbf{B}_y - \mathbf{E}_z - \mathbf{E}_{z,i}) + \\ & + \Delta t \mathbf{B}_{z,i} (v_z(\mathbf{B}_x + \mathbf{B}_{x,i}) - v_x \mathbf{B}_z + \mathbf{E}_y + \mathbf{E}_{y,i}) + \\ & + \Delta t (v_x(\mathbf{B}_{x,i}^2 - C_{\text{rel}}^2) + 2C_{\text{rel}}(v_y \mathbf{B}_z - v_z \mathbf{B}_y + \mathbf{E}_x + \mathbf{E}_{x,i})) \end{aligned} \right] + \\ + \Delta t^3 \left[\begin{aligned} & (\mathbf{B}_{x,i}^2 + C_{\text{rel}}^2)(v_z \mathbf{B}_y - v_y \mathbf{B}_z + C_{\text{rel}}v_x - \mathbf{E}_x - \mathbf{E}_{x,i}) + \\ & + (\mathbf{B}_{x,i} \mathbf{B}_{y,i} + C_{\text{rel}} \mathbf{B}_{z,i})(v_x \mathbf{B}_z - v_z \mathbf{B}_x + C_{\text{rel}}v_y - \mathbf{E}_y - \mathbf{E}_{y,i}) + \\ & + (\mathbf{B}_{x,i} \mathbf{B}_{z,i} - C_{\text{rel}} \mathbf{B}_{y,i})(v_y \mathbf{B}_x - v_x \mathbf{B}_y + C_{\text{rel}}v_z - \mathbf{E}_z - \mathbf{E}_{z,i}) \end{aligned} \right] \quad (3.30) \end{aligned}$$

$$\begin{aligned} aux_y = (2A\gamma)^3 v_y + \\ + 2A\gamma\Delta t \left[\begin{aligned} & 2A\gamma (v_x(\mathbf{B}_z + \mathbf{B}_{z,i}) - v_z(\mathbf{B}_x + \mathbf{B}_{x,i}) - \mathbf{E}_y - \mathbf{E}_{y,i} - C_{\text{rel}}v_y) + \\ & + \Delta t \mathbf{B}_{x,i} (v_x(\mathbf{B}_y + \mathbf{B}_{y,i}) - v_y \mathbf{B}_x + \mathbf{E}_z + \mathbf{E}_{z,i}) + \\ & + \Delta t \mathbf{B}_{z,i} (v_z(\mathbf{B}_y + \mathbf{B}_{y,i}) - v_y \mathbf{B}_z - \mathbf{E}_x - \mathbf{E}_{x,i}) + \\ & + \Delta t (v_y(\mathbf{B}_{y,i}^2 - C_{\text{rel}}^2) + 2C_{\text{rel}}(v_z \mathbf{B}_x - v_x \mathbf{B}_z + \mathbf{E}_y + \mathbf{E}_{y,i})) \end{aligned} \right] + \\ + \Delta t^3 \left[\begin{aligned} & (\mathbf{B}_{y,i}^2 + C_{\text{rel}}^2)(v_x \mathbf{B}_z - v_z \mathbf{B}_x + C_{\text{rel}}v_y - \mathbf{E}_y - \mathbf{E}_{y,i}) + \\ & + (\mathbf{B}_{y,i} \mathbf{B}_{z,i} + C_{\text{rel}} \mathbf{B}_{x,i})(v_y \mathbf{B}_x - v_x \mathbf{B}_y + C_{\text{rel}}v_z - \mathbf{E}_z - \mathbf{E}_{z,i}) + \\ & + (\mathbf{B}_{x,i} \mathbf{B}_{y,i} - C_{\text{rel}} \mathbf{B}_{z,i})(v_z \mathbf{B}_y - v_y \mathbf{B}_z + C_{\text{rel}}v_x - \mathbf{E}_x - \mathbf{E}_{x,i}) \end{aligned} \right] \quad (3.31) \end{aligned}$$

$$\begin{aligned}
aux_z = & (2A\gamma)^3 v_z + \\
& + 2A\gamma\Delta t \left[\begin{aligned} & 2A\gamma(v_y(\mathbf{B}_x + \mathbf{B}_{x,i}) - v_x(\mathbf{B}_y + \mathbf{B}_{y,i}) - \mathbf{E}_z - \mathbf{E}_{z,i} - C_{\text{rel}}v_z) + \\ & + \Delta t \mathbf{B}_{x,i}(v_x(\mathbf{B}_z + \mathbf{B}_{z,i}) - v_z \mathbf{B}_x - \mathbf{E}_y - \mathbf{E}_{y,i}) + \\ & + \Delta t \mathbf{B}_{y,i}(v_y(\mathbf{B}_z + \mathbf{B}_{z,i}) - v_z \mathbf{B}_y + \mathbf{E}_x + \mathbf{E}_{x,i}) + \\ & + \Delta t(v_z(\mathbf{B}_{z,i}^2 - C_{\text{rel}}^2) + 2C_{\text{rel}}(v_x \mathbf{B}_y - v_y \mathbf{B}_x + \mathbf{E}_z + \mathbf{E}_{z,i})) \end{aligned} \right] + \\
& + \Delta t^3 \left[\begin{aligned} & (\mathbf{B}_{z,i}^2 + C_{\text{rel}}^2)(v_y \mathbf{B}_x - v_x \mathbf{B}_y + C_{\text{rel}}v_z - \mathbf{E}_z - \mathbf{E}_{z,i}) + \\ & + (\mathbf{B}_{y,i} \mathbf{B}_{z,i} - C_{\text{rel}} \mathbf{B}_{x,i})(v_x \mathbf{B}_z - v_z \mathbf{B}_x + C_{\text{rel}}v_y - \mathbf{E}_y - \mathbf{E}_{y,i}) + \\ & + (\mathbf{B}_{x,i} \mathbf{B}_{z,i} + C_{\text{rel}} \mathbf{B}_{y,i})(v_z \mathbf{B}_y - v_y \mathbf{B}_z + C_{\text{rel}}v_x - \mathbf{E}_x - \mathbf{E}_{x,i}) \end{aligned} \right] \quad (3.32)
\end{aligned}$$

In each iteration step i , once \vec{r}_i is obtained in “step 1” of this procedure, it is checked whether the new position is within the boundaries of the waveguide. If this is not the case, it means that a collision has taken place $t < t_{\text{collision}} < t + \Delta t$. Then, the normal flow of the algorithm is interrupted to deal with the collision event. The collision instant and position are estimated by projecting the previous position and velocity and assuming a constant velocity until the electron reaches the waveguide boundary. The following iteration will be performed at $t_{\text{collision}} + \Delta t$, with the estimated collision position and the emission velocity as initial conditions. The determination of the emission velocity vector depends on the type of collision (elastic or generating a secondary electron emission), as it has been described in Chapter 3.1.2.

To illustrate a simulation example of this algorithm, the 3-D trajectories of two electrons inside a wedge-shaped waveguide have been computed and plotted in Fig. 3.9. The one on the left shows an electron that drifts towards one of the side-walls, losing most of its energy, after colliding several times against the top and bottom and against the side-wall itself (collision locations marked with a dark red star). On the right, the electron seems to be trapped in a resonant path and to follow curved trajectories between top and bottom walls. These curved lines are, as expected, very similar to the ones formed by the electric field vectors of wedge-shaped waveguides (cf. Fig. 2.4). Please note that, although secondary emission collisions take place, the plots of Fig. 3.9 only show the trajectory of one of the emitted electrons after each collision.

The implemented version of the algorithm can follow several electrons, but not simultaneously. The M effective electrons in the simulation are sequentially launched and tracked. As it is shown in [21], the Velocity Verlet algorithm ensures accuracy and reasonable numerical efficiency provided that the time steps are fine enough (e.g. ~ 750 steps per RF cycle).

3.2.3 Algorithm for the Prediction of the Multipactor Discharge

In Fig. 3.8, the different loops of the multipactor prediction software workflow are shown. Assuming a single launch position ($N_{\text{Launch}} = 1$), for each input power step, M electrons are launched at uniformly separated initial RF cycle phases. The SEEC values obtained in

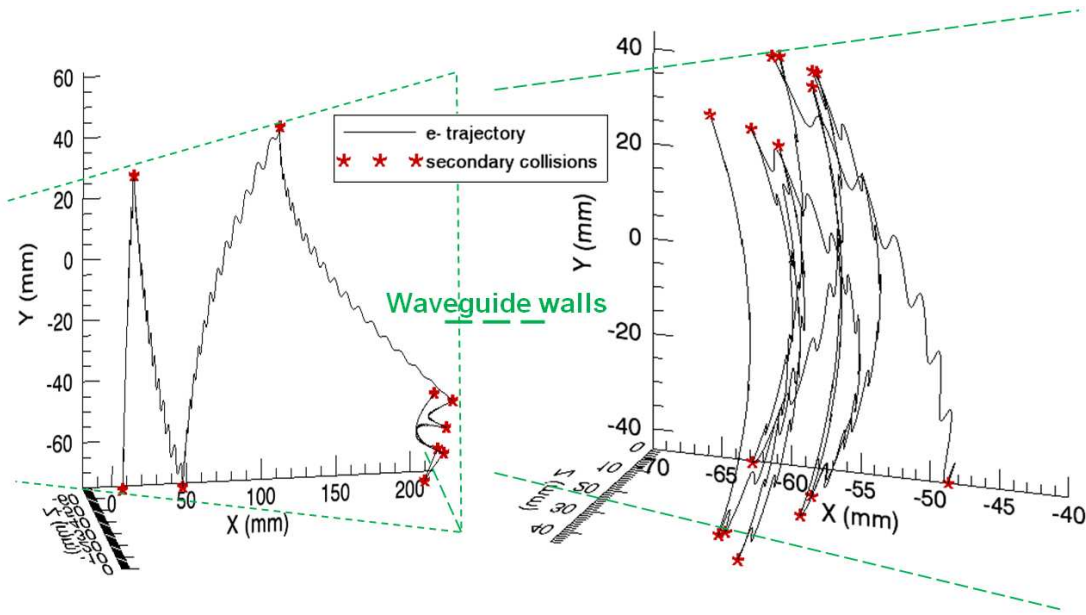


Figure 3.9: Two examples of simulated electron trajectories in a wedge-shaped waveguide and its collisions against the walls. XY -plane is perpendicular to the propagation direction.

the wall collisions of these M electrons will determine the risk of multipactor discharge. The compilation of this information is the responsibility of the collision event chain in the “Electron Tracking Module”, whose prediction algorithm will be detailed here.

To record the generation of secondary electrons in the wall collisions, we have followed a traditional effective electron model [68], but modified according to [69]. Concentrating on a single electron (called effective electron), when a collision happens, the SEEC (δ) is computed, which decides if the electron is elastically reflected ($\delta = 1$) or has produced true secondary ones ($\delta \neq 1$). The actual SEEC value represents the average number of secondary electrons emitted by this incident particle [62, 64, 70]. The probability can also be less than 1, which infers that the electron might have been absorbed. Regardless of the δ -value, the only the effective electron is tracked after the collision, and δ is stored in a common variable and accumulated with the values of consequent wall collisions during its whole simulation lifetime. The tracking of the effective electron finishes when one of the following conditions is fulfilled: maximal RF signal simulation cycles, maximum number of collisions, minimum SEEC in one collision, or minimum accumulated SEEC.

The accumulated SEEC for each effective electron j is called the multiplicity function (formulated in [68]), and is calculated as follows (3.33):

$$e_n^{(j)} = \prod_{i=1}^n \delta_i^{(j)} \quad (3.33)$$

where n is the selected total number of impacts and i is the impact index. The multiplicity factors from the M launched electrons can be added together to compute the “enhanced

counter function” [68] or secondary sum (3.34):

$$\text{Secondary Sum} = \sum_{j=1}^M e_n^{(j)} \quad (3.34)$$

When *Secondary Sum* becomes higher than M , it indicates a statistical electron growth, and therefore a risk of multipactor. Some authors also use the normalised version of (3.34), where the threshold is set to 1 independently of M .

The lowest power value at which the RF multipactor breakdown is likely to happen is hence the multipactor power threshold of the waveguide P_{th} . The corresponding voltage value at this power threshold is V_{th} . As explained in Chapter 3.1.3, there are ranges of input power with multipactor risk, called multipactor “windows”, interleaved with inactive power ranges. These windows are the result of multipactor phenomena of different order [2, 11].

3.2.4 Trapped Trajectories and Launch Position Prediction

In multipactor prediction simulations, electrons should be ideally launched into trapped trajectories, since they provide stable resonant paths, which might result in the highest breakdown probability. In rectangular waveguides, a trapped electron trajectory exists in the centre of the cross section (i.e. $x = 0$ in Fig. 2.1). Electrons launched at such point in y -direction ($\vec{v} = v_y \hat{y}$) do not drift towards the side-walls, as long as the rebounds in the collisions are specular (as it is assumed in earlier studies [42]). This can be simply deduced from (3.21): the electric field of the TE_{10} mode has no component in x -direction, nor has the cross product of $\vec{v} \times \vec{B}$, since the magnetic field has no z -component at the $x = 0$ plane (see Appendix A, or YZ -cut of Fig. 3.10 for a graphical verification). Therefore, the electron will remain in this trapped trajectory, where in addition the electric field has a maximum, which constitutes a worst case for multipactor breakdown risk. Even considering a spread in the launch angle after a collision (see Chapter 3.1.2), the electrons statistically tend to stay in this trapped electron trajectory, which indicates its high stability for simulation purposes.

A first glance at the magnetic field simulation in Fig. 3.11 shows a different scenario in wedge-shaped waveguides. The YZ -cut shows a real part of the magnetic field with z -components different from 0. This means that electrons launched in y -direction would experience shifts towards the side-walls, unlike in the rectangular case. This suggests that a potential trapped trajectory might be more unstable than the rectangular one. Moreover, this trajectory might not lie at $x = 0$.

Due to the fact that the electromagnetic fields in wedge-shaped waveguides are expressed as summation of weighted rectangular waveguide modes, an analytical investigation of whether there are trapped trajectories in wedge-shaped waveguides would be extremely complicated. Therefore, an analogy is established between them and annular section waveguides [42, 46]. The latter have a cross section formed by a circular section delimited by an inner and an outer arc with radii R_1 and R_2 , respectively, as shown with a red dash-dotted line in Fig. 3.12. Due to this particular shape, they are also known as coaxial section waveguides. By convention, the equivalent wedge-shaped waveguide will have the same inclination

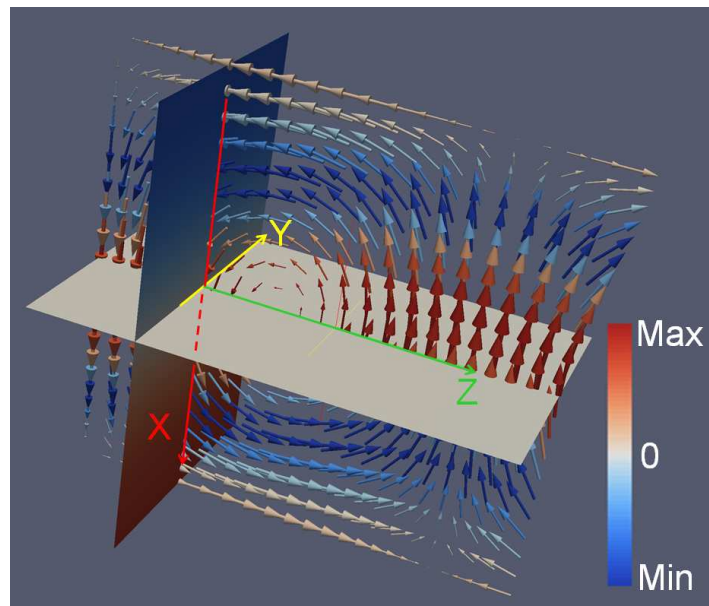


Figure 3.10: Magnetic field of the fundamental mode (TE_{10}) in a rectangular waveguide. XY -plane shows the rectangular cross section. Vectors in the horizontal plane (XZ) represent the absolute value of the magnetic field. The z -component of the real part of the magnetic field is colour-coded in the YZ - and XY -cuts.

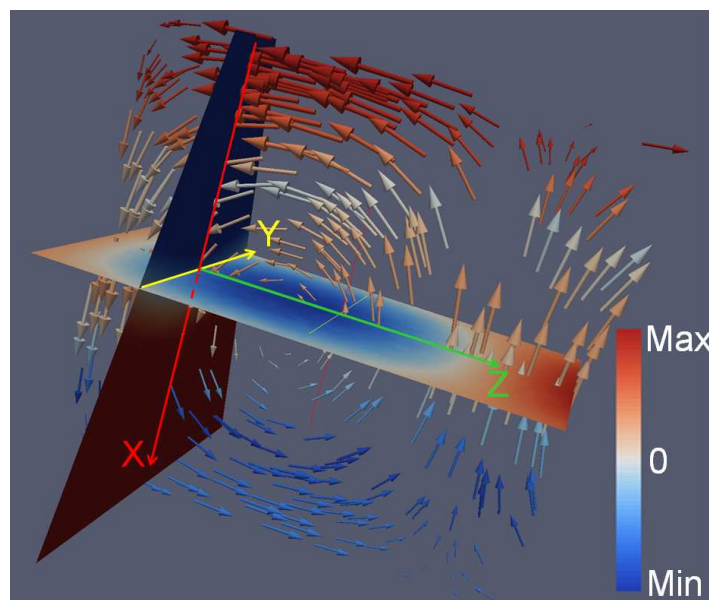


Figure 3.11: Magnetic field of the fundamental mode in a wedge-shaped waveguide. XY -plane shows the wedge-shaped cross section. Vectors in the horizontal plane (XZ) represent the absolute value of the magnetic field. The z -component of the real part of the magnetic field is colour-coded in the YZ - and XY -cuts.

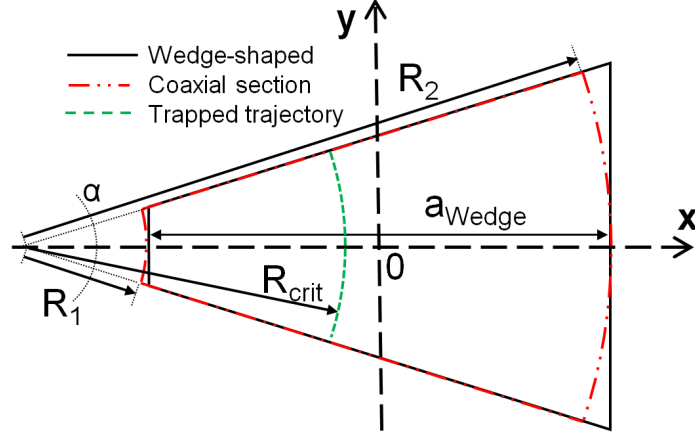


Figure 3.12: Definition of the dimensions of an annular section waveguide and its corresponding wedge-shaped waveguide (convention). R_1 and R_2 are the internal and external radii of the annular section, and R_{crit} is a critical radius with a trapped electron trajectory.

between top and bottom walls α and a width $a_{\text{Wedge}} = R_2 - R_1$. Its side-walls tangentially touch the ones of the annular section at $y = 0$.

Based on the analytical expression of the RF fields, the existence of electron trapped trajectories in such waveguides was theoretically demonstrated by [46]. The formulation of the electric field in [46] is reproduced here:

$$\vec{E} = -\frac{\omega}{c} A(r) \sin(\omega t) \hat{\alpha} \quad (3.35)$$

where \vec{A} is the vector potential of the fundamental mode of the electromagnetic field, $\hat{\alpha}$ the unitary vector in azimuthal direction and c is the light velocity in vacuum. The vector potential depends only on the radial position r , as can be deduced from (3.36):

$$A(r) = A_0 \left[\frac{J_1(k_t \cdot r)}{J_1(k_t \cdot R_1)} - \frac{N_1(k_t \cdot r)}{N_1(k_t \cdot R_1)} \right] \quad (3.36)$$

where A_0 is a constant that depends on the transmitted input power, J_1 and N_1 are the first-order Bessel and Neumann functions, respectively, and k_t is the transverse wavenumber, which can be determined as the smallest positive root of the transcendental equation shown in (3.37):

$$\frac{J_1(k_t \cdot R_2)}{J_1(k_t \cdot R_1)} - \frac{N_1(k_t \cdot R_2)}{N_1(k_t \cdot R_1)} = 0 \quad (3.37)$$

For certain radii r , the centrifugal effect experimented by the electrons might compensate the Miller force. These radii correspond to trapped trajectories, whose location can be estimated by solving (3.38) [46]:

$$\frac{dA(R_0)}{dR_0} = 2 \frac{A(R_0)}{R_0} (\cos \phi_0)^2 \quad (3.38)$$

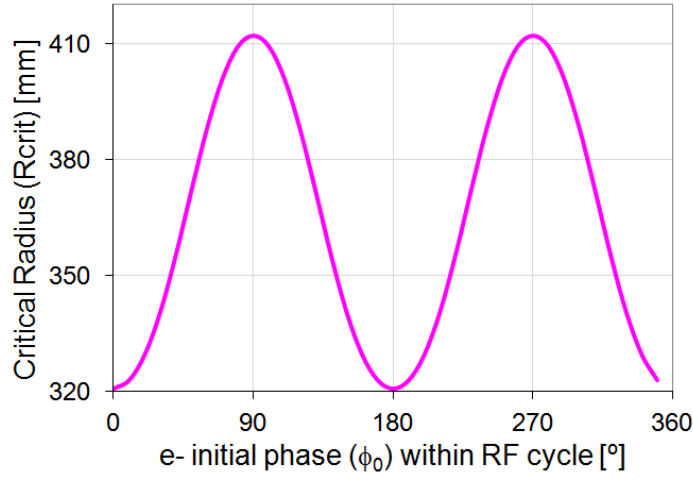


Figure 3.13: Launch radii with trapped electron trajectories of the annular section waveguide with dimensions $R_1 = 216$ mm, $R_2 = 648$ mm and $\alpha = 0.23$ rad, depending on the initial launch phase of the electron within the RF signal cycle. The initial velocity of the electron is assumed to be zero.

where ϕ_0 is the phase of the RF signal at which the electron starts to interact, and R_0 is the radius of the trajectory within the waveguide. By numerically solving (3.38), critical radii $R_0 = R_{\text{crit}}(\phi_0)$ that might lead to resonant paths can be found. Since the solution of the equation depends on ϕ_0 , several trapped trajectories might exist. Although, they might be more unstable than the one in rectangular waveguides, which is independent of ϕ_0 .

As discussed before, an equivalent annular section waveguide can be found for any wedge-shaped waveguide. Hence, (3.38) can also give a good approximation of the wedge-shaped resonant paths. The strategy for the multipactor simulation is to launch the initial electrons from the bottom wall of the wedge-shaped waveguide into one of those critical radii R_{crit} by setting an initial velocity vector tangential to them. The corresponding critical launching locations in the XY -plane can be easily computed as follows:

$$x_{\text{crit}} = R_{\text{crit}} \cdot \cos \frac{\alpha}{2} - \frac{R_1 + R_2}{2} \quad (3.39)$$

$$y_{\text{crit}} = -\frac{h_1 + h_2}{4} + \frac{h_1 - h_2}{2 \cdot a_{\text{Wedge}}} \cdot x_{\text{crit}} \quad (3.40)$$

where h_1 and h_2 have been defined in Fig. 2.1 of Chapter 2.1.1.

In [46], an $R_{\text{crit}} = 320.7$ mm was chosen for a wedge-shaped waveguide with dimensions $R_1 = 216$ mm, $R_2 = 648$ mm, $\alpha = 0.23$ rad and $f = 500$ MHz, for $\phi_0 = 0$. However, (3.38) provides a whole range of critical radii, from 320.7 mm to 412.1 mm, if all possible initial phases are considered, as shown in Fig. 3.13. It has to be noted that the derivation of (3.38) is done assuming a zero initial velocity of the electron, which is not the case in our simulations. A non-zero velocity complicates the calculation of the stable trajectory of the

electrons and does not lead to such a simple closed expression as (3.38). Hence, it should only be interpreted as a first approximation.

Nevertheless, it is not likely that all trapped trajectories/critical radii have the same impact on the multipactor behaviour of the geometry. The influence of other issues, like the voltage distribution along the waveguide cross section, has been considered for establishing additional criteria to identify an eventual “optimal” radius (highest likelihood of MP breakdown) within the predicted critical range. The concept of “equivalent voltage” in wedge-shaped waveguides is not obvious. We define it as the line integral of the electric field in a waveguide arc (3.41), thus depending on the radius where it is calculated.

$$V(R) = \int_{arc} \vec{E} \cdot \vec{dl} \quad (3.41)$$

where \vec{E} is the RF electric field and $\vec{dl} = dl \cdot \hat{\alpha}$. This integrating path correspond to a potential trapped trajectory in wedge-shaped waveguides, which tends to follow the electric field vectors, approximately arranged in an arc geometry (see Fig. 3.9 and Fig. 2.4). The integral is calculated numerically with the Simpson method [71].

The equivalent voltage of the wedge-shaped waveguide proposed in [46] has been calculated for all radii with (3.41) (see Fig. 3.14). By overlapping the equivalent voltage (red-solid line) with the critical radii range presented in Fig. 3.13 (green-shadowed region with dashed bounds in Fig. 3.14), the relations between them can be derived. The fact that the maximum equivalent voltage is located outside the trapped trajectory region evidences the effectiveness of wedge-shaped waveguides in increasing the multipactor threshold. The mismatch between maximum equivalent voltage and location of the trapped trajectory contrasts with the rectangular waveguide case, where they are both in the vertical line in the centre of the geometry.

Since the multipactor behaviour of a structure is closely linked with the voltage, we can make the assumption that, among the critical radii of a wedge-shaped cross section, the optimal one for multipactor prediction should be around the one with the highest equivalent voltage, therefore close to the one which crosses the x -axis at $x = -19.9$ mm ($R_{crit} \approx 400$ mm) in Fig. 3.14. This is the limit of the trapped trajectory region closest to the broader side-wall. The “Launch Position Prediction Module” of the multipactor prediction software (cf. Fig. 3.8) provides, for a given wedge-shaped waveguide, the limits of the trapped trajectories region and the estimated position of the maximum equivalent voltage arc. The user can then select a launch position array with N_{Launch} elements, typically between 4 and 10. Experience shows that the most efficient method is to uniformly cover a fraction of the complete trapped electron region, which should be the one closer to the maximum equivalent voltage arc, plus a certain margin to cover for the differences between wedge-shaped and annular section waveguides.

The methods for the prediction of the launch position of the initial electron proposed here and the additional influence of the equivalent voltage in the choice of the optimal trapped trajectory will be verified by means of appropriate simulations, which are included in the following Chapters 3.3 and 3.4.

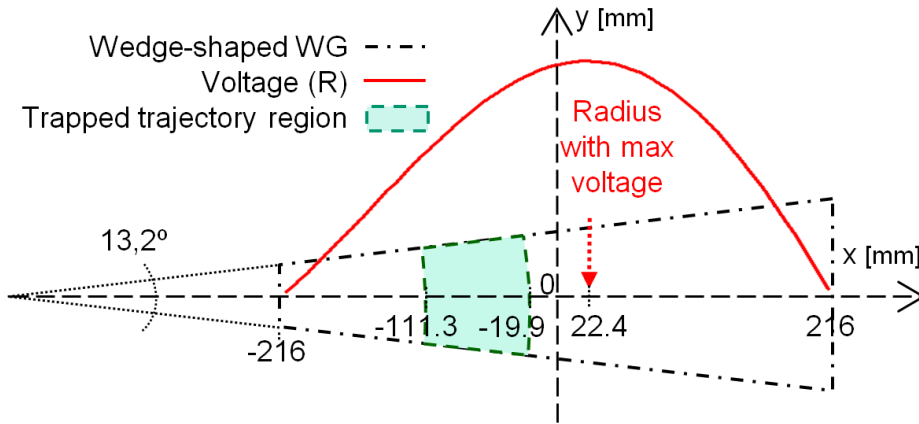


Figure 3.14: Cross section of the wedge-shaped waveguide including the region with trapped electron radii and the equivalent voltage amplitude distribution. Qualitative (unitless) distribution of the equivalent voltage for the whole radii range. Radius with maximum equivalent voltage $R_{\max V} = 454.4$ mm ($x_{\max V} = 22.4$ mm at $y = 0$).

3.3 Validation of the Formulation

3.3.1 Example of Chojnacki

The first analysis of annular section waveguides from a multipactor point of view can be found in [42]. Its multipactor prediction results will be taken here as reference for the validation of our prediction tool.

The two structures proposed in [42] are a rectangular waveguide with dimensions $a = 432$ mm and $b = 102$ mm, and on the other hand, an annular section waveguide with dimensions $R_1 = 216$ mm, $R_2 = 648$ mm and $\alpha = 13.2^\circ$. Both are excited by a harmonic signal at $f = 500$ MHz. The material of the waveguide walls is niobium, and its characteristic SEEC curve can be expressed with the simple model proposed in (3.1), Chapter 3.1.1. The material-characteristic constants applied here are: $\delta_{\max} = 1.6$, $W_{\max} = 200$ eV, $A = 1.55$, $B = 0.9$, $C = 0.79$ and $D = 0.35$.

Our simulations try to reproduce the same conditions, waveguide dimensions and material properties. For our convenience, the annular section has been converted into an equivalent wedge-shaped waveguide (see Chapter 3.2.4) with the following characteristics: $a_{\text{Wedge}} = 432$ mm, $h_1 = 49.9841$ mm, $h_2 = 149.952$ mm, and $\alpha = 13.2^\circ$. It has to be noted that the widths of the rectangular and the wedge-shaped waveguide are identical, which allows similar simulation conditions and a comparison between both results. To emulate the electron rebound algorithm of the simulator in [42], the initial electrons and all secondary ones generated after a collision are launched with an energy of 2 eV normal to the impacting surface. To achieve this, the rebound energy model of the “Electron Tracking Module” has been accordingly adapted (cf. Chapter 3.1.2 and Fig. 3.8). Since the power range in all cases is

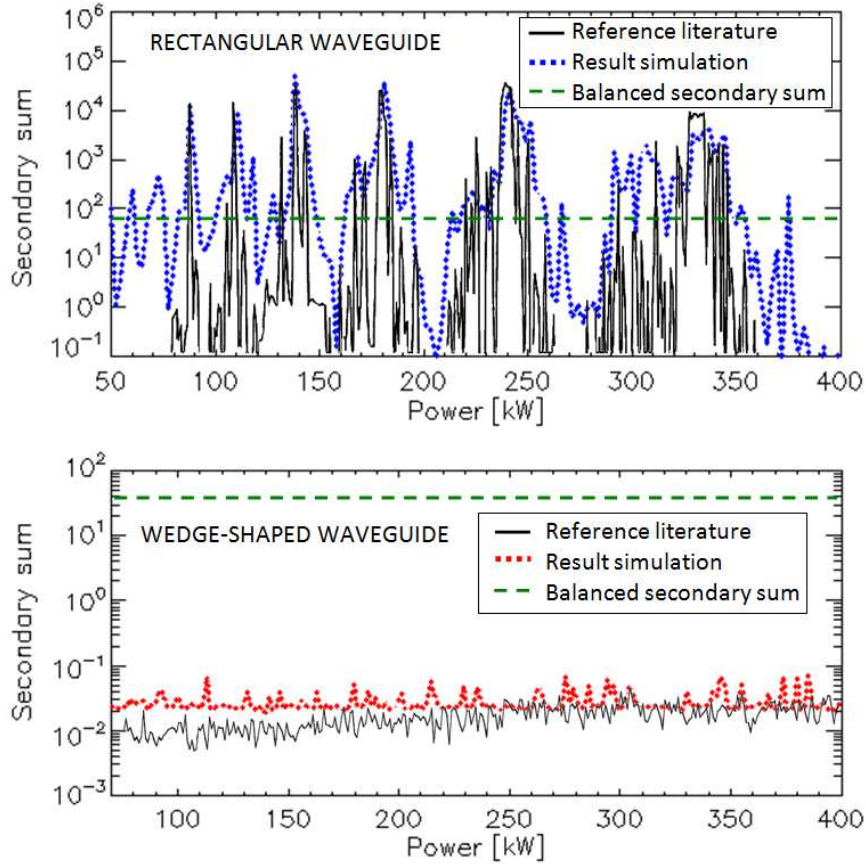


Figure 3.15: Comparison of our simulation results (blue- and red-dotted lines) with the results of Chojnacki (black-solid lines). Top: rectangular waveguide with dimensions $a = 432$ mm, $b = 102$ mm and the launch position of the initial electron at $x = 0$. Bottom: wedge-shaped waveguide with dimensions $a_{\text{Wedge}} = 432$ mm, $h_1 = 49.9841$ mm, $h_2 = 149.952$ mm, $\alpha = 13.2^\circ$ and the launch radius at $R = 290$ mm.

relatively high in all cases, the relativistic effect is considered when calculating the electron motion.

In both cases, $M = 42$ is the number of initial electrons launched at equidistant RF cycle phases and also the secondary sum threshold value. The multiplicity functions are calculated after a maximum of $Coll_{\text{max}} = 20$ impacts of the effective electron against the walls. The maximum simulation lifetime of each effective electron is $t_{\text{max}} = 1000$ RF cycles, the minimum impact energy is 0.1 eV and the minimum accumulated SEEC is $e_{\text{min}} = 10^{-3}$. In Fig. 3.15, the results of our code (dotted lines) are overlaid with the reference curves in [42] (solid lines). The number of launched electrons is $M = 42$, hence this is the secondary sum (enhanced counter function) value that indicates the threshold of the multipactor risk region (green-dashed line in Fig. 3.15).

The top plot of Fig. 3.15 contains the results of the rectangular waveguide, with some

high-risk multipactor power regions. Both curves show a very good agreement in the shape and location of these multipactor windows. The wedge-shaped waveguide results are shown in the bottom plot of Fig. 3.15. Here, both simulation and reference curves confirm that no multipactor risk is expected in this case. To stay in the safe side, this simulation was repeated with different initial electron launching positions around the one chosen in [42], 290 mm, coming to the same conclusion of no multipactor risk.

3.3.2 Example of Semenov

A second validation example has been selected, where trapped electron trajectories were found in a wedge-shaped waveguide [46]. A very similar geometry to the annular section considered in [42] is studied. However, there is a slight modification in the dimensions of the corresponding rectangular waveguide, namely $a = 414.9$ mm and $b = 103.6$ mm, in order to maintain the same cutoff frequency of the fundamental mode as the one of the annular section.

Instead of niobium, the material of the waveguide walls is a type of silver. Its SEY curve is described with a very similar model to (3.2) in Chapter 3.1.1, but without the dependence from the electron impact incidence angle. The exact model is included here (3.42):

$$\delta(W) = \delta_{\max} (\gamma e^{1-\gamma})^{\kappa(\gamma)} \quad (3.42)$$

where $\delta_{\max} = 2.22$, $\gamma = \frac{W}{W_{\max}}$, $W_{\max} = 519$ eV, and $\kappa = \begin{cases} 0.62 & \gamma < 1 \\ 0.25 & \gamma > 1 \end{cases}$.

Furthermore, a spread of the emission velocity and emission angle after a collision is considered [46], since this is a more reliable method than considering a fix rebound of [42] for detecting a multipactor risk. The spread in the emission angles and energy of the electron after the rebound follows the statistical distributions defined in (3.18), (3.17) and (3.19) of Chapter 3.1.2. The average emission energy is $W_C = 2.92$ eV, with a spread of $W_G = 1.2$ eV. The initial electrons are still launched with a velocity vector normal to the wall. In both cases, $M = 1000$ is the number of initial electrons launched at equidistant RF cycle phases, and also the secondary sum threshold value (green-dashed line in Fig. 3.16). The multiplicity functions are calculated after a maximum of $Coll_{\max} = 20$ impacts of the effective electron against the walls. The maximum simulation lifetime of each effective electron is $t_{\max} = 1000$ RF cycles, the minimum impact energy is 0.1 eV, and the minimum accumulated SEEC is $e_{\min} = 10^{-3}$. The results for both waveguides (the rectangular and the wedge-shaped ones) at the given power range (0.2 MW to 1.8 MW) are included in Fig. 3.16. On the one hand, a very good match can be observed in the rectangular waveguide curves in the top of Fig. 3.16. Our secondary sum curves seems however slightly scales with respect to the one of [46]. This is probably motivated by a discrepancy in the $Coll_{\max}$ -value between both algorithms. It is likely that [46] has used a $Coll_{\max} > 20$, since this increase results in an amplification of the *Secondary Sum*-value in multipactor-sensitive regions, and an attenuation in multipactor-free ones, as certified by Fig. 3.16. On the other hand, the wedge-shaped waveguide simulation in the bottom of Fig. 3.16 shows a relatively different shape

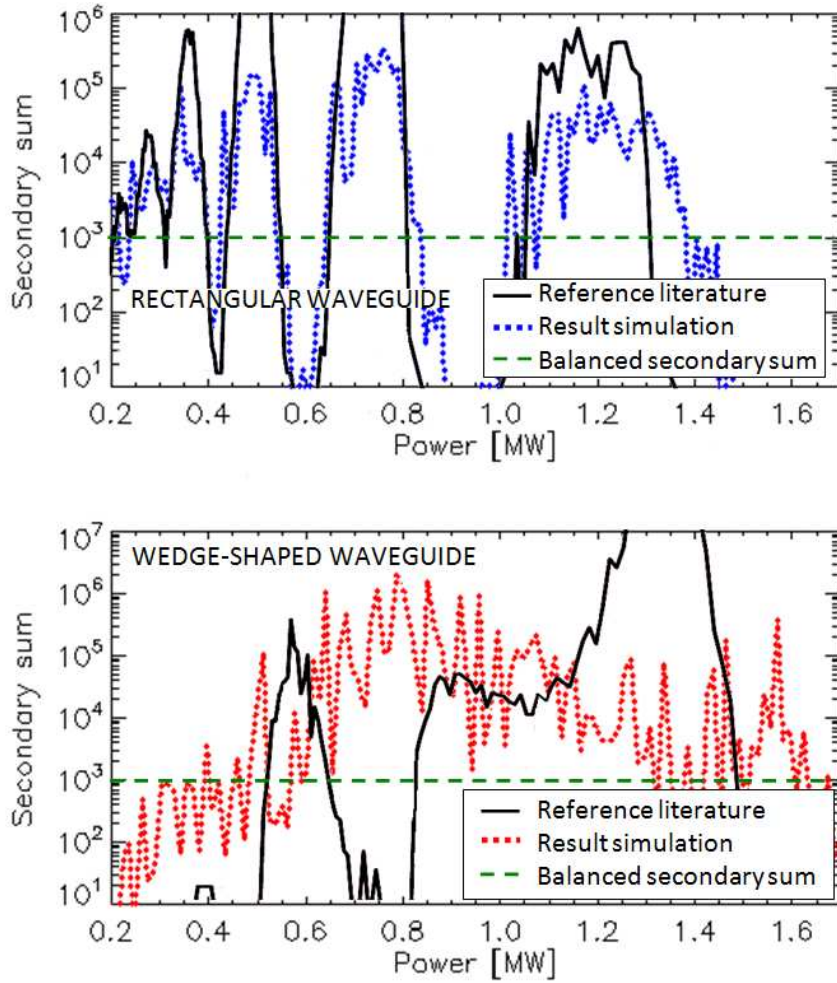


Figure 3.16: Comparison of our simulation results (blue- and red-dotted lines) with the results of Semenov (black-solid lines). Top: rectangular waveguide with dimensions $a = 414.9$ mm, $b = 103.6$ mm and the launch position of the initial electron at $x = 0$. Bottom: wedge-shaped waveguide with dimensions $a_{\text{Wedge}} = 432$ mm, $h_1 = 49.9$ mm, $h_2 = 149.7$ mm, $\alpha = 0.23$ rad and the launch radius at $R = 390.1$ mm.

than the reference curve of [46]. However, the lower and upper multipactor power limits (≈ 0.5 MW and ≈ 1.6 MW, respectively) fit reasonably well. Next, we explain the reasons for this discrepancy and the implications of these simulation results.

According to Chapter 3.2.4, the optimal electron initial position for the wedge-shaped waveguide multipactor simulation should lie around the largest radius within the trapped range ($R_{\text{crit}} \approx 400$ mm), since the voltage is higher there (see Fig. 3.13 and 3.14). This differs from the strategy of [46], where the simulation was done at 320.7 mm, the lowest radius of the trapped range. Looking back at the same simulation in [42], an even lower electron launch radius of 290 mm is used.

In order to verify the best approach, N_{Launch} was set to 9, so that a broader range of initial electron positions was covered. With a launching position corresponding to the radius considered in [46] (320.7 mm), no secondary sum value exceeding the threshold was found along the whole defined input power range. In fact, only the simulations with initial radii between 354 mm and 415 mm show multipactor risks for at least one of the input power steps. Nevertheless, this proves the existence of a range of trapped electron trajectories.

Concerning the electron initial phase loop (cf. Fig. 3.8), which is the instant when the electron starts to interact with the electromagnetic fields, it was observed that the phase element at which the multipactor resonances were stronger, was almost the same for all launch positions and power steps. This seems to contradict the theory expressed in [46] (see also Fig. 3.13), which states that, for each phase of the initial electron, a different launch radius should contain the trapped trajectory. The fact that in our simulations, as well as in [42] and [46], the initial velocity of the electron is different from zero (2.92 eV), which is needed in order to avoid too long simulation times, disturbs this dependency. As already suggested in Chapter 3.2.4, just the trapped trajectories with the highest voltage will determine the highest multipactor resonances. The non-zero initial velocity of the electron and the random direction of the electrons after a collision motivate that electrons end up in this more sensitive trapped trajectories, even if originally launched from other radii. Thus, if the initial speed vector remains constant, all simulation iterations will tend to have similar phase values of the initial electron that result in the strongest multipactor resonances.

The optimal (critical) initial radius has been identified at around 390.1 mm (the one used for the simulation of the wedge-shape case of Fig. 3.16). There, the amount of power values with multipactor risks are the biggest ones, the lowest power threshold is found, and the peaks of the enhanced counter function curve are maximum, which means that the resonant mechanism of the electrons is the strongest there.

These simulation results indicate a good agreement with the prediction of 400 mm of Chapter 3.2.4, which combines the information of the trapped electron trajectory range prediction with the voltage calculations. In the following Chapter 3.4, it will be analysed if this initial position prediction strategy is generally applicable to any wedge-shaped waveguide with arbitrary inclination angles.

The fact that no multipactor risk was detected at the initial position of 320.7 mm, which contradicts the result of [46], and the different curve shapes in the bottom of Fig. 3.16, might

be due to several facts. As explained before, we are dealing with “equivalent” but not identical waveguide cross sections: i.e. annular section and wedge-shaped ones. In addition, both software codes implement completely different algorithms to calculate the electromagnetic fields. Small discrepancies in the distribution of the fundamental mode in the cross section might motivate displacements of the critical radii and the voltage distribution. Another explanation might be a difference in the way the electrons are launched in both algorithms, or inaccuracies regarding the description of the selected launch position in [46]. Nevertheless, the agreement between both secondary sum curves is still acceptable, mainly in the location of the limits of the multipactor risk windows.

3.4 Study of the Optimal Inclination Angle

3.4.1 Introduction to the Angle Sweep Analysis

In this chapter, the optimal inclination angle α between the top and bottom plates of the wedge-shaped waveguide is discussed, by analysing the position and value of the multipactor discharges that take place at the lowest input power step in each case. The simulation parameters and waveguide material properties are the same ones used in Chapter 3.3.2. The rectangular waveguide with $a = 414.9$ mm and $b = 103.6$ mm has been used as reference, and then several wedge-shaped waveguides (identified by the index (i)) with inclination angles $\alpha^{(i)}$ between 1° and 60° have been simulated (all at $f = 500$ MHz), including the one of [42,46] with $\alpha = 13.2^\circ$. The $\alpha_{\text{Wedge}}^{(i)}$ values of each inclination example have been adjusted in order to fit the same f_C value of the fundamental mode of the rectangular waveguide. The mean height of the wedge-shaped waveguides is kept equal to the one of the rectangular waveguide ($\frac{h_1^{(i)} + h_2^{(i)}}{2} = b$), as long as possible. When the minimum length is reached for the narrow side-wall ($h_{1,\text{min}} = 1$ mm), the main heights are forced to exceed the rectangular height b .

3.4.2 Results and Interpretation

The results are summarised in Table 3.1.

Table 3.1: Inclination angle sweep - Multipactor (MP) prediction.

$\alpha [^\circ]$	WG dimensions [mm]		Launch positions with trapped trajectories; x[mm], bottom wall				Computed voltage for $P = 1W$			MP threshold (simulated) [kW]
	α_{Wedge}	h_1	h_2	Start/end (predicted)	Start/end (simulated)	With max MP (simulated)	Max [V]	Location max;x[mm], bottom wall	Value for max MP [V]	
0.0	414.9	103.6	103.6	0.0	-23.0/23.0	0.0	23.3	0.0	23.3	170
1.0	414.94	99.98	107.2	-7.6/-1.7	-22.0/19.0	-4.0	23.0	3.8	23.0	175
2.0	415.1	96.4	110.8	-15.2/-3.4	-26.9/13.1	-8.9	23.1	4.7	23.0	185
5.0	416.8	85.4	121.8	-38.2/-8.5	-35.7/1.22	-13.8	23.0	4.0	22.7	230
10.0	422.7	66.6	140.6	-79.2/-16.9	-56.0/-14.2	-38.0	23.0	12.5	21.2	240
13.2	432.0	49.9	149.7	-113.4/-22.6	-80.3/-19.7	-44.6	22.4	19.4	19.8	230
15.0	435.1	46.3	160.9	-126.5/-24.6	-110.0/-16.9	-57.0	22.9	27.6	19.0	260
20.0	460.8	22.4	184.8	-188.5/-28.1	-136.0/-18.0	-67.0	23.1	37.7	16.6	240
25.0	499.7	1.0	222.6	-248.3/-16.6	-150.0/-8.0	-67.0	24.7	58.1	15.5	330
30.0	498.3	1.0	268.1	-247.8/-18.9	-144.7/-14.3	-62.6	27.1	55.6	17.6	400
35.0	496.5	1.0	314.0	-247.2/-21.6	-116.3/-2.0	-50.0	29.2	49.9	21.1	490
40.0	493.9	1.0	360.6	-246.1/-24.7	-125.2/-4.0	-51.9	31.3	46.4	22.4	500
45.0	490.9	1.0	407.8	-244.7/-28.2	-126.5/3.0	-34.0	33.2	50.6	26.8	580
50.0	487.6	1.0	455.6	-243.2/-32.0	-127/18.0	-32.0	34.9	44.6	28.8	670
55.0	483.3	1.0	504.1	-241.2/-36.2	-118/6.0	-42.0	36.7	38.4	28.9	690
60.0	478.2	1.0	553.2	-238.7/-40.6	-114/-2.0	-40.7	37.7	40.0	30.1	750

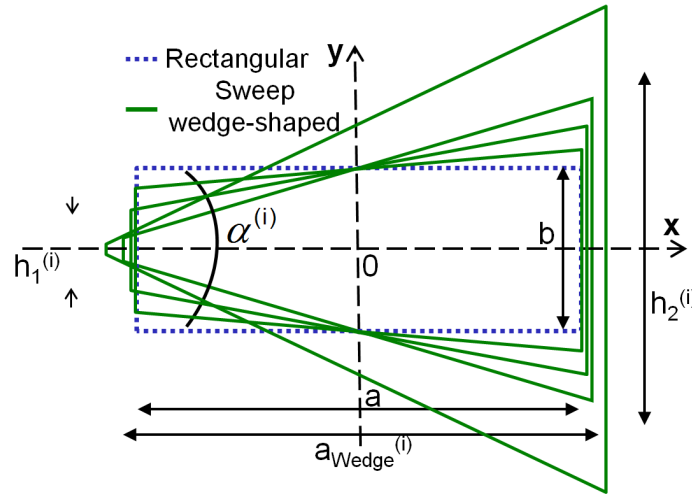


Figure 3.17: Schematic overview of the cross sections of the waveguides applied in this analysis. The cutoff frequency f_C is constant.

Fig. 3.17 gives an overview of the cross sections of the waveguides involved in this sweep analysis. Each row of Table 3.1 contains the inclination angle and dimensions of the wedge-shaped waveguide, the launch positions of the initial electrons with trapped trajectories, the computed voltage, and the obtained multipactor power threshold. The predicted start/end of the launch positions are calculated applying (3.38) and selecting the extreme limits (see Fig. 3.13), whereas the simulated start/end values correspond to the range of initial electron launch positions where the multipactor simulation showed at least one power step with multipactor risk. The initial launch position with maximum multipactor threshold (higher enhanced counter function values and lower power threshold, and therefore the optimal for multipactor prediction) and the maximum voltage were derived like in Chapter 3.3.2. The position of the initial electron located in this arc is also included. The voltage value for maximum multipactor corresponds to the voltage along the arc that contains the simulated launch position with maximum multipactor. It has to be noted that, for the wedge-shaped waveguides with inclination angles between 42° and 60° , the working frequency of 500 MHz also allows the second mode to propagate. However, in this work we only consider the excitation of the waveguide through its fundamental mode. The same effect was already observed in the examples of Table 2.4 in Chapter 2.2.3.

Several conclusions can be extracted from Table 3.1. Firstly, the predicted start/end initial positions of the electrons are similar to the simulated ones. The simulated position ranges are larger than the predicted ones for small inclination angles. This might be due to the random rebound angles after a wall collision, which might push back the electrons to trapped trajectories, even if the initial launch position is outside of them. With increasing inclination angles ($\alpha > 20^\circ$), the predicted start position gets closer to the “narrow” part of the wedge-shape, whereas the simulated position stays closer to the boundary next to the waveguide centre. The justification is that, although resonant trajectories may theoretically exist close

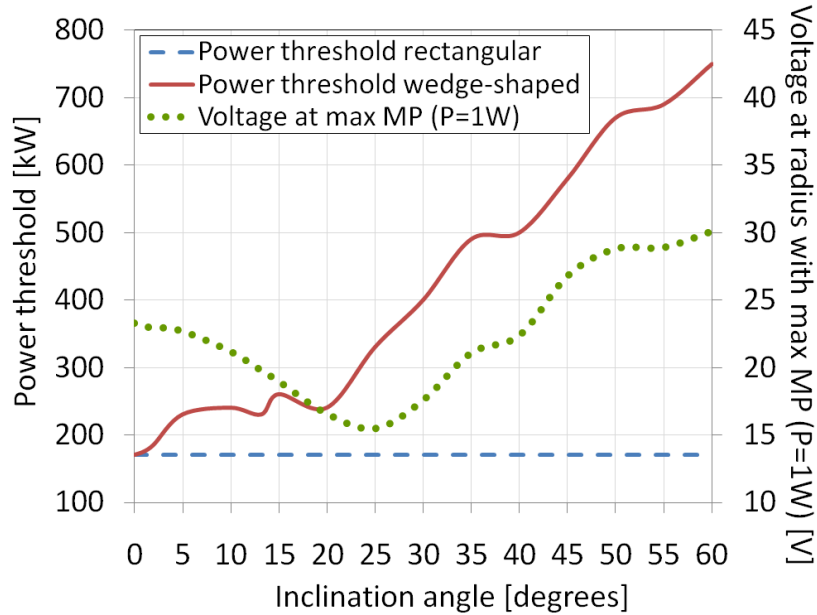


Figure 3.18: Multipactor thresholds and voltage values at the multipactor critical locations for multiple inclination angles.

to the “narrow” side-wall, the voltage there is too low to generate detectable resonances that would lead to a discharge. Finally, we can see that the initial position with maximum multipactor risk is always located close to the simulated end position. We can understand this if we realise that the maximum voltage arc is systematically closer to the “broad” side-wall of the wedge, and therefore the voltage along the critical initial positions range increases with the radius (see also Fig. 3.14). The multipactor enhanced counter function curves do not change much when modifying the initial launch positions around the optimal, but quickly fade when getting closer to the start/end positions, where the resonances are lost.

These results prove that the approach suggested in Chapter 3.2.4 can be successfully applied to limit the computational effort of the multipactor predictions for any wedge-shaped waveguide type, since only the identified limited range of initial positions has to be simulated.

Concerning the maximum voltage values, they remain very similar to the one of the rectangular waveguide, as long as the average height of the waveguide keeps constant. Once the average height starts to increase ($\alpha^{(i)} > 25^\circ$), the maximum voltage logically increases for the same input power. However, the radius where the strongest multipactor risk was simulated does not correspond to the position of maximum voltage. In fact, we can see that the voltage at the position of strongest multipactor risk continuously decreases with increasing inclination angles with equal average height. Fig. 3.18 shows the voltages and multipactor thresholds over the different inclination angles. The simulation prediction for the rectangular waveguide shows a constant threshold of 170 kW. The multipactor thresholds of the wedge-shaped waveguides quickly rise with increasing α and stabilise around 230 kW, around 40%

higher than the one of the equivalent rectangular waveguide. This proves the assumption that wedge-shaped waveguides have a better multipactor-free power range than rectangular ones. Even small inclination angles present this increment in multipactor threshold with respect to the rectangular case.

We can observe that the multipactor threshold quickly rises with respect to the rectangular waveguide case, even for minimal inclination angles. Between 5° and 20° , it remains almost constant, and from 25° on, it rises continuously. However, it has to be noted that this latter rise in the threshold corresponds with the mentioned increase in the mean height of the waveguides.

Concentrating on the voltage curve of Fig. 3.18, the first remarkable fact is that there is a minimum around 25° . In other simulated waveguides, where inclination angles of 30° could be designed without increasing the average height, a continuation in the decreasing tendency of the voltages was observed. This suggests to use inclination angles around these values, or the biggest angle possible below them with equal waveguide mean height. Inclinations between 5° and 30° are also a good design compromise, as they have multipactor threshold values very similar to the optimum case, offering approximately 40% higher power threshold than the equivalent rectangular waveguide.

3.5 Susceptibility Maps

3.5.1 Definition

The multipactor susceptibility maps for a parallel plate model are defined as follows: the abscissa corresponds to the frequency gap product ($f \times d$), where d is the distance between the top and bottom plates, and the ordinate represents the voltage or the power of the input signal. Regions with risk of multipactor are highlighted, creating the well-known susceptibility curves [14] that indicate the multipactor phenomena of all possible orders, as already introduced in Chapter 3.1.3. These curves help in the design of multipactor-free waveguide structures, usually in rectangular waveguide devices for space applications.

In order to provide a similar reference for the design of wedge-shaped waveguides, the following susceptibility map is proposed: the frequency gap product is obtained by multiplying the working frequency by the mean height of the waveguide. Hence, a different curve will be obtained per inclination angle of the wedge-shaped geometry.

By simulating a considerable number of wedge-shaped waveguides at different frequencies, with different gap sizes and inclination angles, the following susceptibility maps were generated. The curves (see Fig. 3.19) show the multipactor voltage threshold V_{th} of the devices (first voltage at which a multipactor risk is detected) and can be compared with the ones of the corresponding rectangular waveguide. The same simulation conditions and waveguide materials as in Chapter 3.4 are used here.

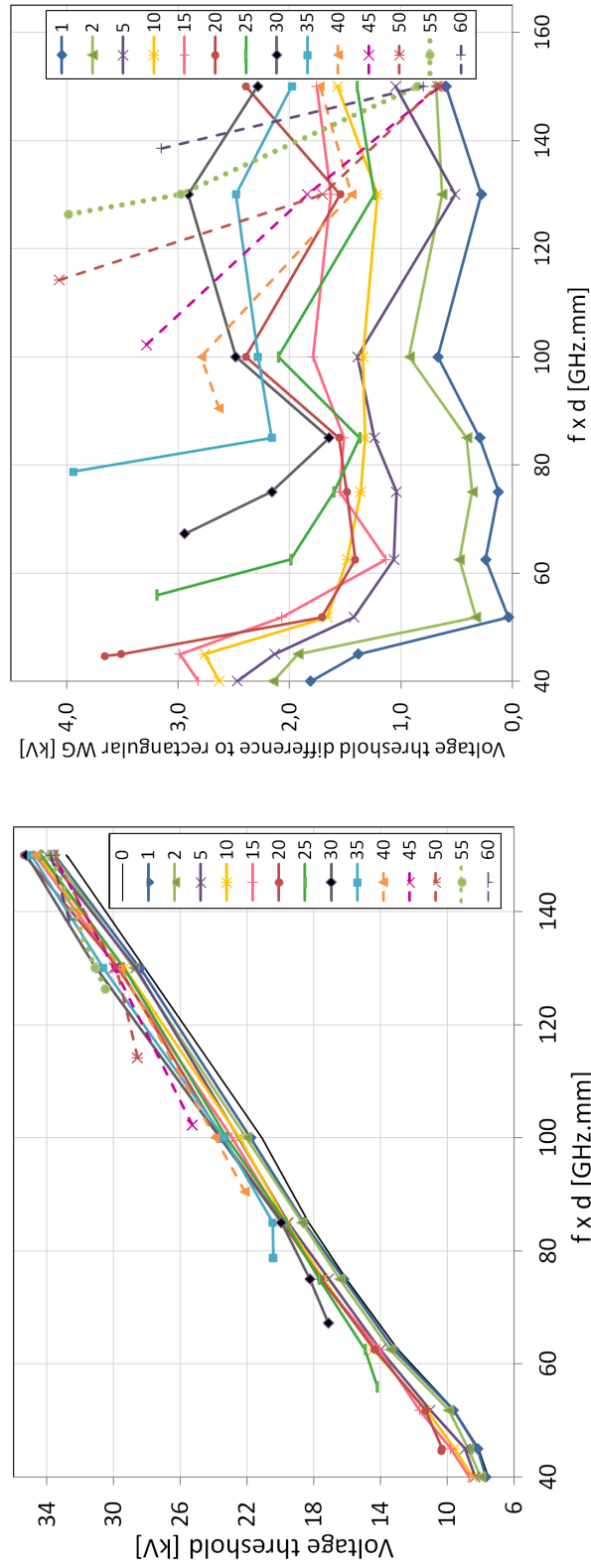


Figure 3.19: Susceptibility map for different inclination angles. (Left) voltage threshold and (right) relative voltage thresholds with respect to the rectangular case. Thresholds after 20 collisions.

The susceptibility curves for all angles verify the results obtained in the previous sections. The V_{th} values are always higher than in the rectangular waveguide case, which coincides with the case $\alpha = 0^\circ$. The improvement in the V_{th} reaches a factor of 1.35, depending on the inclination angle. Small angles up to 5° are fairly close to the rectangular threshold. The V_{th} usually increases with the angle until around 35° , falling slightly again for higher angles. The V_{th} at 30° seems to be the optimum for many of the cases considered in the simulation range, however the improvement with respect to the other angles is not dramatic. For the lower $f \times d$ values (being d the mean height), no results are available for large inclination angles. No wedge-shaped geometries with such large angles were possible, since the mean height was too low and the “narrow” side of the cross section reached its minimum design limit of 1 mm. When travelling towards higher abscissa values, these inclination angles become gradually feasible, like in the case of 25° at $f \times d = 56$ GHz.mm, or 35° at $f \times d = 79$ GHz.mm.

3.6 Summary

The software tool has been verified by comparisons with simulations available in the literature, and then it has been used to analyse the multipactor behaviour depending on the inclination angle between top and bottom walls. This allows confirming the advantage of wedge-shaped waveguides with respect to rectangular waveguides in terms of multipactor breakdown resistance, since they are able to handle typically a 40% higher power.

The improvement of the thresholds with respect to the rectangular waveguide case has to do with the fact that the voltage values in the trapped electron trajectories are lower than the absolute voltage maxima in the cross section. This depends on the inclination angle, which should lie between 5° and 30° .

Finally, susceptibility curves have been derived for this kind of waveguides. This will allow the application of these innovative geometries to more complex microwave devices, like irises, impedance adaptors, lowpass filters, bandpass filters or multiplexers, which can attract the interest of the telecommunications and space industry, or the plasma physics community.

The following step forward is to extend the multipactor threshold predictions to these more complex structures. Furthermore, an experimental verification of these theoretical models is required. All these issues will be dealt with in the following chapters.

Chapter 4

Design of a Wedge-shaped Bandpass Filter

4.1 From Waveguide to Filter

4.1.1 Searching an Implementation

Once the properties of wedge-shaped waveguides have been investigated, the logical way-forward is to search a potential application in the field of space hardware. It should be a device like an antenna feed, a multiplexer output or a filtering structure with narrow gaps or resonators, whose power handling capacity is constrained by the multipactor effect. Here, the introduction of the new topology could offer an advantage with respect to conventional technologies. The multipactor discharge that determines the power threshold of a device is the one that happens at the lowest input power values, which usually takes place in the region with the maximum electric field. In fact, in order to obtain the desired effect, it might be sufficient just to substitute the specific part excited by strong electric fields.

The α -sweeps from previous chapters indicate that rectangular waveguides can be substituted by equivalent wedge-shaped waveguides up to a certain inclination angle, where their average height cannot meet the equivalent rectangular one any more. This maximum angle decreases when the height-to-width ratio of the rectangular cross section is smaller, which is a limiting factor if it is required that both structures keep comparable dimensions. Therefore, this technology is not suitable for substituting rectangular structures in capacitive (constant width and varying heights) lowpass filters, where the risk of multipactor discharge concentrates in the small gaps. Instead, we can consider an inductive (constant height and varying widths) bandpass filter, which is a coupled resonator structure like the one shown in Fig. 4.1. The wedge-shape geometry can be applied to the cross section of the resonators, or even to the whole device.

Consequently, the challenge is to develop or adapt an existing design method to be able to cope with wedge-shaped waveguides, and to provide the structure dimensions for a particular set of standard requirements. A final task is to extend the multipactor prediction tool

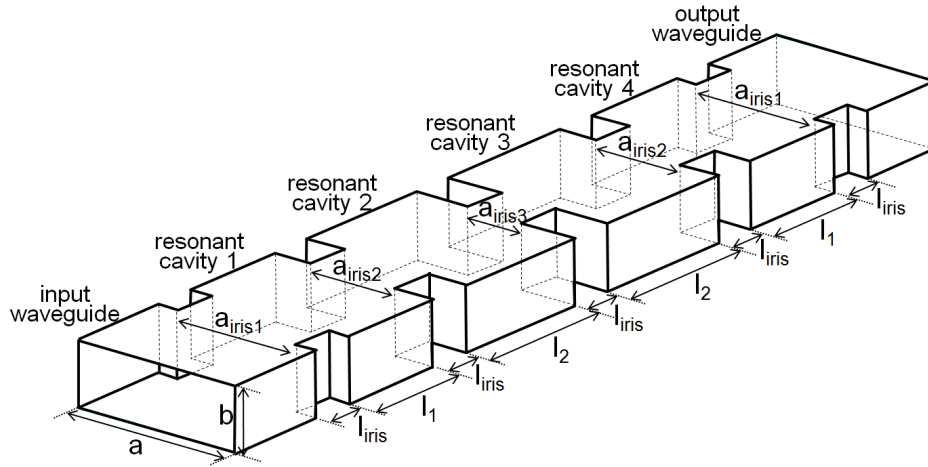


Figure 4.1: Sketch and dimensions of a conventional inductive bandpass filter with its hollow resonators and irises.

presented in Chapter 3 to waveguide devices of finite length. These devices, like the one in Fig. 4.1, are composed of a series concatenation of hollow waveguides of different sizes, with discontinuities perpendicular to the propagation direction involving planar junctions. The following sections will describe how this can be done, and will provide two equivalent designs in rectangular and in wedge-shaped waveguide technologies. Moreover, both designs will be manufactured and tested in the laboratory, in order to experimentally verify the improvement in terms of the multipactor threshold for the wedge-shaped case, as foreseen with the prediction tools.

4.1.2 Filter Requirements

A bandpass filter aims to fulfil a set of requirements, e.g. the centre frequency f_0 , the bandwidth of the pass-band and the return loss threshold. Its dimensions are conditioned by these parameters, although several solutions are often possible. In order to choose a particular configuration, additional design criteria can be considered, like the total size of the filter, the out-of-band response, determining the order of the filter (number of resonators), or the manufacturing constraints. Fig. 4.2 gives a visual definition of the typical requirements. Note that the bandwidth of the filter is defined by the crossing points of the S_{11} curve (filter reflection) with the return loss ripple or threshold. Other conventions prefer to describe the requirements in terms of the 3 dB-bandwidth, whose limits are defined by the 3 dB decay of the transmitted frequency response S_{21} with respect to the S_{21} -value at the centre frequency.

In this chapter, typical filter requirements for space applications in X-band have been chosen. They are listed in Table 4.1. To facilitate the interconnectivity of the device with standard measuring equipment, WR90 waveguides ($a = 22.86$ mm, $b = 10.16$ mm) have been chosen as input and output interfaces.

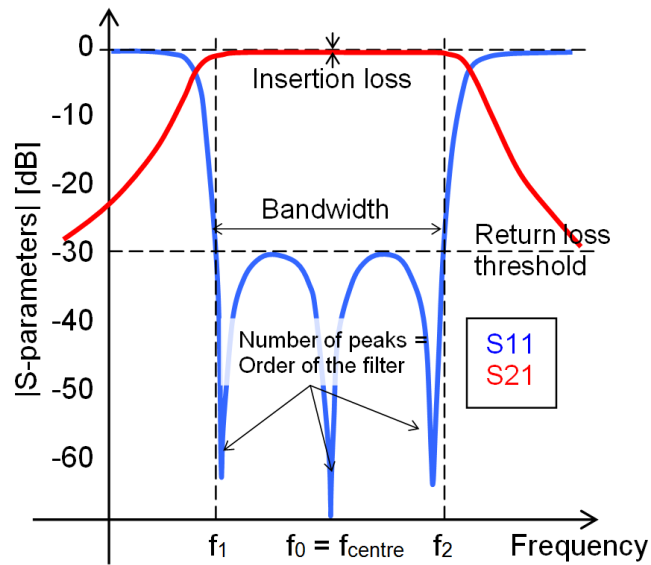


Figure 4.2: Typical bandpass filter frequency response. Main requirement parameters are defined here.

Table 4.1: Bandpass filter requirements.

Parameter	Value
Centre frequency [GHz]	9.5
Bandwidth [MHz]	100
Return loss [dB]	25
Order of the filter	4

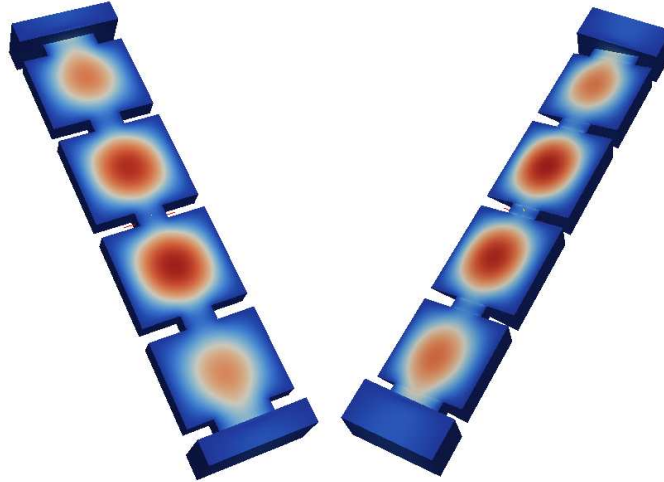


Figure 4.3: 3-D plot of the electric field magnitude distribution perpendicular to the metallic surfaces of a rectangular waveguide (left) and a wedge-shaped waveguide (right) bandpass filter, calculated with FEST^{3D}. Colour table ranges from dark blue (minimum) to dark red (maximum).

4.1.3 Filter Topology and Cross Section

Rectangular waveguide inductive filters, like the one shown in Fig. 4.1, are usually symmetric two-port structures composed of inductive steps (irises with equal height and less width than its input and output stages) and resonators (with a length of about half a wavelength). They are tuned to reject out-of-band frequencies and only let through the pass-band signals. There is a concentration of the electromagnetic fields in the centre of the resonator cavities, as can be seen in the electric field simulation plotted in Fig. 4.3. For a given RF input power, the electric-field values are higher in the central resonators than in the external ones, or at the input and output waveguides. Therefore, it is likely that the RF multipactor breakdown threshold, which is defined by the discharge happening at the lowest input power value, takes place in the central resonators.

These central resonators could be substituted by wedge-shaped ones, as shown in the left-hand side of Fig. 4.4. Note that the iris has also the same inclination as the resonators, since this simplifies the manufacturing process. Also, due to manufacturing simplicity, it was decided to keep the inclination between the top and bottom plates of the filter for the whole structure between the first and last irises, as also shown in the right-hand side of Fig. 4.3. The interface with the input and output WR90 waveguides will look like the one depicted in the right-hand side of Fig. 4.4.

Based on an existing rectangular waveguide filter, a wedge-shaped one will be designed with the same performance goals. For enabling a rigorous comparison, the resonators of both filters will have the same average height and cross-section area, and the same constant width $a = a_{\text{Wedge}}$. The rectangular waveguide filter was designed and manufactured by Tesat-Spacecom (Germany) under an ESA-ESTEC contract according to the criteria listed

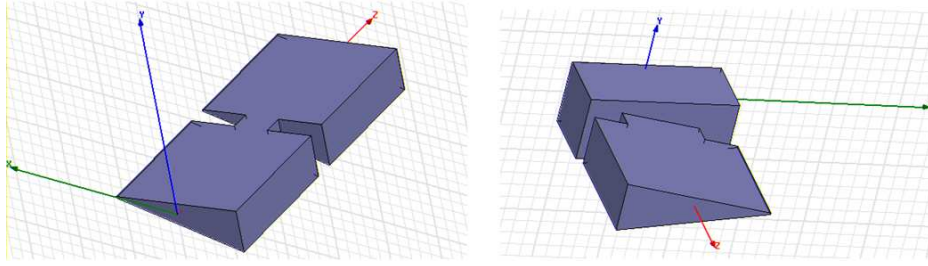


Figure 4.4: 3-D view of the wedge-shaped waveguide central resonator stages (left) and the input waveguide and the first resonator (right) of the wedge-shaped waveguide filter.

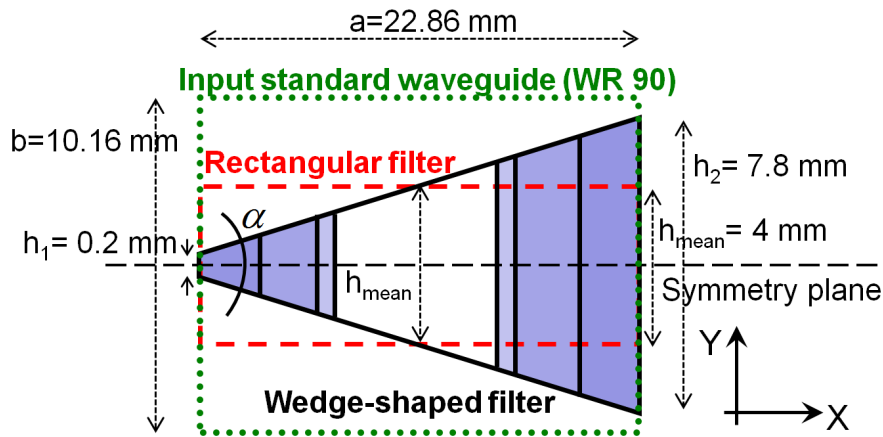


Figure 4.5: Overlapped cross-sectional schematic view of the wedge-shaped waveguide (black-solid lines) and rectangular waveguide (red-dashed lines) filters. Vertical black lines correspond to the irises walls, as seen from the front of the filter. Input waveguides (green-dotted rectangle) are standard WR90 for both filters. The inclination angle is $\alpha = 19^\circ$.

in Table 4.1. In the cross-sectional schematic view shown in Fig. 4.5, it can be seen that the resonator and iris stages have artificially reduced cavity heights ($h_{\text{mean}} = 4$ mm) instead of the standard WR90 height b of conventional filters (e.g. the one shown in Fig. 4.1). This change is necessary in order to reduce the expected multipactor threshold value, which otherwise would have been above the measurable power range available at the laboratory test bed.

In order to have comparable filters, the wedge-shaped cross section will have an average height equal to h_{mean} . In this way, we expect to obtain similar maximum voltage values and, therefore, comparable discharge thresholds. Considering that the minimum height of the smallest side-wall is $h_1 = 0.2$ mm due to manufacturing constraints, inclination angles between $\alpha = 0^\circ$ and $\alpha = 19^\circ$ are possible. Among these, 19° is the one offering better multipactor performance according to the predictions of Chapter 3.4. With this inclination, the height of the largest side-wall becomes $h_2 = 7.8$ mm, as can be seen in Fig. 4.5. Once the wedge-shaped cross section has been defined, the synthesis process of the whole filter

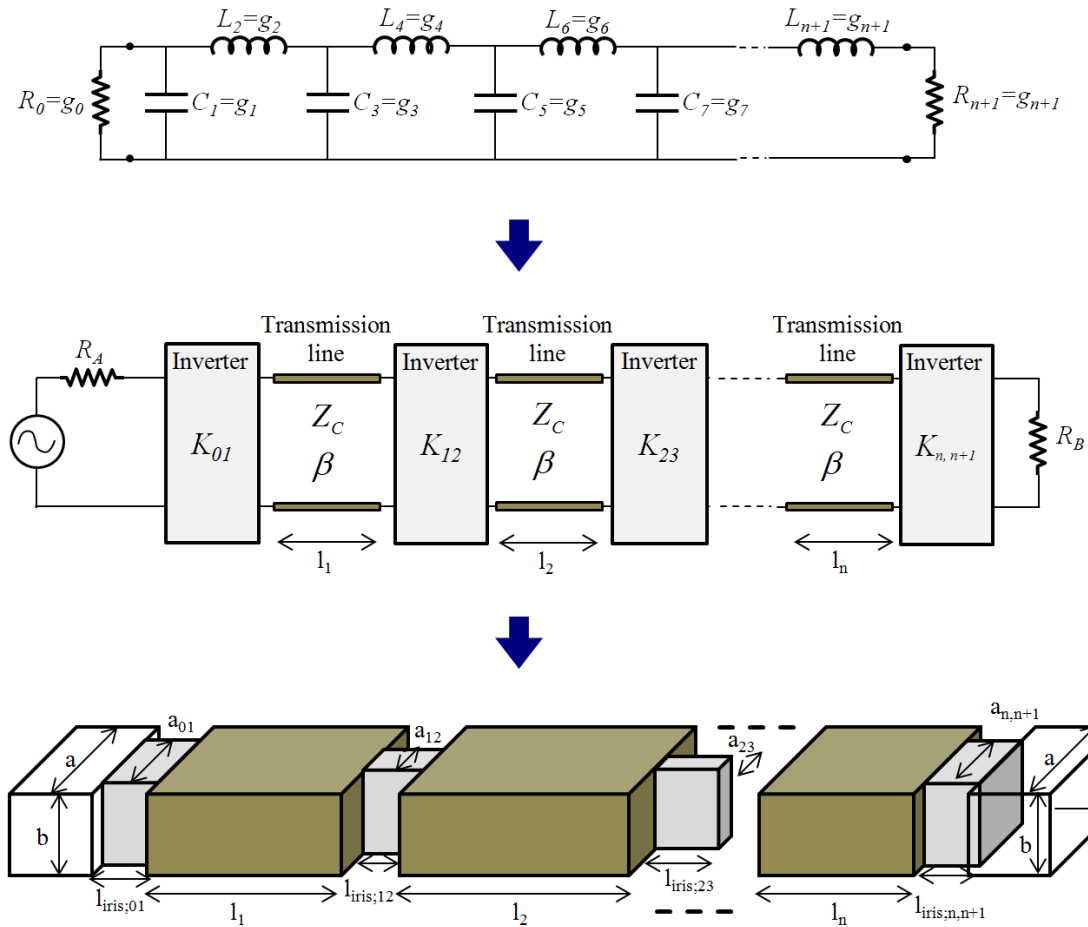


Figure 4.6: Circuit models used for the design procedure of a microwave waveguide filter.

can start.

4.1.4 Design Procedure

The basics of the design procedure of microwave filters was set by [72]. It provided the basis to translate the requirements into an equivalent circuit prototype with lumped elements. The prototype can be then converted into a model with inverters and transmission lines, from which the final dimensions of a coupled resonator structure can be derived (see schematic of the different prototype models in Fig. 4.6). The design algorithm has been further improved through the years in order to correct inaccuracies, avoid the need of a final optimisation step, and extend its validity to wide-band designs [53, 54, 73, 74].

Given the frequency response requirements, several types of filter transfer function schemes can be realised, like Chebyshev, Butterworth or Elliptical ones. Chebyshev is typically chosen due to its out-of-band rejection performance. The first step in the design procedure

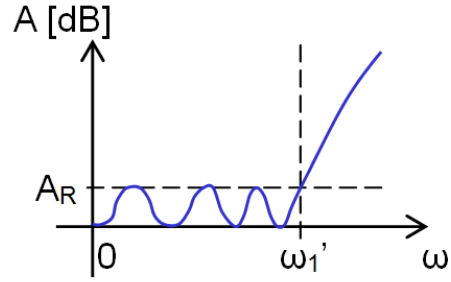


Figure 4.7: Attenuation function of a Chebyshev normalised lowpass filter. It can be then transformed to a bandpass filter by means of proper frequency variable substitutions.

is to determine the order n of an analogous lowpass prototype. The Chebyshev attenuation function is defined in (4.1):

$$A[dB](\omega') = \begin{cases} 10 \log \left[1 + \epsilon \cos^2 \left(n \arccos \frac{\omega'}{\omega'_1} \right) \right] & \omega' \leq \omega'_1 \\ 10 \log \left[1 + \epsilon \cosh^2 \left(n \cosh^{-1} \frac{\omega'}{\omega'_1} \right) \right] & \omega' > \omega'_1 \end{cases} \quad (4.1)$$

being ω'/ω'_1 the normalised angular frequency, with typically ω'_1 being the normalised angular cutoff frequency of the filter, and ϵ a coefficient related to the insertion loss ripple A_R (see Fig. 4.7), as defined in (4.2):

$$\epsilon = 10^{\frac{A_R[dB]}{10}} - 1 \quad (4.2)$$

In the case of bandpass filters, the insertion loss ripple A_R can be calculated from the return loss RL value:

$$A_R[dB] = -10 \log \left(1 - 10^{\frac{RL}{10}} \right) = -10 \log \left(1 - \frac{P_r}{P_{in}} \right) \quad (4.3)$$

being P_r and P_{in} the reflected and the incident power, respectively. By setting an additional rejection requirement at an angular frequency $\omega'_2 > \omega'_1$, (4.1) can be used to derive n . The lowest order that achieves the desired rejection is usually selected for simplicity.

Then, the coefficients g_i of the lumped-element prototype (see upper model of Fig. 4.6), composed of series inductors and lumped capacitors, can be derived [72]. First, some auxiliary coefficients are calculated:

$$\beta = \ln \left(\coth \frac{A_R[dB]}{17.37} \right) \quad (4.4)$$

$$\gamma = \sinh \frac{\beta}{2n} \quad (4.5)$$

$$a_i = \sin \frac{(2i-1)\pi}{2n} \quad (4.6)$$

$$b_i = \gamma^2 + \sin^2 \frac{i\pi}{n} \quad (4.7)$$

being i the i -th resonator (see the numeration of the resonators in the lower model of Fig. 4.6). The prototype coefficients are then obtained as:

$$g_i = \begin{cases} \frac{2a_1}{\gamma} & i = 1 \\ \frac{4a_{i-1}a_i}{b_{i-1}g_{i-1}} & i = 2, n \\ 1 & i = n + 1 \quad n \text{ odd} \\ \coth^2 \frac{\beta}{4} & i = n + 1 \quad n \text{ even} \end{cases} \quad (4.8)$$

Although the lumped-element model corresponds to a lowpass filter, it can be converted into a bandpass filter by means of appropriate frequency transformations. In the same process, the circuit model can be substituted by an equivalent prototype based on inverters and transmission lines, which has a closer behaviour to the one of the final waveguide filter than the circuit model. It is a single-mode model, since the coupling of higher order modes between the filter elements is neglected at this stage of the design process. The coupling coefficients $k_{i,i+1}$ represent the fraction of energy transmitted between adjacent resonators. They can be derived from the lumped-element model coefficients [53]:

$$k_{i,i+1} = 1/\sqrt{g_i g_{i+1}} \quad (4.9)$$

The inverters, which will later become irises, are characterised by the inverter coefficients $K_{i,i+1}$ (valid for narrow-band filters) [53]:

$$K_{i,i+1} = \frac{Nk_{i,i+1}}{1 - (Nk_{i,i+1})^2} \quad (4.10)$$

where N is defined as follows [53]:

$$N = Z_C \cdot \pi \frac{\lambda_{G1} - \lambda_{G2}}{\lambda_{G1} + \lambda_{G2}} \quad (4.11)$$

where Z_C is the characteristic impedance of a waveguide (see (2.15) in Chapter 2.1.4) and $\lambda_{G1}, \lambda_{G2}$ are the guided-wavelength limits corresponding to f_1, f_2 in Fig. 4.2.

In a final step, the inverters are modelled by inductive irises, and the transmission lines by means of half-wavelength resonators. The theoretical value of the S_{21} parameters of the irises can be derived from the inverter coefficients:

$$|S_{21}|_{i,i+1} = \frac{2Z_C}{K_{i,i+1} + Z_C^2/K_{i,i+1}} \quad (4.12)$$

An EM-analysis tool like FEST^{3D} can be used to iteratively search the width of each iris a_{iris} , such that it has a transmission coefficient at f_0 equal to the S_{21} -value calculated with (4.12). The length of the irises l_{iris} is fixed by the designer in the filter specification, and is kept constant for all irises in the structure. Here, for the first time it has to be taken into account whether the waveguide topology of the filter is rectangular or wedge-shaped.

A half-wavelength resonator has initially the following length:

$$l_{\text{half}} = \lambda_G/2 \quad (4.13)$$

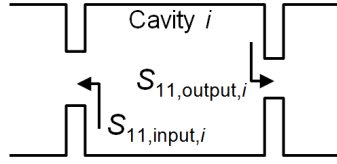


Figure 4.8: Reflection coefficients of the input and output irises of a resonator.

where λ_G is the guided wavelength at the operating frequency (in this case the centre frequency $f_0 = 9.5$ GHz), with the expression (4.14):

$$\lambda_G = \frac{\lambda_0}{\sqrt{1 - \left(\frac{\lambda_0}{\lambda_C}\right)^2}} \quad (4.14)$$

In (4.14), $\lambda_0 = c/f_0$ is the free-space wavelength at f_0 , c being the speed of light in vacuum. $\lambda_C = 2a$ is the cutoff wavelength of the fundamental mode (TE_{10}) of a rectangular waveguide of width a . However, the irises do not behave as ideal inverters, which means that an additional adjustment is required to retrieve a proper filter response.

The information to do this is extracted from the simulated phase at f_0 of the reflection coefficient S_{11} of the input and output irises of each resonator (see example in Fig. 4.8). The values of these phases are usually around, but not exactly equal π (which would be the nominal value for an inverter). The compensation is implemented by modifying the lengths l_i of the adjacent resonators, as indicated next:

$$l_i = \frac{\lambda_G}{4\pi} (\angle S_{11,input,i} + \angle S_{11,output,i}) \quad (4.15)$$

where $\angle S_{11,input,i}$, $\angle S_{11,output,i}$ correspond to the phases of the S_{11} parameter of the input and output irises, respectively, of the i -th resonator.

The design algorithm generates symmetric structures: i.e. the dimensions of the resonator with index i is equal to the one with index $n - i + 1$, and the dimensions of the iris i is equal to the one with index $n - i$. This method can be easily applied to rectangular waveguide filters, since it is already implemented in FEST^{3D}. However, new software modules had to be developed in order to calculate the S-parameters of rectangular-to-wedge and wedge-to-wedge waveguide transitions based on the BI-RME method (see Chapter 2.1 and [56]).

Applying the described procedure, a wedge-shaped filter was designed at ESA-ESTEC (see the right-hand side of Fig. 4.9). The obtained dimensions for the wedge-shaped band-pass filter are summarised in Table 4.2. Considering the mentioned filter symmetry, only the dimensions of half of the structure are listed.

The dimensions of the equivalent rectangular waveguide filter are also included in Table 4.3.

Table 4.2: Dimensions of the wedge-shaped bandpass filter.

WG	a [mm]	b [mm]	l [mm]
Input	22.860	10.160	10.000
Iris 1	13.038	h_2	h_1
Cavity 1	22.860	7.800	0.200
Iris 2	8.086	5.344	2.656
Cavity 2	22.860	7.800	0.200
Iris 3	7.423	5.234	2.766

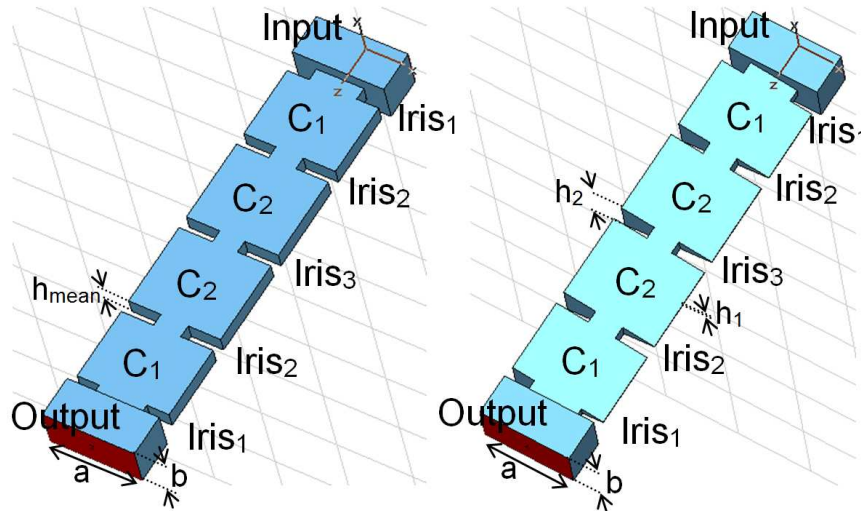


Figure 4.9: 3-D view of a standard inductive filter (left), and a filter with the novel topology based on wedge-shaped waveguides (right).

Table 4.3: Dimensions of the rectangular bandpass filter.

WG	a [mm]	b [mm]	l [mm]
Input	22.860	10.160	10.000
Iris 1	11.830	4.000	3.000
Cavity 1	22.860	4.000	17.825
Iris 2	6.780	4.000	3.000
Cavity 2	22.860	4.000	20.470
Iris 3	6.220	4.000	3.000

4.1.5 Simulation Results

High-Frequency Structure Simulator (HFSS) [48] and FEST^{3D} [50] have been used to validate the two filter design solutions. The rectangular waveguide filter simulation (top plot of Fig. 4.10) shows that the design perfectly complies with the requirements. Both numerical simulation tools, HFSS and FEST^{3D}, offer very similar S-parameters. However, the required CPU time is one order of magnitude less for FEST^{3D}.

In the wedge-shaped filter simulation, in the bottom plot of Fig. 4.10, FEST^{3D} indicates a bandwidth 5% broader than the one for the rectangular filter. Due to the higher complexity of the wedge-shaped filter in comparison with the rectangular one, complete convergence of the results could not be reached with any of the considered tools within a reasonable time frame and considering the available computational capabilities. However, this discrepancy is still acceptable for the experiment purposes. Nevertheless, this slight increase has been taken into account for the multipactor threshold prediction in Chapter 4.4.2, since it is based on the FEST^{3D} EM-fields. Some differences can also be detected between the two simulation results in the location of the S_{11} poles, which is also caused by the mentioned convergence problem. In this case, the FEST^{3D} simulation effort is around 8 times faster than the one with HFSS. In Chapter 4.2.4, these simulation data will be validated with real measurements.

4.2 Hardware and S-parameters Measurement

4.2.1 Preparation of the Manufacturing Models

An assessment of the manufacturing tolerances required by these filters was performed with the help of FEST^{3D}. For a four pole bandpass filter with the required characteristics of this design, a value of $7.78 \mu\text{m}$ comes out as the dimension tolerance requested to guarantee around 20 dB of return loss. The maximum acceptable error could be of $10 \mu\text{m}$. Manufacturing methods like mechanical machining have a typical tolerance of $20 \mu\text{m}$ (left picture of Fig 4.11), which should be avoided in our design. Furthermore, rounded corners would appear in the waveguide cavities, and the milling tool would not be able to carve the narrow side-walls.

Therefore, electroerosion will be applied. In the electronic discharge machining (EDM) method, high-voltage is used to melt away the metal and build the waveguide structure. There are two types of electronic discharge machining: plunge EDM (centre picture of Fig 4.11) and wire EDM (right picture of Fig 4.11). Wire EDM uses a very thin wire, energised with high voltage, that travels from one spool to another. The wire is put in contact with the part being machined to make a linear cut by blasting away material. The part being machined is typically held stationary, while the two spool feeds are moved to steer the saw. This allows to machine more complex shapes, like cones or sharp corners. The part being machined is suspended in an oil solution, which is used to carry away and suspend the machining dust. Plunge EDM uses carbon elements, energised with high voltage, that are pushed into the

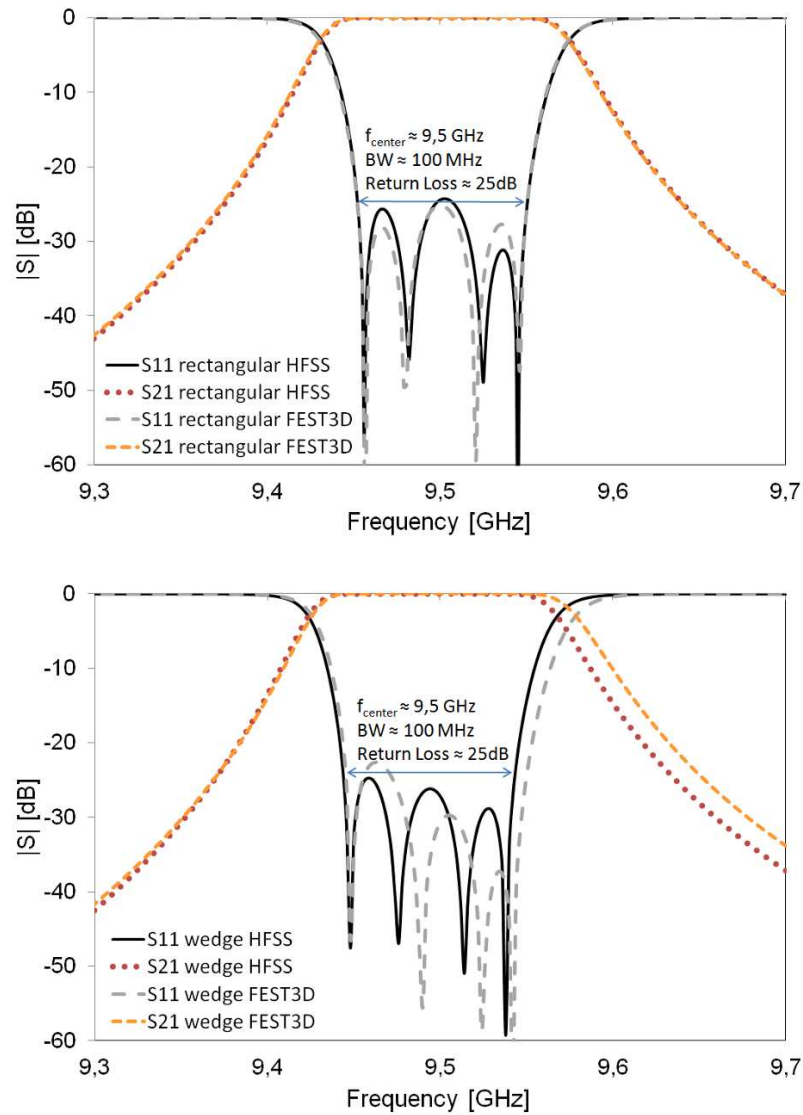


Figure 4.10: Simulated S-parameters of the rectangular (top) and the wedge-shaped (bottom) filter. Each plot includes the results obtained with HFSS and FET^{3D} for comparison.

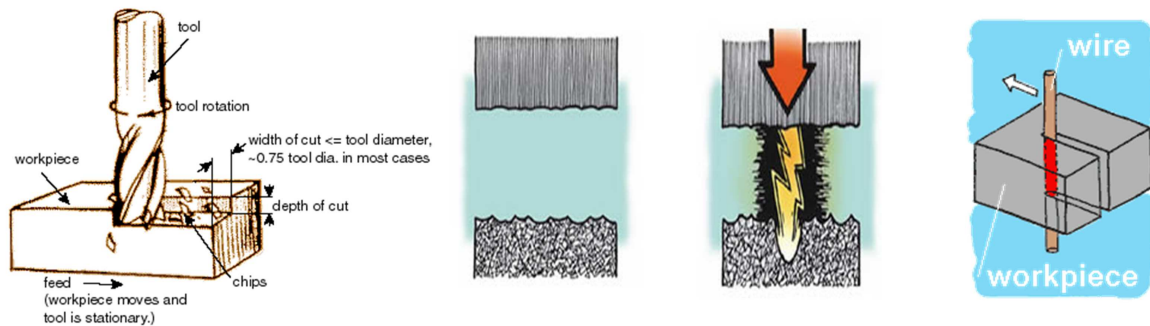


Figure 4.11: Examples of waveguide filter manufacturing processes. Milling (left), plunge EDM (centre) and wire EDM (right).

part being machined to blast away unwanted material. The plunger can be a complex shape and can be moved in x -, y - and z -direction, as well as rotated, enabling even more complex shapes than wire EDM. The typical tolerance of electroerosion is around $5 \mu\text{m}$, which may give us an accurate filter responses quite close to the simulation results. Together with the silver plating, the manufacturer guarantees a tolerance of $10 \mu\text{m}$.

Another important point is the material used for manufacturing the filter. In order to remain as close as possible to the original rectangular waveguide design, the material of the filter should be aluminium, and it should have a silver plating of around $10 \mu\text{m}$ thickness in order to ensure the correct electrical behaviour of the structure. This has also to be taken into account from a multipactor point of view, since the silver has its own characteristic Secondary Emission Yield (SEY). To be able to compare the performance of both filters properly, and to prove the validity of the measurements, the same material should be used for both cases.

According to the synthesised filter dimensions, technical drawings were generated for both structures, as can be seen in Fig 4.12 and Fig. 4.13.

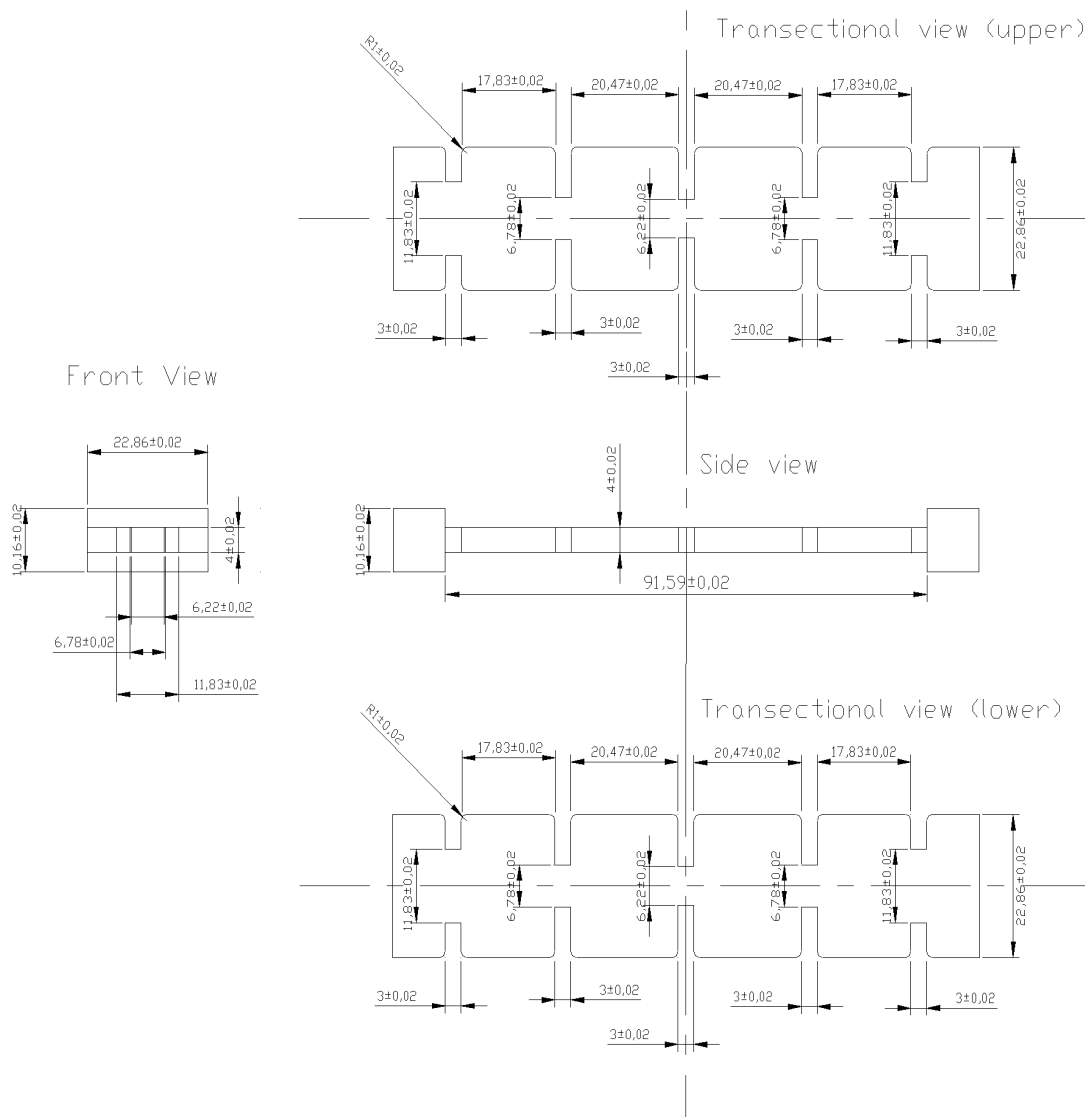


Figure 4.12: Autocad model of the rectangular bandpass filter dimensions.

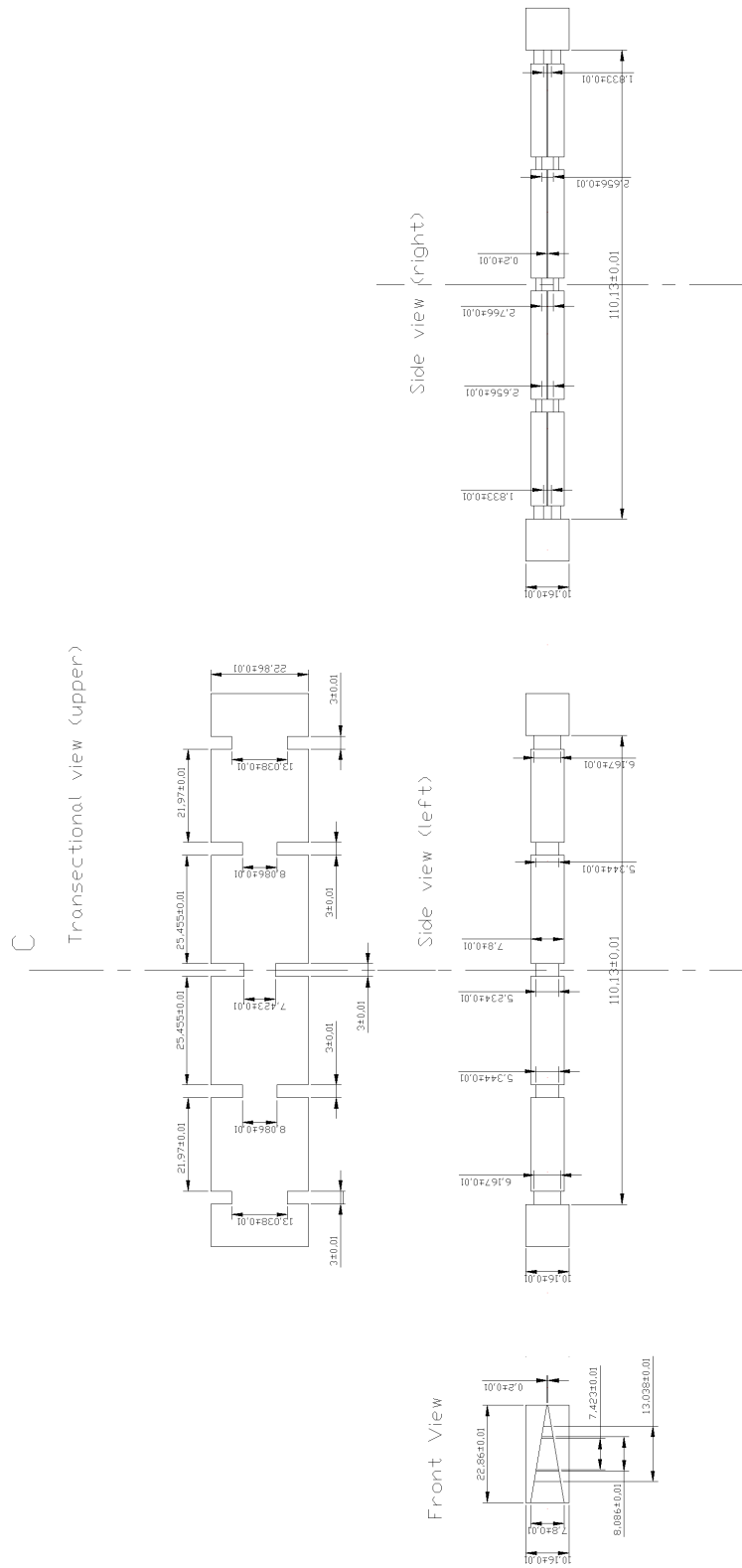


Figure 4.13: Autocad model of the wedge-shaped bandpass filter dimensions.

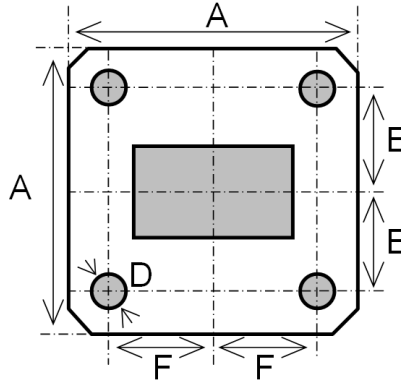


Figure 4.14: Standard rectangular waveguide flange for the input and output interfaces.

Apart from the inner dimensions of the filters, the hardware design needs to specify the full geometry of all hardware pieces, including thickness of the metallic walls, venting holes, junction planes, number and position of screws, etc.

A main element is the input and output interface, which is a standard WR90 waveguide flange. The shape and dimensions of the flange are defined in Fig. 4.14 and Table 4.4.

Another important part of the preparation of the manufacturing model is the venting analysis. The venting holes are cylindrical tubes drilled in the filter hardware walls to allow the transfer of air between the exterior and the hollow part of the waveguide filter during the outgassing process. The calculation of the venting holes required by this device was done with the ECSS Multipactor Tool [51] (see Appendix C.1 and Table 4.5). In total, 16 venting holes are required to outgas the filter hardware in the vacuum chamber within 18 hours (in practice, usually around 24 hours are invested in this process).

4.2.2 Manufactured Bandpass Filters

The rectangular filter, which already existed when starting this investigation, was manufactured with a milling machine procedure in two identical symmetric vertical halves by Tesat-Spacecom, Germany. This procedure offers dimension accuracies of $20\ \mu\text{m}$. The left photo

Table 4.4: Dimensions of a WR90 standard flange.

Dimension	Length [mm]
A	41.400
E	16.260
F	15.490
Hole diameter	4.255

Table 4.5: Input parameters and outputs of the venting analysis of the bandpass filters.

Design parameter	Value
Area inner cavities	76.33 cm ²
Volume inner cavities	13.914 ml
Length venting hole	1 mm
Diameter venting hole	9 mm
Required amount venting holes	16

of Fig. 4.15 shows a front view of the input interface. On the right-hand side of Fig. 4.15, the whole rectangular waveguide filter device can be seen, together with a reference coin in order to appreciate the real size. The junction plane between the halves was set in the vertical symmetry plane (see left-hand side of Fig. 4.15). Since the height of the filter is constant (except for the input and output waveguides), this junction plane has almost no jumps in the metallic contact surface, which is convenient for the proper electric contact and performance of the filter.

A different approach was adopted for the wedge-shaped filter, which was manufactured by Alcatel Espacio (now Thales Alenia Espacio), Spain. Fig. 4.16 includes a front and a general photo of this filter. Due to its unconventional shape, electroforming was chosen as manufacturing method. This technique improves the accuracy of milling (10 μm), since its electrodes shape the metal through electrical discharges, achieving a finer precision than a milling needle with a finite curvature radius. Its drawback is its related high cost. However, a way was found to almost reduce to by a half the manufacturing cost, namely to apply the electroforming to only one of both filter pieces. This can be done by setting the junction plane on the upper inclined wall of the filter (see left-hand side of Fig. 4.16). Hence, one of the hardware pieces is merely a flat lid, whereas the other one contains the cavities and irises of the designed filter. Fig. 4.17, Fig. 4.18 and Fig. 4.19 show more detailed photos of the interior of the wedge-shaped filter, in order to appreciate its peculiar geometry.

Both filters are silver plated with a similar material, and have a total length of around 100 mm, without considering the input and output standard rectangular waveguides.

4.2.3 Contact Problems and Workaround

The first measurements of the S-parameters of the wedge-shaped filter offered disappointing results (see Fig. 4.20), with very few resemblance with the specified and simulated frequency response. After verifying the faithful implementation of the designed dimensions in the metrology laboratory, the possibility of having a contact problem between the filter parts became the most plausible explanation. The most common approach when facing such a problem in waveguide filters is to use a conducting foil in the junction plane of the filter (namely the contact surface of the lid piece in Fig. 4.16) to improve the electrical contact in potential gaps caused by a mechanical inaccuracy. In this case, the material of the foil

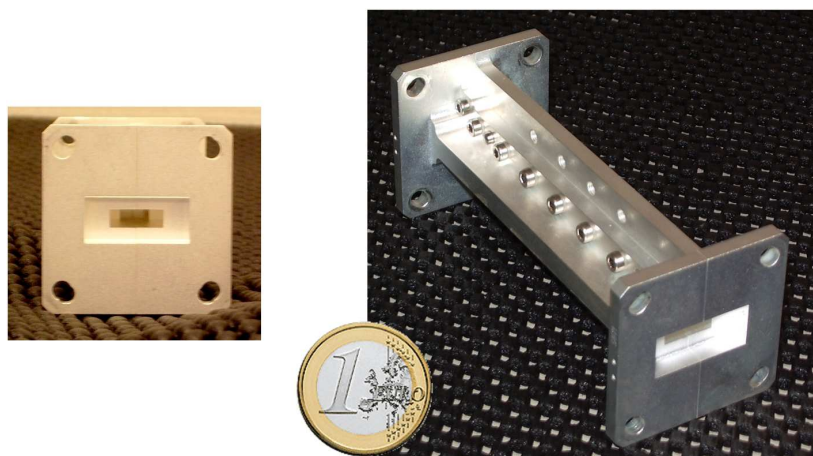


Figure 4.15: Photo of the rectangular waveguide bandpass filter. Front view (left) and overall view (right). Manufactured by Tesat-Spacecom, Germany.

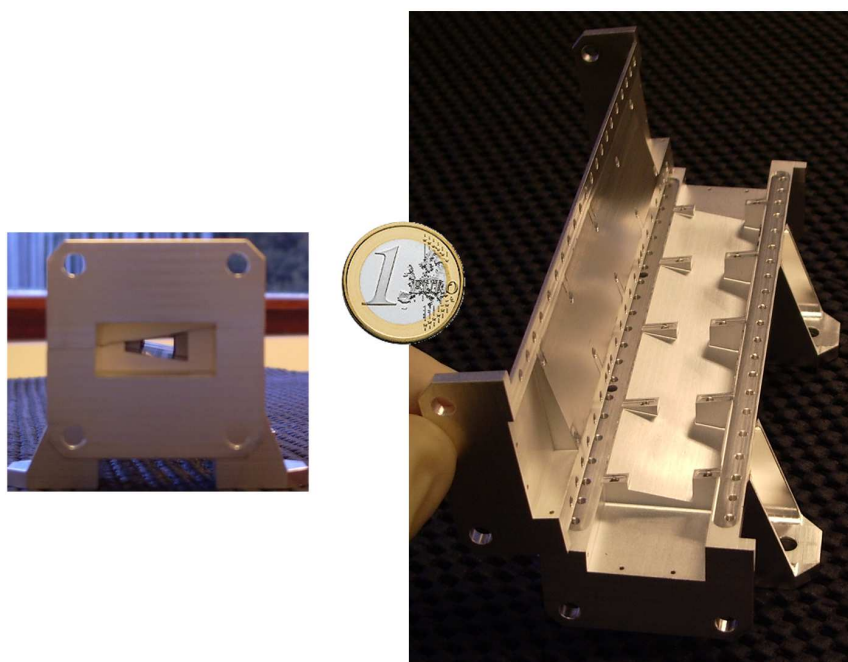


Figure 4.16: Photo of the wedge-shaped waveguide bandpass filter. Front view (left) and inner view of cavities and irises (right). Manufactured by Alcatel Espacio (now Thales Alenia Espacio), Spain.

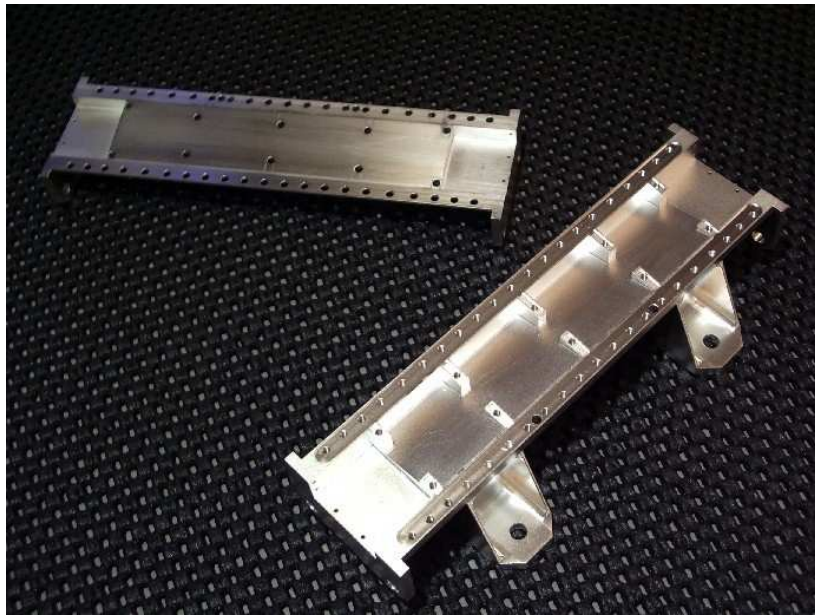


Figure 4.17: Photo of the inner part of the manufactured wedge-shaped filter. Lid has been removed to better visualise the structure.

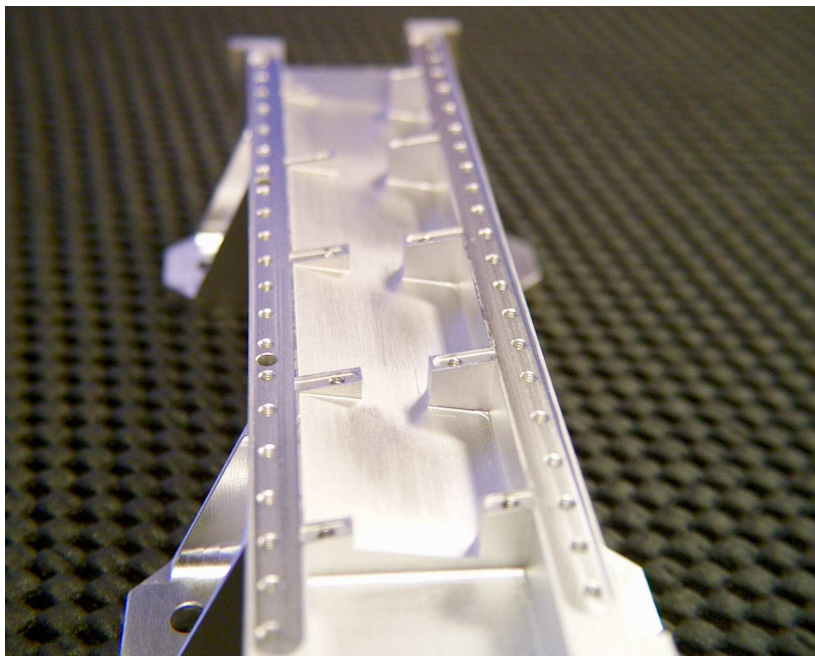


Figure 4.18: Photo of the inner part of the manufactured wedge-shaped filter. Lid has been removed to better visualise the structure.

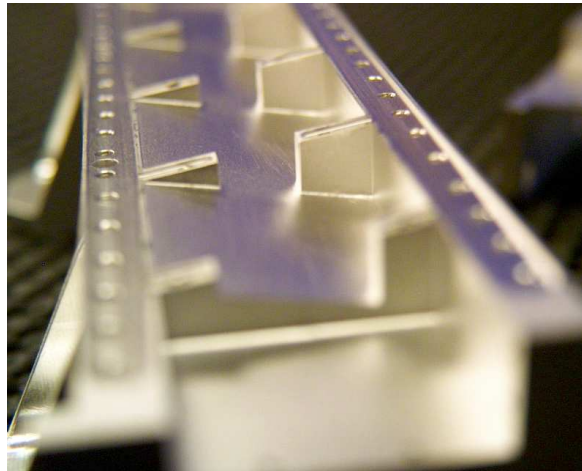


Figure 4.19: Photo with a close zoom on the wedge-shaped cavities of the manufactured filter.

was an alloy composed of indium (60%) and lead (40%). Its melting point is at 180°C , and it has a thickness of $50\ \mu\text{m}$. The softness of this foil allows the metal to fill up potential physical gaps when screwing the filter back together, although a slight modification in the height of the cavities cannot be avoided. In fact, the use of the foil allowed recovering a filter response that was comparable with the expected one. After several tries, we could narrow down the origin of the bad contact to the location where the irises (except for the central one) touch the lid corresponding to the upper broadside wall of the wedge-shaped filter (see Fig. 4.21). In this way, the number and area of the indium-foil strips could be minimised, without unnecessarily invading the filter cavities (see pictures taken with an optical-fibre camera of the foils solving the lack of electrical contact in Fig. 4.22).

Since the filter itself had to be manipulated by introducing an external metallic material to solve the contact problem, it was decided to test the thermal stability of the corrected frequency response before entering in the multipactor testing phase. The thermal stability can be checked in a thermal cycling sequence in the thermal chamber, as described in Appendix C.1. The results of the wedge-shaped filter after and before the thermal cycle have been compared in Fig. 4.23, showing very similar results. This plot also includes the frequency response measured before correcting the contact problem, which reflects the enormous sensibility to mechanical misalignments of the electrical response of the device.

4.2.4 Comparison Between Measured and Simulated Filter Responses

Once the contact problems have been solved, the measured S-parameters of both filters are compared with the expected theoretical performance in Fig. 4.24. In the rectangular-filter case (top of Fig. 4.24), electromagnetic simulation and measurement match well, with the exception of the return loss, which is around $-19\ \text{dB}$ instead of $-25\ \text{dB}$. This difference is quite normal when transforming an ideal design into real hardware, considering the manu-

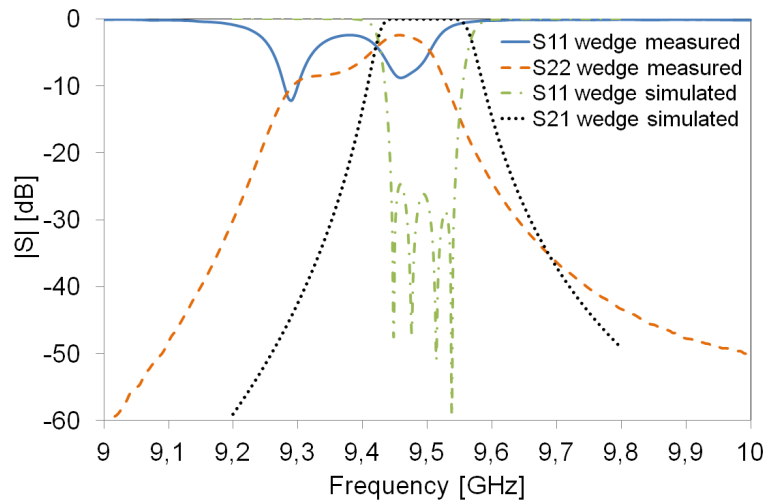


Figure 4.20: Comparison between the measured S-parameters of the wedge-shaped filter with electrical contact problems, and the expected simulated results.

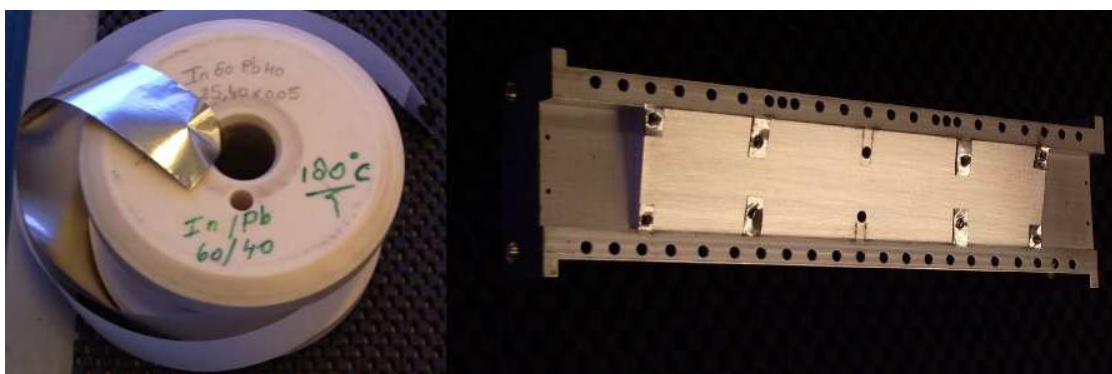


Figure 4.21: Roll of indium foil (left) and indium strips placed on the contact surface between the top filter lid and the filter iris walls (right).

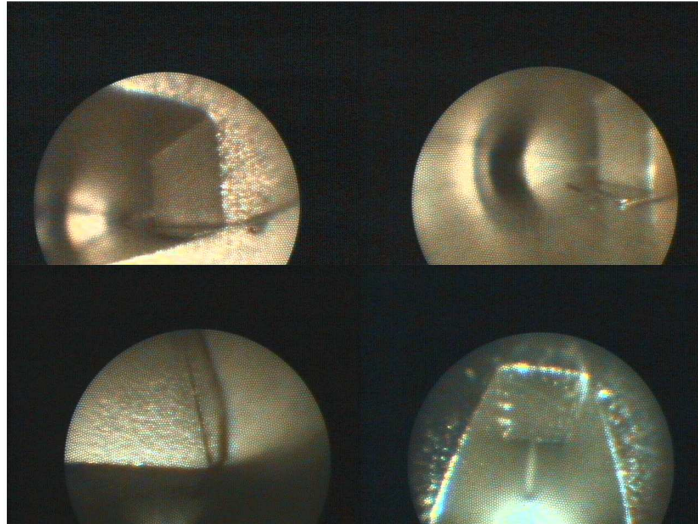


Figure 4.22: Check of the correct placement of the indium foil contact patches to improve the filter conductivity in the junction plane of the tow filter parts. Pictures were taken with an optical-fibre camera, introduced inside the device through the holes of the waveguide filter.

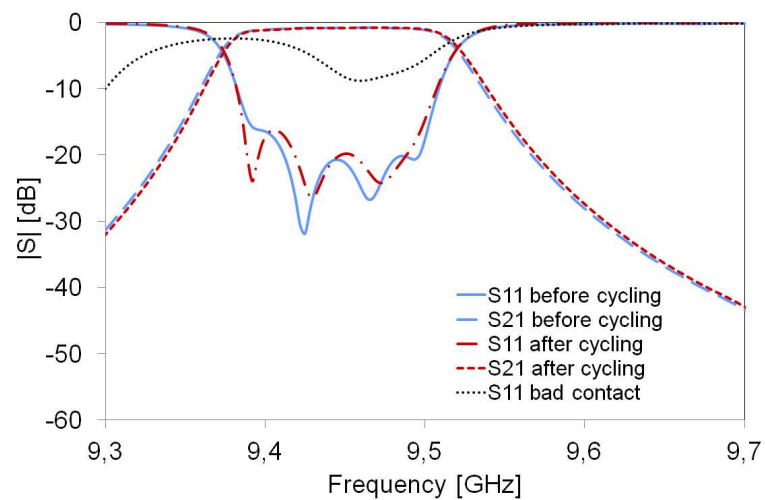


Figure 4.23: Comparison between the S-parameters of the wedge-shaped filter with and without contact problems. Once solved the connection problem, the S-parameters before and after the thermal cycling process can be compared.

facturing tolerances.

The measured S-parameter curves of the wedge-shaped filter show a small frequency shift of 50 MHz towards lower frequencies (bottom of Fig. 4.24), and have a similar bandwidth and rejection slope to the original design. This is confirmed by a full-wave re-simulation of the design (grey-dashed and yellow-long-dashed curves in the bottom plot of Fig. 4.24), considering a constant increase of 50 μm in the heights of the filter cavities and irises. The measurements (blue-solid and purple-dotted curves in the bottom plot of Fig. 4.24) also confirm this tendency. To account for the frequency shift of the wedge-shaped filter with contact foils, the multipactor test is accordingly performed at 9.45 GHz, and not at 9.5 GHz, as it was first planned. Since the indium strips are located in a non-critical region, the filter was accepted for testing. Naturally, this slight frequency discrepancy has to be kept in mind when interpreting the comparison of the multipactor breakdown level with the one of the rectangular filter.

4.2.5 Out-of-band Frequency Response

Another interesting aspect, also confirmed by simulations, is pointed out by the S-parameters measurements. Although both filters have a comparable frequency response around the centre frequency of 9.5 GHz, this is not the case for higher frequencies (> 11 GHz), as demonstrated by the broadband response measurement shown in Fig. 4.25. The filter frequency repetition appears much closer to the pass-band in the wedge-shaped case than in the rectangular case. This can be easily explained considering the modal behaviour of a waveguide resonator [75], expressed as follows:

$$k_{\text{res},l}^2 = k_{\text{C,waveguide}}^2 + \left(\frac{l\pi}{d}\right)^2 \quad (4.16)$$

where $k_{\text{res},l}$ is the l -th order resonant wavenumber, l being an integer, $k_{\text{C,waveguide}}$ is the cutoff wavenumber of the fundamental mode of the filter waveguide (rectangular or wedge-shaped), and $d = \lambda_{\text{G}}/2$ is the resonator length, as introduced in Chapter 4.1.4.

It is simple to obtain the cutoff wavenumber of the rectangular waveguide:

$$k_{\text{C,TE}_{10,\text{rect}}} = \pi/a = 137.428 \text{ rad/m} \quad (4.17)$$

The BI-RME method provides the value for the wedge-shaped waveguide, namely $k_{\text{C},1,\text{wedge}} = 162.9$ rad/m. The consequence is that each of the two filters has different resonator lengths, in order to match the first order resonant wavenumber: $d_{\text{rect}} = 21.806$ mm and $d_{\text{wedge}} = 27.442$ mm. Thereafter, if the second order mode of the resonators ($l = 2$) is considered, which will determine the first filter repetition response, (4.16) provides the following wavenumbers: $k_{\text{res},2,\text{rect}} = 319.232$ rad/m and $k_{\text{res},2,\text{wedge}} = 280.997$ rad/m. The corresponding frequencies are $f_{\text{res},2,\text{rect}} = 15.232$ GHz and $f_{\text{res},2,\text{wedge}} = 13.407$ GHz, which agrees very well with the measured broadband curves of Fig. 4.25.

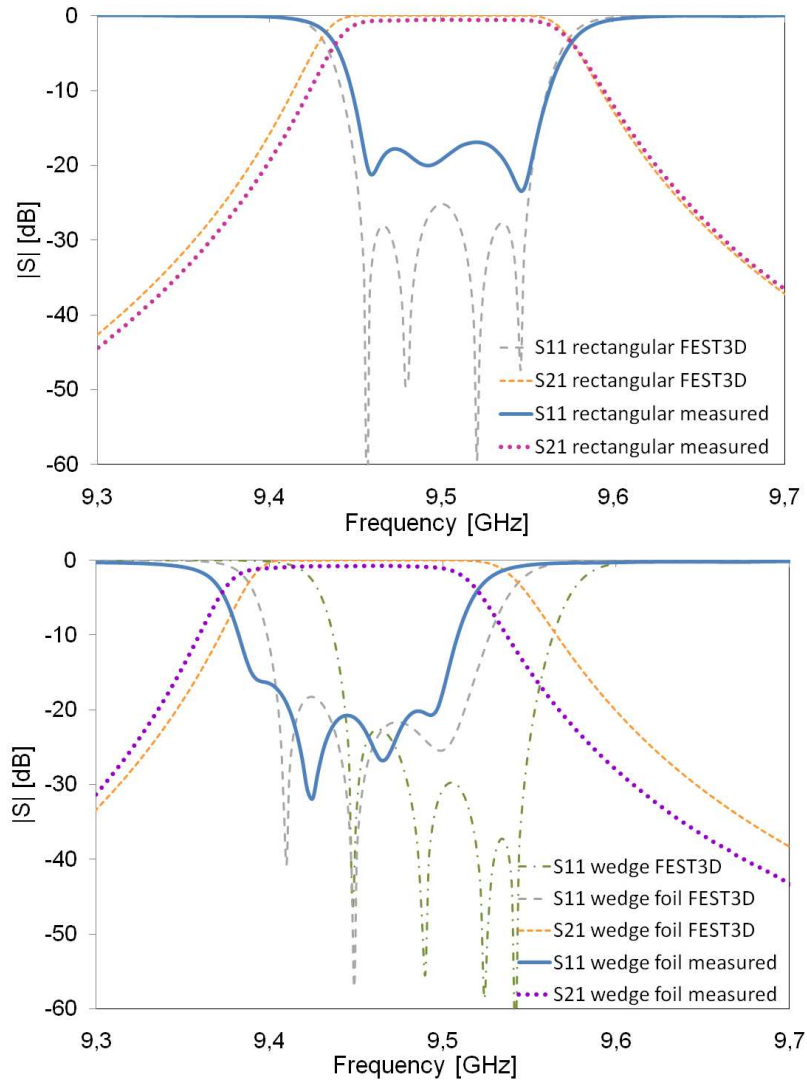


Figure 4.24: Measured S-parameters of the rectangular (top) and the wedge-shaped (bottom) waveguide filter. Each plot includes the simulated results of FEST^{3D} for comparison. In the bottom plot, the simulated response with (simplified approximation) and without (original) contact foils is presented.

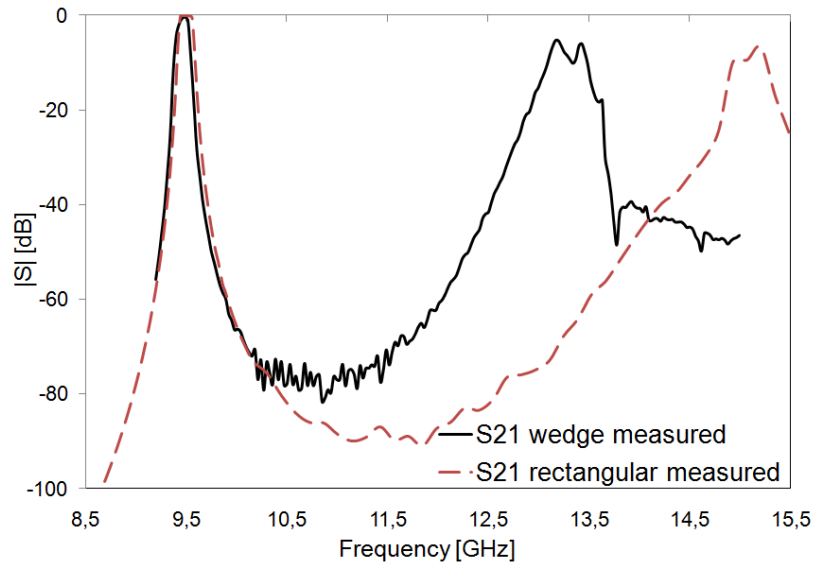


Figure 4.25: Broadband comparison of the S-parameters for the two considered filter structures. The effect of the higher-order modes of the resonator results in filter repetitions at different frequencies placed above the pass-band.

4.3 Multipactor Prediction

4.3.1 Extension of Multipactor Prediction Tool

The multipactor prediction algorithm presented in Chapter 3, based on the Monte-Carlo technique, has been extended within FESTA^{3D} to be able to cope with finite stepped structures. Since the tracking of the electron has already been implemented in 3-D, the only required adaptation of the software was in the EM-field calculation module and in the collision detection module. The calculation of the EM-fields of a filter has been implemented according to [59], and the procedure is the same for wedge-shaped and for rectangular waveguides. The collision detection module has now to take into account also the z -component of the electron location and the front walls in the discontinuities. The accumulation of the SEEC coefficient, the rebound speed and direction of the effective electrons, and the statistical analysis and interpretation of the results work identically as for the infinite waveguide case (see Chapter 3.2).

Concerning the optimal launch position of the effective electrons in the simulation, the voltage maxima must be first identified. For both the rectangular and the wedge-shaped waveguide bandpass filters, the electric field has been simulated and plotted in Fig. 4.26. The maxima of the electric field appear in the mid cross-sectional planes of the two centre cavities (i.e. the second and the third ones considering lossless conductors). In case of the wedge-shaped filter, within this plane perpendicular to the propagation direction (e.g. the centre of the second resonator), the trapped trajectory is then identified as explained in Chapter 3.2.4 for single infinite waveguides. For the rectangular filter, and considering

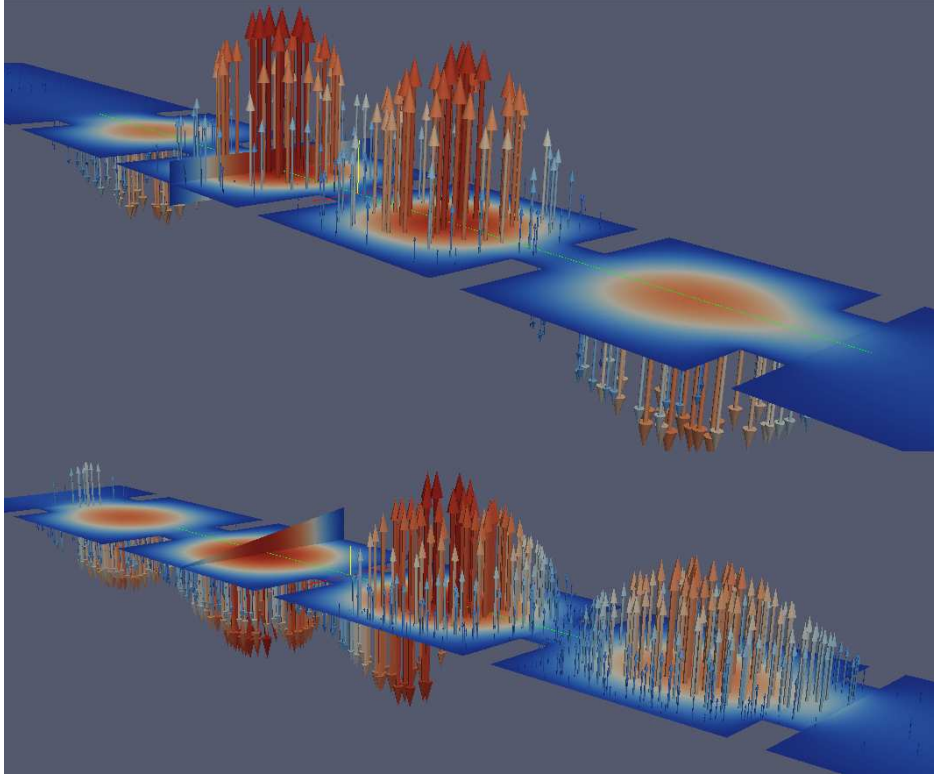


Figure 4.26: Magnitude of the electric field and field vectors on the horizontal plane for the rectangular (top) and the wedge-shaped waveguide bandpass filter (bottom). The maximum values of the fields concentrate in the second and third resonators.

the same cut perpendicular to the propagation direction, the geometrical centre of the cross section is the ideal launch position.

The probability of generation of secondary electrons is governed by the characteristic SEY curve of each wall material, and depends on the kinetics of the impact, as explained in Chapter 3.1.1. The two manufactured filters have silver-coated walls, and their SEEC can be fitted according to (3.8), but with $\delta_{\text{start}} = 0.5$. The rest of the parameters of this model have been set as indicated in Table 4.6. The rest of simulation parameters are derived in the same as the ones used in the prediction examples of Chapter 3.

4.3.2 Traditional Multipactor Prediction Tools

For comparison purposes, the input RF power threshold values of the filters have been also predicted with a tool based on the traditional parallel-plate model [3, 11, 14], such as the ECSS Multipactor Tool [51]. The strategy consists of calculating the voltage values over the cross section at the centre of the second resonator of the device (see Fig. 4.26). This is done for the fundamental mode at 1 W and at the centre frequency 9.5 GHz. For the rectangular waveguide filter, the maximum voltage from this curve is used to derive the RF voltage multipactor threshold. In the wedge-shaped filter, we can apply our voltage definition along

Table 4.6: Values of the characteristic SEY parameters for silver.

Parameter	Variable	Value
Starting SEEC	δ_{start}	0.5
Maximum SEEC normal impact	$\delta_{\text{max}}(0)$	2.22
Fitting constant	r	1.125
Fitting constant	s	0.35
Fitting constant	$k_{\delta} = k_{\text{W}}$	1
Reference energy	$W_0 [eV]$	16.3993
Energy at $\delta_{\text{max}}(0)$	$W_{\text{max}}(0) [eV]$	165
Fitting constant	κ_1	0.56
Fitting constant	κ_2	0.25

wedge arcs (see (3.41) in Chapter 3.2.4). To analogously derive the wedge-shaped filter RF voltage multipactor threshold, the voltage values in the trapped trajectory region have to be used as reference. These are not the positions where the curve is maximum, unlike in the rectangular case. Although ECSS Multipactor Tool is conceived for parallel-plate geometries, we introduce the voltage values as if it would be from a parallel-plate geometry with a gap of the same length as a given trajectory arc. The results of the line integrals are shown in Fig. 4.27 together with corresponding ones of the rectangular case. The maximum of the electric field in the rectangular filter (left-hand side of Fig. 4.27) lies exactly in the centre vertical line of this cross section: $|E|(x = 0 \text{ mm}) = 314.4 \text{ V/cm}$ and $V(x = 0 \text{ mm}) = 125.7 \text{ V}$. The results for the wedge-shaped filter, on the right-hand side, indicate different maximum positions for the electric field and the voltage, as already observed in Chapter 3.4.1, which determines the difference between the multipactor thresholds of both filters. The maximum electric field is located at $x = -0.7 \text{ mm}$ (closer to the smaller side-wall), whereas the arc with maximum voltage crosses the x axis at $x = 2.8 \text{ mm}$. The values of the maxima are: $|E|(x = -0.7 \text{ mm}) = 284 \text{ V/cm}$ and $V(x = 2.8 \text{ mm}) = 124.6 \text{ V}$.

In order to determine which exact voltage value should be used for the multipactor prediction when applying traditional tools, the location of the trapped trajectory has to be estimated (this should correspond with the launch position of the effective electrons of our novel multipactor prediction tool). The limits of the trapped trajectory region for the wedge-shaped geometry of our filter are: from $x = -11 \text{ mm}$ to $x = -0.7 \text{ mm}$ (see right-hand side of Fig. 4.27). Considering that the voltage increases with x , the electrons for the multipactor simulation should be optimally launched close to the arc that crosses the x axis at $x = -0.7 \text{ mm}$. It has to be noted that the voltage inside the wedge-shaped filter is slightly smaller than in the rectangular filter due to the wider bandwidth shown by the S-parameters in Fig. 4.24. This has an effect on the multipactor threshold, as explained in the following subchapters.

According to the described approach, the matching voltage value within the trapped elec-

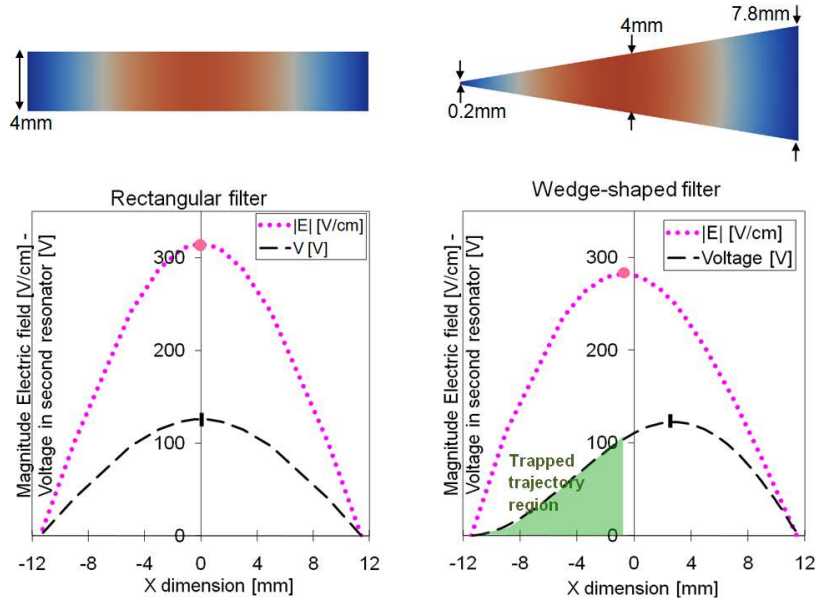


Figure 4.27: Magnitude of the electric field and voltage along the cross section (XY -plane) in the centre plane of the second cavity of the rectangular (left) and of the wedge-shaped (right) filter. The RF input power is 1 W.

tron trajectory regions can be extracted (the plot of Fig. 4.27 indicates 112 V), and then it can be introduced in the parallel-plate-based multipactor prediction tool. In the next subchapters, we verify the quantitative usefulness of this approach based on traditional prediction tools.

4.4 Measured Multipactor Thresholds

4.4.1 Multipactor Test Report

Once the different prediction tools have been presented, their accuracy has to be assessed by comparing their results with the measured thresholds of the real manufactured filters. Both filters were measured and tested under the same conditions and procedures (see details in [76]) in the Payload Systems Laboratory at ESA-ESTEC. First, the device under test (DUT) was placed in the vacuum chamber, close to a Strontium 90 β -emitting radioactive source, to ensure sufficient seeding electrons to initiate a multipactor breakdown. Two global (forward/reverse power nulling and 3rd harmonic) and two local (electron probe detector and photo detector) multipactor detection methods were used (see [3] and Appendix C.2). Then, the chamber was sealed and pumped for 24 hours for outgassing, until reaching a pressure lower than $5 \cdot 10^{-6}$ mbar. The RF source was configured in pulsed mode, with a 2% duty cycle and a pulse repetition frequency of 1 kHz. The multipactor test was started with an input power level of 350 W and the power was then increased in 20 W steps. The dwell time

Table 4.7: Multipactor threshold predictions and measurements.

Filter	Thresholds		
	ECSS MP Tool	FEST ^{3D}	Measured
Rectangular @ 9.5 GHz	447 W	650 W	690 W
Wedge-shaped foil @ 9.45 GHz	558 W	1300 W	850 W

at each power level was 10 min. Once multipaction was detected, the power was lowered back to the previous step. After the discharge has extinguished, the power is risen again, now in smaller steps of 10 W.

All predictions and test measurements have been performed at the centre frequencies of the filters. In the case of the rectangular filter, this frequency agrees with the 9.5 GHz of the original design. For the wedge-shaped waveguide, since the filter response is shifted due to the contact issue already mentioned in Chapter 4.2.3, the test and the prediction centre frequency are 9.45 GHz. Since the change in the geometry of the filter is minimal, its predicted threshold values are almost identical to the hypothetical ones of the original design at 9.5 GHz frequency.

4.4.2 Comparison Between Measurements and Predictions

All results are summarised in Table 4.7. The first column corresponds to the “parallel-plate” model-based predictions, and the second one to the results obtained with our technique (see Chapter 4.3.1), which has been integrated into the FEST^{3D} tool. The last column contains the measurement results.

Regarding the predicted thresholds of ECSS Multipactor Tool, an input power of 447 W has been obtained for the rectangular filter. In the wedge-shaped case, the same parallel-plate technique gives 558 W after introducing the trapped trajectory voltage value $V = 112$ V, corresponding to $x = -0.7$ mm (see Chapter 4.3.2 and the right-hand side plot of Fig. 4.27). Introducing the maximum voltage of $V = 124.6$ V here would result in a lower power threshold, that would be further apart from the measured one. On the other hand, the rectangular filter predictions with our software indicate a threshold around 650 W, which is very close to the measured threshold of 690 W. For the wedge-shaped filter, the threshold predicted by FEST^{3D} is 1300 W. The difference with regard to the measured value of 850 W is higher than for the rectangular filter case, but this is probably due to the materials used for the wedge-shaped case, including the silver plating, which might not be identical to the one used with the rectangular filter.

Another reason for this discrepancy is the fact that our hardware dimensions and experiment conditions (for both rectangular and wedge-shaped filters) result in relatively high order multipactor modes, which can affect the accuracy of the simulation model. Nevertheless, the measurements verify that wedge-shaped bandpass filters offer a better multipactor-free

power range than the rectangular ones, while keeping a similar electrical response. Hence, the improvement predicted in Chapter 2 for individual waveguides can also be translated to more complex devices. In order to interpret the contribution of the wedge-shaped geometry on this achievement correctly, the slightly different bandwidths between the filters leading to slightly different voltage values in the cavities, as mentioned in Chapter 4.2.4, have to be considered. The effect of the voltage difference on the multipactor thresholds was quantified (power factor of 0.983) to allow a one-to-one comparison of the measured thresholds of Table 4.7. Hence, based on the measurements, a final improvement factor between the rectangular and the wedge-shaped filter threshold of $850 \times 0.983/690 = 1.211 \Rightarrow 0.833$ dB is obtained, whereas the simulations show a potential improvement factor of $1300 \times 0.983/650 = 1.967 \Rightarrow 2.937$ dB.

4.5 Summary

4.5.1 Demonstration of Multipactor Resistance

Conventional bandpass filters are typical passive devices widely used at the output (high power) stage of satellite payloads. In cooperation with ESA-ESTEC, such a filter structure based on wedge-shaped cavities has been designed and manufactured. This is the first time that the potential benefit of wedge-shaped waveguides has been verified with a real hardware implementation and test. In this particular case, the wedge-shaped multipactor-free power range was improved from 690 W to 850 W (around 0.83 dB after quantifying the bandwidth difference) with respect to the rectangular waveguide case.

The designed filter structure shows, in addition, that complex microwave devices can be successfully manufactured with wedge-shaped technology. In order to predict the multipactor thresholds for these structures with a certain reliability, specific software tools have been developed. The measurements indicate a qualitative agreement with the simulations, and serve as a first verification step for the multipactor prediction algorithm developed for wedge-shaped waveguides (cf. Chapter 3) and included within FEST^{3D}.

4.5.2 Potential Design Improvements

This first experience with wedge-shaped waveguide technology has inspired several improvement ideas, with the goal of finding the optimal design strategy, as well as enhanced electrical and multipactor performances, and of supporting the search for future applications:

1. More multipactor threshold measurements are necessary to completely validate the accuracy of the wedge-shaped filter structure prediction tool.
2. The inclination angle $\alpha = 19^\circ$ between top and bottom plates improves the multipactor threshold, but it does not seem the optimal one. According to Chapter 3, higher inclination angles might still enhance the multipactor resistance.

3. The contact problem in the wedge-shaped filter was caused by an uneven contact surface (see Chapter 4.2.3). The filters should be manufactured in two symmetrical halves in order to have a completely flat contact plane. This would also reduce the manufacturing complexity and related costs.
4. Out-of-band response degradation: one of the initial design criteria of the wedge-shaped filter was to keep the same input, output and resonator waveguide width along the whole structure, in the same way as done with conventional rectangular waveguide inductive filters. But wedge-shaped waveguides have higher cutoff frequencies for the fundamental mode than a rectangular waveguide with the same width. Consequently, the difference in λ_C between the rectangular and the wedge-shaped waveguide distorts the location of the filter response repetitions (see Fig. 4.25). In order to have the same frequency response as the rectangular filter, both cutoff wavelengths should be substantially identical. A proposal to achieve this is to slightly modify the wedge-shape cross-sectional width until the same λ_C is reached.

These “lessons-learned” will help to develop optimal design guidelines for future multipactor-free wedge-shaped waveguide microwave devices. In the next chapter, we have tried to make use of them for obtaining an enhanced wedge-shaped waveguide filter.

Chapter 5

Optimum Design of Wedge-shaped Bandpass Filters for Improved Multipactor Resistance

5.1 Optimisation Studies

5.1.1 New Design Target

The previous chapter has shown a first implementation of a bandpass filter with inclined top and bottom walls, which shows an improved multipactor performance with respect to the equivalent rectangular one. However, a substantial enhancement of the multipactor behaviour can still be achieved by optimising the design procedure. In order to do so, several parametric analyses will be performed and modifications in the manufacturing process will be proposed.

Another bandpass frequency response has been selected here for implementing the upgraded wedge-shaped filter design strategy. It is a three-pole bandpass filter centred at 12 GHz (Ku-band) with 150 MHz bandwidth. In order to allow more degrees of freedom in the choice of the wedge-shaped geometry, this time both the rectangular and the wedge-shaped filters will be designed from scratch. Two copies of each design (the first with gold plating, the second in bare aluminium) will be manufactured at ESA-ESTEC, The Netherlands, having in this way full control of the whole hardware development chain. The rectangular waveguide filter to serve as a reference for the comparative study will be an equivalent quasi-inductive filter with the same electrical behaviour and Q factor as the wedge-shaped one. The four devices are tested in the Payload Systems Laboratory at ESTEC under space environment conditions, which is useful for increasing the maturity of this technology for a potential future application.

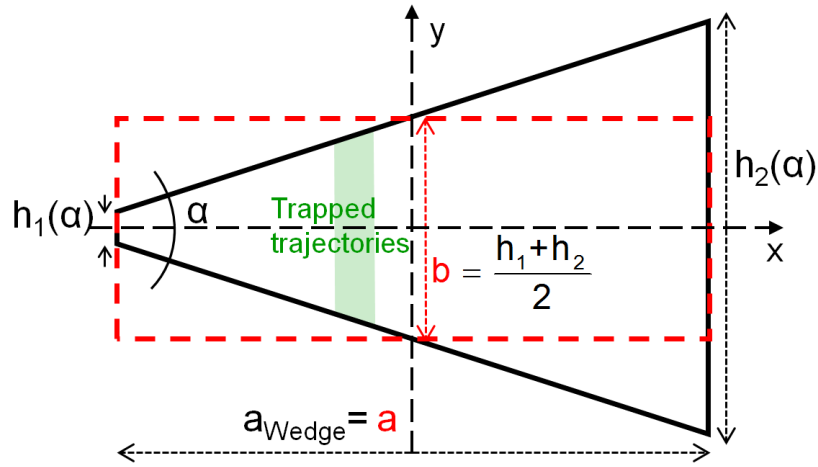


Figure 5.1: Cross-section view of a wedge-shaped (black-solid line) and a rectangular (red-dashed line) waveguide with the same area. The region shaded in green within the wedge-shaped geometry contains the multipactor-critical trapped electron trajectories.

5.1.2 Inclination Angle

The selection of the most suitable inclination angle (α) between the top and the bottom plates is an essential design criterion for the wedge-shaped filter. The cross sections of a wedge-shaped waveguide and of its equivalent rectangular waveguide are depicted in Fig. 5.1. If the width a_{Wedge} is kept constant and the average height is equal to the rectangular waveguide height b , the sizes of the side-walls directly depend on α .

Considering an operating frequency of 12 GHz, a reference rectangular waveguide with width $a = 19.05$ mm (WR75) and height $b = 6.26$ mm has been chosen. This particular height value is equal to the average height of the wedge-shaped waveguides applied in the filter design (described in Chapter 5.2), hence it appeared to be a better choice for comparison purposes in terms of multipactor breakdown than the standard WR75 height. Keeping the width constant and an equal cross-section area (i.e. the average height of each wedge-shaped waveguide is $b = 6.26$ mm), several waveguide cross sections with a sweep of α -values between 0° and 60° can be conceived, each one with the corresponding $h_1(\alpha)$ - and $h_2(\alpha)$ -values. Note that this is only possible up to $\alpha \approx 35^\circ$ for the given reference waveguide dimensions. A lower boundary $h_{1,\text{min}} \geq 0.2$ mm has been set due to manufacturing constraints. Once it is reached, higher α -values result in average heights larger than b and consequently larger cross-section areas. Hence, the inclinations over 35° are not exactly comparable with the rectangular case, but they are still included in the performed analysis. A sketch with the different cross sections that are considered is presented in Fig. 5.2.

In a first step, for each of the wedge-shaped cross sections, a region is identified within where free electrons can follow a resonant path between the top and bottom inclined walls. The necessary condition to enable such a resonant path is that the excited electromagnetic field generates a Miller force that exactly compensates the centrifugal effect experienced by

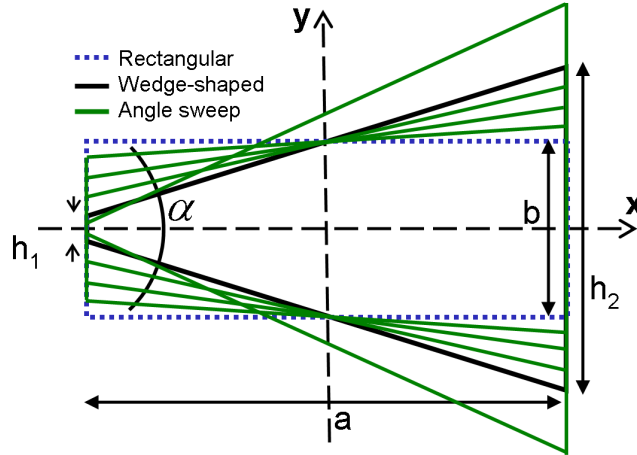


Figure 5.2: Schematic overview of the cross sections of different waveguides covering a sweep of different inclination angles. The width $a_{\text{Wedge}} = a$ is kept constant.

the accelerated free electrons (see [46] and Chapter 3.2.4). This can be identified as a disk section close to the centre of the wedge-shaped cross section (see green highlighted region in Fig. 5.1). Electrons launched from the top or the bottom walls of this region are likely to get trapped in the mentioned resonant trajectories, thus enabling the possibility of a sustained electron growth. The most sensitive location for multipactor discharge effects is the part of the green-highlighted area closer to the broader side-wall. Following this procedure, the voltage in the estimated critical radius has been plotted (dark-blue-solid curve) for all wedge-shaped waveguides considered in this study, as it can be seen in Fig. 5.3.

The boundaries of the trapped trajectory region (as indicated by the green rectangle in Fig. 5.1) are depicted in Fig. 5.3 as green-dashed curves, assigned to the right axis. The limits are always on the negative side of the x -axis, i.e. closer to the narrow side-wall (see Chapter 3.4). The green-dotted line in Fig. 5.3 presents the position chosen for the calculation of the voltage, where the maximum multipactor discharge is expected. The grey-shaded region shows the α -values for which the average height exceeds the value of b . The voltage curve shows a minimum value for $\alpha \approx 30^\circ$, which means that the trapped electrons of this wedge-shaped waveguide will experience the smallest voltage values of all simulated cases. Hence, it is expected that the wedge-shaped waveguide with this inclination angle is the most resistant to multipactor discharges. Consequently, an inclination of $\alpha = 30^\circ$ has been chosen for the optimal design of a multipactor resistant wedge-shaped waveguide bandpass filter.

5.1.3 Out-of-band Frequency Response

One of the optimisation goals is to improve the out-of-band response of the wedge-shaped filter, which showed some drawbacks with respect to the rectangular one in Chapter 4.2.5. In rectangular waveguides, a typical design criterion aims for minimal losses for a given operating frequency. This is the case when the rectangular cross section tends to be square,

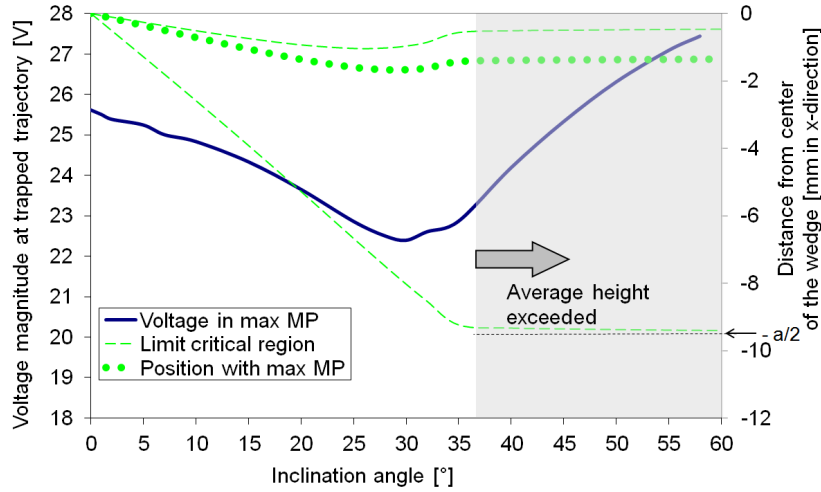


Figure 5.3: Voltage (for 1 W RF input power) in the critical multipactor radius for all the wedge-shaped waveguides considered in the inclination angle sweep: constant width $a_{\text{Wedge}} = a$ and, whenever possible, constant cross-section area. A reference rectangular waveguide with dimensions $a = 19.05$ mm and $b = 6.26$ mm has been selected. Operating frequency 12 GHz. Green curves are assigned to the right axis and represent the location of the trapped trajectories region.

i.e. $b/a \rightarrow 1$ (see Fig.. 2.3). At the same time, it is wished to have a broad monomode frequency range. The operating frequency is usually chosen slightly above the cutoff frequency of the fundamental mode. The difference between the operating frequency and the one of the second order mode determines the monomode bandwidth. As it can be seen in Fig. 2.3, for values of $b/a \leq 0.5$, the cutoff frequency of the second order mode TE_{20} keeps a constant value. If $b/a > 0.5$, the TE_{01} mode becomes the second order mode, and the monomode bandwidth systematically decreases with the b/a ratio. Therefore, the optimal size ratio is 0.5, since it offers the less possible losses without sacrificing monomode bandwidth.

A similar cutoff frequency analysis can be done for wedge-shaped waveguides, as we did in Chapter 2.2.3. The results are shown in Fig. 5.4 (magenta-solid and orange-dashed curves) versus the inclination angle, which are very similar to the ones of the third column of Table 2.4. As a reference, the $f_{\text{C}(1)\text{rect}}$ and $f_{\text{C}(2)\text{rect}}$ of the corresponding equivalent rectangular waveguide were also plotted (brown-dotted and green-dash-dotted curves).

There are relatively abrupt changes in the slopes of the curves: at $\alpha \approx 30^\circ$ for $f_{\text{C}(2)\text{wedge}}$, $\alpha \approx 50^\circ$ for $f_{\text{C}(2)\text{rect}}$ and $\alpha \approx 60^\circ$ for $f_{\text{C}(1)\text{wedge}}$, caused by changes in the mode order. For small inclination angles ($\alpha < 35^\circ$), the wedge-shaped waveguide fundamental mode has a TE_{10} -like electric field pattern, and also similar f_{C} values to those of the rectangular one. For $35^\circ < \alpha < 60^\circ$, the field patterns have a stronger distortion with respect to the TE_{10} , and the differences between $f_{\text{C}(1)\text{wedge}}$ and $f_{\text{C}(2)\text{wedge}}$ are gradually reduced to zero. Within the range of α -values of Fig. 5.4, and especially for $\alpha < 30^\circ$, it can be stated that the first two propagating modes of the wedge-shaped waveguide have a similar behaviour

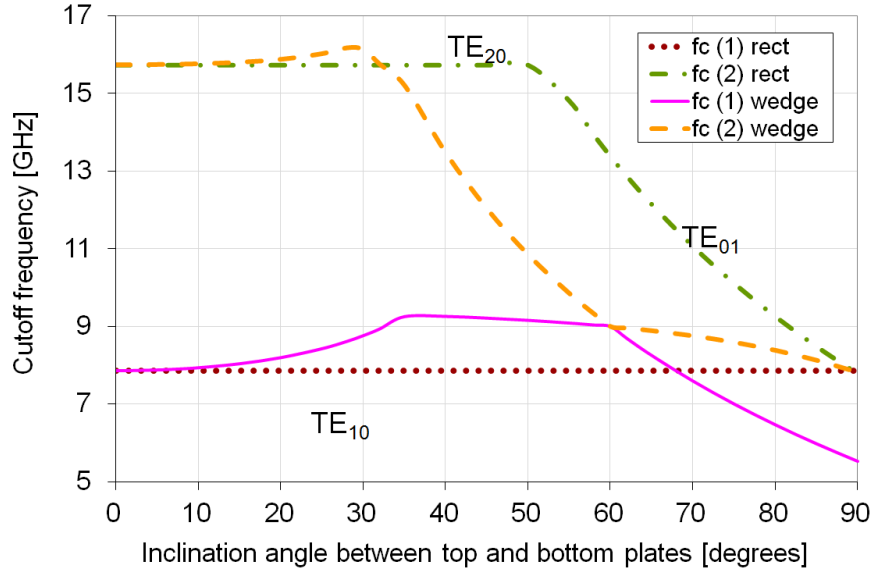


Figure 5.4: Cutoff frequencies of the first two propagating modes of a wedge-shaped waveguide versus the inclination angle: constant width $a_{\text{Wedge}} = a$ and, whenever possible, constant cross-section area. Values are compared to the ones of the reference rectangular waveguide with dimensions $a = 19.05$ mm and $b = 6.26$ mm (b remains constant up to $\approx 50^\circ$).

to the rectangular waveguide ones. However, the wedge-shaped cutoff frequency $f_C(1)$ is consistently higher than the rectangular one for the range of interest. This would have a negative effect on the design of the filter resonators, since it shifts the filter repetition band closer to the pass-band (cf. Chapter 4.2.5).

A solution to avoid this problem is to gradually adapt the value of the wedge-waveguide width (i.e. $a_{\text{Wedge}} \neq a$) in order to obtain an $f_C(1)$ -value equal to the one of the reference rectangular waveguide for each given α -case. The average height of the waveguide is still kept equal to the rectangular b . The considered set of cross sections that are considered in this analysis was shown for a similar example in the Fig. 3.17 of Chapter 3.4. Considering the current geometry, the different wedge-shaped geometries have been derived and its modal solutions are summarised in Fig. 5.5. The blue-solid line represents the required variation of the width with the inclination angle (assigned to the right-hand side axis). Its value is always higher than the width of the rectangular waveguide case ($\alpha = 0^\circ$), reaching a maximum value between 30° and 40° . For a constant average height, the fact of modifying the width means that the criterion of equal cross-section areas cannot be fulfilled anymore. Nevertheless, to keep a constant average height or gap has been chosen as the most important criterion for comparison in terms of high-power behaviour. In any case, the differences in the cross-section values keep always small, since the variation in the a_{Wedge} -values is less than 15%. For the particular analysis of Fig. 5.5, it must be noted that the maximum applicable angle is around 37° , since otherwise more than one mode would be able to propagate at the working frequency of 12 GHz for the chosen waveguide. However, the reduction of the monomode

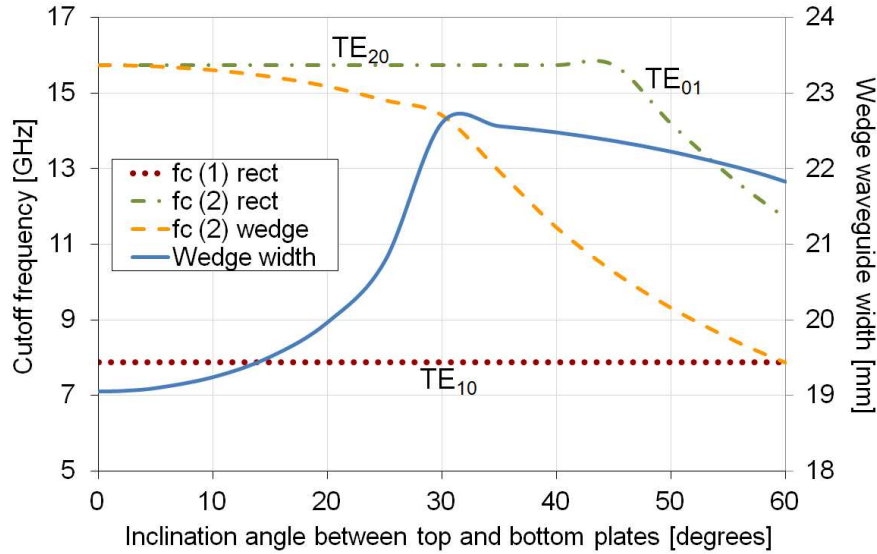


Figure 5.5: Cutoff frequencies of the first two propagating modes of a wedge-shaped waveguide inclination angle sweep: constant cutoff frequency $f_C = 7.869$ GHz and, whenever possible, constant average height. Values are compared to the ones of the reference rectangular waveguide with dimensions $a = 19.05$ mm and $b = 6.26$ mm. Blue-solid curve represents the values of a_{Wedge} .

bandwidth can be acceptable for $\alpha < 30^\circ$.

The analysis of the voltages in the electron trapped trajectories of Chapter 5.1.2 can be then repeated for the new approach of keeping a constant f_C , since it seems to be more convenient for wedge-shaped filters (see Fig. 5.6). Taking into account that both plots (Fig. 5.3 and Fig. 5.6) are represented with the same axes and scales, the main difference is that the voltage curve experiments a deeper minimum here. This is due to the fact that a_{Wedge} is gradually increased with α , thus enlarging the cross-section area and reducing the voltage magnitude for the same normalised input power. The most important conclusion is that the minimum still lies at 30° .

Combining the results from this and the previous subchapter, it can be concluded that $\alpha = 30^\circ$ is the most convenient angle for designing a wedge-shaped bandpass filter with an optimal multipactor behaviour, while keeping the electrical performance of the rectangular reference case.

5.1.4 Manufacturing Enhancements

Several refinements of the manufacturing process are proposed here in order to cope with the additional complexity of the wedge-shaped topology. Waveguide filters are usually manufactured in two halves, which are typically joined together with screws. The junction plane is the cut where the internal cavities of the filter make contact, which is essential for the correct electrical behaviour of the device. The pressure plane is the cut where the screws

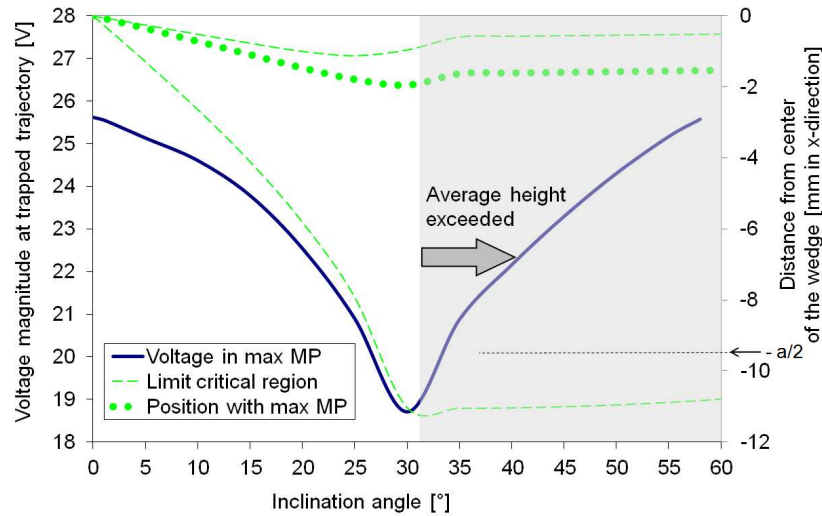


Figure 5.6: Voltage (for 1 W RF input power) in the critical multipactor radius for all the wedge-shaped waveguides considered in the inclination angle sweep: constant f_C and, whenever possible, constant average height. A reference rectangular waveguide with dimensions $a = 19.05$ mm and $b = 6.26$ mm has been selected. Operating frequency 12 GHz. Green curves are assigned to the right axis and represent the location of the trapped trajectories region.

that mechanically hold both halves together make contact. In rectangular waveguide filters, it is common that both junction and pressure plane are the same ones, so that increasing the pressure on the screws will directly translate in junction-plane pressure, avoiding potential electrical-contact problems. However, when manufacturing a wedge-shaped filter, an important aspect is the additional complexity of having non-parallel top and bottom walls, which are also not perpendicular to the vertical side-walls. The solution adopted in Chapter 4.1.2 managed to almost divide by two the manufacturing complexity, since only one of the halves had to be machined with high accuracy. However, it caused contact problems that disturbed the filter frequency response (see Fig. 4.20 in Chapter 4.2.3), since the junction plane was not the same as the pressure plane of the screws. Therefore, we adopted here an approach based on two completely symmetrical halves, leading to a unique junction- and screw-pressure plane, namely a horizontal cut trough the middle of the device. This plane is represented by the x -axis in Fig. 5.1 and is also shown in Fig. 5.7. Although the machining process has to be performed on two pieces, there is no substantial increase in terms of complexity, since both halves are completely identical.

Another improvement with respect to the approach followed in Chapter 4.1.2 is that the four filters, the rectangular and the wedge-shaped gold-plated ones and their respective copies in aluminium, have been manufactured in-house (ESA-ESTEC, The Netherlands) applying a common milling machining process. Hence, the same materials have been used, which ensures a fair comparison procedure. For the wedge-shaped filter, a relatively coarse mill with 1.5 mm curvature radius had to be used (instead of a sharp end one) due to the

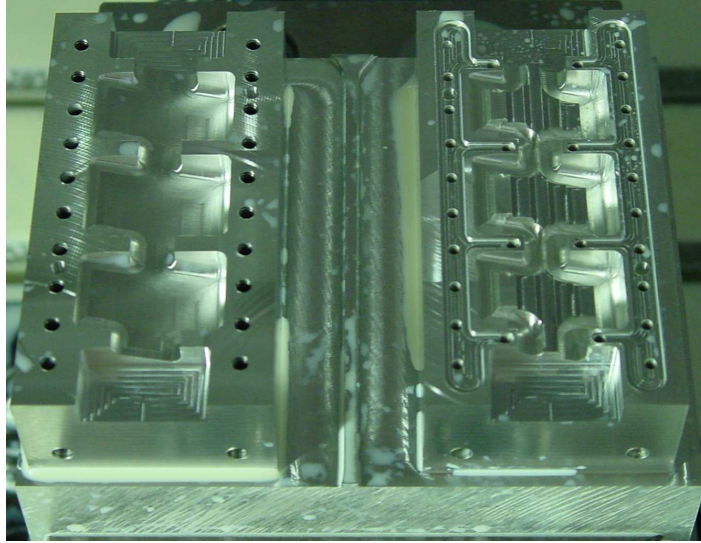


Figure 5.7: Wedge-shaped filter halves during the manufacturing process.

non-parallel plates, which generates some rounded corners in the filter (cf. Fig. 5.7). Since the drill size was known, this was considered in the fine-tuning procedure of the dimensions before starting the manufacturing process.

From a multipactor test point of view, it has to be ensured that there is a sufficient electron seeding in the inner part of the filter. A ^{90}Sr β -emitting radioactive source has been used for this purpose, which produces two different emitters: ^{90}Sr (half-life of 28 years) and ^{90}Y (half-life of just 2 days), with a maximum kinetic energy per electron of 0.546 MeV and 2.28 MeV, respectively. The maximum penetration depth of the ^{90}Y electrons in an aluminium wall is around 5.25 mm. Thus, the external metallic walls of both filter halves have to be considerably thinner than this constraint, which should not be disregarded when preparing the manufacturing model, even if this dimension does not belong to the ones defining the electrical response. For the current design, a thickness value of 1.5 mm has been chosen.

5.2 Second Wedge-shaped Bandpass Design

5.2.1 Structure Characteristics and Requirements

Both filter designs have to meet the same electrical specifications of Table 5.1, which are typical for space applications: 12 GHz centre frequency and 150 MHz bandwidth. The input and output ports are WR75 waveguides, and the order of the filters has been fixed to three, which corresponds to the number of resonators.

They have been designed with the help of FEST^{3D} [50], which implements the automatic rectangular filter dimensional synthesis procedure described in Chapter 4.1.4. The design of the wedge-shaped filter is slightly more complex, since additional computations are required to derive the transfer functions of wedge-to-wedge or wedge-to-rectangular waveguide dis-

Table 5.1: Requirements of the bandpass filters.

Parameter	Value
Centre frequency [GHz]	12
Bandwidth [MHz]	150
Order of the filter	3
Return loss	25

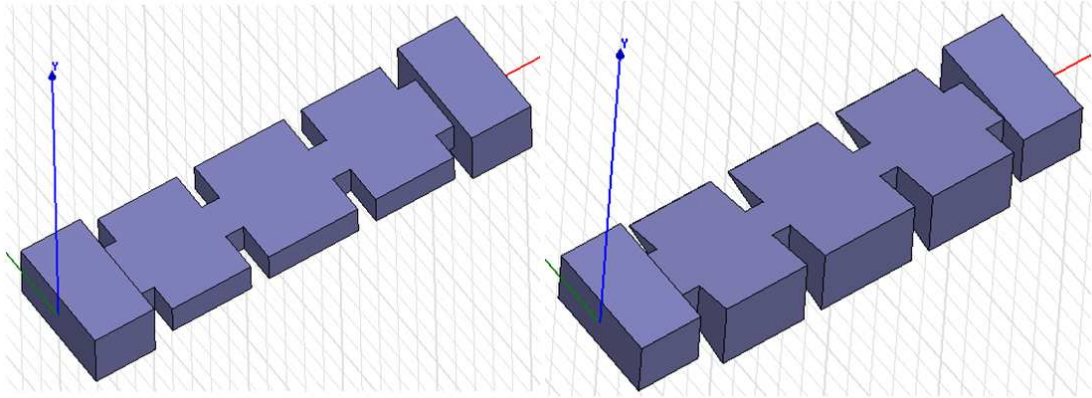


Figure 5.8: 3-D views of the quasi-inductive rectangular (left) and the wedge-shaped filters (right).

continuities. The wedge-shaped filter has been designed first, with an inclination angle of 30° as established in Chapters 5.1.2 and 5.1.3. This inclination is kept constant along all the intermediate stages of the filter, excepting the input and output waveguides (a drawing of this filter can be found on the right-hand side of Fig. 5.8). The minimum gap has been fixed to the manufacturing limit $h_{1,\min} = 0.2$ mm. Larger gaps would result in a RF input power threshold for multipactor discharges exceeding the measuring range of the available equipment. The resulting maximum height is $h_{2,\max} = 12.323$ mm. The width has been iteratively calculated in order to have the same f_C value as for the WR75 fundamental mode.

The rectangular waveguide filter design is a symmetric structure, originally purely inductive (as delivered by FEST^{3D}): H-plane topology with constant height. However, the height of the intermediate stages of the filter must be decreased (corresponding filter drawing is shown on the left-hand side of Fig. 5.8) to perfectly match the Q factor of the wedge-shaped filter (whose simulated value is 5440) and to achieve comparable frequency responses. The reduced height value obtained for this quasi-inductive filter is $b_{\text{rect}} = 5.05$ mm. A comparison of their simulated group delay can be seen in Fig. 5.10. The Q factor is directly linked to the losses in the whole structure, so the rectangular and the wedge-shaped filter designs have as well the same insertion losses due to the finite conductivity of the materials at 12 GHz (0.18 dB for a conductivity value of $6.1 \cdot 10^7$ S/m). Please note that, due to the Q-factor

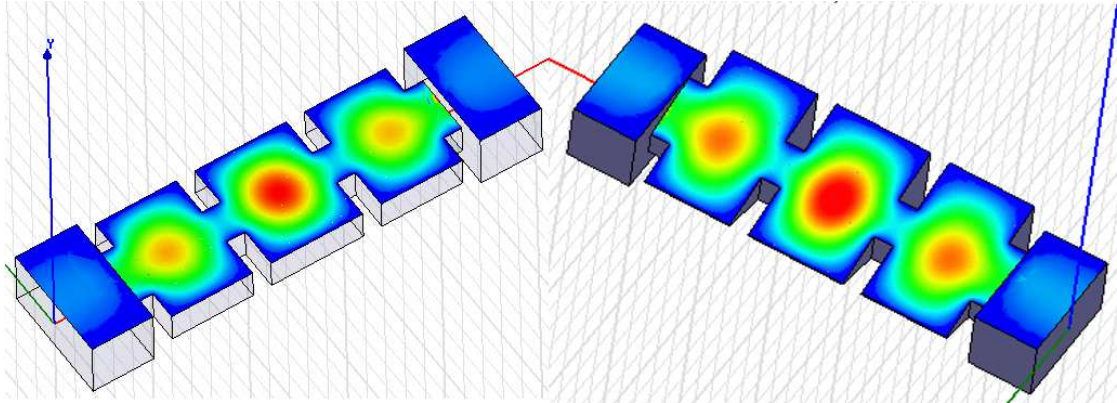


Figure 5.9: 3-D plot of the electric field distribution along the rectangular (left) and the non-parallel plate filters (right).

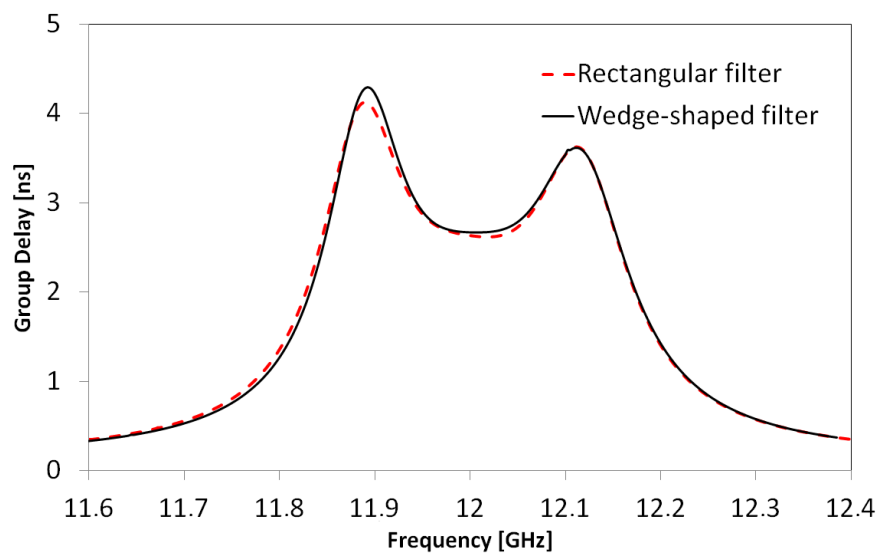


Figure 5.10: Comparison of the group delays of both designs ($\sigma = 6.1 \cdot 10^7$ S/m). Simulation with FEST^{3D}.

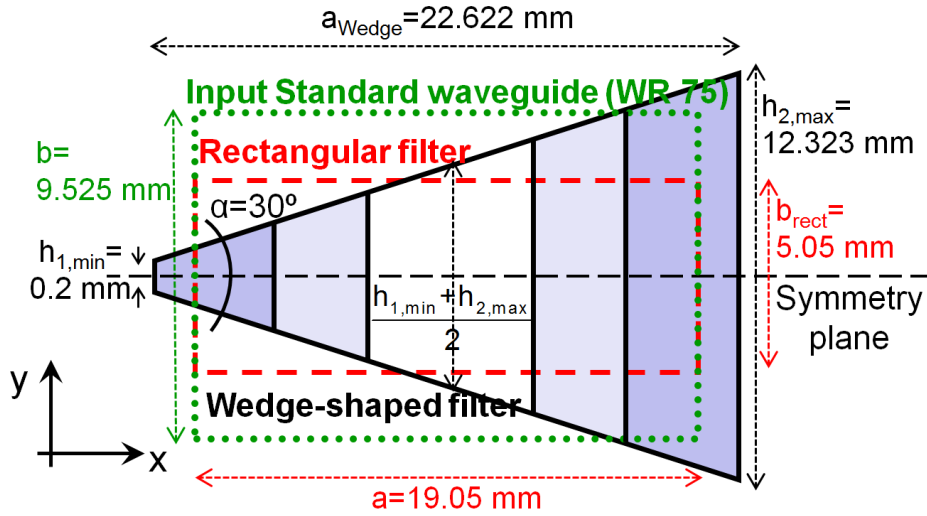


Figure 5.11: Comparative detail of the cross sections of the two considered filter designs. The mean wedge height is slightly different from the rectangular filter height b_{rect} in order to match the Q factors.

Table 5.2: Dimensions of the rectangular waveguide bandpass filter.

WG	a [mm]	b [mm]	l [mm]
Input	19.05	9.525	10
Iris 1	9.744	5.05	3
Cavity 1	19.05	5.05	13.275
Iris 2	6.151	5.05	3
Cavity 2	19.05	5.05	15.062

optimisation, the reduced height of the rectangular filter is slightly smaller than the average height of the wedge-shaped filter ($b_{\text{rect}} = 5.05\text{mm} < \frac{h_{2,\text{max}} + h_{1,\text{min}}}{2} = 6.26\text{mm}$). This ensures a fairer comparison between the rectangular and wedge-shaped filters than the one developed in Chapter 4.

A comparison of the cross sections of both filter designs is depicted in Fig. 5.11, and all dimensions are listed in Tables 5.2 and 5.3. Both filter designs have horizontal symmetry, and are also symmetric with respect to a plane perpendicular to the propagation energy direction and placed at equal distance from the input and output ports. Furthermore, the rectangular waveguide filter design also has also vertical symmetry (see Fig. 5.11).

Fig. 5.12 and Fig. 5.13 show the Autocad drawings of both filters, including all dimensions of the different inner cavities.

Table 5.3: Dimensions of the wedge-shaped waveguide bandpass filter.

WG	a [mm]	b [mm]		l [mm]
Input	19.05	9.525		10
		h_2	h_1	
Iris 1	10.279	9.016	3.507	3
Cavity 1	22.622	12.323	0.2	13.99
Iris 2	6.766	8.074	4.449	3
Cavity 2	22.622	12.323	0.2	15.515

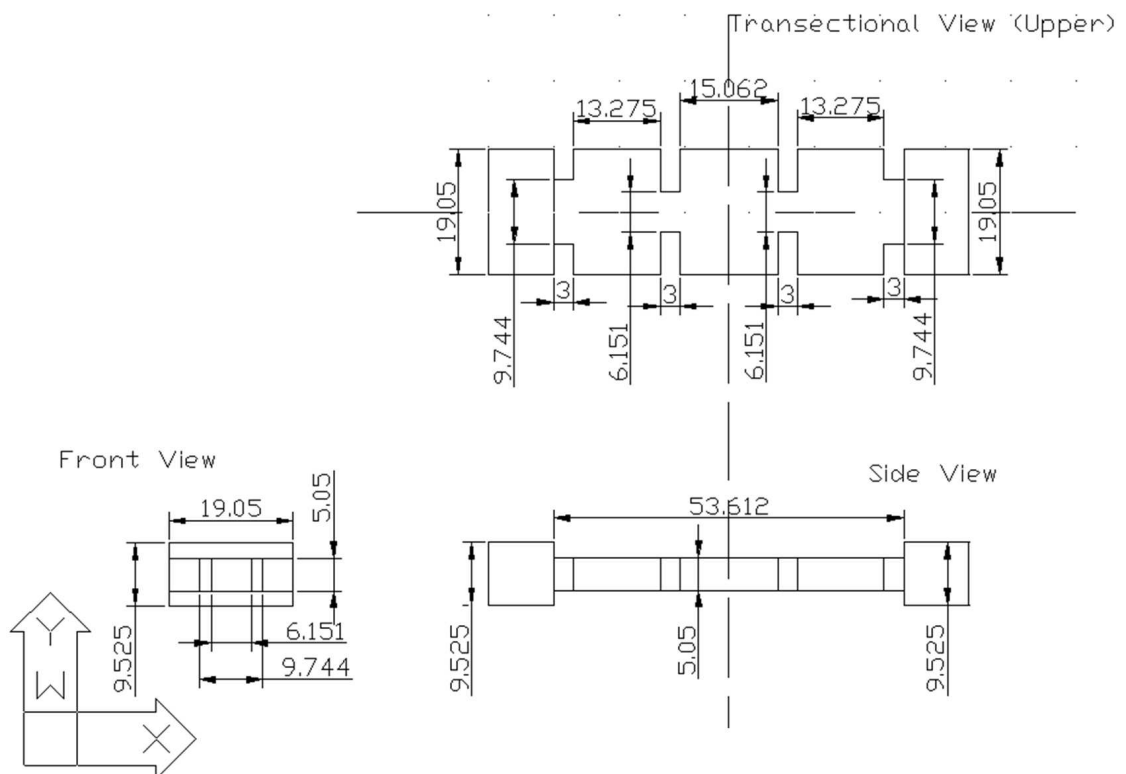


Figure 5.12: Autocad model of the rectangular bandpass filter dimensions.

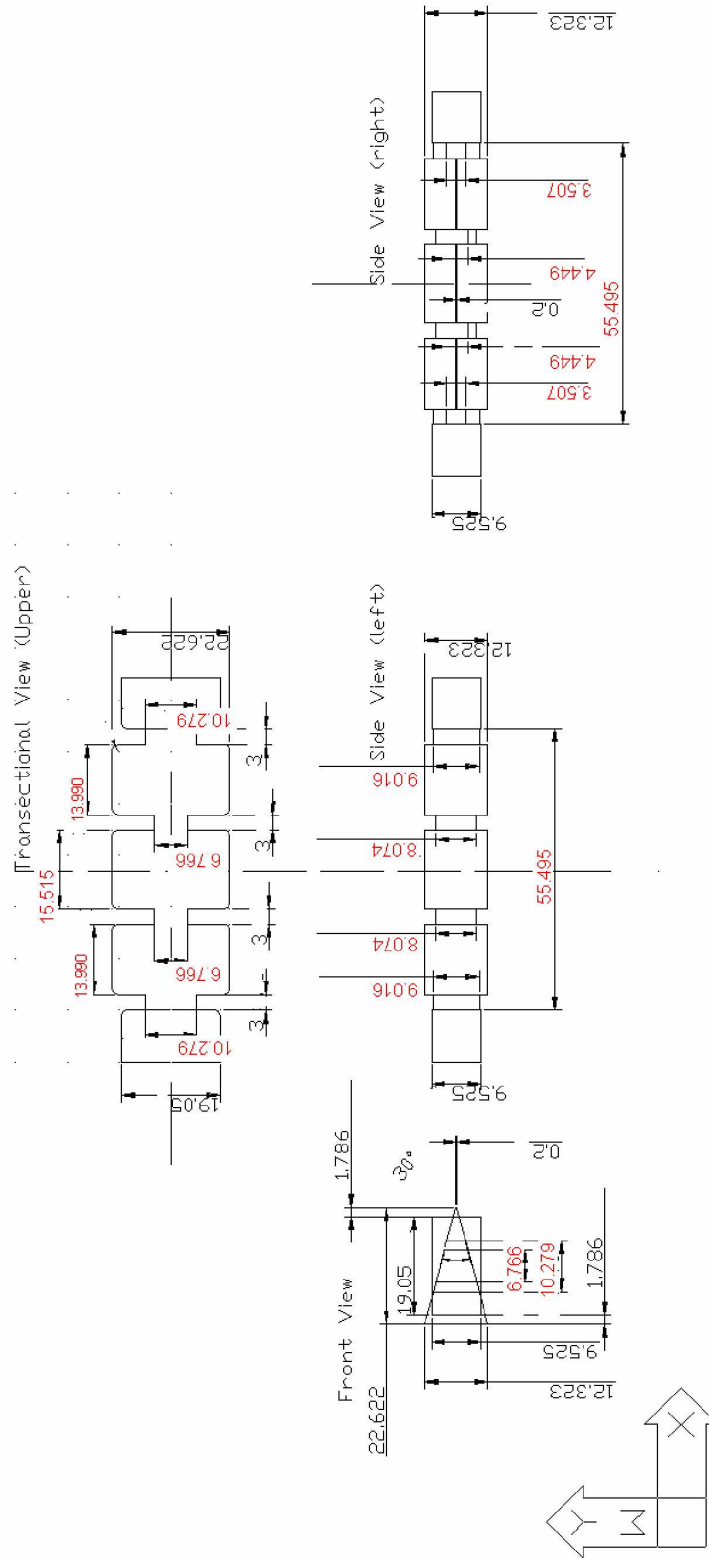


Figure 5.13: Autocad model of the wedge-shaped bandpass filter dimensions. The dimensions marked in red correspond to the re-adjusted dimensions due to the ball-end mill with a high radius of curvature.

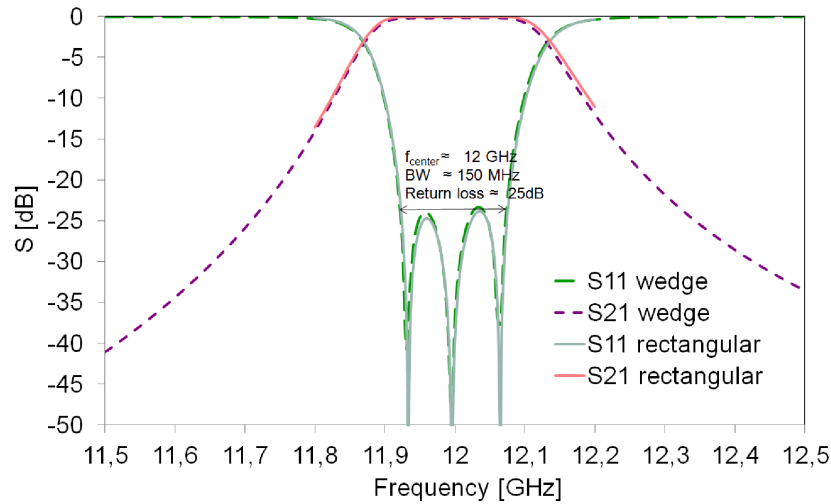


Figure 5.14: Comparison between the simulated S-parameters of both filters (perfect conductor). Simulations have been performed with FEST^{3D}.

Additionally, and with the help of FEST^{3D}, a tolerance analysis was performed before proceeding with the filters' manufacturing process. For a three-pole bandpass filter with the required characteristics of this design, a value of $8.7 \mu\text{m}$ comes out as the dimension tolerance requested to guarantee around 25 dB of return loss, while $12.325 \mu\text{m}$ is required to achieve 20 dB return loss. Hence, a tolerance value of $10 \mu\text{m}$ was fixed for the manufacturing procedures. In the first pair of filters, a gold layer of around $10 \mu\text{m}$ thickness is applied to the hardware in order to ensure an almost lossless behaviour of the structure. This $10 \mu\text{m}$ have to be deducted from the designed dimensions of the cavities and irises before manufacturing. The filter halves of the second pair are just of bare aluminium and do not require any special plating.

5.2.2 Simulation Results

The simulation results of both designs provide a very good match with the specifications. Fig. 5.14 also indicates an almost perfect agreement between the S-parameter curves of both filter designs. Note that this simulation has been performed assuming perfect conductivity of the involved metals.

5.2.3 Manufactured Hardware

The filters have been manufactured with a milling machine method in ESA-ESTEC. In fact, two identical copies of each filter have been done, with the difference that a gold layer has been applied to one pair, and the other one has been left with bare aluminium as inner structure surfaces. Since the hardware was built in-house, the cost was moderate, which allowed the duplication of the hardware devices in order to test the multipactor performance under

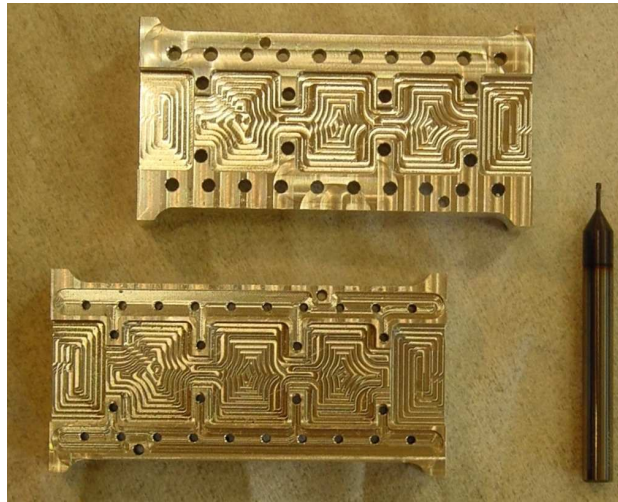


Figure 5.15: Milling process of the two halves of the gold-plated rectangular waveguide filter. Milling tool (0.5 mm radius of curvature) is also shown in this photo.

different materials. A mill with a sharp peak (0.5 mm radius of curvature) was used to manufacture the rectangular filters. However, the complexity of the wedge-shaped filters required a special configuration of the machine, only allowing a ball-end mill of 1.5 mm radius of curvature. Such rounded corners would perturb the electrical performance of the device. Hence, an additional optimisation step of the filter dimensions was required, which was originally not foreseen. The dimensions of the wedge-shaped filter presented in Chapter 5.2.1 already account for this re-adjustment.

Fig. 5.15 and Fig. 5.16 show photos of the manufactured hardware halves, in the rectangular case for the gold-plated version, and in the wedge-shaped case for the aluminium version. The edges of the resonators in Fig. 5.16 clearly show the rounded corners produced by the ball-end mill. The finer mill used for the rectangular waveguides of the filters (the whole rectangular filter and the input and output waveguides of the wedge-shaped one) has left small traces on the metallic walls. The illumination in the photos of Fig. 5.15 and Fig. 5.16 exaggerates the depth of these traces, since in practice these are flat surfaces.

After manufacturing the filters in the ESTEC workshop, they were cleaned in an ultrasonic iso-propanol bath during 15 minutes to remove residues. A chloroform cleaning was exclusively applied to the aluminium filters. The filters were then transported to the laboratory wrapped in lint free tissues and stored in the clean room, inside the nitrogen cabinets, until the tests took place.

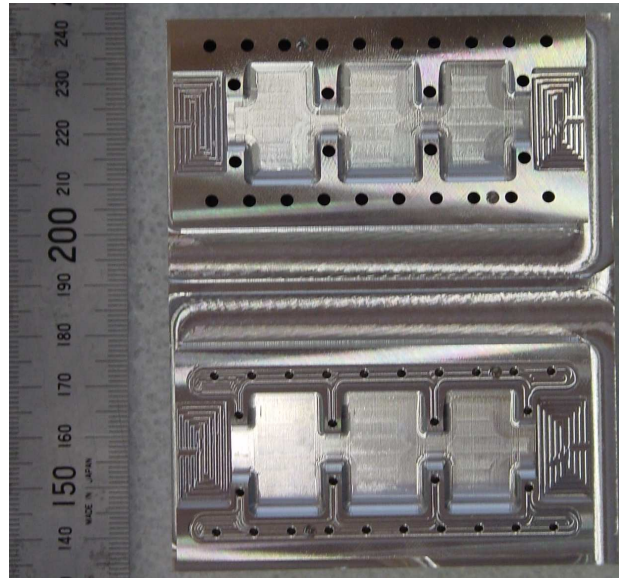


Figure 5.16: Milling process of the two halves of the aluminium wedge-shaped waveguide filter. Inner cavities have been carved with a milling tool with 1.5 mm radius of curvature.

5.3 Electrical Performance

5.3.1 Narrow-band Comparison

The gold-plated manufactured filter pair is shown in Fig. 5.17 and its scattering parameters were measured with a network analyser in the ESA-ESTEC Payload Systems laboratory. In Fig. 5.18 and Fig. 5.19, the measured frequency responses of the gold-plated rectangular and the wedge-shaped filter, respectively, are compared with the corresponding simulations.

The rectangular waveguide filter fulfils almost perfectly the specifications (Table 5.1), just confirming the accuracy of the design process. In the wedge-shaped waveguide case, the measured frequency response is slightly shifted (≈ 35 MHz) towards lower frequencies with respect to the simulated data, probably due to the lower accuracy of the manufacturing process. However, the bandwidth and return losses are according to the expected performance, also considering the tolerance analysis described in Chapter 5.2.

5.3.2 Wide-band Comparison

The S-parameters of the gold-plated pair have also been measured over a wide frequency range. The objective was to verify whether the out-of-band performances of both the rectangular and the wedge-shaped filters were similar, unlike the designs of Chapter 4. The curves are compared in Fig. 5.20, and it can be seen that both out-of-band behaviours match quite well, having a repetition of the pass-band at 19.2 GHz and 19.5 GHz (the simulated repetition was around 19.3 GHz). This result successfully verifies the approach presented in Chapter 5.1.3. There is a first resonance appearing at 17.4 GHz in the wedge-shaped fil-

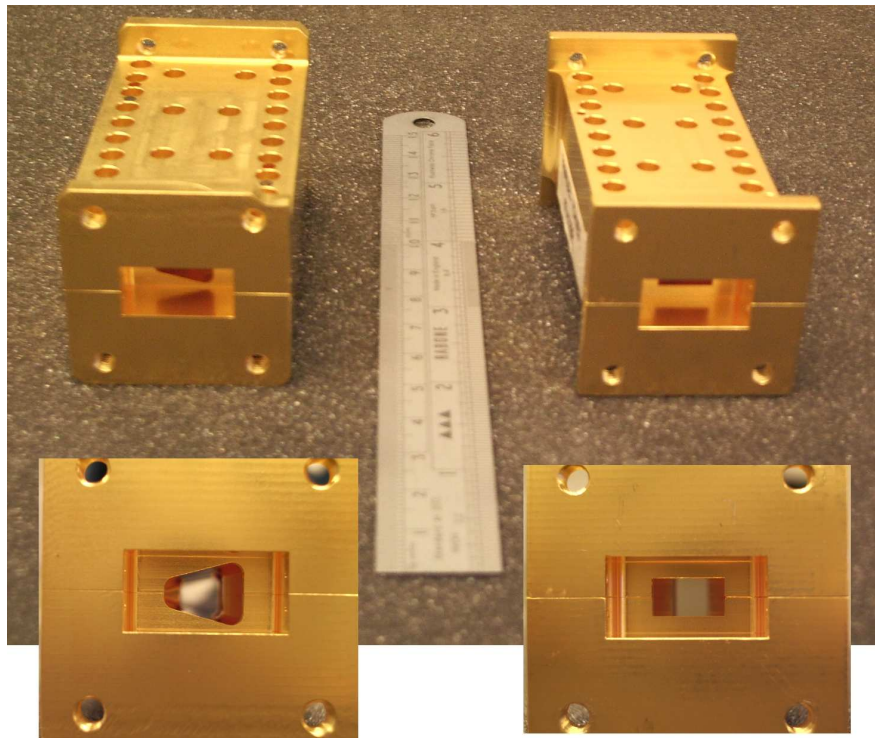


Figure 5.17: Photo of the two manufactured gold-plated filters: wedge-shaped filter (left) and quasi-inductive rectangular filter (right), both with a zoom of the front view.

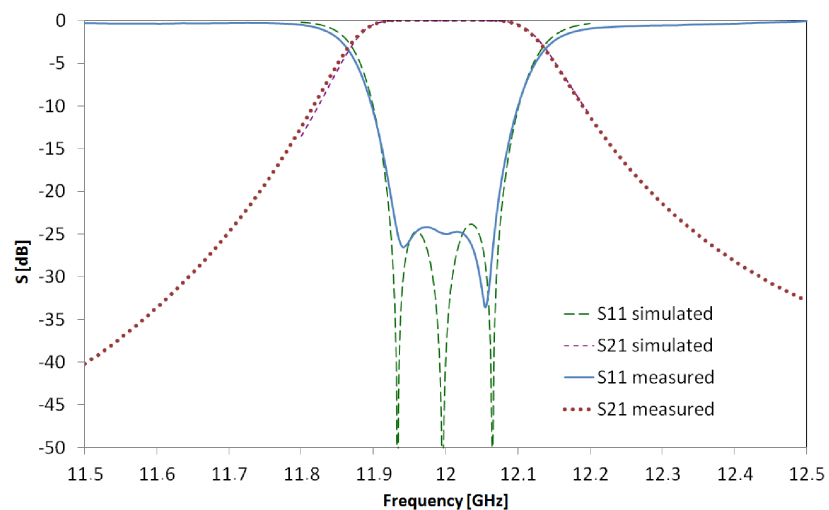


Figure 5.18: Comparison between the simulated and measured S-parameters of the gold-plated rectangular filter.

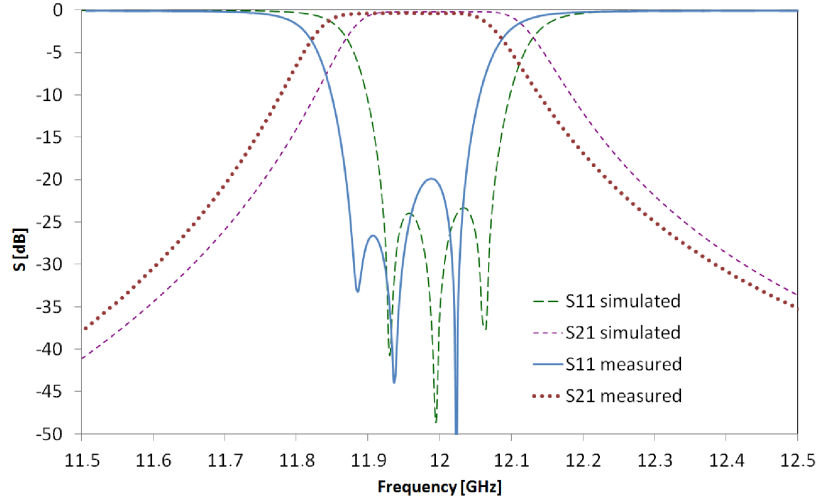


Figure 5.19: Comparison between the simulated and measured S-parameters of the gold-plated wedge-shaped filter.

ter curve, which is related with the higher-order modes generated at these frequencies (cf. Fig. 5.5). In a wedge-shaped waveguide with $\alpha = 30^\circ$, the second- and third-order modes have a lower cutoff frequency than in the rectangular case, which may cause a kind of dual-mode resonance.

Another advantage of the approach described in Chapter 5.1.3 is that both filter designs have a very similar total length of around 74 mm.

5.4 Multipactor Performance

5.4.1 Multipactor Predictions

The two filter pairs, hence two gold-plated and two aluminium devices, were tested in the Payload Systems Laboratory at ESA-ESTEC. In this way, the accuracy of the prediction tools could be verified under different metallic surface conditions. Apart from FEST^{3D}, the ECSS Multipactor Tool [51] was also used for calculating threshold values in the different cases. Proceeding in this way, the relative prediction accuracies can be compared.

The form of the SEY function follows (3.8), as proposed in [64]. The characteristic parameter values applied for the prediction simulations have been listed in Table 5.4. The obtained threshold values with our software (in the framework of FEST^{3D} environment) for the aluminium pair are: 900 W for the rectangular waveguide filter and 3000 W for the wedge-shaped one. The threshold of the gold-plated rectangular waveguide filter is 1500 W. No threshold was detected up to 6.5 kW for the gold-plated wedge-shaped filter. All these values have been obtained after 50 impacts of each effective electron against the metallic walls.

As an additional reference, the multipactor predictions have been also performed with

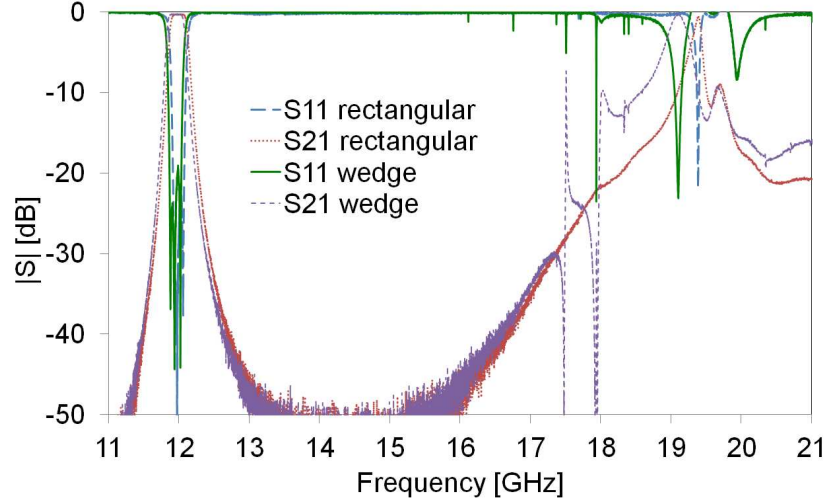


Figure 5.20: Measured out-of-band frequency responses of the gold-plated quasi-inductive and the wedge-shaped filters.

Table 5.4: Values of the characteristic SEY parameters for gold and aluminium.

Parameter	Variable	Gold	Aluminium
Starting SEEC	δ_{start}	0.5	
Maximum SEEC normal impact	$\delta_{\text{max}}(0)$	2	2.98
Fitting constant	r	1.125	
Fitting constant	s	0.35	
Fitting constant	$k_{\delta} = k_W$	1	
First crossover energy	W_1 [eV]	30	23.3
Energy at $\delta_{\text{max}}(0)$	$W_{\text{max}}(0)$	165	150
Fitting constant	κ_1	0.56	
Fitting constant	κ_2	0.25	

the ECSS Multipactor Tool [51]. The same strategy used in Chapter 4.3.2 was applied here. The voltage is calculated in the most likely trapped trajectory, in this case in the second resonator, which is the central one. Then, this value is applied to the parallel-plate multipactor prediction model [3, 11, 14], as if it would be a rectangular filter. The conventional approach is adopted when calculating the voltages and thresholds of the rectangular waveguide filters.

For aluminium, the predicted thresholds are: 580 W for the rectangular filter and 700 W for the wedge-shaped one. The predictions for the gold-plated pair are: 1300 W for the rectangular filter and 1600 W for the wedge-shaped one. It has to be noted that the predictions for the wedge-shaped filters with the ECSS Multipactor Tool are mere approximations, since a wedge has been artificially assumed as a “parallel-plate” geometry. The gap distance has been set equal to the section length of the critical radius identified in Chapter 5.1.2, which in this case is around 7.6 mm.

5.4.2 Multipactor Test Campaign Results

The test-bed configured for the four experiments (2 filters times 2 metallic surfaces) is similar to the one described in Chapter 4 and in Appendix C.1, but at a frequency of 12 GHz (in the wedge-shaped case, 11.965 GHz accounting for the slight frequency shift observed in Fig.5.19). In each case, the procedure started by placing the DUT in the vacuum chamber, close to the radioactive source, to ensure sufficient seeding electrons to initiate a multipactor breakdown. Four multipactor detection methods were used in each experiment: forward/reverse power nulling and third-harmonic detection as global methods, and electron generation and photon emission as local procedures (see Appendix C.2 and [3]). Then, the chamber was sealed and pumped for outgassing during 24 hours, until reaching a pressure $< 1 \cdot 10^{-7}$ mbar at ambient temperature. The RF source was configured in pulsed mode, with a 2% duty cycle and a pulse repetition frequency of 1 kHz; the maximum achievable RF input power was 6.5 kW. The multipactor test was started with an input power level of 500 W and the power was then increased in 20 W steps. The dwell time at each power level was 10 min. Once multipactor was detected, the power steps were reduced to 10 W.

All results are summarised in Table 5.5. The first column corresponds to the predictions with the ECSS Multipactor Tool, and the second one to the results obtained with FEST^{3D}, as already presented in Chapter 5.4.1. The last column of Table 5.5 offers the experimental results. Fig. 5.21 and Fig. 5.22 serve as an example of the screenshots of the network analyser indicating a discharge event.

5.4.3 Evaluation of Results

An excellent agreement is obtained for the rectangular-filter threshold values between FEST^{3D} and the measurements (for both metallic wall materials): multipactor discharges occurred at 1400 W with gold and at 950 W with aluminium. This means that our tool offered a better prediction with respect to the ECSS one, especially for the aluminium filter.

When considering the gold plated wedge-shaped filter, interesting consequences can be

Table 5.5: Multipactor (MP) threshold predictions and measurements at 12 GHz (measurement limit 6.5 kW).

Filter	Thresholds		
	ECSS MP Tool	FEST ^{3D}	Measured
Rectangular (gold)	1300 W	1500 W	1400 W
Rectangular (aluminium)	580 W	900 W	950 W
Wedge-shaped (gold)	1600 W	no detection	no detection
Wedge-shaped (aluminium)	700 W	3000 W	1800 W

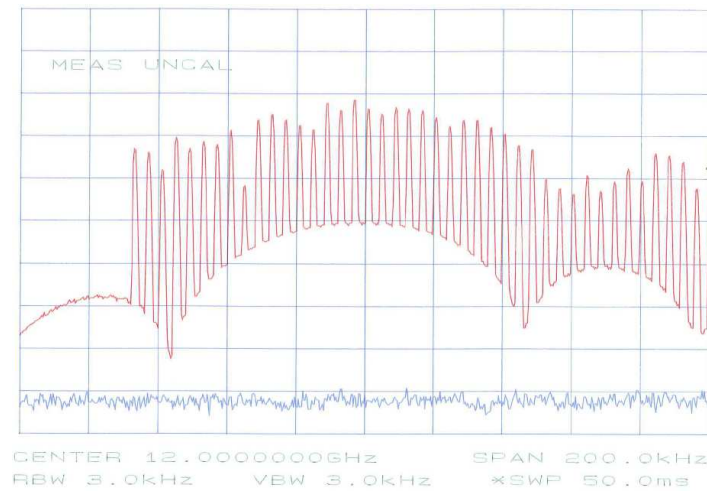


Figure 5.21: Screenshot of the network analyser of the nulling detection chain when indicating a multipactor discharge in the rectangular waveguide filter.

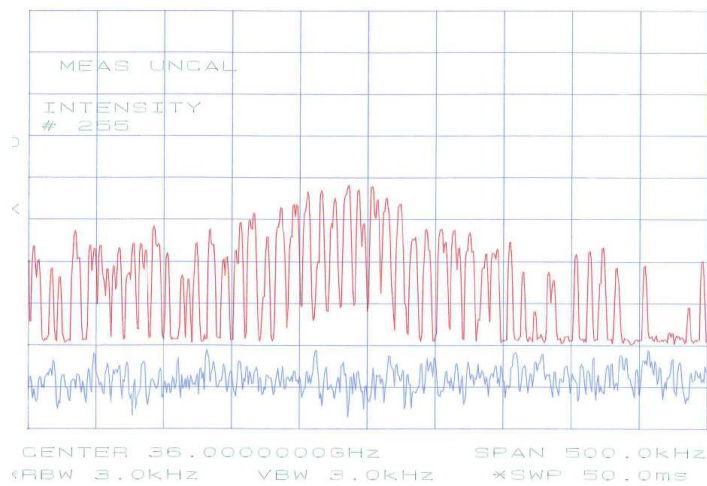


Figure 5.22: Screenshot of the network analyser of the harmonics detection chain when indicating a multipactor discharge in the wedge-shaped waveguide filter.

extracted. Although the ECSS prediction suggests a threshold value of 1600 W, no sustained electron resonance could be detected with FEST^{3D}: in no case the electron growth was sufficient to trigger the simulation threshold for multipactor determination. In fact, the measurements verified this last prediction, since no discharge could be detected for the whole available test-bed power range. In the same wedge-shaped filter, but with aluminium walls instead of gold plating, discharges were measured, namely at 1800 W input power. The approximation obtained with the ECSS Multipactor Tool is very conservative. The predicted threshold of FEST^{3D} is 3000 W, closer to the measurement of 1800 W, but still relatively far away from the measurement.

The simulations show that the accumulated SEEC values of resonant electrons in wedge-shaped waveguides are more unstable than for the rectangular case. In fact, when reducing the number of impacts of each effective electron, e.g. down to 20, while keeping the total number of launched electrons, the predicted threshold decreases to 2500 W, whereas in the rectangular filter the threshold value is less sensitive to the maximum number of impacts of each electron. Additionally, the high multipactor order due to the large gap [23] can explain this discrepancy with the measurements. It should be also noted that, recently, a new multipactor mode has been discovered [77], which extends the region of parameter space for multipactor growth, and whose consideration might improve the multipactor prediction accuracy.

Finally, the excellent multipactor performance of the wedge-shape filter with respect to the rectangular filter is remarkable. In the case of aluminium, there is an increase of around 3 dB in the threshold, beating the results of the first wedge-shaped filter attempt in Chapter 4, and confirming the success of the design upgrades. With gold-plating, multipactor has even been completely suppressed in the wedge-shaped filter within the available experimental capabilities, as it is correctly predicted by our software tool.

5.5 Guidelines for Optimal Design

Having successfully verified the proposed wedge-shaped bandpass filter improvements (see Chapter 4.5), a set of steps can be recommended for designing wedge-shaped waveguide filters with optimal resistance to the multipactor effect:

1. Determination of the dimensions of a rectangular waveguide appropriate to the application, according to the operating frequency and transfer function requirements.
2. Choice of the inclination angle α . The optimum value is 30° , but lower α -values are possible if other constraints are present. Fig. 5.3 suggests that 30° also sets the upper limit for the improvement.
3. Choice of the minimum height $h_{1,\min}$ of the smallest side-wall, in order to obtain the desired Q factor without exceeding the manufacturing tolerances.

4. Derivation of the wedge-shaped resonator waveguide width a_{Wedge} , such that the f_C value is equal to the one of the equivalent rectangular waveguide. This value is slightly larger than the reference one a . In this way, an appropriate out-of-band frequency response is ensured.
5. Derivation of the filter dimensions based on the specifications by means of a synthesis method.
6. Calculation of the theoretical trapped-trajectory range as proposed in Chapter 5.1.2.
7. Multipactor prediction analysis at radii close to this position in the centre of the inner resonator of the device, which will provide the power and equivalent voltage multipactor thresholds. Alternatively, when a susceptibility map such as the one in Chapter 3.5 is available for the given material properties, an approximated estimation of the power and voltage thresholds can be read from it, after applying suitable voltage magnification factors.

The multipactor threshold measurements of the wedge-shaped filter have demonstrated an improvement of 3 dB with respect to the quasi-inductive rectangular one with aluminium, and the complete suppression of this effect in the gold-plated case. The trade-off is obviously related to a slightly higher design complexity, as it becomes obvious from the present and previous chapters. Including the results of Chapter 4.4.1, the advantage of the novel topology has been verified in filters with metallic walls of three different materials: gold, silver and aluminium.

The FEST^{3D} multipactor prediction tool is not extremely accurate for the wedge-shaped filter cases, as it was justified in the previous subchapter, but it is still valuable to have an approximated indication of the multipactor threshold. Nevertheless, the basis is set for the development of microwave devices that include this kind of wedged waveguide topology in critical gaps to avoid the multipactor breakdown, or shift it to higher power levels.

Chapter 6

Conclusiones y Perspectivas

Durante las últimas décadas, la era de las telecomunicaciones ha supuesto toda una revolución en la sociedad, fomentando la comunicación entre los pueblos y facilitando el acceso prácticamente universal a vastas fuentes de información y conocimiento. Aplicaciones como la telefonía móvil, los receptores de señales de posicionamiento o el acceso a internet se han convertido en realidades cotidianas indispensables, cuando hace cincuenta años eran a lo sumo quimeras de la ciencia ficción. Preocupaciones globales, como la meteorología y el cambio climático, la seguridad internacional y la predicción y prevención de catástrofes naturales, han sido igualmente un motor de las telecomunicaciones vía satélite. Esta rápida evolución ha sido posible gracias a los esfuerzos realizados en el desarrollo e innovación de las tecnologías de telecomunicaciones, y en particular de sus aplicaciones espaciales. Con respecto a los dispositivos de microondas embarcados en satélites, este progreso conlleva un aumento constante de los requerimientos de resolución y ancho de banda, lo cual se puede traducir en la exploración de bandas a mayores frecuencias y en un aumento de las potencias de trabajo para compensar las mayores pérdidas de propagación. Además de a los instrumentos de teledetección, como radares de apertura sintética, altímetros o radiómetros, esto también afecta a los subsistemas de radiofrecuencia dedicados a la transmisión de datos de telemetría, seguimiento y control, y a los transpondedores de retransmisión de señales de telecomunicaciones.

El aumento de las potencias de trabajo debe ser compatible con la minimización de los riesgos y costes de los proyectos de satélites, como se ha comentado en el Capítulo 1. Uno de los factores limitantes para las potencias de trabajo en dispositivos de microondas en el espacio, habiendo incluso inutilizado los instrumentos en ciertas misiones, es el efecto multipactor. Por esta razón, cualquier avance en este campo supone un beneficio inmediato para la industria. El escenario ideal sería la eliminación completa del efecto multipactor, y con él de la necesidad de costosas campañas de test para capacitar los dispositivos para su uso en órbita. En la práctica, se persigue el traslado de los umbrales de multipactor a potencias más elevadas, para así ampliar las prestaciones del dispositivo y para, en la medida de lo posible, reducir la complejidad y número de tests a realizar.

Esta tesis ha intentado aportar su contribución en la reducción del efecto multipactor al proponer una nueva geometría en guía de onda con unas propiedades singulares: la guía en

forma de cuña. Las características de esta estructura se han comparado con las de geometrías tradicionales como las guías rectangulares. La ventaja principal es su mayor resistencia al efecto multipactor, ya que la orientación del campo eléctrico del modo fundamental presenta una trayectoria curvilínea dependiente del ángulo de inclinación. Esto dificulta la formación de las típicas trayectorias resonantes que pueden llevar a una avalancha de electrones. Hemos podido comprobar que estas trayectorias también existen en las guías en forma de cuña, pero están situadas en regiones de la sección recta de la guía con voltajes más reducidos que en el caso de una guía rectangular con la misma potencia de entrada. En cuanto a las dimensiones, el máximo ángulo aplicable a las cuñas depende de las dimensiones de la guía rectangular equivalente. Rectángulos con relaciones anchura/altura típicas (0.5 o ligeramente inferiores) pueden ser sustituidos sin problemas por cuñas con las inclinaciones adecuadas (de 5° a 35°) para mejorar el multipactor. La topología en cuña es modular, ya que es posible introducirla únicamente en lugares concretos de una estructura más o menos compleja (filtros, transformadores, multiplexores), donde se presume pueda existir un mayor riesgo de descarga. Utilizar esta geometría es compatible con cualquier otra de las técnicas del estado-del-arte para eliminar el efecto multipactor (ver Capítulo 1.1), como por ejemplo el recubrimiento de las superficies metálicas con películas protectoras especiales.

El primer paso de la investigación ha sido el desarrollo de una herramienta basada en el método BI-RME para el cálculo de los campos electromagnéticos en la guía en forma de cuña. Para ello se ha presentado la formulación basada en los modos normalizados de una guía de onda rectangular de referencia (recordar el Capítulo 2 y el Anexo A). Las primeras experiencias de simulación han permitido identificar ciertos problemas numéricos, que se han solventado eligiendo una dimensión apropiada de las guías rectangulares de referencia. Los resultados han demostrado una suficiente precisión en el cálculo de los campos de la guía en forma de cuña, manteniendo una alta eficiencia. Dado que el cálculo del campo se realiza de forma iterativa en diversos bucles y herramientas, se ha impuesto la estrategia de pre-calcular los campos normalizados (independientes del tiempo y la potencia de entrada) en una rejilla cubriendo la sección recta de la guía. Un procedimiento de interpolación y des-normalización permite recuperar los campos de manera casi inmediata en cualquier lugar e instante y a la potencia deseada conforme los bucles de los simuladores los necesitan.

Aquí, como en los demás problemas específicos afrontados durante la tesis, se han buscado soluciones a medida con alta precisión y eficiencia. En algunas ocasiones, se han empleado métodos conocidos de la literatura, adaptados para nuestro problema particular. En otros casos, al carecer de referencias, se han desarrollado nuevos algoritmos. Por último, ha sido necesario programar algunas nuevas herramientas de análisis, aún existiendo herramientas comerciales con la capacidad de realizar cálculos similares. La justificación es que, habitualmente, las herramientas comerciales tienen un propósito generalista y ofrecen una gran flexibilidad. Esto supone como contrapartida que la eficiencia suele ser subóptima para estructuras concretas, lo cual puede dificultar enormemente análisis paramétricos como los que ha requerido esta investigación. La utilización de herramientas propias muy especializadas y eficientes, como la implementada para el análisis de los campos en guías en forma de cuña y el método de interpolación ya citados, han sido indispensables para el progreso y

culminación exitosa del trabajo de esta tesis doctoral.

El núcleo del análisis teórico es la herramienta para la predicción del efecto multipactor, tanto en guías de onda en forma de cuña como en rectangulares, presentada en el Capítulo 3. Ésta combina un método numérico para el seguimiento de los electrones en un entorno con condiciones de vacío y bajo la influencia de un campo electromagnético, con un estudio estadístico de la población de electrones para detectar los riesgos de descarga de multipactor. Como nuevas aportaciones se pueden destacar la verificación de la existencia de trayectorias resonantes en guías en forma de cuña, la identificación de las posiciones óptimas de lanzamiento de los electrones en las simulaciones, lo cual supone un considerable ahorro computacional, y el estudio paramétrico del comportamiento multipactor de este tipo de guías. Aunque la herramienta ha sido programada para materiales conductores ideales sin pérdidas óhmicas, las formulaciones necesarias para extenderla a metales con conductividad finita se han incluido en el Apéndice B. También se han establecido los límites prácticos del ángulo de inclinación de las paredes superior e inferior, por encima de los cuales la estructura perdería sus propiedades beneficiosas. La herramienta ha sido validada con referencias de la literatura y se han podido confirmar teóricamente las expectativas sobre la nueva topología de guía de onda. Por primera vez, se han generado mapas de susceptibilidad de multipactor para este tipo de guías (en la línea de las ya existentes para el caso de placas paralelas), lo cual es una importante aportación para facilitar su diseño.

El siguiente paso ha sido la implementación de la estructura en forma de cuña en un dispositivo de microondas complejo, como es un filtro paso-banda centrado en 9.5 GHz y con un ancho de banda de 100 MHz. Una vez realizado el diseño, basado en un filtro equivalente disponible en guía rectangular, se ha procedido a la construcción y test de la estructura en el laboratorio, tal y como se describe en el Capítulo 4 y con información adicional en el Anexo C. Ha sido la primera vez que se construye un filtro en cuña (inclinación de 19°) y que se comprueba en el laboratorio la mejora, aunque leve, en el umbral de multipactor de este tipo de topologías con respecto a un filtro equivalente rectangular. Conviene destacar también la validación del proceso de diseño del filtro, adaptado con respecto a la síntesis del caso rectangular, al conseguir una respuesta en frecuencia acorde con los requerimientos. La herramienta de predicción del efecto multipactor se ha extendido para aceptar estructuras con discontinuidades y no sólo guías infinitas, y los resultados se han comparado con las medidas. Se ha comprobado que las predicciones son más precisas que las realizadas con herramientas basadas en el modelo de placas paralelas. Sin embargo, las discrepancias entre medidas y predicción son mayores en el filtro en cuña que en el rectangular. Se han advertido aspectos con margen de mejora, como la potencia umbral, que sólo ha tenido un moderado aumento de 1 dB con respecto a la del filtro rectangular, así como la respuesta fuera de banda y el método de construcción del filtro. Estos defectos en la construcción han causado fallos de contacto entre las piezas que forman la estructura. La corrección de este problema mediante la introducción de láminas de indio en las juntas (ver Capítulo 4.2.3) ha supuesto un desplazamiento en frecuencia (50 MHz) y un ligero ensanchamiento de la banda de paso del filtro (15 MHz). En todo caso, la relevancia de este experimento ha suscitado la solicitud

de una patente europea (ver Capítulo E.2 y [41]).

Con la experiencia adquirida en el primer experimento, se ha diseñado un segundo filtro paso-banda en cuña, así como su equivalente en guía rectangular, centrados en 12 GHz y con un ancho de banda de 150 MHz. Para mejorar las prestaciones del filtro con respecto al presentado en el Capítulo 4, se han intentado optimizar diversos criterios de diseño, tal y como se describe en el Capítulo 5. Un análisis modal de la estructura en cuña ha sugerido la posibilidad de aumentar la anchura de los resonadores para obtener la misma frecuencia de corte que la del filtro rectangular. Esto ha implicado a su vez igualar las respuestas fuera de banda. El filtro se ha construido con la inclinación óptima entre la placas superior e inferior en términos de resistencia al efecto multipactor (30°). En el proceso de construcción se han evitado los problemas mecánicos del intento previo. Todas estas mejoras han sido verificadas con éxito en el laboratorio. La respuesta en frecuencia cumple los requisitos de diseño, a excepción de un leve desplazamiento en la frecuencia central (35 MHz). Los tests de multipactor han indicado una considerable mejora en el umbral de potencia con respecto a su equivalente rectangular (al menos 3 dB), verificada también por los resultados de la herramienta de predicción. La precisión en la predicción del umbral del filtro en cuña sigue sin ser ideal en su comparación con las medidas, pero se considera suficiente para nuestros propósitos. El excelente comportamiento respecto al multipactor compensa la mayor complejidad y los costes de diseño y fabricación. Como orientación para diseños futuros, se han compilado una serie de reglas de diseño para este tipo de filtros. Además, se ha desarrollado una formulación específica para guías en cuña que calcula las pérdidas óhmicas debidas a la conductividad finita de las paredes metálicas de la guía (ver Anexo B). Todo esto debe facilitar la eventual implementación de la tecnología en dispositivos operacionales de las cargas útiles a embarcar en satélites.

Las conclusiones expuestas demuestran que se han cumplido los objetivos de la investigación definidos en el Capítulo 1.2. Se ha estudiado la tecnología y se han sentado las bases para su aplicación en dispositivos espaciales. Utilizando la clasificación de madurez tecnológica definida por la NASA/ESA (ver Fig. 6.1), se puede asignar a los dispositivos de microondas con topología en cuña el nivel TRL 5 (“Component and/or breadboard validation in relevant environment”). Se cumplen las condiciones requeridas por este nivel, ya que varios prototipos han sido construidos y se han testeado en el laboratorio en condiciones de vacío y alta radiación (entorno espacial relevante). Las tecnologías en TRL 5 pueden ser ya consideradas en la planificación de misiones futuras. Durante los primeros ciclos de preparación de la misión se suele invertir una parte del presupuesto en que todas las tecnologías alcancen la madurez suficiente (TRL 8) para poder ser embarcadas en el satélite.

Los satélites para observación de la tierra con instrumentos SAR son candidatos propicios para implementar las guías en cuña. En la actualidad, la ESA está promoviendo nuevos desarrollos para permitir en el futuro el lanzamiento de instrumentos SAR en banda Ka (≈ 30 GHz), muy por encima de las últimas generaciones, centradas en banda L (ALOS-PalSAR), C (Envisat, RadarSat-1,2, Sentinel-1) y X (TerraSAR-X, TanDEM-X, Cosmo-SkyMed). A 30 GHz, las guías de onda típicas son aproximadamente 3 veces más pequeñas que las vistas en banda X en los Capítulos 4 y 5. Las pérdidas de propagación son pro-

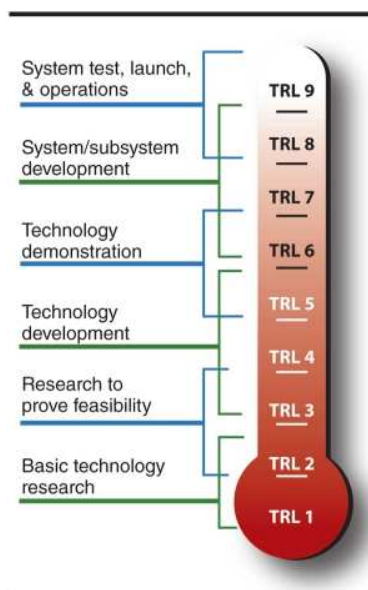


Figure 6.1: Clasificación de niveles de madurez tecnológica - Technology Readiness Level (TRL). Aplicado por NASA y ESA a todo tipo de tecnologías espaciales. Source: https://telecom.esa.int/telecom/media/document/TRL_Handbook.pdf.

porcionales al cuadrado de la frecuencia, por lo tanto 9 veces superiores a las de banda X para la misma distancia, lo que impondría mayores requerimientos de potencia al sistema para mantener la relación señal a ruido. Una configuración típica del instrumento sería la utilización de reflectores parabólicos alimentados por un array de bocinas para transmitir los pulsos radar en la dirección deseada. Las señales electromagnéticas, a una potencia relativamente elevada, suelen entrar en la bocina a través de una guía de ondas, la cual se podría substituir por una geometría en cuña para aumentar la potencia de trabajo o reducir el riesgo de multipactor. Por otra parte, ese mismo satélite puede tener filtros paso-banda como los analizados en esta tesis en el subsistema de transmisión de datos de telemetría, o en el enlace de descarga de datos a tierra. La demanda de mayores frecuencias y potencias de trabajo también existe en estos subsistemas, como demuestran los esfuerzos de la ESA por reservar nuevas cuotas del espectro en banda X y Ka para este propósito, cuando tradicionalmente se utilizaban las bandas S y X. Esto implicaría un mayor riesgo de multipactor, que nuestra topología podría subsanar.

En consecuencia, existe una creciente demanda de soluciones al problema del efecto multipactor en la industria espacial. La guía de onda en forma de cuña ha sido patentada por la ESA [41] y se han publicado diversos artículos demostrando su potencial [44, 47, 76, 78] y despertando el interés de la industria. Ahora, las perspectivas de esta tecnología quedan en manos de la comunidad espacial. Esta decisión no está exenta de riesgos, ya que todavía es necesaria una última inversión para alcanzar TRL 8 y poder embarcarse en una verdadera misión operacional. No debemos olvidar tampoco que la industria espacial es relativamente conservadora. Es reacia al cambio si no ve una absoluta necesidad o una clara

ventaja económica, como sería un ahorro en los costes de validación de dispositivos en el laboratorio. En consecuencia, no cabe esperar una implementación a corto plazo, especialmente en tiempos de una crisis tan profunda como la actual en Europa. Sin embargo, el horizonte puede todavía cambiar cuando las misiones SAR en banda Ka descritas previamente alcancen cierta madurez, y este reto técnico tome una mayor prioridad en las estrategias de innovación. Otra oportunidad puede surgir de la demanda en países emergentes en el ámbito económico y espacial, como Brasil, India, Corea o China.

Este documento culmina con los Anexos D y E. En el primero, he intentado describir mi perfil profesional y académico. El segundo contiene una compilación de contribuciones científicas relacionadas con el trabajo de investigación de esta tesis, que a su vez pueden ser de utilidad para posibles desarrollos futuros.

Appendix A

Formulation of the Electromagnetic Fields of Rectangular Waveguides

A.1 Fields and Power

The formulation of the electromagnetic (EM) fields of rectangular waveguides used throughout this PhD thesis work is defined here. Proposed by [79], all modal solutions are expressed as power-normalised EM field vectors. The modes can be classified in TE- (transverse electric) and TM- (transverse magnetic) modes, and each one is characterised by the pair of indices (m,n) . The normalisation fulfils the following unitary and orthogonality conditions between the different non-degenerate modes:

$$\iint_S (\vec{e}_i \times \vec{h}_j^*) \cdot \hat{n} dS = \delta_{i,j} = \begin{cases} 1 & i = j \\ 0 & i \neq j \end{cases} \quad (\text{A.1})$$

being \vec{e} and \vec{h} the normalised electric and magnetic field vectors, respectively, i and j arbitrary indices for the different possible modes, S the transversal cross-section area of the rectangular waveguide, as shown in Fig. A.1, and \hat{n} the unitary vector in the propagation direction (\hat{z} in Fig. A.1).

If needed, the actual amplitude values of the EM fields (\vec{E} and \vec{H}) can be obtained by applying a transmitted power-dependent factor (K) to the normalised fields, as it will be explained in Appendix A.3 (e.g. $E_x = K \cdot e_x$). This can considerably save computation time in routines that have to iteratively calculate the field values at different time instants and input-power values. The normalised functions also serve as basis functions for the determination of the EM fields in wedge-shaped waveguides by means of the BI-RME method [56].

Please note that several assumptions have been made here: time-harmonic excitation functions, propagation in the z direction and lossless conductors. Considerations about losses due to the finite conductivity of the metals are reported in Appendix B. Other useful EM-field related magnitudes used throughout this work are also included in this appendix.

Usually, the electromagnetic sources follow a sinusoidal time regime. This gives the

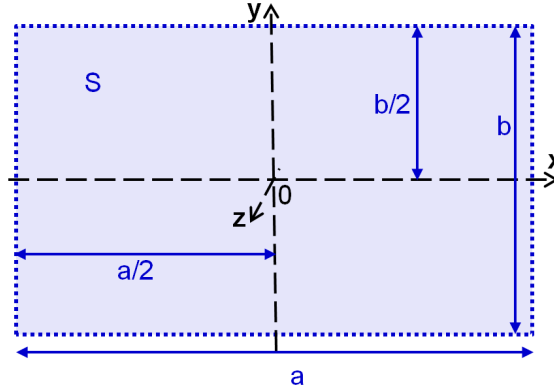


Figure A.1: Cross section of a rectangular waveguide with width a , height b and infinite in the z (propagation) direction. The origin of the Cartesian coordinate system has been placed at the geometric centre of the cross-section surface.

following phasorial notation for the electric fields:

$$\vec{E}(x, y, z, t) = \Re \left[\vec{E}_{\text{env}}(x, y, z) e^{j\omega t} \right] \quad (\text{A.2})$$

\vec{E} being the instantaneous electric field vector, $\omega = 2\pi f$ the angular frequency, t the time, and \Re is the real part operator. The z -dependency of the complex envelope of the electric field ($\vec{E}_{\text{env}}(x, y, z)$) is related to the complex propagation exponential. Assuming a lossless medium, this can be expressed as:

$$\vec{E}_{\text{env}}(x, y, z) = \vec{E}(x, y) e^{-j\beta z} \quad (\text{A.3})$$

$\beta = \sqrt{k^2 - k_C^2}$ being the propagation constant, $k = \frac{\omega}{c}$ the wavenumber in free space, c the speed of light in vacuum and $k_C = \sqrt{k_x^2 + k_y^2}$ the cutoff wavenumber of the rectangular waveguide shown in Fig. A.1. The cutoff wavenumber components in x and y direction for the different modes (m, n) of the rectangular waveguide are:

$$k_x = \frac{m\pi}{a} \quad ; \quad m = 0, 1, 2, \dots \quad (\text{A.4})$$

$$k_y = \frac{n\pi}{b} \quad ; \quad n = 0, 1, 2, \dots \quad (\text{A.5})$$

where a and b are the width and height of the rectangular cross section. Note that the case $m = n = 0$ is not allowed.

In (A.6), the instantaneous expression of the electric field phasor is shown:

$$\vec{E}(x, y, z, t) = \Re \left[\vec{E}(x, y) \right] \cdot \cos(\omega t - \beta z + \phi) |_{\phi=0} = \Re \left[\vec{E}(x, y) \right] \cdot \cos(\omega t - \beta z) \quad (\text{A.6})$$

where ϕ is the initial phase of the wave and it is normally set to zero for simplicity reasons. The instantaneous magnetic field \vec{H} is defined in the same way:

$$\vec{H}(x, y, z, t) = \Re \left[\vec{H}_{\text{env}}(x, y, z) e^{j\omega t} \right] \quad (\text{A.7})$$

The cross product of the instantaneous electric and magnetic fields gives the instantaneous Poynting vector $\vec{\mathbf{N}}$, which is a measure of the transported power density in the waveguide:

$$\vec{\mathbf{N}}(t) = \vec{\mathbf{E}}(t) \times \vec{\mathbf{H}}(t) = \frac{1}{2} \Re \left[\vec{\mathbf{E}} \times \vec{\mathbf{H}} e^{j2\omega t} \right] + \frac{1}{2} \Re \left[\vec{\mathbf{E}} \times \vec{\mathbf{H}}^* \right] \quad (\text{A.8})$$

Often it is more useful to know the average power density over a period of time $T_{avg} = 1/f$ instead:

$$\langle \vec{\mathbf{N}}(t) \rangle = \frac{1}{T_{avg}} \int_0^{T_{avg}} \vec{\mathbf{N}}(t) dt = \frac{1}{2} \Re \left[\vec{\mathbf{E}} \times \vec{\mathbf{H}}^* \right] \quad (\text{A.9})$$

Finally, the Poynting theorem derives the transmitted power P_{Transm} , which is the most common magnitude used in practice for the definition and testing of microwave waveguides:

$$P_{\text{Transm}} = \frac{1}{2} \Re \left[\iint_S \left(\vec{\mathbf{E}}_{\text{T}} \times \vec{\mathbf{H}}_{\text{T}}^* \right) \cdot \hat{\mathbf{n}} dS \right] \quad (\text{A.10})$$

being $\hat{\mathbf{n}} = \hat{\mathbf{z}}$ and the subscript T the transversal vector components.

A.2 Normalised Electromagnetic Fields

The following EM-fields formulation has been defined according to the coordinates of Fig. A.1, and it is valid for all modes. Each mode is characterised by its solution type (TE or TM) and its combination of m, n indices. Note that the letters assigned to the normalised electromagnetic magnitudes are the same as the normal ones but in lower case.

A.2.1 Transverse Electric Case

The TE case fulfils the following conditions:

$$E_z = 0 \quad (\text{A.11})$$

$$H_z \neq 0 \quad (\text{A.12})$$

E-fields

$$e_x^{(\text{TE})} = \sqrt{\frac{\epsilon_m \epsilon_n}{a \cdot b}} \frac{k_y}{k_C} \cos \left(k_x \left(x + \frac{a}{2} \right) \right) \sin \left(k_y \left(y + \frac{b}{2} \right) \right) \quad (\text{A.13})$$

$$e_y^{(\text{TE})} = -\sqrt{\frac{\epsilon_m \epsilon_n}{a \cdot b}} \frac{k_x}{k_C} \sin \left(k_x \left(x + \frac{a}{2} \right) \right) \cos \left(k_y \left(y + \frac{b}{2} \right) \right) \quad (\text{A.14})$$

$$e_z^{(\text{TE})} = 0 \quad (\text{A.15})$$

being m and n integer positive numbers (that cannot be simultaneously 0), and

$$\epsilon_i = \begin{cases} 1 & i = 0 \\ 2 & i > 0 \end{cases} \quad (\text{A.16})$$

H-fields

$$h_x^{(\text{TE})} = \sqrt{\frac{\epsilon_m \epsilon_n}{a \cdot b}} \frac{k_x}{k_C} \sin \left(k_x \left(x + \frac{a}{2} \right) \right) \cos \left(k_y \left(y + \frac{b}{2} \right) \right) \quad (\text{A.17})$$

$$h_y^{(\text{TE})} = \sqrt{\frac{\epsilon_m \epsilon_n}{a \cdot b}} \frac{k_y}{k_C} \cos \left(k_x \left(x + \frac{a}{2} \right) \right) \sin \left(k_y \left(y + \frac{b}{2} \right) \right) \quad (\text{A.18})$$

$$h_z^{(\text{TE})} = -\frac{j}{\omega \mu} \sqrt{\frac{\epsilon_m \epsilon_n}{a \cdot b}} k_C \cos \left(k_x \left(x + \frac{a}{2} \right) \right) \cos \left(k_y \left(y + \frac{b}{2} \right) \right) \quad (\text{A.19})$$

being $\mu = \mu_0$ the permeability in vacuum. Since $h_z^{(\text{TE})}$ cannot be computed applying the normalisation condition, it is directly derived from the frequency-domain Maxwell equations, using the normalised transversal electric fields:

$$H_z = \frac{j}{\omega \mu} \left(\frac{\partial E_y}{\partial x} - \frac{\partial E_x}{\partial y} \right) \quad (\text{A.20})$$

A.2.2 Transverse Magnetic Case

The TM case is defined by the following conditions:

$$E_z \neq 0 \quad (\text{A.21})$$

$$H_z = 0 \quad (\text{A.22})$$

Here, valid modes require both m and n indices to be greater than 0.

H-fields

$$h_x^{(\text{TM})} = \frac{2}{\sqrt{a \cdot b}} \frac{k_y}{k_C} \sin \left(k_x \left(x + \frac{a}{2} \right) \right) \cos \left(k_y \left(y + \frac{b}{2} \right) \right) \quad (\text{A.23})$$

$$h_y^{(\text{TM})} = -\frac{2}{\sqrt{a \cdot b}} \frac{k_x}{k_C} \cos \left(k_x \left(x + \frac{a}{2} \right) \right) \sin \left(k_y \left(y + \frac{b}{2} \right) \right) \quad (\text{A.24})$$

$$h_z^{(\text{TM})} = 0 \quad (\text{A.25})$$

E-fields

$$e_x^{(\text{TM})} = -\frac{2}{\sqrt{a \cdot b}} \frac{k_x}{k_C} \cos \left(k_x \left(x + \frac{a}{2} \right) \right) \sin \left(k_y \left(y + \frac{b}{2} \right) \right) \quad (\text{A.26})$$

$$e_y^{(\text{TM})} = -\frac{2}{\sqrt{a \cdot b}} \frac{k_y}{k_C} \sin \left(k_x \left(x + \frac{a}{2} \right) \right) \cos \left(k_y \left(y + \frac{b}{2} \right) \right) \quad (\text{A.27})$$

$$e_z^{(\text{TM})} = -\frac{j}{\omega \epsilon} \frac{2}{\sqrt{a \cdot b}} k_C \sin \left(k_x \left(x + \frac{a}{2} \right) \right) \sin \left(k_y \left(y + \frac{b}{2} \right) \right) \quad (\text{A.28})$$

being $\varepsilon = \varepsilon_0$ the dielectric permittivity in vacuum. Since $e_z^{(\text{TM})}$ cannot be computed applying the normalisation condition, it is directly derived from the frequency-domain Maxwell equations, using the normalised transversal magnetic fields:

$$E_z = \frac{j}{\omega\varepsilon} \left(\frac{\partial H_x}{\partial y} - \frac{\partial H_y}{\partial x} \right) \quad (\text{A.29})$$

A.3 Retrieval Electromagnetic Fields

Here we describe the unnormalisation procedure to retrieve the actual EM fields from the normalised functions for a given transmitted power.

A.3.1 Transverse Electric Case

First, it is useful to study for the relationship between the transverse magnetic and electric fields for the TE case. The expression for H_z is given by (A.20). The transverse magnetic and electric fields can be then derived applying the following equations:

$$\begin{aligned} \vec{H}_T &= -\frac{\gamma}{k_C^2} \cdot \nabla_T H_z \\ \vec{E}_T &= Z^{(\text{TE})} (\vec{H}_T \times \hat{z}) \end{aligned} \quad (\text{A.30})$$

being ∇ the gradient operator and $\gamma = \alpha + j\beta \stackrel{\text{lossless}}{=} j\beta$ the complex propagation constant. $Z^{(\text{TE})}$ is a variable that can be interpreted as the modal characteristic impedance. It can be also expressed as:

$$Z^{(\text{TE})} = \frac{j\omega\mu}{\gamma} \quad (\text{A.31})$$

Note that the characteristic impedance of a rectangular waveguide is defined as the result of evaluating (A.31) for the TE₁₀ fundamental mode. This is expressed by (A.32):

$$Z_C^{(\text{TE}_{10})} = \frac{j\omega\mu}{\alpha + j\beta^{(\text{TE}_{10})}} \Big|_{\alpha=0} \stackrel{k > k_C}{=} \frac{\omega\mu}{\sqrt{k^2 - (\pi/a)^2}} \quad (\text{A.32})$$

We define a unnormalisation factor $K^{(\text{TE})}$ to convert the normalised electric field func-

tions back to their actual values. We calculate then the transmitted power using (A.10):

$$\begin{aligned}
P_{\text{Transm}} &= \frac{1}{2} \Re \left[\iint_S (\vec{E}_T \times \vec{H}_T^*) \cdot \hat{n} dS \right] = \\
&= \frac{1}{2Z^{(\text{TE})}} \iint_S \|\vec{E}_T\|^2 dS = \frac{K^{(\text{TE})2}}{2Z^{(\text{TE})}} \iint_S (e_x^2 + e_y^2) dS = \\
&= \frac{K^{(\text{TE})2}}{2Z^{(\text{TE})}} \frac{\epsilon_m \epsilon_n}{a \cdot b \cdot k_C^2} \left[k_y^2 \iint_S \cos^2 \left(k_x \left(x + \frac{a}{2} \right) \right) \sin^2 \left(k_y \left(y + \frac{b}{2} \right) \right) dS + \right. \\
&\quad \left. + k_x^2 \iint_S \sin^2 \left(k_x \left(x + \frac{a}{2} \right) \right) \cos^2 \left(k_y \left(y + \frac{b}{2} \right) \right) dS \right] = \\
&= \frac{K^{(\text{TE})2}}{2Z^{(\text{TE})}} \frac{\epsilon_m \epsilon_n}{a \cdot b \cdot k_C^2} \left[k_y^2 \frac{a \cdot b}{\epsilon_m \epsilon_n} + k_x^2 \frac{a \cdot b}{\epsilon_m \epsilon_n} \right] = \frac{K^{(\text{TE})2}}{2Z^{(\text{TE})}} \tag{A.33}
\end{aligned}$$

Finally:

$$K^{(\text{TE})} = \sqrt{2P_{\text{Transm}} Z^{(\text{TE})}} \tag{A.34}$$

The unnormalisation factor must be applied as follows to retrieve the electric and magnetic fields: **E-fields**

$$\vec{E}^{(\text{TE})} = K^{(\text{TE})} \vec{e}^{(\text{TE})} \tag{A.35}$$

H-fields

$$H_z^{(\text{TE})} = K^{(\text{TE})} h_z^{(\text{TE})} \tag{A.36}$$

$$\vec{H}_T^{(\text{TE})} = -\frac{\gamma}{k_C^2} \nabla_T H_z = \frac{K^{(\text{TE})}}{Z^{(\text{TE})}} \vec{h}_T^{(\text{TE})} \tag{A.37}$$

The instantaneous fields can then be calculated multiplying by the complex propagation exponential ($e^{-j\beta^{(\text{TE})}z}$), and then applying (A.2) and (A.7).

A.3.2 Transverse Magnetic Case

The magnetic fields can be unnormalised analogously as in the TE case, considering that E_z is given by (A.29):

$$\begin{aligned}
\vec{E}_T &= -\frac{\gamma}{k_C^2} \cdot \nabla_T E_z \\
\vec{H}_T &= \frac{1}{Z^{(\text{TM})}} (\hat{z} \times \vec{E}_T)
\end{aligned} \tag{A.38}$$

$Z^{(\text{TM})}$ can be also expressed as:

$$Z^{(\text{TM})} = \frac{\gamma}{j\omega\epsilon} \tag{A.39}$$

The unnormalisation factor for the magnetic field of the TM modes is called $K^{(\text{TM})}$, and can be determined by calculating the transmitted power:

$$\begin{aligned}
 P_{\text{Transm}} &= \frac{1}{2} \Re \left[\iint_S (\vec{E}_{\text{T}} \times \vec{H}_{\text{T}}^*) \cdot \hat{n} dS \right] = \\
 &= \frac{Z^{(\text{TM})}}{2} \iint_S \|\vec{H}_{\text{T}}\|^2 dS = \frac{Z^{(\text{TM})} K^{(\text{TM})2}}{2} \iint_S (h_x^2 + h_y^2) dS = \\
 &= \frac{Z^{(\text{TM})} K^{(\text{TM})2}}{2} \frac{4}{a \cdot b \cdot k_{\text{C}}^2} \left[k_y^2 \iint_S \sin^2 \left(k_x \left(x + \frac{a}{2} \right) \right) \cos^2 \left(k_y \left(y + \frac{b}{2} \right) \right) dS + \right. \\
 &\quad \left. + k_x^2 \iint_S \cos^2 \left(k_x \left(x + \frac{a}{2} \right) \right) \sin^2 \left(k_y \left(y + \frac{b}{2} \right) \right) dS \right] = \\
 &= Z^{(\text{TM})} K^{(\text{TM})2} \frac{2}{a \cdot b \cdot k_{\text{C}}^2} \left[k_y^2 \frac{a \cdot b}{4} + k_x^2 \frac{a \cdot b}{4} \right] = \frac{Z^{(\text{TM})} K^{(\text{TM})2}}{2} \tag{A.40}
 \end{aligned}$$

Finally:

$$K^{(\text{TM})} = \sqrt{\frac{2P_{\text{Transm}}}{Z^{(\text{TM})}}} \tag{A.41}$$

The unnormalisation factor has to be applied as follows to retrieve the magnetic and electric fields: **H-fields**

$$\vec{H}^{(\text{TM})} = K^{(\text{TM})} \vec{h}^{(\text{TM})} \tag{A.42}$$

E-fields

$$E_z^{(\text{TM})} = K^{(\text{TM})} e_z^{(\text{TM})} \tag{A.43}$$

$$\vec{E}_{\text{T}}^{(\text{TM})} = -\frac{\gamma}{k_{\text{C}}^2} \nabla_{\text{T}} E_z = K^{(\text{TM})} Z^{(\text{TM})} \vec{e}_{\text{T}}^{(\text{TM})} \tag{A.44}$$

The instantaneous fields can then be calculated multiplying by the complex propagation exponential ($e^{-j\beta^{(\text{TE})}z}$) and then applying (A.7) and (A.2).

Appendix B

Losses in Waveguides due to the Finite Conductivity of the Metallic Walls

B.1 Losses in the Frontal Walls

B.1.1 Implication of Considering Losses in Wedge-shaped Waveguides

Another step towards precision in electromagnetic analysis is the consideration of ohmic losses in the metallic walls of the waveguides due to the finite conductivity of the materials. Traditionally, these losses were neglected for simplicity reasons. However, for certain applications they should be taken into account. A simple approximation is to consider the ohmic losses of the metallic walls in the propagation direction of the microwave signal, as it is done in [79,80]. This perturbation method assumes that the electromagnetic fields of a given mode are the same ones as in the perfect conductor case. Hence, the losses can be directly computed from the known surface current densities of the unperturbed modes, which results in a modal attenuation constant related to the propagation direction. However, this method does not take into account the losses in the metallic walls transversal to the propagation direction. This kind of walls are always present in the waveguide discontinuities (steps, irises) of microwave filters, transformers, or other interfaces. A method for accurately computing the ohmic losses in the transversal metallic walls (planar junctions) of rectangular waveguide devices was implemented and validated in [60] and [81]. This work extends the integral equation formulation originally proposed for a lossless case in [82] to lossy planar junctions.

B.1.2 Coupling Integrals in the Frontal Walls

For wedge-shaped waveguide devices, the consideration of the ohmic losses would also enhance the accuracy of the simulation. The calculation of the different contributions (ohmic losses in the propagation direction and in the transversal discontinuities) is more complicated given the new wedge-shaped geometry. The following coupling integral has to be computed for transversal discontinuities:

$$\int_{A_{\text{WALL}}} \vec{e}_q^{\text{WG1}} \cdot \vec{e}_p^{\text{WG1}} dS = \delta_{p,q} - \int_{A_{\text{IRIS}}} \vec{e}_q^{\text{WG1}} \cdot \vec{e}_p^{\text{WG1}} dS \quad (\text{B.1})$$

The current example considers a discontinuity between a rectangular waveguide $WG1$ and a wedge-shaped waveguide $WG2$, like the one defined in Fig. 2.1 and Fig. 2.6 in Chapter 2.3.1, and the normalised electric field functions introduced in Appendix A.2. Depending of the type of modes involved in this integral, different solutions are derived.

TE-TE

$$\int_{A_{\text{IRIS}}} \vec{e}_q^{\text{WG1(TE)}} \cdot \vec{e}_p^{\text{WG1(TE)}} dS = \frac{\sqrt{\epsilon_m \epsilon_n \epsilon_u \epsilon_v}}{a \cdot b \cdot k_{C,m,n} k_{C,u,v}} (k_{y,n} k_{y,v} \cdot \text{Int1} + k_{x,m} k_{x,u} \cdot \text{Int2}) \quad (\text{B.2})$$

being (m, n) the sub-indices associated to mode q and (u, v) the ones associated to mode p , and Int1 , Int2 integrals whose solutions are given next in this appendix.

TE-TM

$$\int_{A_{\text{IRIS}}} \vec{e}_q^{\text{WG1(TE)}} \cdot \vec{e}_p^{\text{WG1(TM)}} dS = \frac{2\sqrt{\epsilon_m \epsilon_n}}{a \cdot b \cdot k_{C,m,n} k_{C,u,v}} (-k_{y,n} k_{x,u} \cdot \text{Int1} + k_{x,m} k_{y,v} \cdot \text{Int2}) \quad (\text{B.3})$$

TM-TE

$$\int_{A_{\text{IRIS}}} \vec{e}_q^{\text{WG1(TM)}} \cdot \vec{e}_p^{\text{WG1(TE)}} dS = \frac{2\sqrt{\epsilon_u \epsilon_v}}{a \cdot b \cdot k_{C,m,n} k_{C,u,v}} (-k_{x,m} k_{y,v} \cdot \text{Int1} + k_{x,u} k_{y,n} \cdot \text{Int2}) \quad (\text{B.4})$$

TM-TM

$$\int_{A_{\text{IRIS}}} \vec{e}_q^{\text{WG1(TM)}} \cdot \vec{e}_p^{\text{WG1(TM)}} dS = \frac{4}{a \cdot b \cdot k_{C,m,n} k_{C,u,v}} (k_{x,m} k_{x,u} \cdot \text{Int1} + k_{y,n} k_{y,v} \cdot \text{Int2}) \quad (\text{B.5})$$

Note that $Int1$ and $Int2$ appear in all cases. First we define the lines delimiting the wedge-shaped iris in y -dimension (see Fig. 2.1 and Fig. 2.6), being (B.6) the expression for the bottom limit and (B.7) the one for the top limit:

$$f_b(x) = -\frac{h_1 + h_2}{4} - \frac{h_2 - h_1}{2a_{\text{Wedge}}}x \quad (\text{B.6})$$

$$f_t(x) = \frac{h_1 + h_2}{4} + \frac{h_2 - h_1}{2a_{\text{Wedge}}}x \quad (\text{B.7})$$

Now, we can solve the rest of the integrals:

$$Int1 = \int_{-\frac{a_{\text{Wedge}}}{2}}^{\frac{a_{\text{Wedge}}}{2}} \left[\cos \left(k_{x,m} \left(x + \frac{a}{2} \right) \right) \cos \left(k_{x,u} \left(x + \frac{a}{2} \right) \right) \cdot Int3(x) \right] dx \quad (\text{B.8})$$

where

$$Int3(x) = \int_{f_b(x)}^{f_t(x)} \sin \left(k_{y,n} \left(y + \frac{b}{2} \right) \right) \sin \left(k_{y,v} \left(y + \frac{b}{2} \right) \right) dy \quad (\text{B.9})$$

$$Int2 = \int_{-\frac{a_{\text{Wedge}}}{2}}^{\frac{a_{\text{Wedge}}}{2}} \left[\sin \left(k_{x,m} \left(x + \frac{a}{2} \right) \right) \sin \left(k_{x,u} \left(x + \frac{a}{2} \right) \right) \cdot Int4(x) \right] dx \quad (\text{B.10})$$

where

$$Int4(x) = \int_{f_b(x)}^{f_t(x)} \cos \left(k_{y,n} \left(y + \frac{b}{2} \right) \right) \cos \left(k_{y,v} \left(y + \frac{b}{2} \right) \right) dy \quad (\text{B.11})$$

$$\begin{aligned} Int3(x) = & \frac{1}{2(k_{y,n} + k_{y,v})} \sin \left[\frac{(k_{y,n} + k_{y,v})}{4a_{\text{Wedge}}} (a_{\text{Wedge}}(2b - h_1 - h_2) + 2(h_2 - h_1)x) \right] - \\ & + \frac{1}{2(k_{y,n} + k_{y,v})} \sin \left[\frac{(k_{y,n} + k_{y,v})}{4a_{\text{Wedge}}} (a_{\text{Wedge}}(2b + h_1 + h_2) + 2(h_2 - h_1)x) \right] + \\ & + \frac{1}{2(k_{y,n} - k_{y,v})} \sin \left[\frac{(k_{y,n} - k_{y,v})}{4a_{\text{Wedge}}} (a_{\text{Wedge}}(2b + h_1 + h_2) + 2(h_2 - h_1)x) \right] - \\ & + \frac{1}{2(k_{y,n} - k_{y,v})} \sin \left[\frac{(k_{y,n} - k_{y,v})}{4a_{\text{Wedge}}} (a_{\text{Wedge}}(2b - h_1 - h_2) + 2(h_2 - h_1)x) \right] \end{aligned} \quad (\text{B.12})$$

$$\begin{aligned}
Int4(x) = & \frac{1}{2(k_{y,n} + k_{y,v})} \sin \left[\frac{(k_{y,n} + k_{y,v})}{4a_{\text{Wedge}}} (a_{\text{Wedge}}(2b + h_1 + h_2) + 2(h_2 - h_1)x) \right] - \\
& + \frac{1}{2(k_{y,n} + k_{y,v})} \sin \left[\frac{(k_{y,n} + k_{y,v})}{4a_{\text{Wedge}}} (a_{\text{Wedge}}(2b - h_1 - h_2) + 2(h_2 - h_1)x) \right] + \\
& + \frac{1}{2(k_{y,n} - k_{y,v})} \sin \left[\frac{(k_{y,n} - k_{y,v})}{4a_{\text{Wedge}}} (a_{\text{Wedge}}(2b + h_1 + h_2) + 2(h_2 - h_1)x) \right] - \\
& + \frac{1}{2(k_{y,n} - k_{y,v})} \sin \left[\frac{(k_{y,n} - k_{y,v})}{4a_{\text{Wedge}}} (a_{\text{Wedge}}(2b - h_1 - h_2) + 2(h_2 - h_1)x) \right]
\end{aligned} \tag{B.13}$$

Then, (B.12) and (B.13) can be substituted in (B.8) and (B.10), forming a sum of integrals that share a common structure, with the exception of some constant values. The ones of *Int1* have the following form:

$$\begin{aligned}
C_0 \int \cos(C_1(C_2 + x)) \cos(C_3(C_2 + x)) \sin(C_4(C_5 + C_6x)) dx = \\
= \frac{C_0 \cos(C_1C_2 + C_2C_3 - C_4C_5 + (C_1 + C_3 - C_4C_6)x)}{4(C_1 + C_3 - C_4C_6)} - \\
+ \frac{C_0 \cos(C_1C_2 - C_2C_3 + C_4C_5 + (C_1 - C_3 + C_4C_6)x)}{4(C_1 - C_3 + C_4C_6)} - \\
+ \frac{C_0 \cos(C_1C_2 + C_2C_3 + C_4C_5 + (C_1 + C_3 + C_4C_6)x)}{4(C_1 + C_3 + C_4C_6)} + \\
+ \frac{C_0 \cos(-C_1C_2 + C_2C_3 + C_4C_5 + (-C_1 + C_3 + C_4C_6)x)}{4(C_1 - C_3 - C_4C_6)}
\end{aligned} \tag{B.14}$$

where C_n are constants that have to be substituted accordingly depending on the term in the sum. Analogously, the integrals of *Int2* have the form:

$$\begin{aligned}
C_0 \int \sin(C_1(C_2 + x)) \sin(C_3(C_2 + x)) \sin(C_4(C_5 + C_6x)) dx = \\
= -\frac{C_0 \cos(C_1C_2 + C_2C_3 - C_4C_5 + (C_1 + C_3 - C_4C_6)x)}{4(C_1 + C_3 - C_4C_6)} - \\
+ \frac{C_0 \cos(C_1C_2 - C_2C_3 + C_4C_5 + (C_1 - C_3 + C_4C_6)x)}{4(C_1 - C_3 + C_4C_6)} + \\
+ \frac{C_0 \cos(C_1C_2 + C_2C_3 + C_4C_5 + (C_1 + C_3 + C_4C_6)x)}{4(C_1 + C_3 + C_4C_6)} + \\
+ \frac{C_0 \cos(-C_1C_2 + C_2C_3 + C_4C_5 + (-C_1 + C_3 + C_4C_6)x)}{4(C_1 - C_3 - C_4C_6)}
\end{aligned} \tag{B.15}$$

The tedious substitution of these equations to obtain the final expressions of (B.2) to (B.5) has not been included here. However, it is important to note that special attention has to be given when implementing the formula to avoid singularities caused by dividing by 0, which occurs for certain mode indices or waveguide dimensions. Computation time can be

saved if special cases are considered, e.g. modes with indices equal 0, which lead to much simpler analytical expressions.

B.2 Losses in Propagation

B.2.1 Derivation of the Attenuation Constant

For calculating the losses in propagation, the assumption that the waveguide metal has a good, however finite conductivity $\sigma \gg \omega\epsilon$, is made. This justifies using here the same expression of the electromagnetic fields as for the perfect-conductor case. The approach adopted here for determining the propagation losses is based on the superficial impedance of the metal and the penetration depth of the waves in it [79]. The propagation losses can be described by a negative exponential with a real exponent, which is the attenuation constant parameter α_c (see (B.16)).

$$P_{\text{Transm}}(z) = P_{\text{Transm}}(z = 0)e^{-2\alpha_c z} \quad (\text{B.16})$$

Hence, the objective is to estimate this parameter from the known conductivity properties of a particular metal. A different way to express α_c is in terms of the dissipation. The evolution of the transmitted power along the z axis is equal to the negative dissipated power per length unit (P_{Lp}) of the conductors (B.17):

$$\frac{dP_{\text{Transm}}}{dz} = -2\alpha_c P_{\text{Transm}} = -P_{Lp} \Rightarrow \alpha_c = \frac{P_{Lp}}{2P_{\text{Transm}}} \quad (\text{B.17})$$

For calculating P_{Lp} , the surface current density \vec{J}_S is needed, as well as physical properties of the conductor like its penetration depth δ (B.18) and the superficial impedance R_S (B.19), where

$$\delta = \frac{1}{\sqrt{\pi f \mu \sigma}} \quad (\text{B.18})$$

The surface impedance of a conductor is defined as:

$$R_S = \frac{1}{\delta \sigma} = \sqrt{\frac{\pi f \mu}{\sigma}} \quad (\text{B.19})$$

The dissipated power can be computed with a line integral of the squared module of the surface current density \vec{J}_S along the wedge-shaped waveguide contour:

$$P_{Lp} = \frac{R_S}{2} \int_{\text{Wedge-contour}} |\vec{J}_S|^2 dl \quad (\text{B.20})$$

\vec{J}_S is obtained from the component of the magnetic field tangential to the contour:

$$\vec{J}_S = \hat{n} \times \vec{H}|_{\text{Wedge contour}} = (n_y H_z) \hat{x} - (n_x H_z) \hat{y} + (n_x H_y - n_y H_x) \hat{z} \quad (\text{B.21})$$

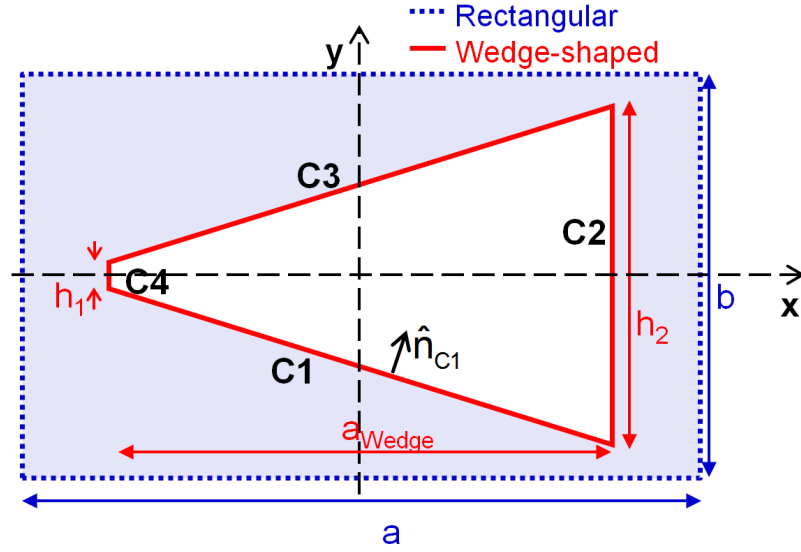


Figure B.1: Contours of a wedge-shaped WG cross section and perpendicular unitary vector.

where \hat{n} is a unitary vector defined in the cross-section plane, perpendicular to the metallic walls and pointing towards the interior of the waveguide. This integral can be decomposed into four sub-integrals, each of them comprising the line integral of one of the contours of the waveguide:

$$P_{Lp} = \frac{R_S}{2} \left[\int_{C1} |\hat{n}_{C1} \times \vec{H}|_{C1}|^2 dl + \int_{C2} |\hat{n}_{C2} \times \vec{H}|_{C2}|^2 dl + \int_{C3} |\hat{n}_{C3} \times \vec{H}|_{C3}|^2 dl + \int_{C4} |\hat{n}_{C4} \times \vec{H}|_{C4}|^2 dl \right] \quad (\text{B.22})$$

being C1 to C4 the contours defined in Fig. B.1. These integrals can be solved analytically, as it will be shown in the next section.

B.2.2 Resolution for the Wedge-shaped Waveguide Case

As an example, the losses in propagation of a wedge-shaped waveguide will be calculated. The magnetic field in a wedge-shaped waveguide is derived as described in Chapter 2.1.

Contour C1

The unitary vector perpendicular to this contour is \hat{n}_{C1} (B.23):

$$\hat{n}_{C1} = \frac{h_2 - h_1}{\sqrt{(h_2 - h_1)^2 + 4a_{\text{Wedge}}^2}} \hat{x} + \frac{2a_{\text{Wedge}}}{\sqrt{(h_2 - h_1)^2 + 4a_{\text{Wedge}}^2}} \hat{y} \quad (\text{B.23})$$

Applying (B.21), the surface current density has the following components, considering the TE fundamental mode (with coefficient 1) of the wedge-shaped waveguide:

$$J_{S,x} = \frac{2a_{\text{Wedge}} K_1^{\text{arb(TE)}}}{\sqrt{(h_2 - h_1)^2 + 4a_{\text{Wedge}}^2}} \sum_{i=1}^{\infty} C I_{1,i}^{\text{TETE}} \cdot h_{z,i}^{\square(\text{TE})} \quad (\text{B.24})$$

being the coupling integral $C I_{1,i}^{\text{TETE}} = \left\langle \vec{e}_{T,1}^{\text{arb(TE)}}; \vec{e}_i^{\square(\text{TE})} \right\rangle$, as introduced in Chapter 2.1, and $h_{z,i}^{\square(\text{TE})}$ the normalised magnetic field of the rectangular waveguide defined in (A.19).

$$J_{S,y} = -\frac{(h_2 - h_1) K_1^{\text{arb(TE)}}}{\sqrt{(h_2 - h_1)^2 + 4a_{\text{Wedge}}^2}} \sum_{i=1}^{\infty} C I_{1,i}^{\text{TETE}} \cdot h_{z,i}^{\square(\text{TE})} \quad (\text{B.25})$$

$$J_{S,z} = \frac{K_1^{\text{arb(TE)}} \cdot (h_2 - h_1)}{Z_1^{\text{arb(TE)}} \sqrt{(h_2 - h_1)^2 + 4a_{\text{Wedge}}^2}} \left(\sum_{i=1}^{\infty} C I_{1,i}^{\text{TETE}} \cdot h_{y,i}^{\square(\text{TE})} + \sum_{i'=1}^{\infty} C I_{1,i'}^{\text{TETM}} \cdot h_{y,i'}^{\square(\text{TM})} \right) - \\ + \frac{K_1^{\text{arb(TE)}} 2a_{\text{Wedge}}}{Z_1^{\text{arb(TE)}} \sqrt{(h_2 - h_1)^2 + 4a_{\text{Wedge}}^2}} \left(\sum_{i=1}^{\infty} C I_{1,i}^{\text{TETE}} \cdot h_{x,i}^{\square(\text{TE})} + \sum_{i'=1}^{\infty} C I_{1,i'}^{\text{TETM}} \cdot h_{x,i'}^{\square(\text{TM})} \right) \quad (\text{B.26})$$

$$\int_{C1} |\vec{J}_s|^2 dl = \frac{K_1^{\text{arb(TE)2}}}{(h_2 - h_1)^2 + 4a_{\text{Wedge}}^2} \cdot
\left[
\begin{aligned}
& (4a_{\text{Wedge}}^2 + (h_2 - h_1)^2) \cdot \sum_{i=1}^{\infty} \sum_{j=1}^{\infty} CI_{1,i}^{\text{TETE}} CI_{1,j}^{\text{TETE}} \int_{C1} h_{z,i}^{\square(\text{TE})} h_{z,j}^{\square(\text{TE})} dl + \\
& + \frac{(h_2 - h_1)^2}{Z_1^{\text{arb(TE)2}}} \cdot \left(\sum_{i=1}^{\infty} \sum_{j=1}^{\infty} CI_{1,i}^{\text{TETE}} CI_{1,j}^{\text{TETE}} \int_{C1} h_{y,i}^{\square(\text{TE})} h_{y,j}^{\square(\text{TE})} dl + \right. \\
& \quad + 2 \sum_{i=1}^{\infty} \sum_{j=1}^{\infty} CI_{1,i}^{\text{TETE}} CI_{1,j}^{\text{TETM}} \int_{C1} h_{y,i}^{\square(\text{TE})} h_{y,j}^{\square(\text{TM})} dl + \\
& \quad \left. + \sum_{i=1}^{\infty} \sum_{j=1}^{\infty} CI_{1,i}^{\text{TETM}} CI_{1,j}^{\text{TETM}} \int_{C1} h_{y,i}^{\square(\text{TM})} h_{y,j}^{\square(\text{TM})} dl \right) - \\
& + \frac{4a_{\text{Wedge}}(h_2 - h_1)}{Z_1^{\text{arb(TE)2}}} \cdot \left(\sum_{i=1}^{\infty} \sum_{j=1}^{\infty} CI_{1,i}^{\text{TETE}} CI_{1,j}^{\text{TETE}} \int_{C1} h_{y,i}^{\square(\text{TE})} h_{x,j}^{\square(\text{TE})} dl + \right. \\
& \quad + \sum_{i=1}^{\infty} \sum_{j=1}^{\infty} CI_{1,i}^{\text{TETE}} CI_{1,j}^{\text{TETM}} \int_{C1} h_{y,i}^{\square(\text{TE})} h_{x,j}^{\square(\text{TM})} dl + \\
& \quad + \sum_{i=1}^{\infty} \sum_{j=1}^{\infty} CI_{1,i}^{\text{TETM}} CI_{1,j}^{\text{TETE}} \int_{C1} h_{y,i}^{\square(\text{TM})} h_{x,j}^{\square(\text{TE})} dl + \\
& \quad \left. + \sum_{i=1}^{\infty} \sum_{j=1}^{\infty} CI_{1,i}^{\text{TETM}} CI_{1,j}^{\text{TETM}} \int_{C1} h_{y,i}^{\square(\text{TM})} h_{x,j}^{\square(\text{TM})} dl \right) + \\
& + \frac{4a_{\text{Wedge}}^2}{Z_1^{\text{arb(TE)2}}} \cdot \left(\sum_{i=1}^{\infty} \sum_{j=1}^{\infty} CI_{1,i}^{\text{TETE}} CI_{1,j}^{\text{TETE}} \int_{C1} h_{x,i}^{\square(\text{TE})} h_{x,j}^{\square(\text{TE})} dl + \right. \\
& \quad + 2 \sum_{i=1}^{\infty} \sum_{j=1}^{\infty} CI_{1,i}^{\text{TETE}} CI_{1,j}^{\text{TETM}} \int_{C1} h_{x,i}^{\square(\text{TE})} h_{x,j}^{\square(\text{TM})} dl + \\
& \quad \left. + \sum_{i=1}^{\infty} \sum_{j=1}^{\infty} CI_{1,i}^{\text{TETM}} CI_{1,j}^{\text{TETM}} \int_{C1} h_{x,i}^{\square(\text{TM})} h_{x,j}^{\square(\text{TM})} dl \right)
\end{aligned}
\right] \quad (\text{B.27})$$

The different integrals along the contour $C1$ in (B.27) can be solved analytically after introducing the corresponding expression of the normalised magnetic field components, substituting y by (B.6) and integrating between $-\frac{a_{\text{Wedge}}}{2}$ and $\frac{a_{\text{Wedge}}}{2}$ over x .

Contour C2

$$\hat{n}_{C2} = -\hat{x} \quad (\text{B.28})$$

The surface current density has the following components:

$$J_{S,x} = 0 \quad (\text{B.29})$$

$$J_{S,y} = K_1^{\text{arb(TE)}} \sum_{i=1}^{\infty} CI_{1,i}^{\text{TE(TE)}} \cdot h_{z,i}^{\square(\text{TE})} \quad (\text{B.30})$$

$$J_{S,z} = -\frac{K_1^{\text{arb(TE)}}}{Z_1^{\text{arb(TE)}}} \left(\sum_{i=1}^{\infty} CI_{1,i}^{\text{TE(TE)}} \cdot h_{y,i}^{\square(\text{TE})} + \sum_{i'=1}^{\infty} CI_{1,i'}^{\text{TE(TM)}} \cdot h_{y,i'}^{\square(\text{TM})} \right) \quad (\text{B.31})$$

$$\int_{C2} \left| \vec{J}_S \right|^2 dl = K_1^{\text{arb(TE)2}} \left[\begin{aligned} & \sum_{i=1}^{\infty} \sum_{j=1}^{\infty} CI_{1,i}^{\text{TE(TE)}} CI_{1,j}^{\text{TE(TE)}} \int_{C2} h_{z,i}^{\square(\text{TE})} h_{z,j}^{\square(\text{TE})} dl + \\ & \left(\sum_{i=1}^{\infty} \sum_{j=1}^{\infty} CI_{1,i}^{\text{TE(TE)}} CI_{1,j}^{\text{TE(TE)}} \int_{C2} h_{y,i}^{\square(\text{TE})} h_{y,j}^{\square(\text{TE})} dl + \right. \\ & + 2 \sum_{i=1}^{\infty} \sum_{j=1}^{\infty} CI_{1,i}^{\text{TE(TM)}} CI_{1,j}^{\text{TE(TM)}} \int_{C2} h_{y,i}^{\square(\text{TE})} h_{y,j}^{\square(\text{TM})} dl + \\ & \left. \sum_{i=1}^{\infty} \sum_{j=1}^{\infty} CI_{1,i}^{\text{TM(TM)}} CI_{1,j}^{\text{TM(TM)}} \int_{C2} h_{y,i}^{\square(\text{TM})} h_{y,j}^{\square(\text{TM})} dl \right) \end{aligned} \right] \quad (\text{B.32})$$

The different integrals along the contour C2 in the summations of (B.32) can be also solved analytically after introducing the corresponding expression of the normalised magnetic field components, substituting x by $\frac{a_{\text{Wedge}}}{2}$ and integrating between $-\frac{h_2}{2}$ and $\frac{h_2}{2}$ over y .

Contour C3

$$\hat{n}_{C3} = \frac{h_2 - h_1}{\sqrt{(h_2 - h_1)^2 + 4a_{\text{Wedge}}^2}} \hat{x} - \frac{2a_{\text{Wedge}}}{\sqrt{(h_2 - h_1)^2 + 4a_{\text{Wedge}}^2}} \hat{y} \quad (\text{B.33})$$

The surface current density has the following components:

$$J_{S,x} = -\frac{2a_{\text{Wedge}} K_1^{\text{arb(TE)}}}{\sqrt{(h_2 - h_1)^2 + 4a_{\text{Wedge}}^2}} \sum_{i=1}^{\infty} C I_{1,i}^{\text{TETE}} \cdot h_{z,i}^{\square(\text{TE})} \quad (\text{B.34})$$

$$J_{S,y} = -\frac{(h_2 - h_1) K_1^{\text{arb(TE)}}}{\sqrt{(h_2 - h_1)^2 + 4a_{\text{Wedge}}^2}} \sum_{i=1}^{\infty} C I_{1,i}^{\text{TETE}} \cdot h_{z,i}^{\square(\text{TE})} \quad (\text{B.35})$$

$$J_{S,z} = \frac{K_1^{\text{arb(TE)}} (h_2 - h_1)}{Z_1^{\text{arb(TE)}} \sqrt{(h_2 - h_1)^2 + 4a_{\text{Wedge}}^2}} \left(\sum_{i=1}^{\infty} C I_{1,i}^{\text{TETE}} \cdot h_{y,i}^{\square(\text{TE})} + \sum_{i'=1}^{\infty} C I_{1,i'}^{\text{TETM}} \cdot h_{y,i'}^{\square(\text{TM})} \right) + \frac{K_1^{\text{arb(TE)}} 2a_{\text{Wedge}}}{Z_1^{\text{arb(TE)}} \sqrt{(h_2 - h_1)^2 + 4a_{\text{Wedge}}^2}} \left(\sum_{i=1}^{\infty} C I_{1,i}^{\text{TETE}} \cdot h_{x,i}^{\square(\text{TE})} + \sum_{i'=1}^{\infty} C I_{1,i'}^{\text{TETM}} \cdot h_{x,i'}^{\square(\text{TM})} \right) \quad (\text{B.36})$$

$$\int_{C3} \left| \vec{J}_S \right|^2 dl = \frac{K_1^{\text{arb(TE)2}}}{(h_2 - h_1)^2 + 4a_{\text{Wedge}}^2}.$$

$$\left[\begin{aligned}
& (4a_{\text{Wedge}}^2 + (h_2 - h_1)^2) \cdot \sum_{i=1}^{\infty} \sum_{j=1}^{\infty} CI_{1,i}^{\text{TE(TE)}} CI_{1,j}^{\text{TE(TE)}} \int_{C3} h_{z,i}^{\square(\text{TE})} h_{z,j}^{\square(\text{TE})} dl + \\
& + \frac{(h_2 - h_1)^2}{Z_1^{\text{arb(TE)2}}} \cdot \left(\begin{aligned}
& \sum_{i=1}^{\infty} \sum_{j=1}^{\infty} CI_{1,i}^{\text{TE(TE)}} CI_{1,j}^{\text{TE(TE)}} \int_{C3} h_{y,i}^{\square(\text{TE})} h_{y,j}^{\square(\text{TE})} dl + \\
& + 2 \sum_{i=1}^{\infty} \sum_{j=1}^{\infty} CI_{1,i}^{\text{TE(TE)}} CI_{1,j}^{\text{TE(TM)}} \int_{C3} h_{y,i}^{\square(\text{TE})} h_{y,j}^{\square(\text{TM})} dl + \\
& + \sum_{i=1}^{\infty} \sum_{j=1}^{\infty} CI_{1,i}^{\text{TM(TM)}} CI_{1,j}^{\text{TM(TM)}} \int_{C3} h_{y,i}^{\square(\text{TM})} h_{y,j}^{\square(\text{TM})} dl
\end{aligned} \right) + \\
& + \frac{4a_{\text{Wedge}}(h_2 - h_1)}{Z_1^{\text{arb(TE)2}}} \cdot \left(\begin{aligned}
& \sum_{i=1}^{\infty} \sum_{j=1}^{\infty} CI_{1,i}^{\text{TE(TE)}} CI_{1,j}^{\text{TE(TE)}} \int_{C3} h_{y,i}^{\square(\text{TE})} h_{x,j}^{\square(\text{TE})} dl + \\
& + \sum_{i=1}^{\infty} \sum_{j=1}^{\infty} CI_{1,i}^{\text{TE(TM)}} CI_{1,j}^{\text{TE(TM)}} \int_{C3} h_{y,i}^{\square(\text{TE})} h_{x,j}^{\square(\text{TM})} dl + \\
& + \sum_{i=1}^{\infty} \sum_{j=1}^{\infty} CI_{1,i}^{\text{TM(TM)}} CI_{1,j}^{\text{TE(TE)}} \int_{C3} h_{y,i}^{\square(\text{TM})} h_{x,j}^{\square(\text{TE})} dl + \\
& + \sum_{i=1}^{\infty} \sum_{j=1}^{\infty} CI_{1,i}^{\text{TM(TM)}} CI_{1,j}^{\text{TM(TM)}} \int_{C3} h_{y,i}^{\square(\text{TM})} h_{x,j}^{\square(\text{TM})} dl
\end{aligned} \right) + \\
& + \frac{4a_{\text{Wedge}}^2}{Z_1^{\text{arb(TE)2}}} \cdot \left(\begin{aligned}
& \sum_{i=1}^{\infty} \sum_{j=1}^{\infty} CI_{1,i}^{\text{TE(TE)}} CI_{1,j}^{\text{TE(TE)}} \int_{C3} h_{x,i}^{\square(\text{TE})} h_{x,j}^{\square(\text{TE})} dl + \\
& + 2 \sum_{i=1}^{\infty} \sum_{j=1}^{\infty} CI_{1,i}^{\text{TE(TM)}} CI_{1,j}^{\text{TE(TM)}} \int_{C3} h_{x,i}^{\square(\text{TE})} h_{x,j}^{\square(\text{TM})} dl + \\
& + \sum_{i=1}^{\infty} \sum_{j=1}^{\infty} CI_{1,i}^{\text{TM(TM)}} CI_{1,j}^{\text{TM(TM)}} \int_{C3} h_{x,i}^{\square(\text{TM})} h_{x,j}^{\square(\text{TM})} dl
\end{aligned} \right)
\end{aligned} \right] \quad (\text{B.37})$$

The integrals are the same as the ones for contour C1. This time, y has to be substituted by (B.7) and the integration has to be done between $-\frac{a_{\text{Wedge}}}{2}$ and $\frac{a_{\text{Wedge}}}{2}$ over x .

Contour C4

$$\hat{n}_{C4} = \hat{x} \quad (\text{B.38})$$

The surface current density has the following components:

$$J_{S,x} = 0 \quad (\text{B.39})$$

$$J_{S,y} = -K_1^{\text{arb(TE)}} \sum_{i=1}^{\infty} CI_{1,i}^{\text{TE TE}} \cdot h_{z,i}^{\square(\text{TE})} \quad (\text{B.40})$$

$$J_{S,z} = \frac{K_1^{\text{arb(TE)}}}{Z_1^{\text{arb(TE)}}} \left(\sum_{i=1}^{\infty} CI_{1,i}^{\text{TE TE}} \cdot h_{y,i}^{\square(\text{TE})} + \sum_{i'=1}^{\infty} CI_{1,i'}^{\text{TE TM}} \cdot h_{y,i'}^{\square(\text{TM})} \right) \quad (\text{B.41})$$

$$\int_{C4} |\vec{J}_S|^2 dl = K_1^{\text{arb(TE)2}} \left[\begin{aligned} & \sum_{i=1}^{\infty} \sum_{j=1}^{\infty} CI_{1,i}^{\text{TE TE}} CI_{1,j}^{\text{TE TE}} \int_{C4} h_{z,i}^{\square(\text{TE})} h_{z,j}^{\square(\text{TE})} dl + \\ & \left(\sum_{i=1}^{\infty} \sum_{j=1}^{\infty} CI_{1,i}^{\text{TE TE}} CI_{1,j}^{\text{TE TE}} \int_{C4} h_{y,i}^{\square(\text{TE})} h_{y,j}^{\square(\text{TE})} dl + \right. \\ & \left. + 2 \sum_{i=1}^{\infty} \sum_{j=1}^{\infty} CI_{1,i}^{\text{TE TE}} CI_{1,j}^{\text{TE TM}} \int_{C4} h_{y,i}^{\square(\text{TE})} h_{y,j}^{\square(\text{TM})} dl + \right. \\ & \left. \sum_{i=1}^{\infty} \sum_{j=1}^{\infty} CI_{1,i}^{\text{TE TM}} CI_{1,j}^{\text{TE TM}} \int_{C4} h_{y,i}^{\square(\text{TM})} h_{y,j}^{\square(\text{TM})} dl \right) \end{aligned} \right] \quad (\text{B.42})$$

The different integrals along the contour C4 in the summations of (B.42) are identical to the ones of contour C2, except for the limits of the integral. Here, x is substituted by $-\frac{a_{\text{Wedge}}}{2}$ and the integral is calculated between $-\frac{h_1}{2}$ and $\frac{h_1}{2}$ over y .

It should be noted that P_{LP} is proportional to P_{Trans} through (2.13), since all contour integrals are proportional to $K_1^{\text{arb(TE)2}}$. Therefore, α_c can be directly derived from the resolution of (B.22).

Appendix C

Multipactor Detection Test

C.1 Test Setup and Procedure

The tests of the multipactor discharges mentioned in this thesis were performed in the laboratories of ESA-ESTEC, Noordwijk, the Netherlands. Formerly part of the Payload Systems Laboratory, the High Power RF Laboratory has been recently transferred to Valencia, Spain, and is now located within the Technical University of Valencia campus (<http://www.val-space.com/highpowerlabrf>). It has the capability of generating microwave signals at different frequency bands up to mm-waves, and can be configured for testing waveguide or coaxial devices. State-of-the-art high power amplifiers and vector network analysers allow handling the increasing frequencies and power requirements of new microwave components for space applications.

The test environment is under certified “clean room” conditions, avoiding the contamination of the test samples by foreign particles like dust, humidity, etc. The essential equipment to reproduce the space scenario conditions are the vacuum chamber (see Fig. C.1) and different high-energy particle generators, like radioactive sources or regulated electron guns [83]. The available vacuum chambers can reduce the pressure to levels below 10^{-7} mbar and actively control the temperature between -120°C and 150°C . A metallic plate also controls the temperature of the test elements as long as they are attached to it inside the chamber (see Fig. C.2). Before starting the multipactor tests, several preliminary procedures are conducted, like the measurement of the frequency response stability over temperature. The first step is to measure it at ambient temperature and a low power signal with a network analyser. Then, a cycling process starts in the thermal chamber Fig. C.3, which subjects the device to a full range of temperature steps during several minutes. After the process is finished, the frequency response is measured again to verify if mechanical stresses caused by temperature gradients have modified it.

The multipactor test setup has two specially designed hermetic input/output interfaces to the vacuum chamber. Outside the vacuum chamber, there is the power conditioning network, which is configured to provide a range of selectable input powers, and a set of radiator loads, which are used to dissipate the power and avoid reflections at the end of the test chain, which



Figure C.1: Vacuum chamber. It reaches a pressure below 10^{-7} mbar.

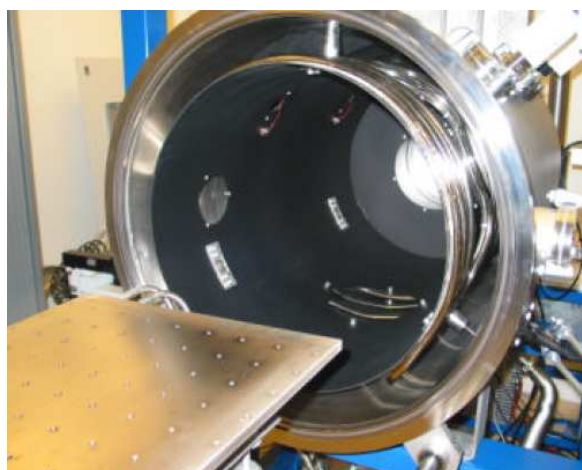


Figure C.2: Metallic plate for the temperature control of the microwave elements inside the vacuum chamber.



Figure C.3: Thermal cycling chamber. Device under test is placed in a hermetic bag.

could distort the test results. Furthermore, a network of power dividers and splitters are installed to enable the measurement of the input, reflected and output power at the vacuum chamber ports, and the introduction of multipactor detection methods, as will be described in more detail in the next Chapter C.2. The device under test (DUT) belongs inside the vacuum chamber, among with temperature sensors and other detection probes (see Fig. C.4 and Fig. C.5). In order to initiate a multipactor discharge, a sufficient free electron seeding in the vicinity of the DUT is required. For this purpose, usually a radioactive source is also introduced in the vacuum chamber. The most common radioactive element, also of relevance for other industrial and medical fields, is a Strontium-90 β -emitting source, with a half-life of 28.8 years. It is placed shortly before sealing (and removed after opening) the chamber door to minimise radiation exposure to the individuals conducting the test. The functional block-diagram of the official ESA test setup is shown in Fig. C.4. This has been the configuration used for all tests performed during this investigation.

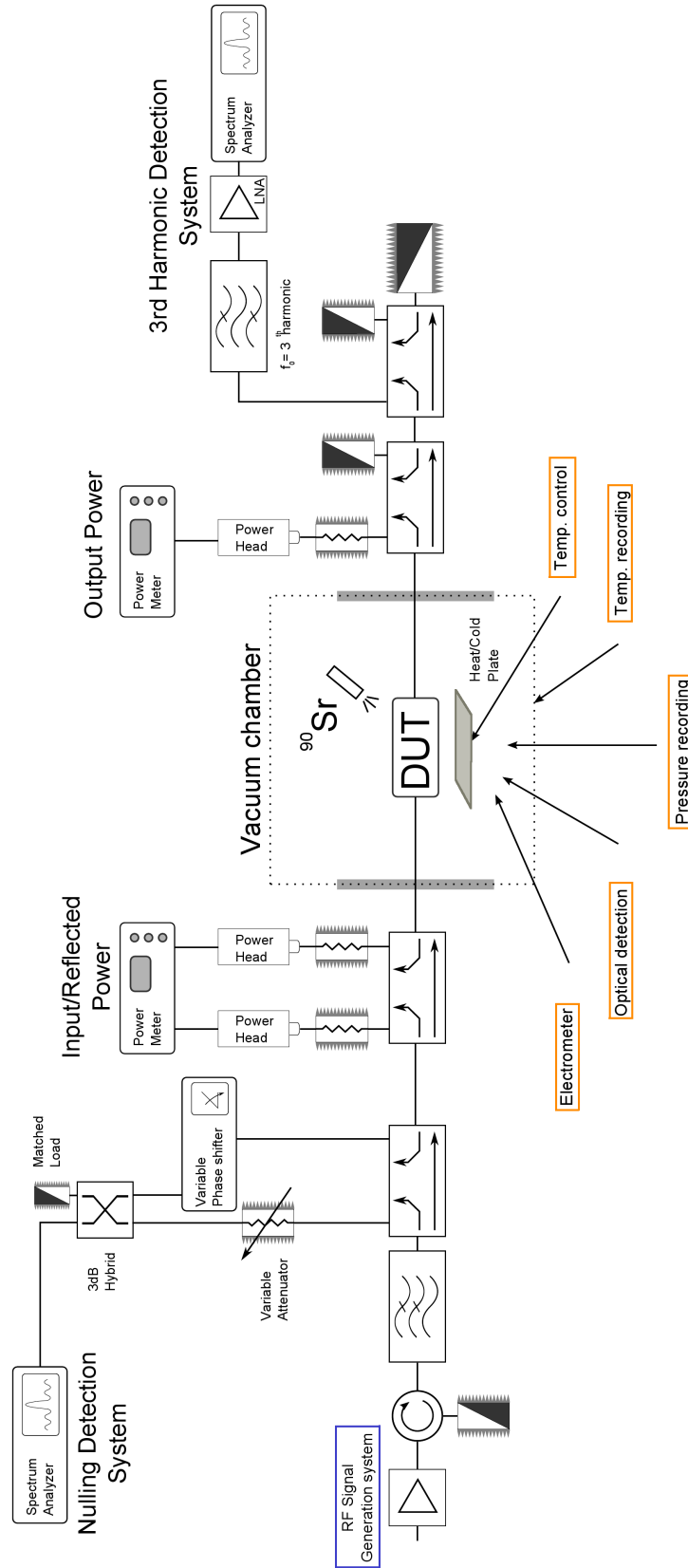


Figure C.4: Scheme of the multipactor test-bed. Source: ESA-Val Space Consortium High Power Laboratory.

Table C.1: Typical parameters and requirements of a multipactor test.

Test requirement	Typical Value
Frequency	Device centre/working frequency
Pressure chamber	$< 2 \cdot 10^{-6}$ mbar
Reference temperature base plate	Ambient
Type of input power	Pulsed
Pulse repetition frequency	1 kHz
Pulse width	$20\mu\text{s}$
Duty cycle	2%

Before starting the actual test, a reference sample with known multipactor behaviour is placed as DUT inside the vacuum chamber and the pressure is reduced. The detection of the power threshold of the reference sample at the specified levels is expected to verify the proper operation and sensitivity of the test setup. Only then, the original DUT replaces the reference sample inside the chamber, and then the outpumping phase restarts. The vacuum chamber has two complementary pumping mechanisms: an electrical pump with a high speed ventilator, and a cryopump suited for achieving high vacuum. The latter consists of a head, located within the chamber, that is kept at an extremely low temperature with the help of liquid nitrogen. The particles and molecules within the test environment condensate and get trapped on the surface of the head, reducing the overall pressure. The cryopump is usually connected right after the electrical pump, when the pressure and amount of molecules is already small, since otherwise its mechanism would quickly saturate. The combination of both methods provides the required space vacuum conditions in a reduced time frame. Even so, this process takes between 12 and 24 hours, and is usually left running overnight before starting the test. During this time, the pressure is gradually reduced not only in the vacuum chamber, but the gases are also evacuated from the interior of the DUT, assuming it has hollow spaces. The gas molecules can flow out of the device through venting holes, like the ones shown in Fig. C.6. Their amount and diameter can be designed with [51], which follows the formulas of [3]). The venting holes are then machined accordingly in the DUT during the manufacturing process. The first 8 to 20 hours, the chamber is left at ambient temperature, and the last 4 hours, the temperature is set to $+65^\circ\text{C}$ to accelerate the outgassing of the last remaining particles. To avoid leakages through the vacuum chamber external interfaces, the test circuit makes use of hermetic membrane discs, that allow the transmission of electromagnetic waves, but act as seal in the input and output waveguides.

The main test requirements can be found in Table C.1. Typically, the centre frequency of filters and other waveguide devices is the one selected for the test. This is not the worst case from a multipactor point of view, since in the edges of the filter bands, higher electric field values can be found, but is more reliable from a repeatability point of view, since the filter frequency response is more stable around the centre frequency than in the limits of the band. In the edges, small frequency shifts would considerably distort the measured results. A pulsed input power is the best option to reduce the power consumption and to avoid

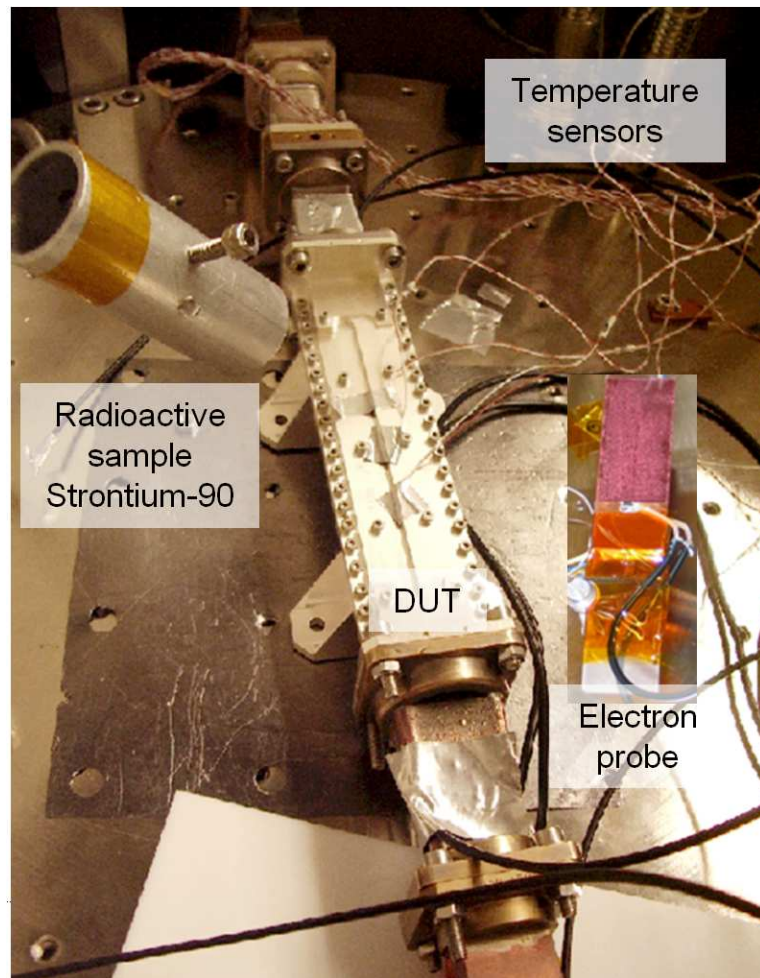


Figure C.5: Device under test, radioactive source, and multipactor detection sensors inside the vacuum chamber.

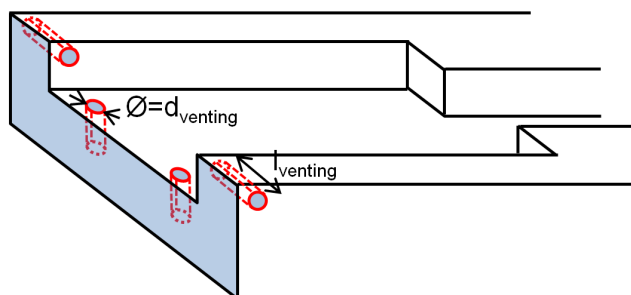


Figure C.6: Design of venting holes for hollow waveguide device multipactor testing.

Table C.2: Power steps schedule. Predicted threshold is 500 W.

Power [W]	Dwell time [min]
200	10
250	10
300	10
350	10
400	10
420	10
440	10
440	10
460	10
480	10
500	10
520	10
540	10
560	10
580	10
600	10
650	10
700	10
750	10
800	10
Total duration [min]	200

overheating the circuit, but depending on the available equipment for each frequency band, continuous wave (CW) power sources are also used.

The RF input power steps are established prior to the test, in order to estimate its total duration. The starting input power is generally 3 dB below the predicted threshold. Each power step is kept for a 10 min period (also known as dwell time), in order to ensure the stabilisation of the setup and the probability of detection. A typical power step schedule is included in Table C.2, assuming a predicted multipactor threshold of 500 W. If a multipactor discharge is detected at a certain power step, the RF input power is reduced to the previous step to extinguish the discharge. Then, the power is increased again in smaller steps (in an example like the one shown in Table C.2, 10 W-steps) with the same duration, until a second and a third event occur. This verifies the power threshold detection and refines the detected value.

C.2 Detection Methods

During a multipactor test, a series of signals and magnitudes are continuously measured in order to monitor the DUT and detect the multipactor discharge. Apart from recording

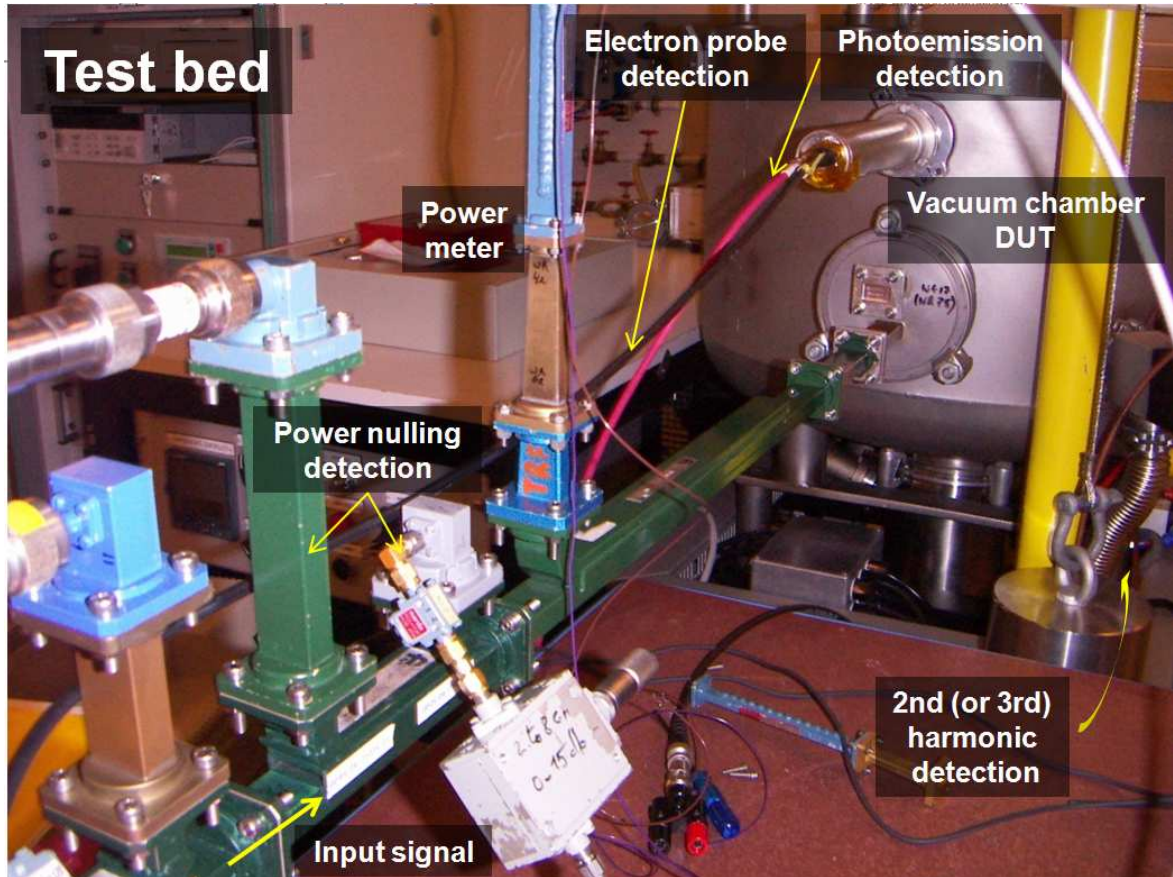


Figure C.7: Photo of the multipactor detection setup.

the insertion loss, return loss and temperature of the DUT, there is a diversity of detection methods, as seen in the photo of Fig. C.7, which were defined in the diagram of Fig. C.4 in the previous section. Such variety is required for cross-checking and to have the absolute certainty that a multipactor discharge has occurred. The multipactor discharge is a physically complicated mechanism, and that can start with “low-level” resonances before creating a full multipactor discharge. The combination of detection methods is, hence, an appropriate way to ensure a common understanding of the multipactor effect and to standardise its detection, enabling the sharing of results among different laboratories.

The multipactor detection methods can be classified in global and local methods. Local detection methods are installed close to the point of the actual discharge in the DUT. On the other hand, global methods are indirect indicators of the multipactor event. Generally, a multipactor detection setup is considered reliable if it implements at least two methods, and if one is global. The following list describes the different methods that were available during the tests performed in the frame of this thesis. Several figures show how an event is displayed in the corresponding measurement screen.

- **Electron probe detector** - local

An electron probe is introduced in the vacuum chamber through an interface, as shown in Fig. C.7. This method relies on the ability of a small positively charged probe (see Fig. C.5) to attract the free electrons generated as a result of a discharge. A high impedance amplifier connected to the probe provides impedance transformation to $50\ \Omega$. An oscilloscope or voltmeter may then be used to monitor the probe current. Fig. C.8 shows the peak indicating a multipactor event.

- **Third-harmonic detection** - global

Since a discharge spreads the input energy over the spectrum, the harmonics of the signal experience a boost in their power levels (cf. Chapter 1.1). Therefore, a detection chain consisting of a coupler, a bandpass filter, a low noise amplifier and a network analyser centred at the third harmonic is placed in the output of the vacuum chamber (see Fig. C.4). For optimum operation, the harmonics generated by the input high power amplifier need to be filtered out. The photo in Fig. C.9 shows the appearance of a multipactor discharge in this kind of detection method, which is very reliable. The upper curve shows the maximum values of the spectrum, while the lower one is showing the instantaneous spectral power density around the third harmonic. If the maximum curve suddenly jumps to a relatively higher level, this indicates a discharge.

- **Nulling of forward/reverse power detection** - global

The principle of this method is very similar to that of the third-harmonic detection. As mentioned in Chapter 1.1, a multipactor discharge also increases the return losses and modifies the phase in a microwave structure. Exploiting this phenomenon, this detection method is set up by coupling a portion of the input and reflected power into a phase- and amplitude-matching network, composed of a variable attenuator and a variable phase shifter (see Fig. C.4 and Fig. C.7). The system is balanced such that the difference between the two signals has a spectral density almost equal to zero. This nulled signal is monitored by a spectrum analyser and is very sensitive to amplitude and phase variations. A multipactor discharge breaks this balance, which results in high peaks in the spectrum analyser screen, like the ones shown in Fig. C.10. One disadvantage of this method is that the phase- and amplitude-matching network has to be adjusted manually, and re-adjustments are frequently required to achieve a good null.

- **Photoemission detection** - local

The photoemission probe is an optic fibre that enters in the vacuum chamber through the same interface as the electron probe (see Fig. C.7), and then is introduced inside the DUT through one of the venting holes. In this way, photoelectric emissions caused by a multipactor or corona discharge can be detected. A visualisation of this phenomenon is shown in Fig. C.11, in this case generated by a corona discharge on a microstrip device.

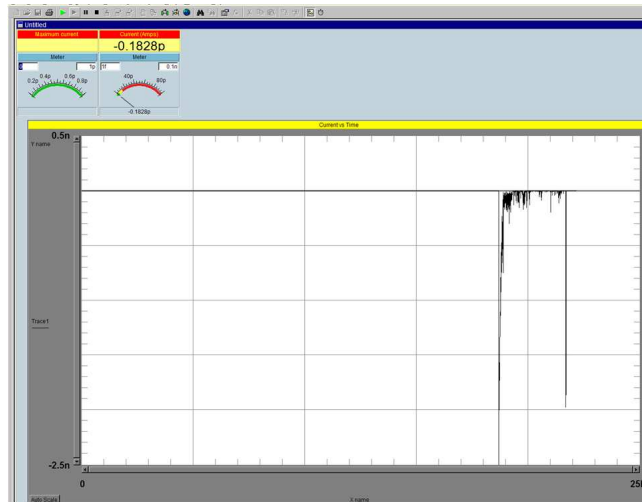


Figure C.8: Reading of the electron probe sensor with the peaks in the graph indicating a multipactor discharge.

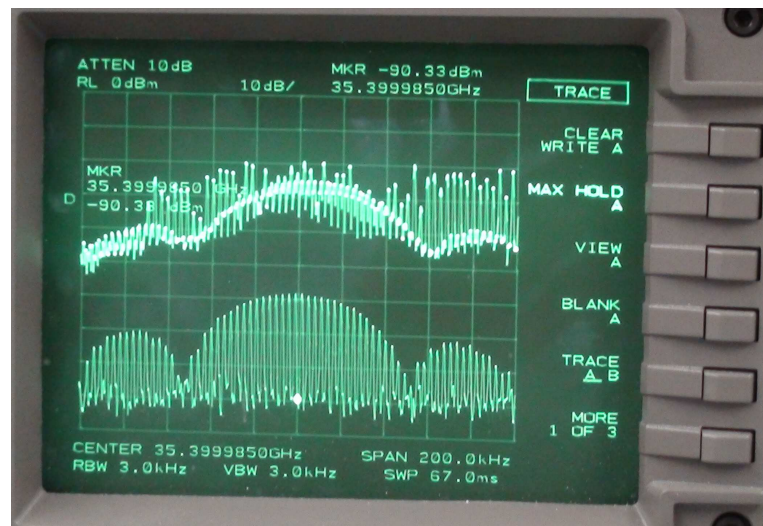


Figure C.9: Screenshot of the spectrum analyser of the third-harmonic detection chain showing a multipactor discharge, indicated by the gap between the maximum curve and the lower actual spectrum measurement. The “Max hold” display mode has been activated.



Figure C.10: Screenshot of the spectrum analyser of the nulling detection chain showing a multipactor discharge, indicated by the gap between the maximum curve (blue line) and the lower actual spectrum measurement (yellow line). Note that the attenuators and phase shifters need to be re-adjusted again to null the actual spectrum. The “Max hold” display mode has been activated.

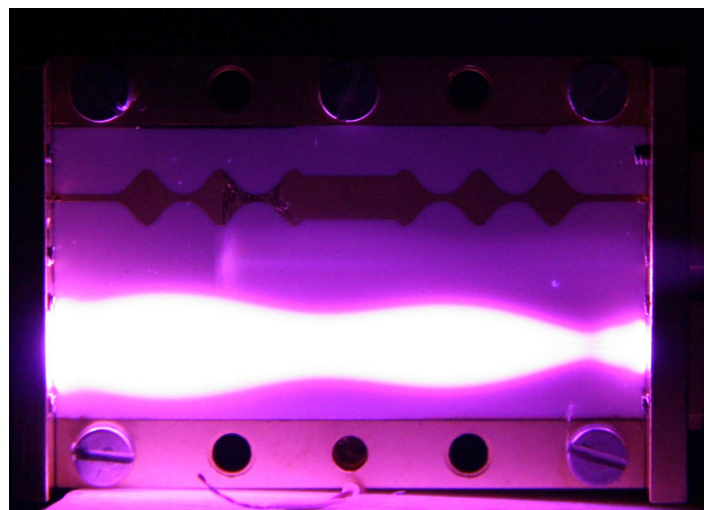


Figure C.11: Recorded photoemission generated by a corona discharge in a microstrip device. Source: ESA.

After the completion of the test procedure and the detection of the corresponding multipactor discharges, a test report is generated, usually including the screenshots of the different detection methods that indicate the multipactor events.

Appendix D

Curriculum Vitae

D.1 Education

- 2003 Advanced Studies Diploma (DEA) in the Telecommunication doctorate program at the Communications Department from the Universidad Politécnica de Valencia (UPV), Valencia, Spain.
- 2002 Master's Degree (MSc) in Telecommunication Engineering from UPV.

D.2 Professional Experience

- Since October 2012: Patent examiner with the European Patent Office, The Hague, The Netherlands.
Responsibilities: Examination of patent applications involving antennas.
- 2012: Earth observation technology engineer with the European Space Agency (ESA), Noordwijk, The Netherlands.
Responsibilities: Coordination of future technology development activities in the frame of the future European Earth observation satellite missions.
Supervisor: Dr. Jörg Callies.
- 2006-2011: Synthetic Aperture Radar (SAR) engineer with the German Aerospace Center (DLR), Microwave and Radar Institute, Satellite System Department, Wessling, Germany.
Responsibilities: Instrument calibration and system engineer of satellite projects like TerraSAR-X, TanDEM-X and Sentinel-1. Coordination of the ground segment commissioning phase of TanDEM-X.
Supervisors: Dr. Manfred Zink and Dr. Marco Schwerdt.

- 2004-2005: Microwave engineer with ESA, within the Microwave and Millimetre-Wave Section, Noordwijk, The Netherlands.

Responsibilities: Filter design and development of innovative waveguide filters for high power applications. Testing of RF multipactor discharges in the Payload Systems Laboratory at ESA-ESTEC.

Supervisors: Mr. David Raboso and Dr. Dietmar Schmitt

- 2003: Research scholarship, Communications Department, UPV, Valencia.

Responsibilities: Development of electromagnetic analysis tools.

Supervisor: Dr. Vicente E. Boria Esbert

- End 2002, beginning 2003: Stage at the Information Area of the UPV, Valencia.

Responsibilities: Development of databases for the university website.

D.3 Fields of Expertise

- **Earth observation satellites:**

Instrument calibration and system engineering of SAR missions.

Commissioning phase planning, coordination and execution.

Bistatic interferometry and Digital Elevation Model (DEM) calibration.

Baseline calibration algorithm development for InSAR systems.

Inter-satellite radiation and synchronisation RF links.

Lidar altimeter (ICESat) performance comparison with airborne SAR DEMs (ESAR-DLR).

- **RF and microwave analysis and design:**

Development and evaluation of electromagnetic simulators: waveguide devices, antenna radiation and wave propagation problems.

Design and manufacturing of innovative microwave waveguide filters.

Implementation of a prediction tool of the multipactor effect (high power vacuum discharge) in innovative microwave waveguide devices.

Practical experience with microwave laboratory measurement equipment: multipactor effect testing and thermal cycling for qualification of space hardware.

D.4 Informatics Skills

- Electromagnetic simulators and design tools:
HFSS, CST Microwave Studio, FEMT^{3D}, Matlab Simulink.
- Programming languages:
IDL, Java, Fortran, C++, XML, Mathematica, Pascal, HTML, Assembler, Visual Basic, data base management with SQL.

D.5 Languages

- English: Fluent at reading, writing and speaking.
- German: Fluent at reading, writing and speaking.
German School of Valencia for primary and secondary studies.
Certificate of German knowledge of the Goethe Institute.
- French: Fluent at reading, good at speaking and writing.
- Dutch: Fair at reading, basic at speaking and writing.
- Spanish: Mother tongue.

Appendix E

Publications

E.1 Papers in International Scientific Journals

- J. Hueso, D. Raboso, C. Ernst, D. Schmitt, V. E. Boria, B. Gimeno, M. Taroncher, and C. Vicente, “Optimized Multipactor-Resistant Wedge-Shaped Waveguide Bandpass Filters,”
IEEE Transactions on Plasma Science - Special Issue Vacuum Discharge Plasmas 2013, vol. 41, no. 8, pp. 2135-2144, August 2013.
- J. Hueso, D. Raboso, D. Schmitt, V. E. Boria, B. Gimeno, and C. Vicente, “Study of the Multipactor Effect in Bandpass Wedge-Shaped Waveguide Filters,”
IEEE Transactions on Electron Devices, vol. 58, no. 9, pp. 3205-3212, September 2011.
- J. Hueso, C. Vicente, B. Gimeno, V. E. Boria, S. Marini, and M. Taroncher, “Multipactor Effect Analysis and Design Rules for Wedge-Shaped Hollow Waveguides,”
IEEE Transactions on Electron Devices, vol. 57, no. 12, pp. 3508-3517, December 2010.
- M. Taroncher, J. Hueso, S. Cogollos, B. Gimeno, V. E. Boria, A. Vidal, H. Esteban, and M. Guglielmi, “Accurate Consideration of Metal Losses at Waveguide Junctions Using Admittance and Impedance Integral Equation Formulations,”
Radio Science, Washington, USA, August 2005.

E.2 Patent

- J. Hueso, D. Raboso, and D. Schmitt,
“Microwave Waveguide Filter with Non-Parallel Plates,”
Patent ESA/PAT/520; publication number: 2890787; filing date: 12-09-2005,
June 2005.

E.3 Papers in International Congresses

- J. Hueso, V. E. Boria, B. Gimeno, C. Vicente, and D. Raboso, “Investigation on the Multipactor Effect in Wedge-Shaped Waveguides,”
in Proc. Mulcopim Workshop 2011, Valencia, Spain, September 2011.
- F. D. Quesada, V. E. Boria, B. Gimeno, D. C. Rebenaque, J. P. Garcia, A. A. Melcón, J. Hueso, D. Schmitt, D. Raboso, C. Ernst, I. H. Carpintero, “Investigation of Multipaction Phenomena in Passive Waveguide Filters for Space Applications,”
in IEEE MTT-S International Microwave Symposium Digest, San Francisco, CA, USA, June 2006.
- M. Taroncher, J. Hueso, S. Cogollos, A. Vidal, V. E. Boria, B. Gimeno, “Efficient and Accurate Consideration of Ohmic Losses in Waveguide Diplexers and Multiplexers,”
in IEEE MTT-S International Microwave Symposium Digest, San Francisco, CA, USA, June 2006.
- J. Hueso, D. Schmitt, D. Raboso, C. Ernst, I. Hidalgo, V. E. Boria, and B. Gimeno, “Design of a Novel Inductive Band-Pass Waveguide Filter to Reduce the Risk of Multipactor Breakdown,”
in Proc. Mulcopim Workshop 2005, Noordwijk, ESTEC, The Netherlands, September 2005.
- J. Hueso, S. Cogollos, B. Gimeno, V. E. Boria, A. Vidal, H. Esteban, and M. Guglielmi, “Accurate Consideration of Metal Losses in Planar Waveguide Junctions Using an Efficient Integral Equation Technique,”
in Proc. MTT-S Dig. 2004, Texas, USA, June 2004.

E.4 Research Reports

- J. Hueso, “Análisis de Uniones Planares en Guías de Onda Incluyendo Pérdidas en los Materiales Conductores,”
Research Work: Diploma de Estudios Avanzados, Doctorado Comunicaciones,
Supervisors: V. E. Boria and S. Cogollos,
Universidad Politécnica de Valencia, Spain, July 2004.
- J. Hueso, “Evaluación de Simuladores Electromagnéticos para el Análisis y Optimización de Dispositivos Pasivos de Microondas,”
Final Project Telecommunication Engineering,
Supervisors: V. E. Boria and B. Gimeno,
Universidad Politécnica de Valencia, Spain, December 2002.

List of Acronyms

2-D	Two-dimensional
3-D	Three-dimensional
Ag	Silver
Ar	Argon
arb	Arbitrary waveguide
Au	Gold
BI-RME	Boundary Integral - Resonant Mode Expansion
BW	Bandwidth
C	Contour
C-band	Frequency band between 4 GHz and 8 GHz.
CN	Cyanide (carbon-nitrogen)
CPU	Central Processing Unit
CrN	Chromium nitride
CST	Computer Simulation Technology
CW	Continuous Wave
DC	Direct Current
DEA	Advanced studies diploma
DEM	Digital Elevation Model
DLR	German Aerospace Center

DUT	Device Under Test
ECSS	European Cooperation for Space Standardisation
EDM	Electronic Discharge Machining
EM	Electromagnetic
env	Envelope
ESA	European Space Agency
ESAR	Airborne Experimental SAR
ESTEC	European Space Technology Centre
FDTD	Finite Difference Time Domain
FEST3D	Full-wave Electromagnetic Simulation Tool
Fig	Figure
H₂	Hydrogen gas
He	Helium
HFSS	High Frequency Structure Simulator
HTML	HyperText Markup Language
HPA	High Power Amplifier
IDL	Interactive Data Language
IEEE	Institute of Electrical and Electronics Engineers
IMUX	Input Multiplexer
In	Indium
InSAR	Interferometric SAR
K-band	Frequency band between 18 GHz and 26 GHz.
Ka-band	Frequency band between 26 GHz and 40 GHz.
Ku-band	Frequency band between 12 GHz and 18 GHz.
L-band	Frequency band between 1 GHz and 2 GHz.
LNA	Low Noise Amplifier

MEST	Multipactor Electron Simulation Tool
MP	Multipactor
MRSE	Microwave Radar Shuttle Experiment
MSc	Master's Degree
N₂	Nitrogen gas
NASA	National Aeronautics and Space Administration
Ne	Neon
OMUX	Output Multiplexer
P-band	Frequency band between 0.216 GHz and 0.415 GHz.
PA	Power Amplifier
Pb	Lead
PhD	Doctorate academic degree
PIM	Intermodulation Product
Q factor	Quality factor of a resonator, defined by the ratio between its centre frequency and its bandwidth, or between its stored energy and its power loss
R	Rectangular
rect	Rectangular
refbox	Reference box
RF	Radio Frequency
RL	Return loss
S	Scattering
S-band	Frequency band between 2 GHz and 4 GHz.
SAR	Synthetic Aperture Radar
SEEC	Secondary Electron Emission Coefficient
SEY	Secondary Emission Yield
SRTM	Shuttle Radar Topography Mission

SQL	Structured Query Language
Sr	Strontium
st	Step
T	Transversal
TE	Transverse-Electric
TiN	Titanium nitride
TL	Transmission line
TM	Transverse-Magnetic
Transm	Transmitted
TRL	Technology Readiness Level
TT&C	Telemetry, Tracking and Telecommand
TWT	Travelling-Wave Tube
UPV	Universidad Politécnica de Valencia
W	Wedge-shaped
WG	Waveguide
WR	Standard designator of the size of a rectangular waveguide. It is accompanied by a number representing the width in hundredths of an inch.
X-band	Frequency band between 8 GHz and 12 GHz.
XML	Extensible Markup Language

List of Symbols

a	Width of a rectangular waveguide / Acceleration vector of an electron
A	Vector potential of the fundamental mode of an annular-section waveguide / Filter attenuation function
A_{IRIS}	Area of an iris in a waveguide discontinuity
A_{WALL}	Area of the frontal wall disc around an iris in a waveguide discontinuity
a_{Wedge}	Width of a wedge-shaped waveguide
α	Inclination angle between top and bottom plates of a wedge-shaped waveguide
$\hat{\alpha}$	Unitary vector in azimuthal direction in an annular-section waveguide
α_C	Attenuation constant parameter of a microwave signal
b	Height of a rectangular waveguide
β	Propagation constant
C	Capacitance
$Coll_{\text{max}}$	Maximum number of collision of the multipactor prediction simulation
d	Gap distance / Diameter
δ	Penetration depth / Average number of emitted electrons from a metallic wall per incident electron impact, SEEC, SEY
δ_{max}	Maximum value of the SEY curve, normally defined for normal impact
δ_{start}	Average number of emitted electrons from a metallic wall per incident electron impact for impact energies below the reference W_0
e	Absolute value of the electron charge / Multiplicity function / Euler's number

E	Instantaneous electric field
ε	Permittivity
ϵ	Factor of the EM fields of a normalised TE mode that depends on the mode indices
eV	Electron Volts
f	Frequency
$f \times d$	Frequency-gap-product
f_C	Cutoff frequency
g	Lumped-element filter model coefficient
γ	Complex argument of the propagation exponential / Relativistic factor
H	Instantaneous magnetic field
$h_{1,2}$	Height of the shortest and tallest side-wall of a wedge-shaped waveguide, respectively
h_{mean}	Average height of a wedge-shaped waveguide. It is the mean of h_1 and h_2
I	Current
j	Imaginary unit
J_1	First order Bessel function
J_S	Surface current density
K	Constant of an inverter / EM field denormalisation factor
k_C	Cutoff wavenumber
k_t	Transverse wavenumber of an annular-section waveguide
l	Waveguide length
L	Inductance
λ	Wavelength
λ_G	Guided-wavelength
M	Maximum number of effective electron used for averaging the different phases in the RF cycle of the multipactor prediction simulation

μ	Permeability
\mathbf{N}	Instantaneous Poynting vector
N_1	First order Neumann function
N_{Launch}	Maximum number of launch positions of the effective electron of the multipactor prediction simulation
N_{Power}	Maximum number of power steps of the multipactor prediction simulation
\hat{n}_{Wall}	Unitary vector normal to a waveguide wall pointing towards the interior of the device
ω	Angular frequency
p	Pressure / linear momentum
P	Power
P_{in}	Incident power
P_{LP}	Propagation losses
pos	Position vector of the electron
P_r	Reflected power
P_{th}	Multipactor power threshold
ϕ	Azimuth-coordinate of the spherical coordinate system
q	Electric charge
R_1	Radius of an annular-section waveguide corresponding to the smaller side-wall of a wedge-shaped waveguide
R_2	Radius of an annular-section waveguide corresponding to the broader side-wall of a wedge-shaped waveguide
R_{crit}	Radius of an annular-section waveguide corresponding to the trapped trajectory arc of a wedge-shaped waveguide
R_S	Surface resistance
S	Cross-section area
S_{max}	Maximum value of the accumulated <i>Secondary Sum</i> of the multipactor prediction simulation. If exceeded, simulation has to be interrupted

σ	Conductivity of a metal
t	Waveguide iris length
T_{avg}	Period of a harmonic signal over which to average its power density
$\theta_{C/E}$	Incidence angle of the collision/rebounded electron on a metallic wall of a waveguide device. Without subscript, just incidence angle or elevation-coordinate of the spherical coordinate system
u	Electron impact energy [eV]
V	Voltage
V_B	Breakdown voltage
v_C	Collision velocity of an electron against a waveguide wall
vel	Velocity vector of the electron
V_{th}	Multipactor voltage threshold
w	Waveguide iris width
W	Electron impact energy in eV
W_0	Reference energy of the SEY curve for the electron impact in eV
W_1	First crossover energy of the SEY curve in eV. It indicates the start of the electron multiplication region
W_2	Second crossover energy of the SEY curve in eV. It indicates the end of the electron multiplication region
W_C	Mean energy of the outbound electron following a statistical distribution
W_G	Standard deviation of the energy of the outbound electron following a statistical distribution
W_{max}	Electron impact energy that statistically generates the maximum possible secondary electrons (δ_{max})
Y	Admittance
Y_C	Characteristic admittance of a waveguide
Z	Impedance
Z_C	Characteristic impedance of a waveguide

Bibliography

- [1] F. Paschen, “Über die zum Funkenübergang in Luft, Wasserstoff und Kohlensäure bei verschiedenen Drucken erforderliche Potentialdifferenz,” *Annalen der Physik*, vol. 273, pp. 69–75, 1889.
- [2] J. R. M. Vaughan, “Multipactor,” *IEEE Transactions on Electron Devices*, vol. 35, pp. 1172–1188, July 1988.
- [3] ECSS Secretariat, “ECSS-E-20-01A: Space Engineering - Multipaction Design and Test,” tech. rep., ESA, May 2003.
- [4] C. Gutton, “Sur la décharge électrique à fréquence très élevée,” *Comptes-Rendus Hebdomadaires des Séances de l’Académie des Sciences*, vol. 178, pp. 467–470, 1924.
- [5] P. T. Farnsworth, “Television by Electron Image Scanning,” *Journal of Franklin Institute*, vol. 2, p. 411, 1934.
- [6] M. A. Furman, “The Electron-cloud Effect in the Arcs of the LHC,” tech. rep., CERN-LHC-Project-report-180, May 1998.
- [7] C. Hill and R. G. Carter, “Investigation of Possible Multipactor Discharge in a Klystron Input Cavity,” *Proceedings of the Vacuum Electronics Conference*, pp. 81–82, 2006.
- [8] J. S. Chang, P. A. Lawless, and T. Yamamoto, “Corona Discharge Processes,” *IEEE Transactions on Plasma Science*, vol. 19, pp. 1152–1166, December 1991.
- [9] C. Vicente, “Passive Intermodulation and Corona Discharge for Microwave Structures in Communication Satellites,” PhD Thesis, Technische Universität Darmstadt, Germany, May 2005.
- [10] J. Way, D. Evans, and C. Elachi, “The SIR-C/X-SAR mission,” *Proceedings of the Geoscience and Remote Sensing Symposium*, vol. 2, p. 593, August 1993.
- [11] A. Woode and J. Petit, “Diagnostic Investigations into the Multipactor Effect, Susceptibility Zone Measurements and Parameters Affecting a Discharge,” tech. rep., ESA-Working paper No.1556, November 1989.

- [12] M. Ludovico, G. Zarba, and L. Accatino, "Multipaction Analysis and Power Handling Evaluation in Waveguide Components for Satellite Antenna Applications," *Antennas and Propagation Society International Symposium*, vol. 2, pp. 266–269, July 2001.
- [13] E. W. B. Gill and A. von Engel, "Starting Potentials of High-Frequency Gas Discharges at Low Pressure," *Proceedings of the Royal Society A*, vol. 192, pp. 446–463, February 1948.
- [14] A. J. Hatch and H. B. Williams, "The Secondary Electron Resonance Mechanism of Low-Pressure High-Frequency Gas Breakdown," *Journal of Applied Physics*, vol. 25, pp. 417–423, April 1954.
- [15] A. J. Hatch and H. B. Williams, "Multipacting Modes of High-Frequency Gaseous Breakdown," *Physical Review*, vol. 112, pp. 681–685, November 1958.
- [16] M. A. Furman and M. T. F. Pivi, "Probabilistic Model for the Simulation of Secondary Electron Emission," *Physical Review Special Topics - Accelerators and Beams*, vol. 5, December 2002.
- [17] V. E. Semenov, E. I. Rakova, D. Anderson, M. Lisak, and J. Puech, "Multipactor in Rectangular Waveguides," *Physics of Plasmas*, vol. 14, March 2007.
- [18] V. E. Semenov, E. I. Rakova, R. Udiljak, D. Anderson, M. Lisak, and J. Puech, "Conformal Mapping Analysis of Multipactor Breakdown in Waveguide Irises," *Physics of Plasmas*, vol. 15, March 2008.
- [19] R. Woo, "Multipacting Discharges between Coaxial Electrodes," *Journal of Applied Physics*, vol. 39, pp. 1528–1533, March 1968.
- [20] V. E. Semenov, N. Zharova, R. Udiljak, D. Anderson, M. Lisak, and J. Puech, "Multipactor in a coaxial transmission line. Part II: Particle-in-cell simulations," *Physics of Plasmas*, vol. 14, March 2007.
- [21] A. Perez, C. Tienda, C. Vicente, S. Anza, J. Gil, B. Gimeno, V. E. Boria, and D. Raboso, "Prediction of Multipactor Breakdown Thresholds in Coaxial Transmission Lines for Travelling, Standing and Mixed Waves," *IEEE Transactions on Plasma Science*, vol. 37, pp. 2031–2040, October 2009.
- [22] S. Riyopoulos, D. Chernin, and D. Dialetis, "Theory of Electron Multipactor in Crossed Fields," *Physics of Plasmas*, vol. 2, pp. 3194–3213, 1995.
- [23] R. A. Kishek, Y. Y. Lau, L. K. Ang, A. Valfells, and R. M. Gilgenbach, "Multipactor Discharge on Metals and Dielectrics: Historical Review and Recent Theories," *Physics of Plasmas*, vol. 5, pp. 2120–2126, 1998.
- [24] A. Kryazhev, M. Buyanova, V. Semenov, D. Anderson, M. Lisak, J. Puech, L. Lapiere, and J. Sombrin, "Hybrid Resonant Modes of Two-Sided Multipactor and Transition to the Polyphase Regime," *Physics of Plasmas*, vol. 9, pp. 4736–4743, 2002.

- [25] V. Semenov, A. Kryazhev, D. Anderson, and M. Lisak, "Multipactor Suppression in Amplitude Modulated Radio Frequency Fields," *Physics of Plasmas*, vol. 8, pp. 5034–5039, November 2001.
- [26] S. Anza, M. Mattes, C. Vicente, J. Gil, D. Raboso, V. E. Boria, and B. Gimeno, "Multipactor Theory for Multicarrier Signals," *Physics of Plasmas*, vol. 18, no. 032105, 2011.
- [27] S. Anza, C. Vicente, D. Raboso, J. Gil, B. Gimeno, and V. E. Boria, "Enhanced Prediction of Multipaction Breakdown in Passive Waveguide Components Including Space Charge Effects," *IEEE MTT-S International Microwave Symposium Digest*, pp. 1095–1098, June 2008.
- [28] W. C. Tang and C. M. Kudsia, "Multipactor Breakdown and Passive Intermodulation in Microwave Equipment for Satellite Applications," *Proceedings of the IEEE 1990 Military Communications Conference (MILCOM)*, vol. 1, pp. 181–187, September 1990.
- [29] M. Ezoe, M. Nakanishi, N. Masayuki, and J. Shouguo, "Effects of Interfacial Phenomena on Dielectric Breakdown of Filled Epoxy Resin," *Proceedings of the Eleventh International Symposium on High Voltage Engineering*, vol. 4, no. 467, pp. 244–247, 1999.
- [30] J. Tückmantel, C. Benvenuti, D. Bloess, D. Boussard, G. Geschonke, E. Habel, N. Hilleret, S. Juras, H. P. Kindermann, J. Uythoven, C. Wyss, and M. Stirbet, "Improvements to Power Couplers for the LEP2 Superconducting Cavities," *Proceedings of the Particle Accelerator Conference*, vol. 3, pp. 1642–1644, May 1995.
- [31] R. L. Geng and H. S. Padamsee, "Exploring Multipacting Characteristics of a Rectangular Waveguide," *Proceedings of the Particle Accelerator Conference*, vol. 1, pp. 429–431, April 1999.
- [32] E. Hall, "On a New Action of the Magnet on Electric Currents," *American Journal of Mathematics*, vol. 2, no. 3, pp. 287 – 292, 1879.
- [33] W. G. Dunbar, D. L. Schweickart, J. C. Horwath, and L. C. Walko, "High Frequency Breakdown Characteristics of Various Electrode Geometries in Air," *Conference Record of the Power Modulator Symposium*, pp. 221 – 224, 1998.
- [34] R. L. Geng, H. S. Padamsee, and V. D. Shemelin, "Multipacting in a Rectangular Waveguide," *Proceedings of the Particle Accelerator Conference*, June 2001.
- [35] K. Primdahl, R. Kustom, and J. Maj, "Reduction of Multipactor in RF Ceramic Windows Using a Simple Titanium-Vapor Deposition System," *Proceedings of the Particle Accelerator Conference*, vol. 3, pp. 1687–1689, May 1995.
- [36] S. Feltham and D. Raboso, "Coatings to Prevent Multipactor Effect in High Power Components for Space," Final Report, ESA-ESTEC, 1989.

- [37] D. Raboso, L. Galán, I. Montero and D. Wolk, “Porous Metal Coating for Suppressing Secondary Emission and Multipactor,” 2006. identifier: ESA/PAT/524; filing date: 2006.
- [38] A. Hatch, “Suppression of Multipacting in Particle Accelerators,” *Nuclear Instruments and Methods*, vol. 41, no. 2, pp. 261 – 271, 1966.
- [39] J. R. Montejo-Garai, J. A. Ruiz-Cruz, and J. M. Rebollar, “Design of Self-Equalised Elliptic Filter Channels in Ka-Band Implemented in Rectangular H-Plane Waveguide,” *Proceedings of the 36th European Microwave Conference*, pp. 1087–1090, September 2006.
- [40] I. Arnedo, J. Gil, N. Ortiz, T. Lopetegi, M. A. G. Laso, M. Sorolla, M. Thumm, D. Schmitt, and M. Guglielmi, “Ku-band High-power Lowpass Filter With Spurious Rejection,” *Electronic Letters*, vol. 42, pp. 1460–1461, December 2006.
- [41] J. Hueso, D. Raboso, and D. Schmitt, “Microwave Waveguide Filter with Non-Parallel Plates,” 2005. Publication number: 2890787 ; identifier: ESA/PAT/520; filing date: 12-09-2005; publication date: 05-06-2009.
- [42] E. Chojnacki, “Simulation of a Multipactor-Inhibited Waveguide Geometry,” *Physical Review Special Topics - Accelerators and Beams*, vol. 3, p. 032001, March 2000.
- [43] R. L. Geng, H. Padamsee, S. Belomestnykh, P. Goudket, D. M. Dykes, and R. G. Carter, “Suppression of Multipacting in Rectangular Coupler Waveguides,” *Nuclear Instruments and Methods in Physics Research A*, no. 508, pp. 227–238, 2003.
- [44] F. D. Quesada, V. E. Boria, B. Gimeno, D. C. Rebenaque, J. P. Garcia, A. A. Melcón, J. Hueso, D. Schmitt, D. Raboso, C. Ernst, and I. Hidalgo, “Investigation of Multipaction Phenomena in Passive Waveguide Filters for Space Applications,” *IEEE MTT-S International Microwave Symposium Digest*, pp. 246–249, June 2006.
- [45] U. Jordan, D. S. Dorozhkina, V. E. Semenov, T. Olsson, D. Anderson, M. Lisak, J. Puech, I. M. Nefedov, and I. Shereshevskii, “Microwave Corona Breakdown Around Metal Corners and Wedges,” *IEEE Transactions on Plasma Science*, vol. 35, June 2007.
- [46] V. E. Semenov, E. I. Rakova, N. Zharova, D. Anderson, M. Lisak, and J. Puech, “Simulations of the Multipactor Effect in Hollow Waveguides with Wedge-Shaped Cross Section,” *IEEE Transactions on Plasma Science*, vol. 36, pp. 488–493, April 2008.
- [47] J. Hueso, C. Vicente, B. Gimeno, V. E. Boria, S. Marini, and M. Taroncher, “Multipactor Effect Analysis and Design Rules for Wedge-Shaped Hollow Waveguides,” *IEEE Transactions on Electron Devices (TED)*, vol. 57, pp. 3508–3517, December 2010.
- [48] Ansoft, “HFSS: 3-D Full-wave Electromagnetic Field Simulation,” 2009.

- [49] Computer Simulation Technology, “CST Microwave Studio v.5,” 2005.
- [50] AuroraSAT, “Full-Wave Electromagnetic Simulation Tool 3-D v.6.6,” June 2012.
- [51] ESA-ESTEC and AuroraSAT, “ECSS Multipactor Tool,” 2010.
- [52] J. Lara, F. Pérez, M. Alfonseca, L. Galán, I. Montero, E. Román, and D. Raboso, “Multipactor Prediction for On-Board Spacecraft RF Equipment with the MEST Software Tool,” *IEEE Transactions on Plasma Science*, vol. 34, pp. 476–484, April 2006.
- [53] F. Vanin, D. Schmitt, and R. Levy, “Dimensional Synthesis for Wideband Waveguide Filters,” *IEEE MTT-S International Microwave Symposium Digest*, vol. 2, pp. 463–466, June 2004.
- [54] P. Soto, E. Tarín, V. E. Boria, C. Vicente, J. Gil, and B. Gimeno, “Accurate Synthesis and Design of Wideband and Inhomogeneous Inductive Waveguide Filters,” *Transactions on Microwave Theory and Techniques*, vol. 58, pp. 2220–2230, August 2010.
- [55] G. Conciauro, M. Guglielmi, and R. Sorrentino, *Advanced Modal Analysis: CAD Techniques for Waveguide Components and Filters*. Hoboken, New Jersey: John Wiley and Sons, 1998.
- [56] S. Cogollos, S. Marini, V. E. Boria, P. Soto, A. Vidal, H. Esteban, J. V. Morro, and B. Gimeno, “Efficient Modal Analysis of Arbitrarily Shaped Waveguides Composed of Linear, Circular, and Elliptical Arcs Using the BI-RME Method,” *IEEE Transactions on Microwave Theory and Techniques*, vol. 51, no. 12, pp. 2378–2390, 2003.
- [57] P. Overfelt and D. White, “TE and TM Modes of Some Triangular Cross-Section Waveguides Using Superposition of Plane Waves,” *IEEE Transactions on Microwave Theory and Techniques*, vol. 34, pp. 161–167, January 1986.
- [58] A. Álvarez, G. Connor and M. Guglielmi, “New Simple Procedure for the Computation of the Multimode Admittance or Impedance Matrix of Planar Waveguide Junctions,” *IEEE Transactions on Microwave Theory and Techniques*, vol. 44, pp. 413–418, March 1996.
- [59] S. Cogollos Borrás, “Caracterización Modal de Guías Arbitrarias y Aplicación a Dispositivos de Microondas,” PhD Thesis, Universidad Politécnica de Valencia, Spain, May 2002.
- [60] J. Hueso, “Análisis de Uniones Planares en Guías de Onda Incluyendo Pérdidas en los Materiales Conductores,” Research Work: Diploma de Estudios Avanzados, Doctorado Comunicaciones, Universidad Politécnica de Valencia, Spain, July 2004.
- [61] G. F. Dionne, “Origin of Secondary-electron-emission Yield-curve Parameters,” *Journal of Applied Physics*, vol. 46, pp. 3347–3351, August 1975.

- [62] J. R. M. Vaughan, "A New Formula for Secondary Emission Yield," *IEEE Transactions on Electron Devices*, vol. 36, p. 1963, September 1989.
- [63] J. R. M. Vaughan, "Secondary Emission Formulas," *IEEE Transactions on Electron Devices*, vol. 40, p. 830, April 1993.
- [64] C. Vicente, M. Mattes, D. Wolk, H. Hartnagel, J. Mosig, and D. Raboso, "Multipactor Breakdown Prediction in Rectangular Waveguide Based Components," *IEEE MTT-S International Microwave Symposium Digest*, June 2005.
- [65] J. D. Jackson, *Classical Electrodynamics (3rd ed.)*. New York: Wiley, 1998.
- [66] L. Verlet, "Computer Experiments on Classical Fluids. I. Thermodynamical Properties of Lennard-Jones Molecules," *Physical Review*, vol. 159, pp. 98–103, July 1967.
- [67] Q. Spriter and M. Walter, "Classical Molecular Dynamics Simulation with the Velocity Verlet Algorithm at Strong External Magnetic Fields," *Journal of Computational Physics*, vol. 152, pp. 102–119, June 1999.
- [68] E. Somersalo, P. Ylä-Oijala, D. Porch, and J. Sarvas, "Computational Methods for Analyzing Electron Multipacting in RF Structures," *Particle Accelerators*, vol. 59, pp. 107–141, 1998.
- [69] A. Coves, G. Torregrosa-Penalva, C. Vicente, B. Gimeno, and V. E. Boria, "Multipactor Discharges in Parallel-Plate Dielectric-Loaded Waveguides Including Space-Charge Effects," *IEEE Transactions on Electron Devices*, vol. 55, pp. 2505–2511, September 2008.
- [70] A. Shih and C. Hor, "Secondary Emission Properties as a Function of the Electron Incidence Angle," *IEEE Transactions on Electron Devices*, vol. 40, p. 824, April 1993.
- [71] E. Whittaker and G. Robinson, *The Trapezoidal and Parabolic Rules: A Treatise on Numerical Mathematics*. New York: Dover, 1967.
- [72] S. B. Cohn, "Direct-coupled-resonator Filters," *Proceedings of the Institute of Radion Engineers (IRE)*, vol. 45, pp. 187–196, February 1957.
- [73] G. Matthaei, L. Young, and E. M. T. Jones, *Microwave Filters, Impedance-matching Networks and Coupling Structures*. Artech House, 1964.
- [74] R. W. Daniels, *Approximation Methods for Electronic Filter Design*. New York: McGraw-Hill, 1974.
- [75] D. M. Pozar, *Microwave Engineering*. John Wiley and Sons, 1998.

- [76] J. Hueso, D. Schmitt, D. Raboso, C. Ernst, I. Hidalgo, V. E. Boria, and B. Gimeno, "Design of a Novel Inductive Bandpass Waveguide Filter to Reduce the Risk of Multipactor Breakdown," *Proceedings of the 5th International Workshop Multipactor, Corona and Passive intermodulation in Space RF Hardware Conference (MULCOPIM)*, pp. 67–78, September 2005.
- [77] R. A. Kishek, "Ping-pong Modes: a New Form of Multipactor," *Physical Review Letters*, vol. 108, no. 35003, pp. 1218–1221, 2012.
- [78] J. Hueso, D. Raboso, D. Schmitt, V. E. Boria, B. Gimeno, and C. Vicente, "Study of the Multipactor Effect in Bandpass Wedge-Shaped Waveguide Filters," *IEEE Transactions on Electron Devices (TED)*, vol. 58, pp. 3205–3212, September 2011.
- [79] R. E. Collin, *Series on Electromagnetic Wave Theory: Field Theory of Guided Waves*. New York: IEEE Press, 2nd ed., 1991.
- [80] C. A. Balanis, *Advanced Engineering Electromagnetics*. New York: John Wiley and Sons, 1989.
- [81] M. Taroncher, J. Hueso, S. Cogollos, B. Gimeno, V. E. Boria, A. Vidal, H. Esteban, and M. Guglielmi, "Accurate Consideration of Metal Losses at Waveguide Junctions Using Admittance and Impedance Integral Equation Formulations," *Radio Science*, August 2005.
- [82] G. Gerini, M. Guglielmi, and G. Lastoria, "Efficient Integral Equation Formulations for Impedance or Admittance Representation of Planar Waveguide Junction," *IEEE MTT-S International Microwave Symposium Digest*, vol. 3, pp. 1747–1750, June 1998.
- [83] D. Raboso, U. Wochner, M. Baumann, and M. König, "Regulated Electron Gun for RF Testing," 2006. identifier: ESA/PAT/523; filing date: 2006.